School of Chemical and Petroleum Engineering

Carbon Nanotubes Based Nanostructured Catalysts for Water Electrolysis and Fuel Cells

Yi Cheng

This thesis is presented for the Degree of

Doctor of Philosophy

of

Curtin University

September 2014

Declaration

To the best of my knowledge and belief this thesis contains no material previously published by any other person except where due acknowledgement has been made.

This thesis contains no material which has been accepted for the award of any other degree or diploma in any university.

Signature:……

Date:……...

ABSTRACT

Water splitting and fuel cells are considered the most important energy storage and conversion technologies and have attracted tremendous attention. However, the widely commercial applications of these technologies are hindered by the low catalytic activity and durability of catalysts. CNTs have been extensively applied as catalysts or supports to develop catalysts with enhanced activity and durability for their unique properties such as large specific surface area, excellent chemical and mechanical properties and high electrical conductivity. The overall objective of this thesis is to develop high active, durable CNTs based catalysts. And this thesis includes two parts: part 1 focuses on CNTs and their hybrids for water splitting especially on the most difficult half reaction-OER, and part 2 concentrates on developing PtRu-CNTs catalysts for fuel cell applications.

Part 1

The electrochemical properties of the CNTs were investigated in the first part of this thesis. Pristine CNTs composed of between 2-7 concentric tubes and an outer diameter of 2-5 nm have been demonstrated of outstanding catalytic activity for the OER in alkaline solution as compared with single-walled and multi-walled CNTs (SWNTs & MWNTs), and they also show better activity for HER and OER. One hypothesis is that for the OER, HER and ORR on CNTs with specific number of walls, efficient electron transfer occurs through electron tunneling between outer walls and inner tubes, which significantly promotes the charge transfer reaction of OER, HER and ORR at the surface of outer wall of the CNTs. For SWNTs, such

separation of functionality for OER, HER and ORR is not possible, while effective separation or dual functionality of the CNTs diminishes as the increase of number of walls due to the reduced driven force such as dc bias or photo activated electron follow across the walls or layers of MWNTs.

The mechanism and kinetics for OER on CNTs were studied. The electrocatalytic activities of CNTs show distinctive volcano-type dependence on the number of concentric tubes or walls of CNTs and the best activities are obtained on CNTs composed of between 2-7 concentric tubes in acid, neutral and alkaline solutions. The OER is limited by the deprotonation of water in acid and neutral conditions, which results in the high Tafel slope and high overpotential for OER in acid and neutral conditions. The concentration of OH^- plays a vital role in OER on all the CNTs. OER on CNTs composed of between 2-7 concentric tubes in alkaline solutions shows higher kinetics and enhanced activities. The favorable kinetics parameters demonstrated the proposed tunneling effect which highlights the favorable electron transfer pathway in the inner tubes for CNTs composed of between 2-8 concentric tubes and with an OD of 2-5 nm.

Based on the distinctive proterties of CNTs, zinc phthlocyanine functionalized CNTs were developed for photo electrochemical water oxidation. The zinc phthalocyanine functionalized CNTs with 2-7 concentric tubes show enhanced photo-electrochemical activity for water oxidation due to the enhanced electron transfer and electron-hole separation properties through tunneling effect.

A Metal-CNTs (M-CNTs) hybrids were synthesized by arc-discharge (M-CNTs-Arc) and CVD (M-CNTs-CVD), and the M-CNTs hybrids exhibit a core-shell like structure, in which metal nanoparticles (NPs) encapsulated by graphite shell are

connected by double walled CNTs or single walled CNTs. M-CNTs-Arc with $NiCo_{0.16}Fe_{0.34}$ metal core connected by double walled CNTs shows very high activity and superior stability for OER, achieving a current density of 100 A g^{-1} at overpotential (η) of 0.29 V and 500 A g^{-1} at η = 0.37 V in 1 M KOH solution. This is probably the highest activity reported for OER in alkaline solutions.

Part 2

In the second part of the thesis, PtRu based catalysts with average size of ~ 3 nm were supported onto noncovalent functionalized CNTs through microwave assisted self-assembly method. The influences of the functionalization agents such as poly (diallyldimethylammonium chloride) (PDDA); PEI; 1-aminopyrene (AP); terahydrofuran (THF) were investigated. Nitrogen-containing functional groups of the functionalization agents play a critical role in the electrocatalystic activity of PtRu NPs supported on CNTs. PtRu NPs supported on PEI, AP and PDDA functionalized CNTs exhibited significantly higher electrocatalystic activity and stability for the electro-oxidation of methanol as compared with PtRu supported on THF-CNTs and conventional acid-treated CNTs. The superior activity of PtRu supported on functionalized CNTs is most likely due to the strong interaction between the electron rich nitrogen-containing functional groups of the functionalization agents such as PEI, AP, PDDA and the PtRu NPs assembled on CNTs.

Based on the understanding on the controlled synthesis of nanoparticle alloys, $PtRuCo_x$ NPs with a Co-rich PtRuCo core and PtRu skinned shell supported on CNTs have been developed by successive dealloying and annealing the PtRuCo alloy particles prepared by self-assembly of Pt, Ru, and Co into PEI functionalized CNTs. The best results were obtained on dealloyed $PtRuCo_x$ NPs annealed at 450 ^oC, which

exhibits ~1 nm thick PtRu shell and Co rich PtRuCo core. The chronoamperometry studies at 0.4 V (*vs*. Ag/AgCl) show that core-shell structured $PtRuCo_x$ catalysts exhibit a high activity (40 A g^{-1}_{pt}) and significant tolerance towards CO poisoning for MOR as compared with PtRuCo alloy (8 A g^{-1}_{Pt}) and conventional PtRu/C (25 A g^{-1}_{Pt}) electrocatalysts. The core-shell structured $PtRuCo_x$ is also structurally stable; maintaining 74% of the activity after 1000 cycles between -0.2 to 1 V (*vs*. Ag/AgCl), significantly higher than 49% for PtRuCo alloy catalysts and 25% for PtRu/C catalysts under identical test conditions. The substantially enhanced electrocatalytic activity and durability of core-shell structured $PtRuCo_x$ indicate great potential to enhance the catalystic properties by fine-tuning of the nanoscale architecture.

Acknowledgements

Firstly, I would like to express my sincerest gratitude to my supervisor, Prof. San Ping Jiang, who supported me throughout the whole PhD project with patience and expertise. Under his continuous guidance, support and inspiration, I had made substantial progress in cultivating my scientific research ability. More importantly, his charismatic personality, nice smile and prudent working attitude always inspire me, and worth learning for my whole life. Without him, my thesis can not finish successfully.

I want to show my deep grateful to the director of the institute, Prof. Chun-zhu Li for providing such nice research facilities. I also want to thanks the technique assistance from Prof. Martin Saunders from UWA, and thank you for the supports from Prof. Peikang Shen from Sun Yat-Sen University, Prof. Huiming Cheng and Chang Liu from Shenyang National Laboratory for Material Science.

I would like to thanks our group members and the classmates in the department of Chemical Engineering for their friendship and help (in no particular order): Dr. Kongfa Chen, Dr. Na Ai, Dr. Yi Wang, Dr. Kun Zhang, Dr. Xun Hu, Dr. Shu Zhang, Dr. Ling Zhao, Dr. Beibei He, Dr. Dehua Dong, Dr Chunbo Jiang, Xin Shao, Zhitao Wang, Lei Zhang, Tingting Li, Liping Wu, Shuai Wang, Jin Zhang, Chengcheng Wang, and Mortaza Gholizadeh. I also would like to thank you Amir Memar for his contribution of testing the photo-electrochemical activity.

I deeply appreciate my friends, David, Nina, Fang Cheng for their help offered. Thanks my friends in China who always support me.

Most of all, I would like to thank my family, mother, father and my litter brother, who always support me without condition. Without their selfless love and concern, it

would be impossible for me to complet this thesis.

To my beautiful girlfriend Shou Zhang, who sacrificed her youth waiting for me.

LIST OF PUBLICATIONS

[1] **Cheng, Y.;** Xu, C.; Shen, P. K.; Jiang, S. P., Effect of nitrogen-containing functionalization on the electrocatalytic activity of PtRu nanoparticles supported on carbon nanotubes for direct methanol fuel cells. *Applied Catalysis B: Environmental* **2014,** *158–159* (0), 140-149.

[2] **Cheng, Y.;** Jiang, S. P., Highly effective and CO-tolerant PtRu electrocatalysts supported on poly(ethyleneimine) functionalized carbon nanotubes for direct methanol fuel cells. *Electrochimica Acta* **2013,** *99* (0), 124-132.

[3] **Cheng, Y.**; Liu, C.; Cheng, H.-M.; Jiang, S. P., One-Pot Synthesis of Metal–Carbon Nanotubes Network Hybrids as Highly Efficient Catalysts for Oxygen Evolution Reaction of Water Splitting. *ACS Applied Materials & Interfaces* **2014,** *6* (13), 10089-10098.

[4] **Cheng, Y**.; Xu, C.; Jia, L.; Gale, J. D.; Zhang, L.; Liu, C.; Shen, P. K.; Jiang, S. P., Pristine carbon nanotubes as non-metal electrocatalysts for oxygen evolution reaction of water splitting. *Applied Catalysis B: Environmental* **2015,** *163* (0), 96-104.

[5] **Cheng, Y**.; Shen, P. K.; Jiang, S. P., NiOx nanoparticles supported on polyethylenimine functionalized CNTs as efficient electrocatalysts for supercapacitor and oxygen evolution reaction. *International Journal of Hydrogen Energy*. Accepted.

[6] Zhang, J.; **Cheng, Y.;** Lu, S.; Jia, L.; Shen, P. K.; Jiang, S. P., Significant promotion effect of carbon nanotubes on the electrocatalytic activity of supported Pd NPs for ethanol oxidation reaction of fuel cells: The role of inner tubes. *Chem. Commun.* **2014**. Accepted

[7] **Cheng Y.**, Shen P. K., Saunders M., Jiang S. P.. Core-Shell Structured PtRuCox Nanoparticles on Carbon Nanotubes as Highly Active and Durable Electroctalysts for Direct Methanol Fuel Cells. *Electrochimica Acta* **2015**.

Table of Contents

List of Figures

List of Tables

List of Abbreviations

OER- Oxygen Evolution Reaction ORR- Oxygen Reduction Reaction
HER- Hydrogen Evolution Reaction MOR- Methanol Oxidation Reaction
PEMFCs- Proton Exchange Membrane Fuel Cells or Polymer Electrolyte Membrane Fuel Cells DMFCs- Direct Methanol Fuel Cells
CNTs- Carbon Nanotubes SWNTs- Single-Walled CNTs
DWNTs- Double-Wall CNTs MWNTs- Multi-Walled CNTs
CVD- Chemical Vapor Deposition PEI- Polyethylenimine
XRD- X-ray Diffraction XANES- X-ray Absorption Near Edge Structure
XPS- X-ray Photoelectron Spectroscopy ESA- Electrochemical Active Surface Area
TEM- Transmission Electron Microscope TG- Thermo gravimetric
GCE- Glass Carbon Electrode SCE- Saturated Calomel Electrode
LSV- Linear Scan Voltammetry CV- cyclic voltammetry

Chapter 1: Introduction

1.1 Background

The on growing concerns on global warming, climate change and environmental pollution, as well as global energy crisis urge human being to develop environmentally friendly technologies for renewable energy storage and conversion. Hydrogen, which can simultaneously reduce the dependence on crude oil and the emission of greenhouse gases and other pollutants, is considered as a clean energy carrier similar to electricity and has been touted as a replacement for fossil fuels. However, the key fact is that H_2 is not a source of energy but only a way of storing and transporting it. So hydrogen fuel must be "manufactured" by extracting it from water and methane[1-4]. One of the most important hydrogen production processes is methane reforming, in which carbon dioxide will be released into the atmosphere[5]. Splitting water molecules, $H_2O \rightarrow 2H_2 + O_2$, using renewable power sources or nuclear energy to produce hydrogen is considered the only technology that can currently make large amounts of hydrogen without using fossil fuels. Solar energy is a renewable energy source of sufficient scale to meet rising global energy demand[6], however, the widespread utilization of solar energy is impeded unless efficient and cost-effective methods for its storage can be realized[6-9]. Nature executes solar-to-fuels conversion on a massive scale in green plants and microorganisms through the process of photosynthesis, while only 1% of the incident solar energy is stored in the form of fuels in plant biomass[10]. Using commercially available photovoltaic PV device with electrolyzer system can generate hydrogen from solar power at efficiencies exceeding 20%[10, 11]. However, the efficiency of the photo- or electro-

chemical water splitting is still very low and greatly constrained by the high overpotentials of OER because it is thermodynamically and kinetically unfavorable for removing of four electrons to form oxygen-oxygen double bond[12-14].

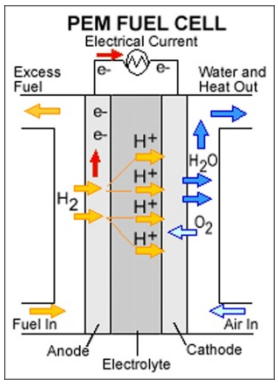

Figure 1.1 The schematic of PEMFC

As a critical loop in the hydrogen economy, PEMFCs are a type of fuel cell being developed for transport applications as well as for stationary fuel cell and portable fuel cell applications. Conceptually, a PEMFC is simply a device that takes in oxygen from the air and hydrogen/small liquid organic molecules from a tank, and react them in a controlled way to produce electric power (Figure 1.1). In practice, PEMFCs typically utilize platinum based catalysts on the anode to split the hydrogen/small liquid organic molecules into positive ions (protons) and negative electrons. The proton passes through the membrane to the cathode to combine with oxygen to produce water. The electrons must pass through an external circuit to rejoin the H_2 ion on the cathode. The chemical equation of hydrogen PEM fuel cell is:

Anode: $2H_2 \rightarrow 4H^+ + 4e^-$

Cathode: $O_2 + 4H^+ + 4e^- \rightarrow 2H_2O$

Each cell produces approximately 1.1 volts, so to reach the required voltage the cells are combined to produce stacks[15-17]. If methanol were used as fuel, DMFCs are named. DMFCs are promising candidates as power sources for portable electronic devices due to the advantages of high volumetric energy density (17,900 kJ/L) and easy storage of methanol fuel, and has been extensively studied [18, 19]. However, after more than ten years of development, challenges, including the cutting back on the use of expensive catalysts and hydrogen production for fuel-cell vehicles, remain.

As mentioned above, the catalysts are the key components for fuel cell and water splitting. Hence, it is of critical importance to develop catalysts with high activity, superior stability and low cost for fuel cells and water splitting. CNTs and its hybrids are intensively studied for ORR [20-23], fuel oxidation [24, 25] and water splitting[26, 27] for its unique properties such as large specific surface area, excellent mechanical and electrical properties. It is widely accepted that incorporating catalyst with CNTs can not only increase the activity, but also the durability due to the excellent electron transfer ability and chemical inertness of CNTs[28, 29]. Huge amount of efforts were invested into developing CNTs hybrids, but, challenges remain. CNTs need to be functionalized due to the inert nature in order to obtain high dispersion of metal-CNTs hybrids owing to the chemical inert of pristine CNTs [30, 31]. Exploring easy and simple method to functionalize the CNTs to improve the activity and stability of metal-CNTs hybrids based catalysts simultaneously, and studying the influence of different functionalization agents on the performance of catalysts are of great significance.

1.2 Objectives and outline of the thesis

In general, CNTs without N and P doping have little electrocatalytic activity. We discovered that the activity of water electrolysis on CNTs is closely related with the

properties of CNTs such as number of walls or diameter rather than the impurities or surface area [Australia Patent, Application number 2013900671]. However, it mechanism lie behind this phenomeneon is remain unexplored. The main objective of the PhD project is to investigate the electro-chemical properties of CNTs as function as the number of walls and developing Metal-CNTs hybrids for water splitting and fuel cells. More specifically, the project has the following objectives:

- Studying the role of inner tubes or walls of CNTs on the activity for OER, HER and ORR.

- Studying the electrocatalytic activity of metal-CNTs hybrids with the aim to develop high active, stable and low cost catalysts for OER.

- Investigating the dye functionalized CNTs for photo electrochemical water oxidation.

- Studying the role of the N-containing polyelectrolyte and/or solvent on the morphology, distribution and electrocatalytic activity of the Pt-based NPs supported on CNTs.

- Developing the PtRu core-shell nanoparticles (NPs) that supported on CNTs to achieve both better activity and stability at the same time.

Based on the objectives as listed above, this thesis consists of 10 chapters. Chapter 2 is focusing on the literature review of the state-of-the-art in the field. The experimental results and discussions are presented in chapters 3-9. In chapter-10, conclusions of the thesis were made and the suggestions for future work were proposed.

Chapter 1: Introduction

This chapter briefly introduced the background of water splitting and fuel cells. The objective and the outline of the thesis are presented.

Chapter 2: Literature Review

Three parts were included in this chapter. Firstly, the principle of water splitting by electrolysis and the latest development of metal based catalysts for HER and OER were summarized. Secondly, the Pt based catalysts especially the methods for developing core-shell structures were briefly summarized. Thirdly, the properties of CNTs and the application of CNTs in the area of water splitting and fuel cells were discussed.

Chapter 3: Pristine Carbon Nanotubes as Non-metal Electrocatalysts for Oxygen Evolution Reaction of Water Splitting (*This chapter is based on the paper published on* ***Applied Catalysis B: Environmental****.)*

This chapter demonstrates, for the first time, that pristine CNTs composed of between 2-7 concentric tubes and an outer diameter of 2-5 nm have an outstanding activity for the OER in alkaline solution as compared with SWNTs & MWNTs.

Chapter 4: Beneath the Surface: The Role of Inner Tubes on the Electrocatalytic Activity of Pristine Carbon Nanotubes in Alkaline Solutions

CNTs with 2-7 concentric tubes or walls show significantly better activity for H_2 evolution, O_2 evolution and O_2 reduction reactions, as compared to SWNTs and

MWNTs. Such activity is related to the effect of inner tubes of CNTs rather than the surface active sites or properties of CNTs.

Chapter 5: Oxygen Evolution Reaction on Pristine Carbon Nanotubes: Kinetics and Mechanism

This chapter further studied the kinetics and mechanism of OER on CNTs in acid, neutral and alkaline solutions. The OER mechanism was illustrated through study the Tafel slope and reaction order. The rates determine steps of OER on the CNTs were further explored.

Chapter 6: Non-covalently functionalized Carbon Nanotubes with Zinc Phthalocyanines for Photo-electrochemical Water Oxidation

This chapter is the extension of chapter 3-5, and developed a zinc phthalocyanine functionalized CNTs for photo electrochemical water oxidation. The results provide a new opportunity for developing photo-catalysts using CNTs with 2-7 concentric tubes.

Chapter 7: One-Step Synthesized Metal-Carbon Nanotubes Network Hybrids as Highly Efficient Catalysts for Oxygen Evolution Reaction of Water Splitting (*This chapter is based on the paper published on* ***ACS Applied Materials & Interfaces****.)*

Two metal-carbon nanotubes (M-CNTs) hybrids were synthesized by arc-discharge and CVD methods as electrocatalysts for OER in alkaline solutions. The results demonstrate a highly efficient, scalable and low-cost one-step synthesis method for developing highly active and stable catalysts for electrochemical water splitting in alkaline solutions.

Chapter 8: Effect of Nitrogen-containing Functionalization on the Electrocatalystic Activity of PtRu Nanoparticles Supported on Carbon Nanotubes for Methanol Oxidation of Fuel Cells (*This chapter is based on the paper published on* **Applied Catalysis B: Environmental***.)***

PtRu NPs with average size of ~ 3 nm are supported onto poly (diallyldimethylammonium chloride) (PDDA); polyethylenimine (PEI); 1-aminopyrene (AP); terahydrofuran (THF) functionalized MWNTs using microwave assisted self-assembly method. Nitrogen-containing functional groups of the functionalization agents play a critical role in the electrocatalystic activity of PtRu NPs supported on CNTs. The superior activity of PtRu supported on functionalized CNTs is most likely due to the strong interaction of the electron rich nitrogen-containing functional groups of the functionalization agents such as PEI, AP and in less extend PDDA and the PtRu NPs assembled on CNTs.

Chapter 9: New Core-Shell Structured PtRuCo$_x$ Nanoparticles Supported on Carbon Nanotubes as Highly Active and Durable Electroctalysts for Direct Methanol Fuel Cells (*This chapter is published* **Electrochemica Acta)***

New PtRuCo$_x$ nanoparticles (NPs) with a Co-rich PtRuCo core and PtRu skinned shell supported on CNTs were developed as electrocatalysts for MOR. The core-shell PtRuCo$_x$ NPs were prepared through a successive dealloying and annealing treatment of PtRuCo alloy particles. The core-shell structured PtRuCo$_x$ that supported on CNTs not only show enhance activity for methanol oxidation but also structurally stable; maintaining 74% of the activity after 1000 cycle between -0.2 to 1 V (*vs*. Ag/AgCl).

Chapter 10: Conclusions and Recommendations

The overall achievements of this thesis are summarized and the recommendations for future studies are listed in this chapter.

References

1. K. Zeng and D. Zhang, *Progress in Energy and Combustion Science*, 2010, 36, 307-326.
2. D. Pletcher and X. Li, *International Journal of Hydrogen Energy*, 2011, 36, 15089-15104.
3. A. Ursua, L. M. Gandia and P. Sanchis, *Proceedings of the Ieee*, 2012, 100, 410-426.
4. M. Carmo, D. L. Fritz, J. Merge and D. Stolten, *International Journal of Hydrogen Energy*, 2013, 38, 4901-4934.
5. D. R. Palo, R. A. Dagle and J. D. Holladay, *Chemical Reviews*, 2007, 107, 3992-4021.
6. H. B. Gray, *Nature Chemistry*, 2009, 1, 7-7.
7. T. R. Cook, D. K. Dogutan, S. Y. Reece, Y. Surendranath, T. S. Teets and D. G. Nocera, *Chemical Reviews*, 2010, 110, 6474-6502.
8. M. G. Walter, E. L. Warren, J. R. McKone, S. W. Boettcher, Q. Mi, E. A. Santori and N. S. Lewis, *Chemical Reviews*, 2010, 110, 6446-6473.
9. *Nat Photon*, 2012, 6, 136-137.
10. Y. Surendranath and D. G. Nocera, in *Progress in Inorganic Chemistry*, John Wiley & Sons, Inc., 2011, DOI: 10.1002/9781118148235.ch9, pp. 505-560.
11. D. G. Nocera, *Accounts of Chemical Research*, 2012, 45, 767-776.
12. H. Dau, C. Limberg, T. Reier, M. Risch, S. Roggan and P. Strasser, *Chemcatchem*, 2010, 2, 724-761.
13. R. L. Doyle, I. J. Godwin, M. P. Brandon and M. E. G. Lyons, *Physical Chemistry Chemical Physics*, 2013, 15, 13737-13783.
14. I. C. Man, H.-Y. Su, F. Calle-Vallejo, H. A. Hansen, J. I. Martínez, N. G. Inoglu, J. Kitchin, T. F. Jaramillo, J. K. Nørskov and J. Rossmeisl, *Chemcatchem*, 2011, 3, 1159-1165.
15. G. Sandstede, E. J. Cairns, V. S. Bagotsky and K. Wiesener, in *Handbook of Fuel Cells*, John Wiley & Sons, Ltd, 2010, DOI: 10.1002/9780470974001.f104011.
16. M. M. Mench, in *Fuel Cell Engines*, John Wiley & Sons, Inc., 2008, DOI: 10.1002/9780470209769.ch6, pp. 285-379.
17. S. Srinivasan and B. Kirby, in *Fuel Cells*, Springer US, 2006, DOI: 10.1007/0-387-35402-6_9, ch. 9, pp. 441-573.
18. X. Zhao, M. Yin, L. Ma, L. Liang, C. Liu, J. Liao, T. Lu and W. Xing, *Energy & Environmental Science*, 2011, 4, 2736-2753.
19. Y. L. Hsin, K. C. Hwang and C.-T. Yeh, *Journal of the American Chemical Society*, 2007, 129, 9999-10010.

20. D. C. Higgins, D. Meza and Z. Chen, *The Journal of Physical Chemistry C*, 2010, 114, 21982-21988.
21. J. Zhang, S. Tang, L. Liao, W. Yu, J. Li, F. Seland and G. M. Haarberg, *Journal of Power Sources*, 2014, 267, 706-713.
22. W. Yang, Y. Wang, J. Li and X. Yang, *Energy & Environmental Science*, 2010, 3, 144-149.
23. B. P. Vinayan and S. Ramaprabhu, *Nanoscale*, 2013, 5, 5109-5118.
24. C. Hu, Y. Cao, L. Yang, Z. Bai, Y. Guo, K. Wang, P. Xu and J. zhou, *Applied Surface Science*, 2011, 257, 7968-7974.
25. Y. Cheng and S. P. Jiang, *Electrochimica Acta*, 2013, 99, 124-132.
26. H.-Y. Wang, F.-M. Wang, Y.-Y. Wang, C.-C. Wan, B.-J. Hwang, R. Santhanam and J. Rick, *The Journal of Physical Chemistry C*, 2011, 115, 8439-8446.
27. H. Kim and S. H. Moon, *Carbon*, 2011, 49, 1491-1501.
28. W. Li, C. Liang, J. Qiu, W. Zhou, H. Han, Z. Wei, G. Sun and Q. Xin, *Carbon*, 2002, 40, 791-794.
29. X. Wang, W. Li, Z. Chen, M. Waje and Y. Yan, *Journal of Power Sources*, 2006, 158, 154-159.
30. L. J. Meng, C. L. Fu and Q. H. Lu, *Prog. Nat. Sci.*, 2009, 19, 801-810.
31. A. Hirsch and O. Vostrowsky, in *Functional Molecular Nanostructures*, ed. A. D. Schluter, Springer-Verlag Berlin, Berlin, 2005, vol. 245, pp. 193-237.

Chapter 2: Literature Review

2.1 Introduction

World energy consumption will grow by 56 % between 2010 and 2040, and the total world energy use will rise from 524 quadrillion British thermal units (Btu) in 2010 to 630 quadrillion Btu in 2020 and to 820 quadrillion Btu in 2040 according to *International Energy Outlook 2013*. Among them, about 80% are from fossil fuels. The sustainability of fossil fuel based energy and the consequent environmental issues, such as global warming and pollutant gas emission, are the major challenges that human being is facing[1, 2]. Consequently, finding alternative energy sources and developing high-efficient, environmentally friendly and low-cost technologies for renewable energy storage and conversion to meet the increasing global energy demands and environmental issues are the general consensus between scientists and policy makers[1].

Hydrogen has long been considered the most promising clean candidate to replace fossil fuels for its advantage of high energy density. The solar energy is the only ultimately source of energy and is of enormous potential for hydrogen production. For example, the solar power density is around 1 kW m^{-2} on a clear day which in totoal is approximately 10 000 greater than the current primary energy consumption of the entire world. Owing to the diurnal variation in local isolation, widespread utilization of solar energy remains challenging unless efficient and cost-effective technologies for its storage can be realized[3-6]. The solar energy can be stored in the form of hydrogen by water splitting through mimic the solar-to-fuels conversion in green

plants and microorganisms. The direct configuration to generate hydrogen by splitting water is to use a photovoltaic (PV) device which produces electricity to drive the electrolyzer by collecting solar radiation[7, 8]. The hydrogen produced from water splitting is of high purity and is considered the idea candidate for PEM fuel cells[9, 10]. However, the efficiency of the photo- or electro-chemical water splitting is still very low and is greatly constrained by the high overpotentials of OER because it is thermodynamically and kinetically unfavorable for removing of four electrons to form oxygen-oxygen double bond[11-13].

On the other hand, there are great interests in developing different kinds of high-efficient and low-cost clean energy conversion technologies, such as fuel cells, as a replacement for combustion-based energy sources due to rising global energy demands, depletion of fossil fuel reserves, and environmental pollution problems[14-16]. PEMFCs, which produces electricity from the electrochemical oxidation of small molecule fuels, such as hydrogen, methanol or ethanol, is attracting significant interests from researchers. Membrane electrode assembly (MEA), where fuel such as hydrogen or methanol is oxidized on the anode and oxygen is reduced on the cathode, is the key component in a PEMFCs. Fuel-cell MEAs must meet three major criteria: cost, performance and durability. The catalysts remain one of the major challenges for developing commercial viable fuel cells[15, 17]. Most MEA catalysts used today are based on Pt (in the form of nanoparticles (NPs) dispersed on carbon black supports), which has a decisive impact on costs due to the high price of this scarce precious metal. The cathode ORR and the anode oxidation of methanol is orders of magnitude slower than the anode hydrogen oxidation reaction and thus limits performance, so almost all researches and developments focus on improving the activity for cathode

ORR[17] and anode MOR[18, 19]. And platinum (Pt) is considered best-known catalyst for ORR[20, 21], MOR[19, 22] and has been intensively studied.

Developing active, durable and low-cost catalysts for fuel cells and water splitting is remaining the hot-spot in research. Huge amount of efforts have been invested in this area in the past two decades. Considering the scope of this thesis, the literature review in this chapter includes three parts:

1) The principle of water splitting through electrolysis and the catalysts for HER and OER are summarized.

2) Due to the wide application and study of Pt based catalyst, the second part of this chapter will briefly review the latest strategies in the development of the active and/or durability of Pt based catalysts for fuel cells applications and especially focus on the core-shell structures.

3) CNTs are known as a promising candidate as catalysts supports for fuel cells and water splitting. In the third part of this chapter, the properties of CNTs and the latest application of CNTs in the area of developing catalyst for fuel cells and water splitting will be reviewed.

2.2 Water electrolysis

2.2.1 The principle

The overall water electrolysis can be described by the following equation:

$$2H_2O \rightarrow 2H_2 + O_2 \qquad (1)$$

The whole process is composed of HER on the cathode and OER on the anode of the electrolyzer[8, 23, 24]. Hence in alkaline solution the corresponding cathode and anode reactions are

$4H_2O + 4e \rightarrow 2H_2 + 4OH^-$ (2)

$4OH^- \rightarrow O_2 + 2H_2O + 4e$ (3)

And in acid, water electrolysis can be described as follow

$4H^+ + 4e \rightarrow 2H_2$ (4)

$2H_2O \rightarrow O_2 + 4H^+ + 4e$ (5)

In neutral conditions, water electrolysis is

$4H_2O + 4e \rightarrow 2H_2 + 4OH^-$ (2)

$2H_2O \rightarrow O_2 + 4H^+ + 4e$ (5)

Eq. 2 and 4 is for HER and it is rapid and fairly reversible. The water electrolysis is more favorable in acid and alkaline conditions due to large amount of deprotonated water molecules are available for OER (in alkaline) or HER (in acid), this also explains why water electrolysis in neutral condition is more kinetically difficult. The overall water electrolysis is an uphill reaction with highly positive change in Gibbs free energy regardless in acid, neutral or alkaline conditions, indicating the process is an endothermic and nonspotaneous chemical reaction. Hence, an energy input must be applied to drive the thermodynamic unfavorable reaction (1). The theoretical minimum voltage, which denoted as reversible cell voltage for electrolysis, can be expressed as function of $\triangle G$ by means of[11, 23, 25]

$V_{rev} = \triangle G/zF$ (6)

Where z is the number of electron moles transferred per hydrogen mole (z = 2) and F is the Faraday constant, which represents the charge on one mole of electrons (96 485 C/mol).

Practically, thermal energy is also provided by means of electricity and the total energy required to split one mole of water is determined by the enthalpy change ($\triangle H$). In ideal water electrolysis process, the minimum voltage for water electrolysis

known as thermo-neutral (tn) voltage is determined by the enthalpy. Hence, in ideal condition, the V_{tn} can be expressed by[23]

$V_{tn} = V_{\Delta H} = \Delta H/zF = (\Delta G + T\Delta S)/zF$ (7)

Here, T is the temperature and ΔS is the entropy change. Practically, the $V_{tn} > \triangle H/zF$ in electrolysis due to the thermodynamic irreversibility related to water vapor contained in hydrogen and oxygen follows and thermal losses due to convection and radiation.

At standard temperature and pressure (298.15 K and 1 atm), G^o = 237.21 kJ mol^{-1}, ΔS^o = 0.1631 kJ/mol K, and ΔH^o = 285.84 kJ/mol. Thus, the V_{rev} and the V_{tn} of an electrolytic cell at standard conditions are obtained: V_{rev} =1.229 V and V_{tn} = 1.481 V respectively. Hence, water electrolysis operated under 1.48 V and above 1.231 V requires additional heat supply from surroundings even neglecting ohmic and other losses, otherwise electrochemical water electrolysis will lead to the cell cooling down[23].

2.2.1.1 Overpotential

Overpotential is the potential applied on an electrode to initiate the electrode reaction over or above the equilibrium potential, which is the deviation of the observed the applied cell voltage V_{op} (electrolysis) from the thermodynamic reversible cell voltage V_{rev} [Eq. (6)]. Hence the overpotential for electrolysis can be expressed as:

$\eta = V_{op} - V_{rev} = \eta_{OER} + \eta_{HER} + \eta_{\Omega}$ (8)

Electrolysis overpotentials are relate to a kinetic hindrance of individual elementary reaction steps due to activation barriers for OER and HER. The overpotential for OER is significantly higher than that for HER due to OER involves four electron transfer process. Normally, several hundred millivolts overpotential are required in order to

generate oxygen at an appreciable rate[25-27]. Consequently, there are considerable research efforts devoted to decreasing oxygen evolution overpotentials.

2.2.1.2. Tafel slope

Tafel slopes are preferred to evaluate the intrinsic properties of OER catalysts due to the Tafel slope's ability to distinguish between electronic and geometric (surface-area) effects compared with the relative apparent catalyst performance based on exchange current densities[28]. In the process of OER, overpotential is result from the kinetic hindrance of individual elementary reaction steps due to activation barriers[25]. On this basis, overpotential as function of the current density is linked with the slowest of the elementary reaction steps, the rate-determining step (RDS), with the highest kinetic activation barrier. The Tafel equation can be acquired from the slope by plotting overpotential η as a function of the current density j obtained from steady-state polarization in logarithm form,

$\eta = a + b \log j$ (9)

Where b is the Tafel slope. Eq(9) imply that a plot of η will be linear with a Tafel slope b and intercept a.

2.2.1.3 Turn-over frequency (TOF)

Turnover frequency (TOF) is derived from the turn over number, and is used to refer turnover per unit time. In recent years, the concept of a turnover frequency (TOF) has been increasingly applied to surface catalysis. The TOF for OER may be defined as the number of oxygen molecules generated per surface catalytic site per second. Accordingly, the TOF can be calculated as follows[12]

$$\mathrm{TOF} = \frac{1}{N_{\mathrm{cat}}}\frac{\mathrm{d}N_{\mathrm{O_2}}}{\mathrm{d}t} = \frac{i_E N_{\mathrm{A}}}{nFN_{\mathrm{cat}}} = \frac{1}{4}\frac{j_E}{Q} \quad (12)$$

where N_{cat} is the number of catalytic sites, N_{O2} is the number of molecules of oxygen produced, N_A is Avogadro's number, Q is the charge and, i_E and j_E are the current and current density at a potential E associated with oxygen evolution.

2.2.2 Electrocatalysts for water electrolysis

Water electrolysis includes HER on the cathode and OER on the anode. HER is facile on noble metals, such as Pt, Ru and Rh, for example, Pt is consider the best catalyst for OER with an overpotential of around 0-20 mV in acid and 0-100 mV in alkaline solution. However, industrial hydrogen evolution was initially carried out on mild steel and nickel electrodes due to the high cost of noble metals. Researches recently focus on developing low-cost materials for HER with high activity. On the other hand, due to the kinetically unfavorable of OER compared with HER, considerable research efforts have been devoted to the design, synthesis and characterization of OER catalysts over the past several decades with the aim of achieving high amount of oxygen with low overpotential and at low cost.

2.2.2.1 Electrocatalysts for HER

HER, as a fundamental step of electrochemical water splitting, requires a favorable catalyst to achieve fast kinetics for practical applications. The best materials for hydrogen evolution are noble metals: Pt, Pd, Rh or Ir. Trasatti investigated the HER in acid solution, a volcano plot through plotting the exchange currents for HER vs. the strength of intermediate metal-hydrogen (M-H) bond, and the volcano plots indicate that Pt slightly better than Pd, then comes Rh, Ir[29]. However these materials cannot be used directly as solid metals for industrial processes because of their high cost.

Strategies were developed to improve the electrocatalytic activity of HER on noble metals. Subbaraman et al. discovered that a controlled arrangement of nanometer-scale $Ni(OH)_2$ clusters on platinum electrode surfaces can achieve a factor of 8 activity increase in catalyzing the HER relative to state-of-the-art metal and metal-oxide catalysts. The high HER activity is attributed to the bifunctional effect between the edges of the $Ni(OH)_2$ clusters and Pt surfaces[30]. In order to reduce the noble metal loading, Pt and Pd monolayer catalysts were developed. Greeley et al. performed a series of detailed measurements of the exchange-current density for pseudomorphic Pd overlayers on the close-packed surfaces of Au, Pt, PtRu, Rh, Ir, Ru, and Re single-crystal transition metal substrates. The order of activity for HER is Pd/PtRu>Pd/Pt>Pd/RhPd/Ir>Pd/Ru>Pd/Re≈Pd/Au[31]. Kelly et al. explores the opportunity to substantially reduce the cost of HER electrocatalysts by supporting one monolayer (ML) of platinum (Pt) on low-cost molybdenum carbide (Mo_2C) substrate. The ML Pt-Mo_2C thin film showed Pt-like HER activity while displaying excellent stability under HER conditions[32]. Sub-monolayer to monolayer (ML) of Pt supported on tungsten carbide (WC) allows for a significant decrease in Pt costs for HER[33]. Density functional theory (DFT) calculations and experimental measurements indicate that the ML Pt-WC surface exhibits chemical and electronic properties that are very similar to bulk Pt for simple reactions such as the HER[34].

Replacement of Pt with earth-abundant materials would be attractive to facilitate the global scalability of the potential clean-energy technologies. Molybdenum disulfide MoS_2, which exhibits high HER activity and good stability in acidic solutions, is a potential alternative to replace Pt. Jaramillo et al. demonstrated the HER activity of MoS_2 is correlate linearly with the number of edge sites on the MoS_2 catalyst. The DFT-calculated ΔG_H of the MoS_2 edge site is slightly positive at +0.08 eV. The

calculations suggest only 1 in 4 edge atoms evolve molecular H_2 at a given time, unlike Pt(111) which operates at a H-coverage of ~1 ML. If all MoS_2 edge sites could be made to adsorb H, activity could be increased by a factor of 4 [35]. Kibsgaard et al. design the surface structure of MoS_2 to preferentially expose edge sites to improve catalysis by synthesizing contiguous large-area thin films of a highly ordered double-gyroid MoS_2 network with nanoscaled pores. The high surface curvature of this catalyst mesostructure exposes a large fraction of edge sites leading to excellent activity for electrocatalytic hydrogen evolution[36]. Similar with MoS_2, monolayered nanosheets of chemically exfoliated WS_2 were demonstrated as efficient catalysts for HER with very low overpotentials. Analyses indicate that the enhanced electrocatalytic activity of WS_2 is associated with the high concentration of the strained metallic octahedral phase in the as-exfoliated nanosheets [37].

Nickel phosphide NPs (Ni_2P) have been investigated for electrocatalytic activity and stability for the HER in acidic solutions. The authors claim that Ni_2P NPs had among the highest HER activity of any non-noble metal electrocatalyst reported to date, producing H_2(g) with nearly quantitative faradaic yield, while also affording stability in aqueous acidic media[38]. Cobalt phosphide NPs, CoP, have also been prepared and evaluated as electrocatalysts for the HER under strongly acidic conditions (0.50 M H_2SO_4, pH 0.3). Electrodes comprised of CoP NPs on a Ti support (2 mg cm^{-2} mass loading) produced a cathodic current density of 20 mA cm^{-2} at an overpotential of -85 mV. The CoP/Ti electrodes were stable over 24 h of sustained hydrogen production in 0.50 M H_2SO_4[39]. The results demonstrate the potential of these groups of catalysts.

Recently, metal free HER electrocatalysts were realized. Zheng et al. reported a metal-free catalyst, consisting of carbon and nitrogen only, by coupling graphitic-

carbon nitride (g-C_3N_4) with nitrogen-doped graphene (*N*-graphene; NG). This metal-free hybrid shows comparable electrocatalytic HER activity with the existing well-developed metallic catalysts, such as nanostructured MoS_2 materials, although its activity is not as high as that of the state-of-the-art Pt catalyst. Electrochemical measurements in combination with thermodynamic calculations reveal that its unusual electrocatalytic properties originate from a synergistic effect of this hybrid nanostructure, in which g-C_3N_4 provides highly active hydrogen adsorption sites, while N-graphene facilitates the electron-transfer process for the proton reduction. The findings provide new avenues towards replacing noble metals for HER[40].

2.2.2.2 Metal based catalysts for OER

2.2.2.2.1 Noble metal based catalyst for OER

Proton exchange membrane electrolyzers are promising candidates for energy storage due to the advantages of higher current densities (capable of achieving values above 2 A cm^{-2}), high voltage efficiency, rapid system response and high gas purity[41-43]. PEM electrolyzer requires high active OER catalysts that are stable in acid, and noble metal based on Ru, Ir, Pd, Pt, Au and their alloys are important candidates for developing OER catalysts in acid electrolyte[26, 44, 45]. Since early 1960s, large amount of researches have been conducted to search for high performance OER catalysts[45-49]. For example, Damjanov et al. studied the kinetics of the OER on Rh, Ir, and Pt-Rh alloys using a liquid electrolyte, showing activities in the following order: Pt < Pt-Rh < Rh < Ir [50]. Miles and Thomason studied the periodic variations of overvoltage for OER in acid solutions (0.1 M H_2SO_4, 80±2 ^oC) by cyclic voltammetry, and proved that the order of OER activity is Ir∼Ru > Pd > Rh > Pt > Au > Nb> Zr ∼ Ti ∼ Ta (Fig. 2.1).[26] Peter Strasser group comparatively investigated the Ru, Ir and Pt bulk

materials and carbon supported NPs in 0.1 M $HClO_4$, and they observation demonstrate the OER activities of both bulk materials and NPs form oxides are in the order of oxidized Ru> oxidized Ir > oxidized Pt[27]. And a Tafel slope of 44, 63, 145 mV dec^{-1} were observed on bulk Ru, Ir and Pt electrode, which indicates the kinetics on Ru and Ir are superior to Pt. These findings point out that Ir NPs emerge as a future nanoscaled OER catalyst for acidic PEM electrolyzer devices due to the higher stability of Ir compared with Ru[27]. It is widely accepted that the most active noble metals for OER are Ru and Ir oxide in acid, however, this concept is overturned by the latest report of Danilovic et al., who found that the most active oxide is Os (Fig. 2.2), and the consequence of activity for OER in acid media is Os >> Ru > Ir > Pt >> Au, however, the stability of Os << Ru < Ir < Pt << Au [45]. Hence, Ru and Ir base OER electrode are still considered as the most important candidates that are suitable for developing high active and durable anode catalysts for PEM electrolyzers and reversible PEM fuel cells.

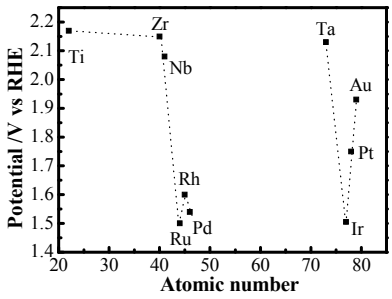

Figure 2.1. Summary of cyclic voltammetric results for various metallic elements in 0.1M H_2SO_4 at 80 ^oC. The potential vs. RHE is shown where the current density attains 2 mA cm^{-2} using a potential sweep rate of 50 mV s^{-1}.[26]

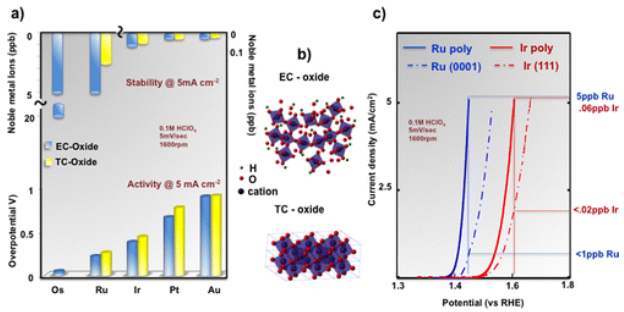

Figure 2.2. Relationships between activity and stability of the OER on monometallic oxides. (a) Inverse trends in activity and stability of oxide materials prepared by thermal chemical (TC) and electrochemical (EC) methods; (b) Schematic representation of the crystalline rutile TC-oxide and amorphous EC-oxide structures. (c) Current–potential curves recorded during the first positive sweep for the OER on single crystal and polycrystalline electrodes. The lower defect density single crystals are less active but more stable than the polycrystalline electrodes, confirming that, in addition to the nature of metal element, defects play one of a central roles in the activity stability relationships. [45]

2.2.2.2.2 Fe, Co, Ni and Mn mono-oxide

The high cost of RuO_2 and IrO_2 and their poor long-term stability in alkaline conditions renders their widespread commercial utilization. Hence base transition metals such as Fe, Co, Ni and Mn become the choice for OER although the OER overpotentials are higher than RuO_2 and IrO_2[51, 52]. Lian investigated nickel and cobalt metal electrodes in 1 M KOH, and the results indicate that both preoxidized and potential cycled Ni electrodes show better activity than Co electrode in terms of Tafel slope and current density. For example, The Tafel slope for preoxidized electrode and cycled Ni electrode is 44 mV dec^{-1} and 38 mV dec^{-1} respectively, which are much lower than that obtained on corresponding Co electrode with a number of 52 and 49 mV dec^{-1} respectively. And the current densities observed are about 4.8 and 28 mA cm^{-2} at 0.7 V vs Hg/HgO for preoxidized and potential cycled Ni electrodes respectively, which is more than 4 times of that of Co electrode[53]. Trotochaud et. al.

prepared FeO_x, CoO_x NiO_x and MnO_x thin films with 2-3 nm by solution-cast, and the overpotentials of FeO_x, CoO_x NiO_x and MnO_x for OER are 0.405, 0.381, 0.3 and 0.514 V in 1 M KOH, and the Tafel slopes are 51, 42, 29 and 49 mV dec^{-1}, indicating the activities for OER are in the order of $NiO_x > CoO_x > FeO_x > MnO_x$[54]. Markovic group establish the overall catalytic activities for OER as a function of a fundamental property, $OH–M^{2+\delta}$ bond strength ($0 \leq \delta \leq 1.5$). The activities, with trends of Mn < Fe < Co < Ni, are governed by the strength of the $OH\text{-}M^{2+\delta}$ (Ni < Co < Fe < Mn). These trends are found to be independent of the source of the OH, either the supporting electrolyte, providing a foundation pathway for rational design of 'active sites' for practical alkaline OER electrocatalysts[55].

2.2.2.2.3 Binary and ternary oxides based on Fe, Co and Ni

First-row transition metal oxides such as Ni, Co, Mn and Fe are widely studied for their relatively good activity for OER. However, they are still not able to meet the requirement for application because the M-O bond strength is either to strong or too weak, which result in high overpotential for OER[13]. However, the M-O bond binding energy can be tuned by preparing binary and ternary metal oxides. Wu and Scott prepared nanoscale $Cu_xCo_{3-x}O_4$ ($0 < x < 1$) particles with average size of 20-30 nm and demonstrated that incorporation of Cu in the spinel lattice of Co_3O_4 shifted the Co^{3+}/Co^{4+} redox peak as well as the onset potential for OER to more negative potentials. The $Cu_xCo_{3-x}O_4$ electrodes exhibited satisfying stability during repetitive cyclic voltammetry[56]. A number of mixed hydroxides were prepared by Li et al. based on nickel incorporated with Cu, Mn, Cr, Co, and Fe. The results indicate that doping Ni with Cu and Mn has adverse effect on the performance for OER. Addition of Co and Cr in Ni will slightly increase the activity for OER. However, addition of Fe will

significantly increase the current density and lower the onset potential as well as the Tafel slope[57].

It has long been known that iron impurities in nickel oxide batteries facilitate the OER, which is parasitic to the battery charging process[58]. Corrigan originally reported the iron doped nickel oxides for OER in 25 w% alkaline solutions in 1987. The addition of Fe into nickel oxide will bring down the overpotential for OER continuously as the content of Fe increase from trace to 50%. Even at low concentrations, iron impurities in nickel oxide have a dramatic effect on the OER kinetics. The Tafel slopes decrease from 70 mV dec^{-1} with nickel oxide itself to 20 to 25 mV dec^{-1} with high concentrations iron in 25 w% alkaline solutions, indicating the change of rate determine steps[48]. Since then, Fe-Ni alloys, Fe-Ni oxides/hydroxides have been widely studied[54, 59-62].

Landon et al. fabricated mixed Fe-Ni oxides using evaporation induced self-assembly, hard templating and dip coating. Doping Ni with Fe can substantially improve the activity for OER in alkaline solution, and a peak in catalytic activity is observed near 10 mol % Fe for all three synthesis methods[48, 62-64]. XRD and Raman conclusively identified the formation of a spinel $NiFe_2O_4$ phase in coexistence with NiO at low Fe concentrations and the formation of Fe_2O_3 at higher Fe concentrations. The primary oxidation state of the Fe in the mixed oxide was identified using XANES analysis and found to be +3. EXAFS showed that the average coordination of Fe atoms increases under OER conditions possibly because of an increase in octahedrally coordinated Fe in $NiFe_2O_4$ [65].

Louie and Bell[66] conducted a detailed investigation on the electrochemical activity of electrodeposited Ni-Fe film for OER in alkaline solution. The results indicate that the

interaction between Ni and Fe leads to an improvement of OER activity. As the increase of Fe incorporated into the Ni-Fe film, the $Ni(OH)_2$/NiOOH redox couple shifts to positive potentials and the peak area decreases (Fig.2.3 A). At Fe content is or over 41%, the oxidation peaks are disappeared. A strong linear relationship is observed between reduction peak potential and the Fe content (Fig.2.3 B), and the electron transferred during the $Ni(OH)_2$/NiOOH redox decrease from 1.2 for pure Ni film to 0.5 for films containing 90% Fe, which indicates the average oxidation state of Ni decrease from 3.2 to 2.5. Ni-Fe film with a composition of 40% Fe exhibits OER activity roughly 2 orders of magnitude higher than that of a freshly deposited Ni film and about 3 orders of magnitude higher than that of Fe film. And the specific current density varies by 2-times and the overpotenial by 20 mV when the Fe composition varies in the range of 15-50% (Fig.2.3 C), which is consistent with the discrepancies found in literatures for the Ni-Fe system with the optimum composition has been reported as high as 50%[48] and as low as 10%[57, 65]. A slightly decrease of Tafel slope as the increase of Fe concentration in Ni-Fe films in the range 0-40%, and a slight increase as the Fe concentration further increase (Fig.2.3 D). However, the Tafel slopes for aged Ni films and mixed Ni-Fe films are close to 40 mV dec^{-1}, while those for as deposited Ni films and pure Fe films are ~55 mV dec^{-1}. The reaction order in OH^- is unity for all films, with the exception of as-deposited Ni films. The authors propose that the OER reaction on Ni-Fe films is composed of an initial reversible discharge of an OH^- ion followed by a rate-limiting electron transfer step which results in the formation of a physisorbed hydrogen peroxide intermediate[66].

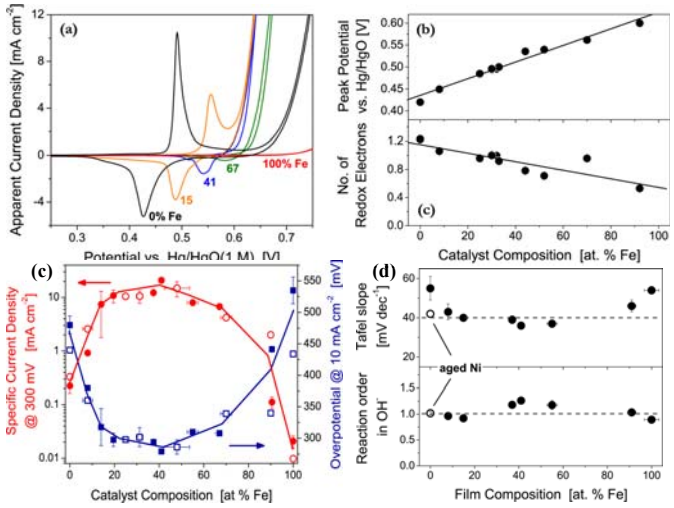

Figure 2.3. Ni-Fe films with Fe concentration ranging from 0-100% were prepared.[66]

Photochemical metal-organic deposition (PMOD) was used to prepare amorphous metal oxide films containing specific concentrations of iron, cobalt, and nickel to study how metal composition affects heterogeneous electrocatalytic for OER[67]. Lower onset potential for OER is obtained when the iron concentration is maintained in the range of 20-40% for binary and ternary films (Fig. 2.4). At higher Fe concentrations, the onset potential steadily increases till it reaches the worst value of the series for α-FeO_x. No obvious trends were observed along the Co-Ni axis of the ternary plots, suggesting that cobalt and nickel induces similar effects on the films properties. The Tafel slopes were remarkably sensitive to the amount of iron presented. In the absence of iron, for example, higher concentrations of nickel were found to produce higher Tafel slopes. Films rich in nickel afforded Tafel slopes over the 70-80 mV dec^{-1} range, while films with a high abundance of cobalt produced slope of 60 mV dec^{-1}. The presence of iron in any of the films produced Tafel slopes of 30-40 mV dec^{-1}, where an iron concentration of 40- 60% generated optimal Tafel slopes for both the binary and the ternary mixtures. The long-term stability by 24 h chronopotentiometry experiments at current density of 1 mA cm^{-2} demonstrate that both α-$Fe_{40}Co_{40}Ni_{20}O_x$ and α-$Fe_{40}Ni_{60}O_x$ show the best stability among the 21 sample tested. The collective

XPS and electrochemical data indicate that the presence of iron in the films tends to stabilize higher oxidation levels of the metals after the initial oxidation[67].

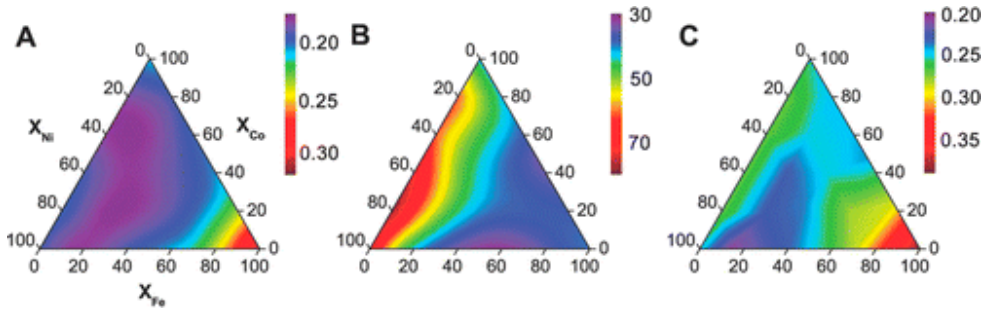

Figure 2.4. Contour plots of kinetic parameters extracted from Tafel plots recorded on 21 independent amorphous (mixed-) metal oxide films: (A) onset η in units of V; (B) Tafel slopes in units of mV dec^{-1}; and (C) η (in units of V) required to reach j=0.5 mA cm^{-2}. [67]

2.2.2.2.4 Perovskites

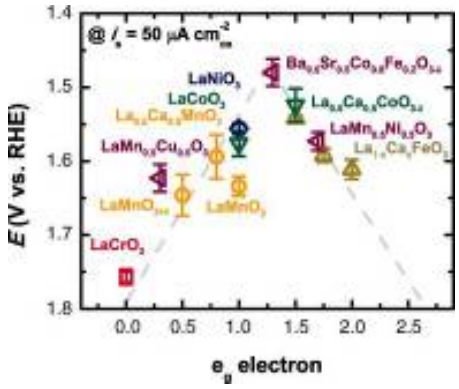

Figure 2.5. The relation between the OER catalytic activity, defined by the overpotentials at 50 μA cm^{-2}_{ox} of OER current, and the occupancy of the e_g-symmetry electron of the transition metal (B in ABO_3). Data symbols vary with type of B ions (Cr, red; Mn, orange; Fe, beige; Co, green; Ni, blue; mixed compounds, purple), where x= 0, 0.25, and 0.5 for Fe. Error bars represent SDs of at least three independent measurements. The dashed volcano lines are shown for guidance only. [73]

Intensive research efforts have been invested in developing low-cost transition metal oxides as an alternative to precious-metal-based materials. Among them, perovskites, a broad class of crystalline minerals with structure of ABO_3 system, have been widely studied as ORR and OER catalysts for over a century[47, 49, 68-72]. The physico-chemical and catalytic properties of perovskites can be modified by substituting ions of the same or different oxidation states in the A and B sites. A systematic investigation was made to correlate the electrocatalytic properties of perovskites (ABO_3) for OER. The OER electrocatalytic activities of substituted perovskite ($A_{1-x}A'_xBO_3$, where A is a lanthanide mainly La, A' is an alkaline earth metal mainly Sr, and B is a first-row transition metal) were studied systematically. The Tafel slopes for OER at lower overpotentials were ~43, ~65, ~120, ~125, ~200, and 175-235 mV dec^{-1} for $LaNiO_3$, $A_{1-x}A'_xCoO_3$ (A = La, Nd, Gd; A' = Sr, Ce, Th), $La_{1-x}Sr_xFeO_3$, $La_{1-x}A'_xMnO_3$ (A'=Sr, K, Ca), $La_{1-x}Sr_xCrO_3$ and $La_{1-x}Sr_xVO_3$, respectively. The authors claim that the OER rate does not related with semiconductor properties of perovskites. The OER rate increases with the pH, with decrease of magnetic moment, with decrease of stability of the perovskite lattice, with decrease of the enthalpy for formation of the transition metal hydroxides, and with increase in the number of d-electrons in the transition metal ions. A volcano relation for OER on perovskites was constructed based on the activity descriptors M^z-OH[49]. Suntivich et al. proposed that the e_g filling of surface transition metal cations can greatly influence the binding of OER intermediates on the perovskites surface and thus the OER activity. The highest OER activity among all oxides studied as predicted by the e_g activity descriptor is $Ba_{0.5}Sr_{0.5}Co_{0.8}Fe_{0.2}O_{3-\delta}$ (BSCF). And $Ba_{0.5}Sr_{0.5}Co_{0.8}Fe_{0.2}O_{3-\delta}$ was demonstrated with intrinsic activity that is at least an order of magnitude higher than that of the state-of-the-art iridium oxide catalyst in alkaline media. The intrinsic OER activities of perovskites exhibit a volcano-shaped dependence on the occupancy of the 3d electron with an e_g symmetry

of surface transition metal cations in an oxide (Fig.2.5)[73]. Yang group reported double perovskites $(Ln_{0.5}Ba_{0.5})CoO_{3-\delta}$ (Ln=Pr, Sm, Gd and Ho) as a family of highly active catalysts for the OER upon water oxidation in alkaline solution. These double perovskites are stable with comparable activities as $Ba_{0.5}Sr_{0.5}Co_{0.8}Fe_{0.2}O_{3-\delta}$. $(Pr_{0.5}Ba_{0.5})CoO_{3-\delta}$ was found to have the lowest voltage for the onset overpotential, indicative of the highest OER activity among them[68].

2.3 Pt based catalysts for PEM fuel cells

The design of inexpensive, stable, and catalytically active materials for the ORR and MOR is the ultimate goal in catalyst development, and these require fundamental breakthroughs and understanding of the catalytic process on different materials. Pt is the most active catalyst for fuel cell applications, how to achieve high performance with low Pt loading is remain challenging. The intrinsic activity of NPs depends on not only particle size[74-76], shape[77, 78] and composition[77, 79], but also the atom arrangement of the metal atoms in the particle[80]. In general, different approaches (or a combination of them) can be utilized to achieve the triangle angle challenges performance, cost and durability. Specially, these methods include: a) controlling the morphology and crystallography; b) alloying Pt with other elements; c) controlling the arrangement of Pt and/or alloying metal atom in the single NPs; d) developing nanoporous NPs with increase ESA and d) developing single-atom or sub-nano Pt based clusters.

Research recently focuses on the manipulation of nanoparticle structure in order to optimize the catalyst activity without increasing the loading of Pt[81, 82]. Core@shell electrocatalysts for fuel cells have the advantages of a high utilization of Pt and the modification of its electronic structures toward tunable activities with the corrosion-

resistant Pt[81, 83-87]. To date, reports on core@shell ORR catalysts can be classified by their synthetic approaches, which include the seed mediated sequential method[84, 88, 89], the galvanic-replacement reaction[90-92], and structural rearrangement[80, 93, 94]. The core-shell structured NPs with monolayer or several layers of precious group metals on non-precious group metals core are of great potenital to reduce the Pt loading and to increase the activity by tuning the activity of the shell metal through interactions with the core[81, 85, 87, 95-97].

2.3.1 Seed mediated sequential method

Seed-mediated synthesis method or seeding growth method is a very popular chemical colloidal method that has been employed for the preparation of noble metal NPs with a variety of morphologies[98, 99]. The seeding growth method has also been know as an effective strategy to produce core-shell, multi-shell structures[84, 88, 89]. In this method, preformed fine metal particles are added to an appropriate growth solution for further growth as seeds or core. The seed or core particles are often produced by reducing metal ions using a suitable reducing agent. The growth solutions contain the same or different metal ion(s) along with other additives such as dopants, capping and etching agents, and so on[98]. Zhang et. al. prepared a carbon-supported Fe@Pt NPs using a sequential reduction process. The Fe core was first synthesized by reduction of $FeSO_4$ using $NaBH_4$ in an aqueous solution containing well-dispersed carbon in the presence or absence of ammonia borane in air at room temperature. Second, the atoms in the outer layer of the Fe core were sacrificed to reduce Pt^{2+} [89]. The Ru@Pt core-shell NPs were synthesized by using a sequential polyol process by coating Pt on the Ru seeds colloid with presence of polyvinylpyrrolidone stabilizers (MW = 55,000). The Ru@Pt core-shell nanoparticle

catalyst comprising a Ru core covered with an approximately 1-2-monolayer-thick shell of Pt atoms exhibits preferential CO oxidation in hydrogen[95]. Serpell et al. reported a new supramolecular route for the synthesis of core@shell NPs based on an anion coordination protocol by binding the shell metal to the surface of the preformed primary metal core before reduction[83]. Wang et. al designed and developed highly active and stable Pd_3Cu_1@ Pt/C (ORR) and Pd@PdIr (HOR) electrocatalysts through surfactant-free synthesis of core/C and the subsequent exclusive shell formations on the core using the Hantzsch ester as a reducing agent methods[84]. Fabricating sub-nanometer-thick core-shell nanocatalysts are effective for obtaining high surface area of an active metal with tunable properties. The key to fully realize the potential of this approach is how to produce atomically ordered core-shell NPs. Hsieh et al. reported an ordered structural transition from ruthenium hcp to platinum fcc stacking sequence at the core-shell interface via a ethanol-based green synthesis method. The significantly enhanced CO tolerance and the superior stability demonstrated in accelerated stress tests at ultra-low catalyst loadings show promising potential of this structure, and show the promising application of this novel structures[88].

2.3.2 Galvanic replacement reaction

Galvanic replacement is an electrochemical process that involves the oxidation of one metal (sacrificial template) by the ions of another metal which has a higher reduction potential[90, 100]. These reactions involve a corrosion process that is driven by the difference in the electrochemical potentials of two metallic species. Galvanic replacement reaction is a versatile method for preparing hollow metallic and monolayer core-shell nanostructures[90-92, 100, 101]. Sasaki et. al reported a new class of highly stable, active electrocatalysts comprising platinum monolayer shell on

palladium-gold alloy core NPs by depositing Pt monolayers on PdAu nanoparticle surfaces using the galvanic displacement of a Cu monolayer, which was obtained by underpotential deposition of a Cu monolayer on the reduced surfaces of the Pd_9Au_1 NPs[101]. A Pt shell with controlled morphology and thickness on a Pd and Pd_3Co core were developed using galvanic displacement of an underpotentially deposited (UPD) Cu monolayer mediated electrodeposition method[81]. Pt monolayer deposited on late-transition metals or their alloys, such as PtPb, PdPb, and PdFe intermetallic compound NPs, were prepared by the galvanic replacement with Pt atoms of an underpotentially deposited (UPD) Cu monolayer on the catalyst electrode as well. The activities of these catalysts for ORR, expressed as half-wave potential, $E_{1/2}$, increase in the sequence: Pt/PdPb < $Pt/PdFe_{550}$ < Pt/PtPb, all of then show better activity significantly better than standard Pt/C.[102] Similar strategies were applied to prepare PdCu porous structure[103]

2.3.3 Structural rearrangement

Thermal annealing can rearrange the atom in controlled potential and it is a good method to obtain intermetallic alloy phase with improved activity and stability[104-106]. Thermal annealing can also lead to the segregation of Pt atoms to the surface in controlled atmosphere.[94, 97] Wang et al. investigated 132 binary-alloyed nanoparticle systems (groups 8 to 11 in the Periodic Table) using density functional theory (DFT) and systematically explore their segregation energies to determine core-shell preferences. The results indicate that Pt alloying with Ni, Ir, Rh, Co, Os, Ru and Fe are of preferential to form Pt shell structures due to the favorable segregation energies of Pt[97]. For example, annealing the PtNi NPs will lead to formation of Pt-skeleton-type surface structure with improved activity[82]. PtM (M = Co, Ni, Fe) annealed alloy

surfaces form the outermost Pt-skin surface layer, which consists only platinum atoms[107], and the Pt-skined surface higher activity compared with Pt-skeleton and pure Pt-polycrystalline with nominally the same surface composition (100 at. % Pt). Pt_3Co NPs synthesized using an impregnation reduction method and annealed at 400 ^oC and 700 ^oC under H_2 atmosphere leading to the formation of ordered Pt_3Co intermetallic cores with a 2-3 atomic-layer-thick platinum shell, and this structure exhibits over 200% increase in mass activity and over 300% increase in specific activity for the O_2 reduction reaction when compared with the disordered Pt_3Co alloy NPs as well as Pt/C [108]. Thermal annealing of Pt based alloy is attracting increasing interest recently for it is a method can not only achieve high activity but superior long-term stability at the same time.

2.4 Carbon nanotubes and their applications in developing fuel cells and water splitting catalysts

CNTs are seamless cylinders composed of one or more curved layers of graphene with either open or closed ends[109, 110]. Since the awareness of CNTs in 1991[109], it has been extensively studied as multifunctional composite materials[111], catalysts support[111-114], nanoelectronics devices[115], circuits and computers[116] for its unique properties such as large specific surface area, excellent mechanical and electrical properties [111, 112, 114, 117, 118]. CNT-related commercial activity has grown most substantially during the past decade. Since 2006, worldwide CNT production capacity has increased at least 10-fold, and the price of MWNTs have decreased from 45 000 to 100 \$ kg^{-1} and the productivity increased to several hundred tons per year for commercial applications in Li ion battery and nanocomposites[110, 119]. Due to the large volume of publications and the widely applications, huge amount of reviews were

published from the chemistry and properties of CNTs[120-122] to the applications[120, 123-125], and to health and safety considerations[110, 119, 124, 126, 127]. Here we briefly summarized the properties of CNTs and their application as catalysts support in PEMFCs and water splitting.

2.4.1 Properties of CNTs

CNTs are seamless cylinders composed of one or more curved layers of graphene[109, 110]. According to the layers of curved graphene, CNTs are normally classified as SWNTs (Fig. 2.6 left) which consists of a single layer of graphene sheet seamlessly rolled into a cylinder, DWNTs (Fig. 2.6 middle) which compose of two layers of curved graphene, and MWNTs (Fig. 2.6 right) which composed of multiple concentric tubes. The gaps between two nearby concentric tubes is around 0.34 nm. The circular curvature will cause quantum confinement and σ-π rehybridization, hence the π obital is more delocalized out of the carbon plane, which make the CNTs mechanically stronger, electrically and thermally more conductive than graphite.

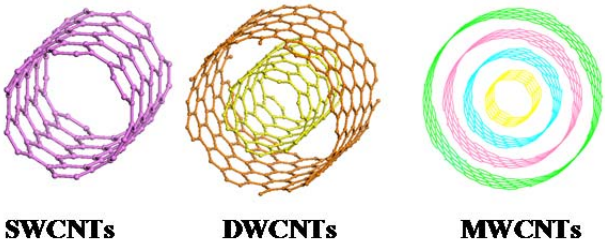

Figure 2.6. The schematic structure of SWNTs, DWNTs and MWNTs

The chemical, physical and electrochemical properties of CNTs are widely studied and their properties can be summarized as follow[116, 128-132]:

1) The physical properties of SWNTs depend on the chirality index (n, m), which makes the SWNTs be metallic or semiconductor depending on band gaps that are relatively large (~0.5 eV) or small (~10 meV) [128, 132, 133]. Slightly changes in tube

diameter and wrapping angle, defined by the chirality indices (n, m), will shift their electrical conductivity from metallic state to semiconducting state, and change the band gap. Normally, 1/3 SWNTs would be expected as metallic and the other 2/3 would be expected as semiconductors. Liu et al. investigated the chirality of over 400 single walled nanotubes from one growth condition, and they discovered that for nanotube diameters between 1.7 and 2.1 nm, semiconducting species are highly enriched, and metallic ones completely dominate for nanotube diameters larger than 2.3 nm[134], which indicates the diameter is also a determine parameter for the properties of CNTs. SWNTs have inspired a vast range of proposed applications including transistors, logic gates, and field emission sources etc.[135]. However, this structure can not be fully exploited until the structurally pure SWNTs can be realized. After more than two decades investigation, recently Yang et al. show that SWNTs of a single chirality, (12, 6), can be produced directly with an abundance higher than 92 % when using tungsten-based bimetallic alloy nanocrystals as catalysts. The authors claim that using high-melting-point alloy nanocrystals with optimized structures as catalysts might be able to pave the way for total chirality control in SWNT growth and will thus promote the development of SWCNT applications[136].

2) DWNTs are intriguing materials that exhibit properties intermediate between those SWNTs and multi walled CNTs. DWNTs exhibit band gaps that are sufficiently large for field effect transistors[137] and high stability for aggressive chemical[138], mechanical and thermal treatment[139] compared with single walled CNTs and MWNTs [132, 139, 140]. The electronic structure of a DWNT is affected not only by the curvatures of the tubes but also by the inter-wall coupling strength/distance. Decreasing the distance between the walls leads to a change of electron type. For example, DWNT is compose of two

semiconductor tubes, the whole tube will be semiconductor if the distance of two walls is too far, and will be metallic if the distance is shorter enough[130].

3) Larger diameters tubes are found to have a greater density of defects such as vacancies or interstitials.

4) CNTs, especially SWNTs, are ideal for optical and optoelectronic applications due to the direct band gap, well defined band gap and subband structure[119].

5) CNTs are chemical stable with enhanced oxidation resistance for chemical reactions due to the well-defined short-range and long-range ordering[141, 142].

6) The structure of the CNTs allows a faster and efficient electron and heat transport. The CNTs show a volume resistivity in the 10^{-2}-10^{-3} Ω cm typical range. MWNTs are typically metallic and can carry currents of up to 10^{9} A cm^{-2}. Theoretically, metallic nanotubes have an electrical current density more than 1,000 times greater than metals such as silver and copper. The thermal conductivity of CNTs is ~3,000-3,500 W mK^{-1} at room temperature[143].

7) Owing to the covalent sp^2 bonds between individual carbon atoms, a nanotube shows a Young's modulus of 1.2 TPa, a tensile strength around a hundred times higher than steel and can tolerate huge strains before mechanical failure[144-146]. Since CNTs have a low density for a solid of 1.3-1.4 gm/cm³, its specific strength can reach up to 48,462 kN·m/kg, which is the best of known materials[147].

2.4.2 Synthesis of CNTs

Controllable synthesizing of CNTs with desirable structure and properties is the prerequisite of CNTs applications. In the past two decades, methods, including arc discharge, laser ablation, and chemical vapor deposition (CVD) methods, have been developed to produce CNTs with preferential properties[148, 149]. CNTs produced from

arc discharge or laser ablation generally have fewer structural defects due to the higher growth temperature. The CVD growth is the most promising method for mass CNTs production due to the advantages of mild synthesis condition, high yield, simple facility and low cost[119, 132, 148, 150-152].

Single-, double-, or multi-walled CNTs, can be prepared by using catalysts under controlled conditions. During the formation of CNTs, the carbon feedstock is firstly decomposed into carbon atoms and hydrogen on an active catalysts surface. Then carbon atoms diffuse into the metal particles till the solution (metal-carbon) becomes saturated. The precipitation of graphite carbon from the metal surface starts when supersaturation occurs then forms a cylinder CNT if the condition is right[119]. The catalyst is playing a key role for CNTs growth. The transitional metals, such as Fe, Co, Ni, Au, Pd, Ag, Pb, Mn, Cr, Ru, Mo, Cu, have been widely studied[153]. Nanosized iron-group metals (Fe, Co, Ni) are known for their ability to catalyze SWNT growth in chemical vapor deposition[154]. And recently semiconductor NPs catalysts such as Ge, Si and SiC have been developed in order to develop metal-free CNTs[149].

2.4.3 Functionalization of CNTs

CNTs have been extensively studied as catalysts support for fuel cells and water splitting due to their unique properties such as large specific surface area, excellent mechanical and electrical properties[117, 155-162]. For example, it has been reported that the CNT-supported Pt (Pt/CNT) catalysts exhibit higher catalytic activity and higher electrochemical stability as compared to Pt/C[163-166]. However, the as-prepared CNTs are insoluble in all organic solvents and aqueous solutions due to the inert chemical properties of the CNTs, which make them difficult to manipulate, hence limit their

applications. Consequently, it is necessary to modify or functionalize the surface of CNTs to introduce anchor sites before catalyst deposition.

In general, CNTs can be functionalized by covalent attachment of chemical groups through bonding to the π-conjugated skeleton of the CNTs or by non-covalent adsorption or wrapping of various functional polyelectrolytes or compounds. The covalent functionalization methods including sidewall halogenation, hydrogenation, and radical additions and so on are intensively studied[129]. The most common covalent functionalization involves the attachment of carbonyl and hydroxyl groups via an acid oxidation treatment with a mixture of HNO_3/H_2SO_4 or by plasma etching[167, 168]. The distributions of carbonyl and carboxyl groups generated by acid treatment are not particularly homogeneous and would lead to the aggregation of NPs and low utilization of nanostructured electrocatalysts[169]. The distribution of catalysts on acid treated CNTs can be improved by introducing more active sites via treatment with ethylenediamine[170] and polyaniline[171]. But CNTs that were initially treated by acid oxidation prior to the treatment of polyelectrolyte introduce structural defects and disrupts the delocalized pi electron system in the CNT sidewalls, and consequently alter the electronic and mechanical properties to a degree that would significantly affect the performance of the electrocatalysts. Therefore, development of a better and more effective functionalization methods that can not only introduce high density and homogeneous surface functional groups but also has little or no structural damage to CNTs have been attracting increasing interests. The noncovalent interaction is based on van der Waals forces or *ð-ð* stacking, and it is controlled by thermodynamics. Non-covalent functionlization of CNTs by various surfactants[168], aromatic compounds[168, 170], functional polymers[163, 172] and biomolecules[158] has been intensively studied as such functionalization is effective to introduce high density and uniform active sites

with little detrimental effect on CNTs. The functionalization of CNTs has been widely studied in the past two decades. Regarding functionalization of CNTs, more details can refer to [ref. 111 and 129][111, 129].

2.4.4 CNTs as catalyst support

The carbon black catalysts are undergoing electrochemical oxidation to produce surface oxides and eventually to CO_2 at the cathode during fuel cell operation, hence lead to aggregation of NPs and the degradation of the catalysts performance[173, 174]. The high specific surface area, high electrical conductivity, high mechanical strength and corrosion-resistance of CNTs make them promising candidates for catalyst supports in fuel cell[173]. It has been demonstrated that Pt/CNTs catalyst with 12 wt% Pt loading could deliver a 10% higher fuel cell voltage and twice power density than 29% Pt/C in hydrogen PEM fuel cells[175]. Li et al. demonstrated that using CNTs as supports for cathode catalysts in a direct methanol single cell produces better performance compared to XC-72 carbon[176]. Electrochemical surface oxidation of carbon black Vulcan XC-72 and MWNT has been compared following potentiostatic treatments up to 168 h under condition simulating PEMFC cathode environment. MWNTs are electrochemically more stable than Vulcan XC-72 with less surface oxide formation, and show lower loss of Pt surface area, low extend of particle aggregation (Fig. 2.7) and ORR activity[177]. Pt NPs were supported onto highly graphitized MWNTs, and the electrochemical investigation suggested that the HG-MWCNT had a higher electrochemical stability. The author claim that the high stability is because of the lower corrosion rate of highly graphitized MWNT and the stronger interaction between metal and carbon support[178]. Asgari compared the electrochemical stability of Pt/MWNT and Pt/SWNTs, and found that Pt/MWNT is

electrochemically more stable compared with Pt/SWNT for fuel cell catalysts due to the serious detachment of Pt particles from SWNT support[179]. Due to the excellent chemical stability and electronic property of CNTs, noble metal based NPs supported on CNTs were intensively studied in the past decades for fuel cells[169, 180-184] and variety of preparation methods were reported and summarized. Here we are not going to discuss them in detail because many reviews were published in this area, and if you interested, please refer to some good reviews such as reference [ref. 118, 173, 185 and 186][118, 173, 185, 186].

CNTs are considered as promising candidates to develop noble metal-free catalysts for water splitting, and they present new opportunities to develop active, durable and low-cost catalysts. Wu et al. developed a hybrid consisting of Co_3O_4 nanocrystals supported on SWNTs via a simple self-assembly approach. The Co_3O_4/SWNTs hybrid electrode for the OER exhibits much enhanced catalytic activity as well as superior stability for OER under neutral and alkaline conditions compared with bare Co_3O_4, which only performs well in alkaline solution[112]. Polyoxometalates (POM) supported on CNTs exhibit enhanced activity for OER under dark or illuminated conditions[114]. Cobalt-embedded nitrogen-rich CNTs can efficiently electrocatalyze the HER with activities close to that of Pt under acidic, neutral or basic media[187]. Ultrathin nickel-iron layered double hydroxide (LDH) nanoplates supported on oxidized MWNTs achieved a current density of 10 A g^{-1} at η = 0.228 V in 1 M KOH with catalysts loading of 0.25 mg cm^{-2}. Growth of LDH nanoplates on the functional groups on CNTs contributed to the optimal OER activity of the NiFe-LDH/CNT complexes[117]. Recently, multifunctional catalysts are attracted increasing interests. Dai group prepared a series of multifunctional base trasition metals based inorganic/nanocarbon hybrids for fuel cell and water splitting applications by strongly

coupling the inorganic metal oxides and nanocarbon materials. This method affords strong chemical attachment and electrical coupling between the electrocalytic NPs and nanocarbon, resulting precious metal-free catalyst with improve activity and durability for fuel cell and electrolysis[188].

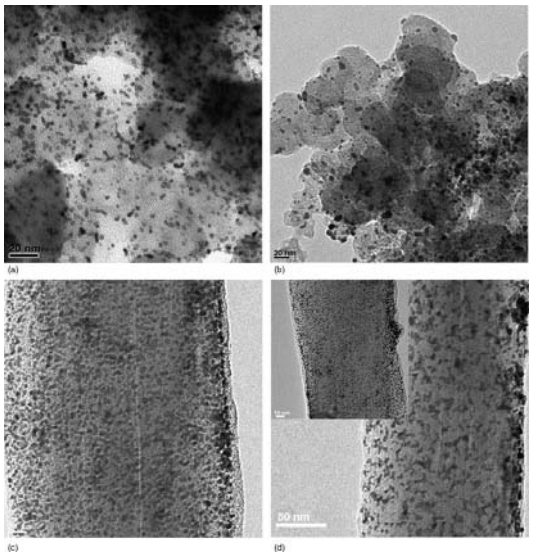

Fig. 2.7 TEM micrographs of (a) Pt/Vulcan XC-72 before durability test, (b) Pt/Vulcan XC-72 after durability test for 168 h, (c) Pt/MWNTs before durability test, and (d) Pt/MWNTs after durability test for 168 h. Inset of (d) shows a typical region.[177]

2.4.5 CNTs based metal free catalysts

2.4.5.1 Pristine CNTs

It is reported that CNTs exhibit some activity toward ORR in alkaline solutions through 2-electron reduction of O_2 to HO_2^- in alkaline conditions, and the enhanced O_2 reduction are caused by quinone functionalities of carbon materials[189-192]. And the ORR activity of MWNTs is demonstrated pH-dependence. Kruusenberg et al. investigated oxygen electro-reduction on MWNTs in 0.5 M H_2SO_4 solution, acetate buffer (pH 5), phosphate buffers (pH 6, 7 and 8), borate buffer (pH 10), 0.01 M KOH, 0.1 M KOH and in 1 M KOH solution, using the rotating disk electrode (RDE)

method. The overpotentials for O_2 reduction increase with decreasing pH. The half-wave potentials ($E_{1/2}$) of oxygen reduction on MWNTs are higher in solutions of high pH. At lower pHs (pH < 10) the value of $E_{1/2}$ did not essentially depend on the solution pH[193]. Dubey et al.[194] reported anode made of MWNTs results in enhancement of exchange current density compared to graphite anode in a conventional alkaline water electrolysis cell. Misra et al.[195] applied hydrophobic aligned MWNTs forests as electrochemical cells for the electro-decomposition of water. With a voltage of -10V, hydrogen evolution appeared near the surface of the CNTs and oxygen bubbles formed around the counter-tungsten electrode[195].

It is widely believed that pristine CNTs function only as support materials to wire up more active electrocatalytic materials unless modified or doped[196, 197], and the activity that reported for pristine carbon materials are debatable because the trace amount of metal impurities are existed in the CNTs products[198]. However, this dispute has been solved by the recent research from Byers et al[199], who visualized the electrochemical reduction of oxygen (hydrogen peroxide generation) at high resolution along pristine (defect-free) regions of individual SWNTs, and demonstrated that SWNTs, in fact, exhibit activity for O_2 reduction to H_2O_2 and the activity is comparable to that of standard gold electrocatalysts (Figure 2.8)[199]. CNT films can act as easy-to-make and flexible electrodes with a high stability and performance superior to graphite for generation of non-oxidizing gases such as hydrogen from solution, CNT film electrodes are two orders of magnitude lighter and require much lower overpotential for faradaic splitting of water[200]. Compared to nanocarbonmetal/metal oxide electrocatalysts, nanocarbon electrocatalysts can be engineered without significant changes to the overall composition and provides a large number of models and tools to modify the surface chemistry and thus the electrocatalytic behavior. [199]

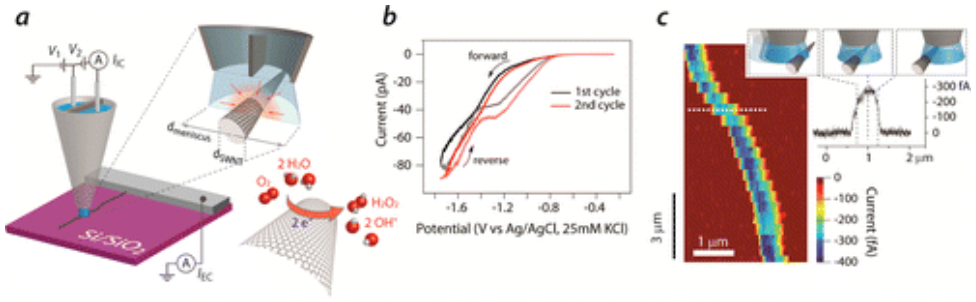

Figure 2.8. Electrochemical reduction of oxygen (hydrogen peroxide generation) at high resolution along pristine (defect-free) regions of individual SWNTs (a) SECCM setup showing a theta pipet positioned directly above an individual SWNT creating a well-defined tiny meniscus electrochemical cell for local electrochemical measurements and substrate mapping. A voltage, V_1, permits control of the working electrode potential, while an ion current (I_{IC}) between the two barrels of the pipet, generated by V_2, is used for precise pipet positioning. An electrochemical current (I_{EC}) is measured when the meniscus makes contact with the SWNT. Illustration (not to scale) of the enhanced mass transport and well-defined geometry of the SECCM setup, where $d_{meniscus}$ and d_{SWNT} correspond to meniscus and SWNT diameter, respectively. (b) Cyclic voltammograms of the ORR at a pristine *individual* SWNT. Scan rate: 100 mV/s. (c) Electrochemical map recorded at a substrate potential of −1.0 V vs Ag/AgCl QRCE for a pristine *individual* SWNT. Inset contains a line scan profile illustrating the evolution of the measured electrochemical current as the meniscus advanced across the SWNT. All measurements carried out in aerated PBS (pH 7.2) with 25 mM KCl.[199]

2.4.5.2 Modified CNTs

In addition of heteratom doped CNTs, another group of metal-free catalysts with low-nitrogen or nitrogen-free CNTs are developed for ORR recently. Li et al. demonstrate that partially unzipping the “few-walled CNTs” via oxidation and high temperature reaction with ammonia, creating nanoscale sheets of graphene attached to the inner tubes, can act as ORR catalysts in both acid and alkaline conditions. The authors claim that the graphene sheets formed from the unzipped part of the outer wall of the

CNTs are responsible for the catalytic activity (Fig. 2.9). The inner walls remain intact and retain their electrical conductivity, which facilitates charge transport during electrocatalysis. And graphene sheets contain extremely small amounts of irons originated from nanotube growth seeds, and nitrogen impurities, which facilitate the formation of catalytic sites and boost the activity of the catalyst[197]. Wang et al. recently demonstrated that polyelectrolyte functionalized CNTs could act as metal free electrocatalysts for ORR through the intermolecular charge-transfer from the CNTs to the functionalized PDDA (Fig. 2.10)[201]. The XPS results indicate the PDDA N1s peak for PDDA-CNT shifted negatively to lower binding energy by ~0.5 eV, which indicates that PDDA acts as a p-type dopant to positively charge carbon atoms in the conjugated electron-rich nanotube carbon plane[201]. This work opens a new area to develop metal-free ORR catalysts for fuel cells even though the activity is still significantly lower than Pt/C.

Recently, it is reported that introduction of defects into CNTs will greatly increase the activity of CNTs for ORR and HER. Miller et al. demonstrated that anodic pre-treatment of pristine SWNTs forests show enhanced activity for ORR due to the introduction of defects[202]. Waki et al. found that the formation of topological defects on the MWNTs through successive oxidation by refluxing in sulfuric acid and concentrated nitric acid and annealing in argon at high temperature can significantly enhance the activity for ORR in acid compared with pristine MWNTs[203]. Cui et al. developed activated CNTs as a metal-free electrocatalysts for the HER with good durability in acidic electrolytes. This catalyst shows onset overpotential and an exchange current density of 100 mV and 16.0×10^{-3} mA cm^{-2}, respectively. The author proposed that the acidic groups, such as -COOH, on CNTs act as proton relays, and CNTs capture and store electrons easily from the electrode during the cathodic

scan, and their excellent electrical conductivity also facilitates fast and efficient electron transport along CNTs. Subsequently, these electrons are transferred rapidly from CNTs to the acidic groups, leading to the reduction of protons to form hydrogen[204].

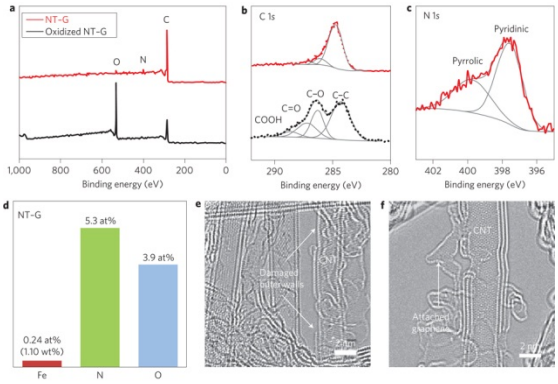

Figure 2.9. Structural and compositional characterization of carbon nanotube–graphene complexes. **a**, XPS survey spectra of as-oxidized material (oxidized NT–G) and final catalyst (NT–G). **b**,**c**, High-resolution C 1*s* XPS spectra (**b**) and N 1*s* spectra (**c**) of as-oxidized material (oxidized NT–G, black) and final catalyst (NT–G, red). Oxidized NT–G is reduced and doped with nitrogen during the high-temperature ammonia annealing. **d**, Chart showing the percentages of iron, nitrogen and oxygen in the final NT–G material measured by ICP-MS and XPS. **e**,**f**, Aberration-corrected TEM images of the NT–G material, showing damaged outer walls and exfoliated graphene pieces attached to double- or triple-walled carbon nanotubes (CNTs).[197]

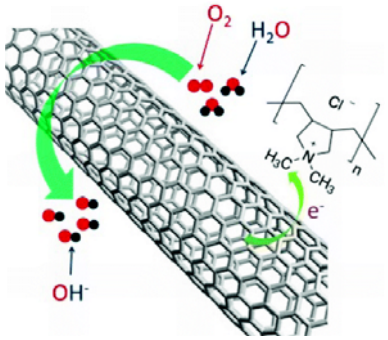

Figure 2.10. Illustration of charge transfer process and oxygen reduction reaction on PDDA-CNT. [201]

2.4.5.3 Heteroatom doped CNTs

It is widely known that doping carbon materials with heteroatom such as N[196, 205], B[206], S[207] and P[208] can significantly increase the activity for ORR. The aim of doping is to break the electro neutrality of CNTs to create charged sites favorable for O_2 adsorption and effectively utilization the carbon pi electrons for O_2 reduction. In the case of nitrogen doped CNTs, pyridine-like, pyrrole-like and graphitic N is responsible for the ORR active sites[196]. The incorporation of electron-accepting nitrogen atoms in the conjugated carbon plane provides a four-electron pathway for the ORR on CNTs with a superb performance[196, 209]. Due to the huge amount of publications that on doped carbon materials for ORR, and the thesis does not focus on ORR, hence the doped CNTs will not be summarized here, and detailed information please refer to reviews by Dai[173] and Wang[210].

Recently, metal free OER, and HER catalysts were also developed based on doped carbon materials. Zhao et al developed a nitrogen-doped carbon material for OER in alkaline media, and the material generated a current density of 10 $mA\,cm^{-2}$ at the overpotential of 0.38 V. The electrochemical and physical studies indicate that the high OER activity of the nitrogen/carbon materials is originated from the pyridinic-nitrogen- or/and quaternary-nitrogen-related active sites[211]. Tian et al. developed N-doped graphene/single walled CNTs hybrid for both ORR and OER[212]. Graphitic carbon nitride (g-C_3N_4) hybridized with a small number of MWNTs was synthesized using cyanamide as precursor. The optimal CNT content is found to be ~0.2 wt% in the composite, which displays a 2.4-fold enhancement in photocatalytic water splitting over pure g-C_3N_4[200]. A new class of graphitic carbon nanosheet-carbon nanotube three dimensional composites has been developed through self-assembly of graphitic carbon nitride nanosheets and CNTs. The composites exhibited high activity and stability for OER[213]. A metal-free hybrid catalyst based on graphitic-carbon

nitride with nitrogen-doped graphene was synthesized, and it shows an unexpected HER activity with comparable overpotential and Tafel slope to some of well-developed metallic catalysts. Experimental observations in combination with DFT calculations reveal that its unusual electrocatalytic properties are originate from an intrinsic chemical and electronic coupling that synergistically promotes the proton adsorption and reduction kinetics[40]. B-doped graphene also has been demonstrated with efficient electrocatalytic activity for HER[214].

Even though huge amount of literatures show ORR is significantly improved on heteroatom-doped CNTs/graphene surfaces. While Wang et al. argues that there is typically no sufficient effort to characterize the doped materials to verify that they are indeed free of any trace metal for ORR. They demonstrated that trace (ppm) levels of metallic impurities, such as manganese oxide, found in graphene have profound influences on the observed ORR potentials. However, their results also show that Fe_3O_4, NiO and Co_3O_4 supported on glass carbon (GC) electrodes show negligible activity when compared with GC. In light of these findings, the authors highly recommended to perform precise and complete characterizations of all materials employed for the catalysis of ORR[198].

2.5 Remarks and perspectives

Water electrolysis is constraint by OER, and OER catalysts have long been investigated and they are recently gaining increasing interests again. Noble metal catalysts are playing an important role in developing efficient PEM electrolyser, and Ir and Ru based structures are the state-of-the-art catalyst for PEM electrolysis applications. However, it is remaining challenge to develop ultra-low noble metal catalysts for OER with long-term stability. On the other hand, noble metal free catalysts are widely studied in alkaline conditions, and Ni-Fe or Ni-Fe-Co system,

regardless in forms of oxides, hydroxides or in supported form with CNTs, have been demonstrated the most active OER catalysts in alkaline conditions. Perovskites also show promising opportunities, but their activities are still lower than Ni-Fe system by comparing the data reported at this stage. Due to OER is rely on oxides catalysts, most of which are not conductive, hence imbedding OER oxides with conductive CNTs are of promising application for electro-chemical water splitting. And recently, N-doped carbon materials have been proved of very good activity for OER, and these metal free OER catalysts are gaining increasing attention and offer more opportunities.

Then we reviewed the strategies developed for design Pt based nanostructures for fuel cells applications with the aim to improve catalytic activity, long-tern durability and to reduce the cost without comprising the performance. Core-shell structures bring new opportunities, and especially the Pt shell intermetallic core structure obtained by annealing Pt based NPs show enhanced activity and stability simultaneously, which are promising for developing high performance fuel cells.

CNTs provide more opportunity to develop more efficient and stable catalysts for fuel cell and water splitting, especially in the area of developing noble metal-free and metal-free catalysts. However, the activities of heteroatom doped CNTs are still not able to compare with that of noble metal based catalysts at this stage. Recently, it is reported that the introduction of defects can enhance the ORR activity, and pristine CNTs are also reported show some activity for ORR and HER. However, the electrochemical properties of CNTs are still remaining unexplored. Hence exploring the intrinsic properties of different types of CNTs and coordination metal-free or noble metal free catalysts with CNTs by revealing the synergistic effects might be able to offer new opportunities.

References

1. D. J. LePoire, *Sustainability*, 2014, 6, 1489-1503.
2. L. Olsson, J. C. Hourcade and J. Kohler, *J. Environ. Dev.*, 2014, 23, 3-14.
3. T. J. Kucharski, N. Ferralis, A. M. Kolpak, J. O. Zheng, D. G. Nocera and J. C. Grossman, *Nat Chem*, 2014, 6, 441-447.
4. *Nat Photon*, 2012, 6, 136-137.
5. W. W. He, K. J. Wu, K. Wang, T. F. Shi, L. Wu, S. X. Li, D. Y. Teng and C. H. Ye, *Sci. Rep.*, 2014, 4.
6. F. Jin, X. Zeng, J. Liu, Y. Jin, L. Wang, H. Zhong, G. Yao and Z. Huo, *Sci. Rep.*, 2014, 4.
7. S. Y. Reece, J. A. Hamel, K. Sung, T. D. Jarvi, A. J. Esswein, J. J. H. Pijpers and D. G. Nocera, *Science*, 2011, 334, 645-648.
8. T. J. Meyer, *Nature*, 2008, 451, 778-779.
9. H. B. Gray, *Nature Chemistry*, 2009, 1, 7-7.
10. N. Demirdöven and J. Deutch, *Science*, 2004, 305, 974-976.
11. H. Dau, C. Limberg, T. Reier, M. Risch, S. Roggan and P. Strasser, *Chemcatchem*, 2010, 2, 724-761.
12. R. L. Doyle, I. J. Godwin, M. P. Brandon and M. E. G. Lyons, *Physical Chemistry Chemical Physics*, 2013, 15, 13737-13783.
13. I. C. Man, H.-Y. Su, F. Calle-Vallejo, H. A. Hansen, J. I. Martínez, N. G. Inoglu, J. Kitchin, T. F. Jaramillo, J. K. Nørskov and J. Rossmeisl, *Chemcatchem*, 2011, 3, 1159-1165.
14. M. M. Mench, in *Fuel Cell Engines*, John Wiley & Sons, Inc., 2008, DOI: 10.1002/9780470209769.ch6, pp. 285-379.
15. S. Specchia, C. Francia and P. Spinelli, in *Electrochemical Technologies for Energy Storage and Conversion*, Wiley-VCH Verlag GmbH & Co. KGaA, 2011, DOI: 10.1002/9783527639496.ch13, pp. 601-670.
16. G. Sandstede, E. J. Cairns, V. S. Bagotsky and K. Wiesener, in *Handbook of Fuel Cells*, John Wiley & Sons, Ltd, 2010, DOI: 10.1002/9780470974001.f104011.
17. M. K. Debe, *Nature*, 2012, 486, 43-51.
18. X. Zhao, M. Yin, L. Ma, L. Liang, C. Liu, J. Liao, T. Lu and W. Xing, *Energy & Environmental Science*, 2011, 4, 2736-2753.
19. H. Huang and X. Wang, *J. Mater. Chem. A*, 2014, 2, 6266-6291.
20. M. K. Jeon, C. H. Lee, G. I. Park and K. H. Kang, *Journal of Power Sources*, 2012, 216, 400-408.
21. C. Song and J. Zhang, in *PEM Fuel Cell Electrocatalysts and Catalyst Layers*, ed. J. Zhang, Springer London, 2008, DOI: 10.1007/978-1-84800-936-3_2, ch. 2, pp. 89-134.
22. A. J. Appleby, *Catalysis Reviews*, 1971, 4, 221-244.
23. D. Pletcher and X. Li, *International Journal of Hydrogen Energy*, 2011, 36, 15089-15104.

24. E. Rasten, G. Hagen and R. Tunold, *Electrochimica Acta*, 2003, 48, 3945-3952.
25. Y. Surendranath and D. G. Nocera, in *Progress in Inorganic Chemistry*, John Wiley & Sons, Inc., 2011, DOI: 10.1002/9781118148235.ch9, pp. 505-560.
26. M. H. Miles and M. A. Thomason, *Journal of the Electrochemical Society*, 1976, 123, 1459-1461.
27. T. Reier, M. Oezaslan and P. Strasser, *Acs Catalysis*, 2012, 2, 1765-1772.
28. M. G. Walter, E. L. Warren, J. R. McKone, S. W. Boettcher, Q. Mi, E. A. Santori and N. S. Lewis, *Chemical Reviews*, 2010, 110, 6446-6473.
29. S. Trasatti, *Journal of Electroanalytical Chemistry and Interfacial Electrochemistry*, 1972, 39, 163-184.
30. R. Subbaraman, D. Tripkovic, D. Strmcnik, K.-C. Chang, M. Uchimura, A. P. Paulikas, V. Stamenkovic and N. M. Markovic, *Science*, 2011, 334, 1256-1260.
31. J. Greeley, J. K. Nørskov, L. A. Kibler, A. M. El-Aziz and D. M. Kolb, *ChemPhysChem*, 2006, 7, 1032-1035.
32. T. G. Kelly, K. X. Lee and J. G. Chen, *Journal of Power Sources*, 2014, 271, 76-81.
33. D. V. Esposito, S. T. Hunt, A. L. Stottlemyer, K. D. Dobson, B. E. McCandless, R. W. Birkmire and J. G. Chen, *Angewandte Chemie International Edition*, 2010, 49, 9859-9862.
34. D. V. Esposito and J. G. Chen, *Energy & Environmental Science*, 2011, 4, 3900-3912.
35. T. F. Jaramillo, K. P. Jørgensen, J. Bonde, J. H. Nielsen, S. Horch and I. Chorkendorff, *Science*, 2007, 317, 100-102.
36. J. Kibsgaard, Z. Chen, B. N. Reinecke and T. F. Jaramillo, *Nat Mater*, 2012, 11, 963-969.
37. D. Voiry, H. Yamaguchi, J. Li, R. Silva, D. C. B. Alves, T. Fujita, M. Chen, T. Asefa, V. B. Shenoy, G. Eda and M. Chhowalla, *Nat Mater*, 2013, 12, 850-855.
38. E. J. Popczun, J. R. McKone, C. G. Read, A. J. Biacchi, A. M. Wiltrout, N. S. Lewis and R. E. Schaak, *Journal of the American Chemical Society*, 2013, 135, 9267-9270.
39. E. J. Popczun, C. G. Read, C. W. Roske, N. S. Lewis and R. E. Schaak, *Angewandte Chemie International Edition*, 2014, 53, 5427-5430.
40. Y. Zheng, Y. Jiao, Y. Zhu, L. H. Li, Y. Han, Y. Chen, A. Du, M. Jaroniec and S. Z. Qiao, *Nat Commun*, 2014, 5.
41. M. Carmo, D. L. Fritz, J. Merge and D. Stolten, *International Journal of Hydrogen Energy*, 2013, 38, 4901-4934.
42. S. D. Greenway, E. B. Fox and A. A. Ekechukwu, *International Journal of Hydrogen Energy*, 2009, 34, 6603-6608.
43. A. Marshall, B. Børresen, G. Hagen, M. Tsypkin and R. Tunold, *Energy*, 2007, 32, 431-436.
44. J. C. Cruz, A. Ramos Hernandez, M. Guerra-Balcazar, A. U. Chavez-Ramirez, J. Ledesma-Garcia and L. G. Arriaga, *International Journal of Electrochemical Science*, 2012, 7, 7866-7876.

45. N. Danilovic, R. Subbaraman, K.-C. Chang, S. H. Chang, Y. J. Kang, J. Snyder, A. P. Paulikas, D. Strmcnik, Y.-T. Kim, D. Myers, V. R. Stamenkovic and N. M. Markovic, *The Journal of Physical Chemistry Letters*, 2014, 5, 2474-2478.
46. M. Musiani, *Chem. Commun.*, 1996, DOI: 10.1039/cc9960002403, 2403-2404.
47. J.-I. Jung, H. Y. Jeong, J.-S. Lee, M. G. Kim and J. Cho, *Angewandte Chemie International Edition*, 2014, 53, 4582-4586.
48. D. A. Corrigan, *Journal of the Electrochemical Society*, 1987, 134, 377-384.
49. J. O. M. Bockris and T. Otagawa, *Journal of the Electrochemical Society*, 1984, 131, 290-302.
50. A. Damjanovic, A. Dey and J. O. M. Bockris, *Journal of the Electrochemical Society*, 1966, 113, 739-746.
51. C. C. L. McCrory, S. Jung, J. C. Peters and T. F. Jaramillo, *Journal of the American Chemical Society*, 2013, 135, 16977-16987.
52. K. Mette, A. Bergmann, J.-P. Tessonnier, M. Hävecker, L. Yao, T. Ressler, R. Schlögl, P. Strasser and M. Behrens, *Chemcatchem*, 2012, 4, 851-862.
53. K. Lian, S. J. Thorpe and D. W. Kirk, *Electrochimica Acta*, 1992, 37, 169-175.
54. L. Trotochaud, J. K. Ranney, K. N. Williams and S. W. Boettcher, *Journal of the American Chemical Society*, 2012, 134, 17253-17261.
55. R. Subbaraman, D. Tripkovic, K.-C. Chang, D. Strmcnik, A. P. Paulikas, P. Hirunsit, M. Chan, J. Greeley, V. Stamenkovic and N. M. Markovic, *Nat Mater*, 2012, 11, 550-557.
56. X. Wu and K. Scott, *Journal of Materials Chemistry*, 2011, 21, 12344-12351.
57. X. Li, F. C. Walsh and D. Pletcher, *Physical Chemistry Chemical Physics*, 2011, 13, 1162-1167.
58. R. L. Tichenor, *Industrial & Engineering Chemistry*, 1952, 44, 973-977.
59. E. Potvin and L. Brossard, *Materials Chemistry and Physics*, 1992, 31, 311-318.
60. R. N. Singh, J. P. Pandey and K. L. Anitha, *International Journal of Hydrogen Energy*, 1993, 18, 467-473.
61. D. A. Corrigan, R. S. Conell, C. A. Fierro and D. A. Scherson, *The Journal of Physical Chemistry*, 1987, 91, 5009-5011.
62. C.-C. Hu and Y.-R. Wu, *Materials Chemistry and Physics*, 2003, 82, 588-596.
63. E. Guerrini, M. Piozzini, A. Castelli, A. Colombo and S. Trasatti, *J Solid State Electrochem*, 2008, 12, 363-373.
64. E. L. Miller and R. E. Rocheleau, *Journal of the Electrochemical Society*, 1997, 144, 3072-3077.
65. J. Landon, E. Demeter, N. İnoğlu, C. Keturakis, I. E. Wachs, R. Vasić, A. I. Frenkel and J. R. Kitchin, *Acs Catalysis*, 2012, 2, 1793-1801.
66. M. W. Louie and A. T. Bell, *Journal of the American Chemical Society*, 2013, 135, 12329-12337.

67. R. D. L. Smith, M. S. Prévot, R. D. Fagan, S. Trudel and C. P. Berlinguette, *Journal of the American Chemical Society*, 2013, 135, 11580-11586.
68. A. Grimaud, K. J. May, C. E. Carlton, Y.-L. Lee, M. Risch, W. T. Hong, J. Zhou and Y. Shao-Horn, *Nat Commun*, 2013, 4.
69. S. Raabe, D. Mierwaldt, J. Ciston, M. Uijttewaal, H. Stein, J. Hoffmann, Y. Zhu, P. Blöchl and C. Jooss, *Adv. Funct. Mater.*, 2012, 22, 3378-3388.
70. K. J. May, C. E. Carlton, K. A. Stoerzinger, M. Risch, J. Suntivich, Y. L. Lee, A. Grimaud and Y. Shao-Horn, *J. Phys. Chem. Lett.*, 2012, 3, 3264-3270.
71. J. O. Bockris and T. Otagawa, *J. Phys. Chem.*, 1983, 87, 2960-2971.
72. M. Risch, A. Grimaud, K. J. May, K. A. Stoerzinger, T. J. Chen, A. N. Mansour and Y. Shao-Horn, *The Journal of Physical Chemistry C*, 2013, 117, 8628-8635.
73. J. Suntivich, K. J. May, H. A. Gasteiger, J. B. Goodenough and Y. Shao-Horn, *Science*, 2011, 334, 1383-1385.
74. M. Nesselberger, S. Ashton, J. C. Meier, I. Katsounaros, K. J. J. Mayrhofer and M. Arenz, *Journal of the American Chemical Society*, 2011, 133, 17428-17433.
75. R. J. Isaifan, S. Ntais and E. A. Baranova, *Applied Catalysis A: General*, 2013, 464–465, 87-94.
76. K. Kinoshita, *Journal of the Electrochemical Society*, 1990, 137, 845-848.
77. C. Cui, L. Gan, M. Heggen, S. Rudi and P. Strasser, *Nat Mater*, 2013, 12, 765-771.
78. Y. Kim, H. J. Kim, Y. S. Kim, S. M. Choi, M. H. Seo and W. B. Kim, *The Journal of Physical Chemistry C*, 2012, 116, 18093-18100.
79. V. R. Stamenkovic, B. S. Mun, M. Arenz, K. J. J. Mayrhofer, C. A. Lucas, G. Wang, P. N. Ross and N. M. Markovic, *Nature Materials*, 2007, 6, 241-247.
80. D. Wang, H. L. Xin, R. Hovden, H. Wang, Y. Yu, D. A. Muller, F. J. DiSalvo and H. D. Abruña, *Nat Mater*, 2012, advance online publication.
81. J. X. Wang, H. Inada, L. Wu, Y. Zhu, Y. Choi, P. Liu, W.-P. Zhou and R. R. Adzic, *Journal of the American Chemical Society*, 2009, 131, 17298-17302.
82. C. Wang, M. Chi, D. Li, D. Strmcnik, D. van der Vliet, G. Wang, V. Komanicky, K.-C. Chang, A. P. Paulikas, D. Tripkovic, J. Pearson, K. L. More, N. M. Markovic and V. R. Stamenkovic, *Journal of the American Chemical Society*, 2011, 133, 14396-14403.
83. C. J. Serpell, J. Cookson, D. Ozkaya and P. D. Beer, *Nat Chem*, 2011, 3, 478-483.
84. S. J. Hwang, S. J. Yoo, J. Shin, Y.-H. Cho, J. H. Jang, E. Cho, Y.-E. Sung, S. W. Nam, T.-H. Lim, S.-C. Lee and S.-K. Kim, *Sci. Rep.*, 2013, 3.
85. P. Ochal, J. L. G. de la Fuente, M. Tsypkin, F. Seland, S. Sunde, N. Muthuswamy, M. Ronning, D. Chen, S. Garcia, S. Alayoglu and B. Eichhorn, *Journal of Electroanalytical Chemistry*, 2011, 655, 140-146.
86. K. Kuttiyiel, K. Sasaki, Y. Choi, D. Su, P. Liu and R. R. Adzic, *Nano Letters*, 2012, DOI: 10.1021/nl303362s.

87. S. Alayoglu, P. Zavalij, B. Eichhorn, Q. Wang, A. I. Frenkel and P. Chupas, *Acs Nano*, 2009, 3, 3127-3137.
88. Y.-C. Hsieh, Y. Zhang, D. Su, V. Volkov, R. Si, L. Wu, Y. Zhu, W. An, P. Liu, P. He, S. Ye, R. R. Adzic and J. X. Wang, *Nat Commun*, 2013, 4.
89. X.-B. Zhang, J.-M. Yan, S. Han, H. Shioyama and Q. Xu, *Journal of the American Chemical Society*, 2009, 131, 2778-2779.
90. X. Xia, Y. Wang, A. Ruditskiy and Y. Xia, *Advanced Materials*, 2013, 25, 6313-6333.
91. C. Xu, Y. Liu, J. Wang, H. Geng and H. Qiu, *ACS Applied Materials & Interfaces*, 2011, 3, 4626-4632.
92. Y. Yang, J. Liu, Z.-W. Fu and D. Qin, *Journal of the American Chemical Society*, 2014, 136, 8153-8156.
93. C. Cui, M. Ahmadi, F. Behafarid, L. Gan, M. Neumann, M. Heggen, B. R. Cuenya and P. Strasser, *Faraday Discussions*, 2013, 162, 91-112.
94. M. Ahmadi, F. Behafarid, C. Cui, P. Strasser and B. R. Cuenya, *Acs Nano*, 2013, DOI: 10.1021/nn403793a.
95. S. Alayoglu, A. U. Nilekar, M. Mavrikakis and B. Eichhorn, *Nature Materials*, 2008, 7, 333-338.
96. V. R. Stamenkovic, B. Fowler, B. S. Mun, G. Wang, P. N. Ross, C. A. Lucas and N. M. Markovic, *Science*, 2007, 315, 493-497.
97. L.-L. Wang and D. D. Johnson, *Journal of the American Chemical Society*, 2009, 131, 14023-14029.
98. T. K. Sau and A. L. Rogach, in *Complex-Shaped Metal Nanoparticles*, Wiley-VCH Verlag GmbH & Co. KGaA, 2012, DOI: 10.1002/9783527652570.ch1, pp. 7-90.
99. S. E. Habas, H. Lee, V. Radmilovic, G. A. Somorjai and P. Yang, *Nat Mater*, 2007, 6, 692-697.
100. M. H. Oh, T. Yu, S.-H. Yu, B. Lim, K.-T. Ko, M.-G. Willinger, D.-H. Seo, B. H. Kim, M. G. Cho, J.-H. Park, K. Kang, Y.-E. Sung, N. Pinna and T. Hyeon, *Science*, 2013, 340, 964-968.
101. K. Sasaki, H. Naohara, Y. Choi, Y. Cai, W.-F. Chen, P. Liu and R. R. Adzic, *Nat Commun*, 2012, 3, 1115.
102. T. Ghosh, M. B. Vukmirovic, F. J. DiSalvo and R. R. Adzic, *Journal of the American Chemical Society*, 2009, 132, 906-907.
103. M. Shao, K. Shoemaker, A. Peles, K. Kaneko and L. Protsailo, *Journal of the American Chemical Society*, 2010, 132, 9253-9255.
104. J. Kim, C. Rong, J. P. Liu and S. Sun, *Advanced Materials*, 2009, 21, 906-909.
105. J. Kim, Y. Lee and S. Sun, *Journal of the American Chemical Society*, 2010, 132, 4996-4997.
106. H. Chen, Y. Yu, H. L. Xin, K. A. Newton, M. E. Holtz, D. Wang, D. A. Muller, H. D. Abruña and F. J. DiSalvo, *Chemistry of Materials*, 2013, 25, 1436-1442.
107. J. Greeley and M. Mavrikakis, *Nat Mater*, 2004, 3, 810-815.

108. D. Wang, H. L. Xin, R. Hovden, H. Wang, Y. Yu, D. A. Muller, F. J. DiSalvo and H. D. Abruña, *Nat Mater*, 2013, 12, 81-87.
109. S. Iijima, *Nature*, 1991, 354, 56-58.
110. M. F. L. De Volder, S. H. Tawfick, R. H. Baughman and A. J. Hart, *Science*, 2013, 339, 535-539.
111. D. Eder, *Chemical Reviews*, 2010, 110, 1348-1385.
112. J. Wu, Y. Xue, X. Yan, W. Yan, Q. Cheng and Y. Xie, *Nano Research*, 2012, 5, 521-530.
113. F. M. Toma, A. Sartorel, M. Iurlo, M. Carraro, P. Parisse, C. Maccato, S. Rapino, B. Rodriguez Gonzalez, H. Amenitsch, T. Da Ros, L. Casalis, A. Goldoni, M. Marcaccio, G. Scorrano, G. Scoles, F. Paolucci, M. Prato and M. Bonchio, *Nature Chemistry*, 2010, 2, 826-831.
114. F. M. Toma, A. Sartorel, M. Iurlo, M. Carraro, S. Rapino, L. Hoober-Burkhardt, T. Da Ros, M. Marcaccio, G. Scorrano, F. Paolucci, M. Bonchio and M. Prato, *Chemsuschem*, 2011, 4, 1447-1451.
115. C. Rutherglen, D. Jain and P. Burke, *Nature Nanotechnology*, 2009, 4, 811-819.
116. T. Ando, *Npg Asia Materials*, 2009, 1, 17-21.
117. M. Gong, Y. Li, H. Wang, Y. Liang, J. Z. Wu, J. Zhou, J. Wang, T. Regier, F. Wei and H. Dai, *Journal of the American Chemical Society*, 2013, 135, 8452-8455.
118. Y. Xiang, S. Lu and S. P. Jiang, *Chem. Soc. Rev.*, 2012, 41, 7291-7321.
119. Q. Zhang, J.-Q. Huang, W.-Z. Qian, Y.-Y. Zhang and F. Wei, *Small*, 2013, 9, 1237-1265.
120. D. Eder, *Chemical Reviews*, 2010, 110, 1348-1385.
121. R. L. McCreery, *Chemical Reviews*, 2008, 108, 2646-2687.
122. A. Alexiadis and S. Kassinos, *Chemical Reviews*, 2008, 108, 5014-5034.
123. A. C. Dillon, *Chemical Reviews*, 2010, 110, 6856-6872.
124. N. Saito, H. Haniu, Y. Usui, K. Aoki, K. Hara, S. Takanashi, M. Shimizu, N. Narita, M. Okamoto, S. Kobayashi, H. Nomura, H. Kato, N. Nishimura, S. Taruta and M. Endo, *Chemical Reviews*, 2014, 114, 6040-6079.
125. D. S. Su, S. Perathoner and G. Centi, *Chemical Reviews*, 2013, 113, 5782-5816.
126. N. Karousis, N. Tagmatarchis and D. Tasis, *Chemical Reviews*, 2010, 110, 5366-5397.
127. G. Ouyang, C. X. Wang and G. W. Yang, *Chemical Reviews*, 2009, 109, 4221-4247.
128. H. Dai, *Accounts of Chemical Research*, 2002, 35, 1035-1044.
129. D. Tasis, N. Tagmatarchis, A. Bianco and M. Prato, *Chemical Reviews*, 2006, 106, 1105-1136.
130. C. Shen, A. H. Brozena and Y. H. Wang, *Nanoscale*, 2011, 3, 503-518.
131. P. R. Bandaru, *Journal of Nanoscience and Nanotechnology*, 2007, 7, 1239-1267.
132. R. Andrews, D. Jacques, D. Qian and T. Rantell, *Accounts of Chemical Research*, 2002, 35, 1008-1017.
133. D. A. Britz and A. N. Khlobystov, *Chemical Society Reviews*, 2006, 35, 637-659.

134. K. Liu, X. Hong, Q. Zhou, C. Jin, J. Li, W. Zhou, J. Liu, E. Wang, A. Zettl and F. Wang, *Nat Nano*, 2013, 8, 917-922.
135. M. C. Hersam, *Nat Nano*, 2008, 3, 387-394.
136. F. Yang, X. Wang, D. Zhang, J. Yang, LuoDa, Z. Xu, J. Wei, J.-Q. Wang, Z. Xu, F. Peng, X. Li, R. Li, Y. Li, M. Li, X. Bai, F. Ding and Y. Li, *Nature*, 2014, 510, 522-524.
137. T. Shimada, T. Sugai, Y. Ohno, S. Kishimoto, T. Mizutani, H. Yoshida, T. Okazaki and H. Shinohara, *Applied Physics Letters*, 2004, 84, 2412-2414.
138. A. H. Brozena, J. Moskowitz, B. Shao, S. Deng, H. Liao, K. J. Gaskell and Y. Wang, *Journal of the American Chemical Society*, 2010, 132, 3932-3938.
139. A. A. Green and M. C. Hersam, *Nat Nano*, 2009, 4, 64-70.
140. A. A. Green and M. C. Hersam, *Acs Nano*, 2011, 5, 1459-1467.
141. S. Aksel and D. Eder, *Journal of Materials Chemistry*, 2010, 20, 9149-9154.
142. B. Frank, A. Rinaldi, R. Blume, R. Schlögl and D. S. Su, *Chemistry of Materials*, 2010, 22, 4462-4470.
143. E. Pop, D. Mann, Q. Wang, K. Goodson and H. Dai, *Nano Letters*, 2005, 6, 96-100.
144. M. M. J. Treacy, T. W. Ebbesen and J. M. Gibson, *Nature*, 1996, 381, 678-680.
145. B. WenXing, Z. ChangChun and C. WanZhao, *Physica B: Condensed Matter*, 2004, 352, 156-163.
146. A. Krishnan, E. Dujardin, T. W. Ebbesen, P. N. Yianilos and M. M. J. Treacy, *Physical Review B*, 1998, 58, 14013-14019.
147. R. Purohit, K. Purohit, S. Rana, R. S. Rana and V. Patel, *Procedia Materials Science*, 2014, 6, 716-728.
148. M. Kumar and Y. Ando, *Journal of Nanoscience and Nanotechnology*, 2010, 10, 3739-3758.
149. L.-L. Tan, W.-J. Ong, S.-P. Chai and A. R. Mohamed, *Catalysis Today*, 2013, 217, 1-12.
150. M. Lubej and I. Plazl, *Chem. Biochem. Eng. Q.*, 2012, 26, 277-284.
151. V. Jourdain and C. Bichara, *Carbon*, 2013, 58, 2-39.
152. G. D. Nessim, *Nanoscale*, 2010, 2, 1306-1323.
153. J.-P. Tessonnier and D. S. Su, *Chemsuschem*, 2011, 4, 824-847.
154. G. N. Ayre, T. Uchino, B. Mazumder, A. L. Hector, J. L. Hutchison, D. C. Smith, P. Ashburn and C. H. de Groot, *Journal of Physics-Condensed Matter*, 2011, 23.
155. H. J. Wang, H. Yu, F. Peng and P. Lv, *Electrochem. Commun.*, 2006, 8, 499-504.
156. J. E. Thomas, A. R. Bonesi, M. S. Moreno, A. Visintin, A. M. C. Luna and W. E. Triaca, *Int. J. Hydrog. Energy*, 2010, 35, 11681-11686.
157. Y. Y. Mu, H. P. Liang, J. S. Hu, L. Jiang and L. J. Wan, *J. Phys. Chem. B*, 2005, 109, 22212-22216.
158. G. N. Ostojic, J. R. Ireland and M. C. Hersam, *Langmuir*, 2008, 24, 9784-9789.
159. Y. Y. Ou and M. H. Huang, *J. Phys. Chem. B*, 2006, 110, 2031-2036.

160. Z. W. Liu, Q. Q. Shi, F. Peng, H. J. Wang, R. F. Zhang and H. Yu, *Electrochem. Commun.*, 2012, 16, 73-76.
161. S. H. Tang, G. Q. Sun, S. G. Sun, J. Qi, Q. Xin and G. M. Haarberg, *J. Electrochem. Soc.*, 2010, 157, B1321-B1325.
162. X. M. Wang, N. Li, L. D. Pfefferle and G. L. Haller, *Journal of Physical Chemistry C*, 2010, 114, 16996-17002.
163. S. Wang, S. P. Jiang and X. Wang, *Nanotechnology*, 2008, 19.
164. J. Prabhuram, T. S. Zhao, Z. K. Tang, R. Chen and Z. X. Liang, *J. Phys. Chem. B*, 2006, 110, 5245-5252.
165. Y. Y. Huang, J. D. Cal, S. Y. Zheng and Y. L. Guo, *Journal of Power Sources*, 2012, 210, 81-85.
166. S. Y. Wang, S. P. Jiang, T. J. White, J. Guo and X. Wang, *Journal of Physical Chemistry C*, 2009, 113, 18935-18945.
167. Z. Q. Tian, S. P. Jiang, Y. M. Liang and P. K. Shen, *J. Phys. Chem. B*, 2006, 110, 5343-5350.
168. L. Meng, C. Fu and Q. Lu, *Progress in Natural Science*, 2009, 19, 801-810.
169. S. Wang, X. Wang and S. P. Jiang, *Langmuir*, 2008, 24, 10505-10512.
170. S. Murugesan, K. Myers and V. Subramanian, *Applied Catalysis B-Environmental*, 2011, 103, 266-274.
171. K. R. Reddy, B. C. Sin, K. S. Ryu, J.-C. Kim, H. Chung and Y. Lee, *Synthetic Metals*, 2009, 159, 595-603.
172. Y. L. Hsin, K. C. Hwang and C.-T. Yeh, *Journal of the American Chemical Society*, 2007, 129, 9999-10010.
173. L. Dai, D. W. Chang, J.-B. Baek and W. Lu, *Small*, 2012, 8, 1130-1166.
174. K. H. Kangasniemi, D. A. Condit and T. D. Jarvi, *Journal of the Electrochemical Society*, 2004, 151, E125-E132.
175. T. Matsumoto, T. Komatsu, K. Arai, T. Yamazaki, M. Kijima, H. Shimizu, Y. Takasawa and J. Nakamura, *Chem. Commun.*, 2004, DOI: 10.1039/b400607k, 840-841.
176. W. Li, C. Liang, J. Qiu, W. Zhou, H. Han, Z. Wei, G. Sun and Q. Xin, *Carbon*, 2002, 40, 791-794.
177. X. Wang, W. Li, Z. Chen, M. Waje and Y. Yan, *Journal of Power Sources*, 2006, 158, 154-159.
178. J. Wang, G. Yin, Y. Shao, Z. Wang and Y. Gao, *The Journal of Physical Chemistry C*, 2008, 112, 5784-5789.
179. M. Asgari and E. Lohrasbi, *ISRN Electrochemistry*, 2013, 2013, 7.
180. W. Ye, H. Hu, H. Zhang, F. Zhou and W. Liu, *Applied Surface Science*, 2010, 256, 6723-6728.
181. H.-Y. Lee, W. Vogel and P. P.-J. Chu, *Langmuir*, 2011, 27, 14654-14661.

182. V. Bambagioni, C. Bianchini, A. Marchionni, J. Filippi, F. Vizza, J. Teddy, P. Serp and M. Zhiani, *Journal of Power Sources*, 2009, 190, 241-251.
183. C. Hu, Y. Cao, L. Yang, Z. Bai, Y. Guo, K. Wang, P. Xu and J. Zhou, *Applied Surface Science*, 2011, 257, 7968-7974.
184. D. Wang, S. Lu and S. P. Jiang, *Electrochimica Acta*, 2010, 55, 2964-2971.
185. B. Wu, Y. Kuang, X. Zhang and J. Chen, *Nano Today*, 2011, 6, 75-90.
186. M. S. Saha and A. Kundu, *Journal of Power Sources*, 2010, 195, 6255-6261.
187. X. Zou, X. Huang, A. Goswami, R. Silva, B. R. Sathe, E. Mikmeková and T. Asefa, *Angewandte Chemie*, 2014, 126, 4461-4465.
188. Y. Liang, Y. Li, H. Wang and H. Dai, *Journal of the American Chemical Society*, 2013, 135, 2013-2036.
189. Z. Chen, D. Higgins, H. Tao, R. S. Hsu and Z. Chen, *Journal of Physical Chemistry C*, 2009, 113, 21008-21013.
190. K. Gong, F. Du, Z. Xia, M. Durstock and L. Dai, *Science*, 2009, 323, 760-764.
191. L. Yang, S. Jiang, Y. Zhao, L. Zhu, S. Chen, X. Wang, Q. Wu, J. Ma, Y. Ma and Z. Hu, *Angewandte Chemie-International Edition*, 2011, 50, 7132-7135.
192. Q. Shi, F. Peng, S. Liao, H. Wang, H. Yu, Z. Liu, B. Zhang and D. Su, *J. Mater. Chem. A*, 2013, 1, 14853-14857.
193. J. Zhu, S. P. Jiang, R. Wang, K. Shi and P. K. Shen, *J. Mater. Chem. A*, 2014, 2, 15448-15453.
194. L. Qu, Y. Liu, J.-B. Baek and L. Dai, *Acs Nano*, 2010, 4, 1321-1326.
195. D.-W. Wang and D. Su, *Energy & Environmental Science*, 2014, 7, 576-591.
196. Y. Zhao, R. Nakamura, K. Kamiya, S. Nakanishi and K. Hashimoto, *Nat Commun*, 2013, 4.
197. G.-L. Tian, M.-Q. Zhao, D. Yu, X.-Y. Kong, J.-Q. Huang, Q. Zhang and F. Wei, *Small*, 2014, 10, 2251-2259.
198. Y. L. Chen, J. H. Li, Z. H. Hong, B. Shen, B. Z. Lin and B. F. Gao, *Physical Chemistry Chemical Physics*, 2014, 16, 8106-8113.
199. T. Y. Ma, S. Dai, M. Jaroniec and S. Z. Qiao, *Angewandte Chemie International Edition*, 2014, 53, 7281-7285.
200. B. R. Sathe, X. Zou and T. Asefa, *Catalysis Science & Technology*, 2014, 4, 2023-2030.
201. L. Wang, A. Ambrosi and M. Pumera, *Angewandte Chemie International Edition*, 2013, 52, 13818-13821.
202. Y. Li, W. Zhou, H. Wang, L. Xie, Y. Liang, F. Wei, J. C. Idrobo, S. J. Pennycook and H. Dai, *Nat Nanotechnol*, 2012, 7, 394-400.
203. S. Wang, D. Yu and L. Dai, *Journal of the American Chemical Society*, 2011, 133, 5182-5185.
204. T. S. Miller, J. V. Macpherson and P. R. Unwin, *Physical Chemistry Chemical Physics*, 2014, 16, 9966-9973.

205. K. Waki, R. A. Wong, H. S. Oktaviano, T. Fujio, T. Nagai, K. Kimoto and K. Yamada, *Energy & Environmental Science*, 2014, 7, 1950-1958.
206. W. Cui, Q. Liu, N. Cheng, A. M. Asiri and X. Sun, *Chem. Commun.*, 2014, 50, 9340-9342.
207. K. Tammeveski, K. Kontturi, R. J. Nichols, R. J. Potter and D. J. Schiffrin, *Journal of Electroanalytical Chemistry*, 2001, 515, 101-112.
208. M. Zhang, Y. Yan, K. Gong, L. Mao, Z. Guo and Y. Chen, *Langmuir*, 2004, 20, 8781-8785.
209. G. Jürmann and K. Tammeveski, *Journal of Electroanalytical Chemistry*, 2006, 597, 119-126.
210. D. Qu, *Carbon*, 2007, 45, 1296-1301.
211. I. Kruusenberg, N. Alexeyeva and K. Tammeveski, *Carbon*, 2009, 47, 651-658.
212. P. K. Dubey, A. S. K. Sinha, S. Talapatra, N. Koratkar, P. M. Ajayan and O. N. Srivastava, *International Journal of Hydrogen Energy*, 2010, 35, 3945-3950.
213. A. Misra, J. Giri and C. Daraio, *Acs Nano*, 2009, 3, 3903-3908.
214. J. C. Byers, A. G. Güell and P. R. Unwin, *Journal of the American Chemical Society*, 2014, 136, 11252-11255.

Chapter 3: Pristine Carbon Nanotubes as Non-metal Electrocatalysts for Oxygen Evolution Reaction of Water Splitting

3.1 Introduction

Hydrogen production from water splitting driven by renewable energy, such as hydro, solar or wind power is a most environmentally friendly pathway to meet the constantly growing demand for renewable energy storage and conversion technologies. For example, the most mature solar-driven water splitting technology is the combination of commercial photovoltaic (PV) modules with water electrolyzers [1]. However, the practical application of water electrolysis or water splitting is greatly constrained by the high overpotentials (η) required and the slow rate of the OER because the release of O_2 involves the formation of an oxygen-oxygen bond with an overall four-electron process [2]. Hence, developing efficient catalysts with high activity and durability for OER is of great technological and scientific significance in the application of renewable energy storage and conversion technologies.

There are substantial progresses on developing electrocatalysts for water splitting through decades of sustained efforts. These include noble metals and metal-oxides-based OER catalysts, such as Pt [3, 4], Pd [5], Au [5], Ir [4], Ru [4], RuO_2 [6], IrO_2 [7] and their combination [8], but their wide spread application is limited due to their high cost and scare resources. Water splitting under alkaline conditions allows the use of non-noble metals and inexpensive various oxide catalysts. Transition metal oxides, such as

MnO_2 [9, 10], Co_2O_3 [11-13], $NiCoO_3$ [14], Ni-Fe oxide [15] and $Fe_xCo_yNi_zO_x$ [16] have shown relatively good activity that are comparable to RuO_2 and IrO_2 in alkaline solutions. Some perovskite oxides such as $Ba_{0.5}Sr_{0.5}Co_{0.8}Fe_{0.2}O_{3-\delta}$ (BSCF) also exhibit high activity for OER in alkaline solution [17]. However, the low conductivity of these oxides are problematic in practical applications.

CNTs are seamless cylinders composed of one or more curved layers of graphene with either open or closed ends. These materials have been extensively studied as catalyst supports due to their unique properties, such as large specific surface area, excellent mechanical and electrical properties [12, 18-21]. Co_2O_3 particles supported on oxidized MWNTs yielded a current density of 10 mA cm^{-2} at an overpotential (η) of 0.39 V in 0.1 M KOH solution [22], significantly better than Co_2O_3 nanocrystals. Ultrathin nickel-iron layered double hydroxide nanoplates supported on oxidized MWNTs achieved a current density of 10 A g^{-1} at η = 0.228 V in 1 M KOH with catalysts loading of 0.25 mg cm^{-2} [20]. Li *et al.*[23] developed a mononuclear ruthenium complex supported on MWNTs, which show high electrocatalystic activity and low η for water oxidation reaction. Modifying CNTs by nitrogen-doping can substantially enhance the electrocatalytic activity for oxygen reduction and OER in alkaline solutions [24, 25]. However, it is generally believed that pristine CNTs without nitrogen-doping or supported metal or metal oxide nanoparticles would have little electrocatalytic activity for the water oxidation reactions.

Here we demonstrate, for the first time, that the as-received pristine CNTs with a diameter of 2-5 nm and composed mainly of 2-7 concentric tubes have extremely high electrochemical activities for the OER in alkaline solutions, as compared with SWNTs and MWNTs. And the pristine CNTs composed mainly of 2-7 concentric tubes have relatively high electrochemical activities for HER and ORR compared with SWNTs and MWNTs.

3.2 Experimental

3.2.1 Materials

CNTs with different number of walls and diameters were obtained from commercial sources including Nanostructured & Amorphous Materials, Inc., USA, Beijing Dk Nano technology Co., LTD, China and Shenzhen Nano, China. In order to reduce the possible effect of the metal catalysts, such as cobalt and nickel in the CNTs samples, on the OER, the as-received CNTs samples were purified as follow: 50 mg CNTs were dispersed in 50 mL HCl (30 wt %) solution before ultrasonicated for 1 h, then the dispersions were separated and the sludge were dispersed in a fresh 50 mL HCl (30 wt %) solution, followed by stirring overnight. The CNTs pellets were collected and transfer into a Teflon digestion tank and 10 mL HCl solution was added and digested at 120 ^{o}C overnight. After the digestion, the CNTs were washed by fresh HCl, and then by 5 mol L^{-1} HNO_3 for 3 times before rinsed thoroughly by DI water. The purified CNTs were dried and collected. Activated carbon (Sigma-Aldrich), graphite (Sigma-Aldrich), 50% Pt/C (Alfa Aesar), Ru/C (20 wt% Ru on Vulcan carbon black, Premetek Co.), KOH (Sigma-Aldrich), Nafion solution (5% in isopropanal and water, Sigma-Aldrich) were received and used without further treatment.

3.2.2 Characterization

The BET surface area of CNTs, activated carbon and graphite were characterized using a Gemini 2360 surface area analyzer. The Raman spectra were recorded in air at room temperature using a Perkin–Elmer GX FT-IR/Raman spectrometer with a back-scattered configuration and equipped with a Nd:YAG laser at 1064 nm as its light

source. CNTs were characterized using a TEM JEOL3000 operated at 200 kV. The average outer diameter (OD) and number of walls of CNTs were estimated by measuring 100 randomly chosen CNTs in the TEM images.

Thermo gravimetric (TG, Q5000) analyses were performed under air upon equilibration at 100 °C for 15 min, followed by a ramp of 10 °C min^{-1} up to 800 °C to estimate the content of the impurities in the CNTs samples. The elements of the impurities or trace metals were analyzed using Inductively Coupled Plasma (ICP-OES, IRIS Intrepid Ⅱ XSP, USA). The solutions for ICP analysis were prepared as follow: as received CNTs and the purified CNTs were digested using microwave dissolver (SINEO, HDS-8G) with acid mixture containing 10 mL HNO_3 (65%), 1 mL $HClO_4$ and 2 mL HF (the procedure was set as: 150 ^oC, 5 min; 180 ^oC, 5 min; 200 ^oC, 10 min; 230 ^oC, 20 min).

The electrochemical measurements were conducted in a three-electrode cell with a Luggin capillary, using a Gamery Reference 3000 Potentiostat. The tip of the Luggin capillary was placed 3 mm beneath the working electrode. The working electrode is prepared as follows. Generally, 1 mg of electro-catalyst was ultrasonically mixed in 2 mL Nafion solution to form a homogeneous ink, followed by pipetting 5 μL of the electro-catalyst ink onto the surface of a GCE. The diameter of GCE was 5 mm. The Ohmic potential drop between the working electrode and the tip of the Luggin capillary was estimated by measuring the impedance value at the frequency of 30 kHz. A Pt wire and SCE were used as the counter and reference electrodes, respectively. Potentials in the present study were given versus RHE reference electrode ($E_{RHE} = E_{vs\ SCE} + E_{SCE} + 0.059\times pH$, where $E_{SCE} = 0.247V$ vs RHE at 20 ^oC).

The LSV was conducted at a sweep rate of 1 mV s^{-1} in the potential range between 0-

1 V (vs SCE). Tafel plots were recorded at a sweep rate of 1 mV s^{-1} with the electrode initially conditioned at a potential of 0.65 V (vs. SCE) for 5 min before the potential scan. Tafel plots were IR corrected. Impedance curves were recorded under open circuit and different dc bias with frequency range from 0.1 Hz to 100 kHz and the signal amplitude of 10 mV using a Gamery Reference 3000 Potentiostat. Electrode polarization resistance, R_p, was measured by the differences between the high and low frequency intercepts. Without specification, the catalyst loading was 0.025 mg cm^{-2} and the measurements were conducted at GCE with rotating speed of 2000 rpm. The chronopotentiometry was conducted at different current density with catalysts loading of 0.1 mg cm^{-2}. For comparison, a commercial 20%Ru/C and 50%Pt/C was also investigated for OER under identical conditions. The reproducibility of the electrochemical activity of the CNTs for the OER in alkaline solution was confirmed by repeating the experiments for at least 3-5 times under identical conditions.

3.2.3 Calculations for Turnover Frequencies

The surface area of Pt is determined by measuring the charges ($Q_{Pt,H}$) from the H-adsorption or desorption peak of its CV curve. Each surface Pt atom is assumed to correspond to one chemisorbed H atom. The charges ($Q_{Pt,S}$) associated with a smooth Pt surface is accepted to be 210 μC cm^{-2}. Hence, the electrochemical surface area of the Pt electrode = $Q_{Pt,H}/Q_{Pt\,S}$. The current used for TOF calculation are obtained from LSV at 1 mV s^{-1}.

Mass nominated active surface area of 50% Pt-C:

560.995 μC/210m = 2.671 cm^2 /0.005 mg = 60.67 cm^2 /mg Pt

Number of Pt surface atom

50% Pt-C: $(210*10^{-6}*0.5*N_A)*2.671/ 96485.3=1.75*10^{15}$, N_A is Avogadro's constant

(6.02×10^{23});

The TOF of CNTs is calculated as follow:

Number of surface C atom:

$N_C=m_L/12/N_W$

m_L is the loading of CNTs, N_W is the average number of walls.

$TOF = I\ N_A/\ (96485.3n\cdot\ N_C)$

Where N_A is Avogadro's constant (6.02×10^{23}); n the the electron transfer number (4 for O_2), I is the current obtained at 1.8 V.

3.3 Results and Discussion

3.3.1 Characterization of CNTs

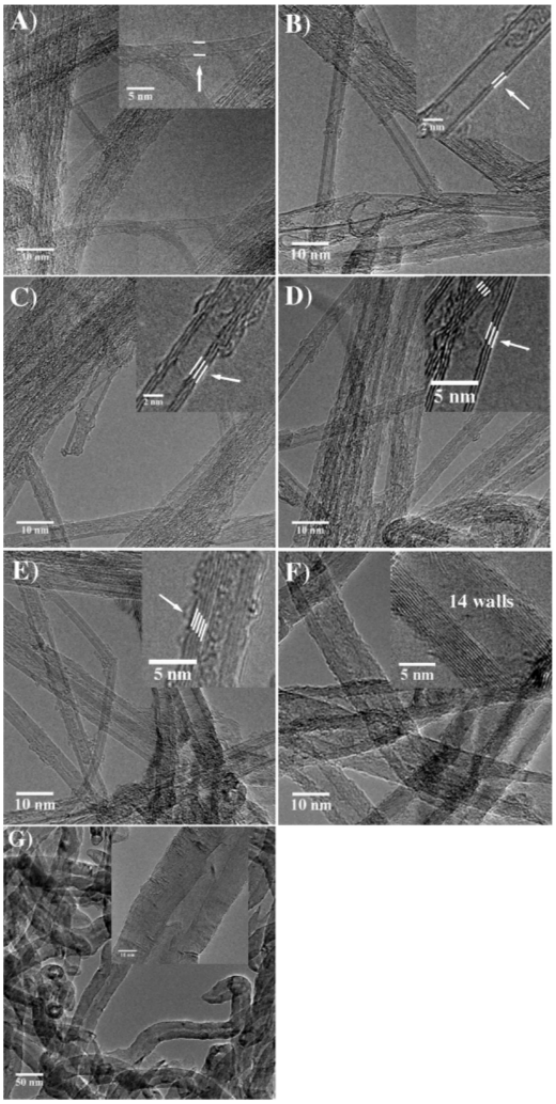

Figure 3.1. TEM micrographs of CNTs studied. A) CNTs-1, mainly SWNTs (79%) with OD = 1.97 nm, B) CNTs-2, mainly DWNTs (65%) with OD = 3.3 nm, C) CNTs-3, mainly TWCNTs (52%) with OD = 3.8 nm, D) CNTs-4, mainly TWCNTs (57%) with OD =4 nm, E) CNTs-5, mainly CNTs with 3-10 walls and OD = 5.1 nm, F) CNTs-6, mainly CNTs with 12 walls and OD = 13.9 nm, G) CNTs-7, typical MWNTs with the number of walls exceeding 30 and OD = 20-40 nm.

Fig. 3.1 is the TEM micrographs of CNTs samples used in the present study. According to the TEM images, no metal NPs were observed, indicating the good purity of our CNTs samples. The OD and number of walls were taken as the average of the measurement from the TEM images (Fig. 3.2, 3.3). Based on the size distribution, the CNTs were categorized as belonging to one of several different groups labeled as CNTs-n, where n = 1-7. CNTs-1 mainly consists of SWNTs (79%), some DWNTs, and generally occurs as bundles with an average OD of 1.97±0.40 nm (Fig. 3.1 A). CNTs-2 are mainly DWNTs (65%) with OD = 3.3±0.89 nm (Fig. 3.1 B), while CNTs-4 is similar to CNTs-3 mainly with triple-walled CNTs (TWCNTs, 52-57%) and OD = 3.8 - 4 nm (Figure 3.1 C and D). As the number of walls increases to 3-10 (the average number of walls is taken as 7), the OD also increases to 5.1±0.98 nm for CNTs-5 (Figure 3.1 E). CNTs-6 and CNTs-7 are MWNTs with the number of walls exceeding 12 and OD = 15-35 nm (Fig.3.1 F and G). The BET surface areas vary from 643-679 m^2 g^{-1} for CNTs-1, 2 and 3 to 175 - 85 m^2 g^{-1} for MWNTs. The number of walls, OD and BET surface areas of CNTs used in this study are given in Table 3.1.

Table 3.1. BET, outer diameter, number of walls, I_D/I_G ratios of CNTs samples.

CNTs	CNTs-1	CNTs-2	CNTs-3	CNTs-4	CNTs-5	CNTs-6	CNTs-7
Number of walls	1 (79%) 2 (16%) 3 (5%)	2 (65%) 3 (23%) 4 (5%)	2 (25%) 3 (52%) 4 (10%) 5 (8%)	3 (57%) 4 (20%) 5 (19%)	3 (5%) 4 (11%) 5 (25%) 6 (17%) 7 (16%) 8 (17%) 9 (9%)	>12	>30
$\bar{n}$	1	2	3	3	7	12>	30>
Outer diameters (nm)	1.97±0.4	3.3±0.89	3.8±0.63	4.0±0.66	5.1±0.98	13.9±5.2	35.2±8.5
Surface area (m^2/g)	651	679	643	459	485	174	85
I_D/I_G	0.16	0.51	0.76	0.94	1.35	2.50	2.86

*$\bar{n}$ is the average of number of walls of CNTs samples, taking as an integer number.

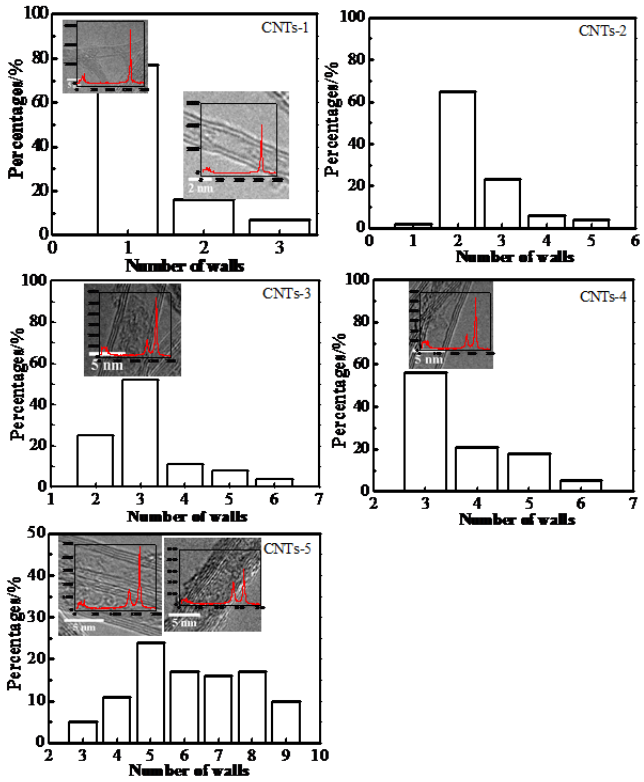

Figure 3.2. Distribution of number of walls of CNTs samples.

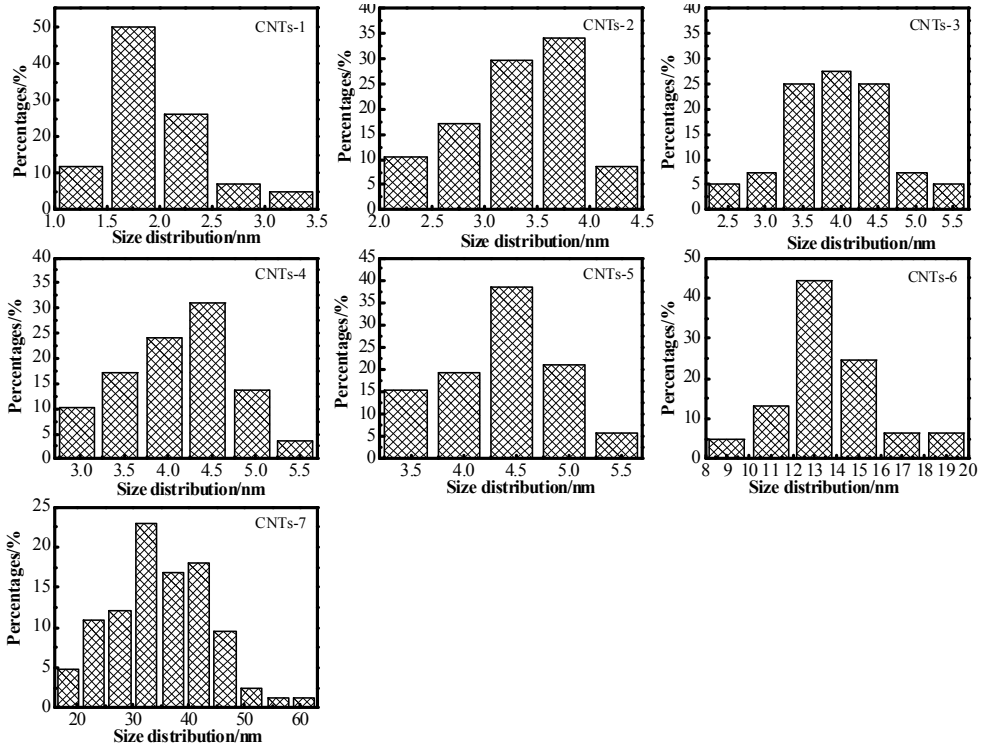

Figure 3.3. Distribution of outer diameters of CNTs samples.

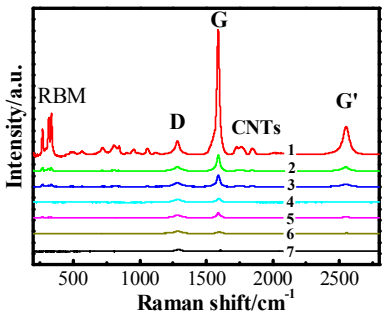

Figure 3.4. Raman spectra of CNTs with different OD and number of walls.

Raman spectra provide more details on the CNTs with different sizes and number of walls (Fig. 3.4). For CNTs-1, the radial breathing mode (RBM) observed around CNTs 200-300 cm^{-1} is typical characteristics for SWNTs [41-43]. For CNTs-2 and CNTs-3, the intensity of RMB is much smaller and no RMB was observed for large diameter CNTs-4, CNTs-5, CNTs-6 and CNTs-7. The Raman spectra show that the intensities of the *G* band (~1590 cm^{-1}) and *G'* band (~2700 cm^{-1}) decrease with an increasing number of walls and OD. The ratio of the intensities of the *D* band near 1300 cm^{-1} to the *G* band, I_D/I_G are 0.155, 0.51, 0.76, 0.94, 1.35, 2.50 and 2.86 for CNTs-1; CNTs-2, CNTs-3, CNTs-4, CNTs-5, CNTs-6 and CNTs-7, respectively. The I_D/I_G ratio increases with the increasing number of walls and OD as multiple graphite layers lead to a greater quantity of structural defects[26, 27]. The dominant RBM peaks and much smaller I_D/I_G observed on CNTs-1 indicate that CNTs-1 is dominated by SWNTs, while for CNTs-2 and CNTs-3, the dominant CNTs are DWNTs and TWCNTs, respectively. These results are consistent with that of the high resolution TEM images as shown in Fig. 3.1.

Figure 3.5 is the TGA curves of CNTs samples before and after the HCl purification treatments. The as received CNTs-1, CNTs-6 and CNTs-7 contain ~2 wt% ash, and it is ~5wt% for CNTs-2, CNTs-3, CNTs-4 and CNTs-5. The composition of metal elements in CNTs before and after purification was analyzed by ICP, and the results

are present in Table 3.2. The trace metal elements in ash contain Fe, Co, Ni and Mo. The results indicate that the total amount of trace metals was reduced considerably after purification. For example, as-received CNTs-2 and CNTs-3 contain about 2.32 wt% and 2.02 wt% Co, and after purification, only 0.81 wt% and 0.57 wt% Co were detected in CNTs-2 and CNTs-3, respectively. The amount of Mo also is reduced by more than 50% after purification.

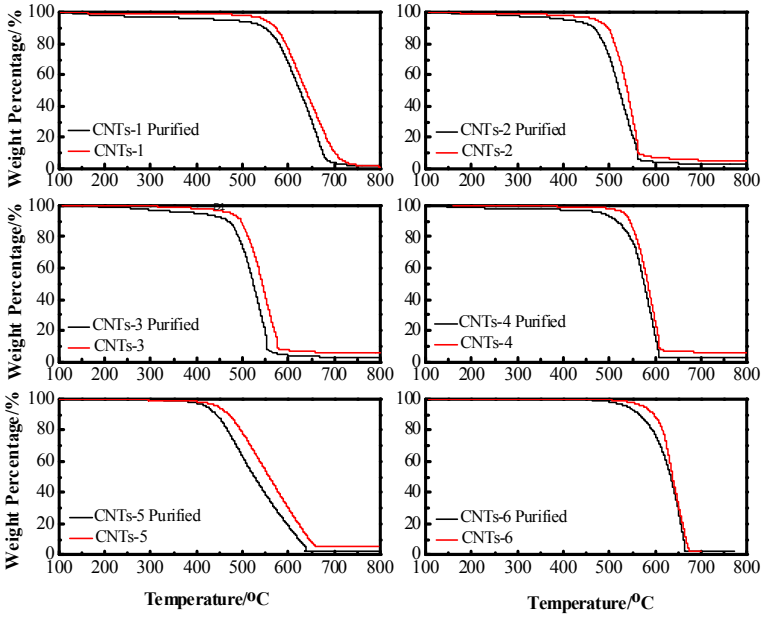

Figure 3.5. TGA curves of CNTs samples before and after purification treatment.

Table 3.2. Metal impurities composition in as-received CNTs and purified CNTs by ICP.

CNTs		CNTs-1	CNTs-2	CNTs-3	CNTs-4	CNTs-5	CNTs-6	CNTs-7
As received W/W %	Ash	1.56	4.82	5.1	5.2	5.16	2.16	2.39
	Co	0.08	2.32	2.02	-	0.5	-	-
	Fe	0.43	0.30	0.26	0.29	0.35	0.28	0.54
	Mo	0.04	0.75	0.73	0.79	0.11	-	0.84
	Ni	0.08	0.08	0.04	0.17	0.019	0.25	0.21
CNTs		CNTs-1	CNTs-2	CNTs-3	CNTs-4	CNTs-5	CNTs-6	CNTs-7
Purified W/W %	Ash	1.21	2.08	2.15	2.54	2.28	2.08	1.83
	Co	0.07	0.81	0.57	-	0.38	-	-
	Fe	0.29	0.23	0.23	0.28	0.17	0.21	0.29
	Mo	0.03	0.30	0.27	0.34	0.09	0.01	0.49
	Ni	0.05	0.04	0.03	0.15	0.015	0.2	0.17

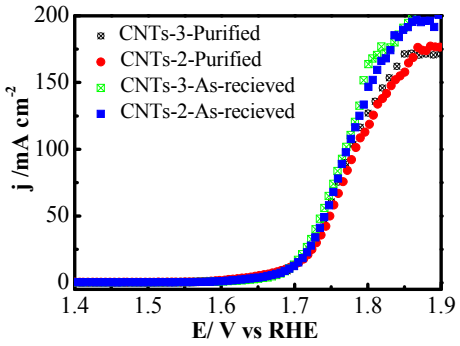

Figure 3.6. Liner scans voltammetry of as-received CNTs-2 and CNTs-3 and purified CNTs-2 and CNTs-3 for OER. The performance was measured at scan rate of 1 mV s^{-1} in 1 M KOH solution with CNTs loading 0.025 mg cm^{-2}.

Fig. 3.6 is the electrochemical activity for OER on CNTs-2 and CNTs-3 before and after purification treatment. The activity of CNTs samples after purification are slightly lower than that of as-received CNTs samples before the HCl treatment, despite the significant reduction in the trace elements in the as-received CNTs samples. For example, as-received CNTs-2 contains 3.45 wt% trace metals such as Co, Fe, Mo, and Ni, after HCl purification, the trace metal contents reduced to 1.38 wt%, 2.5 times lower than that in the received sample. Similar reduction in the trace metal elements was also observed for CNTs-3. However, the electrochemical activity of CNTs-2 and CNTs-3 for OER before and after purification treatment is close, indicating that the presence of trace metals on the electrocatalystic activity of CNTs for OER is minor and can be ignored under the conditions of the present study.

3.3.2 Electrochemical activity for OER

Fig. 3.7A shows the typical LSV curves of CNTs for the OER measured in 1 M KOH solution at rotating rate of 2000 rpm with a scan rate of 1 mV s^{-1}. Fig. 3.7 B and C are the plots of the average current densities measured at 1.8 V (*vs*. RHE) and onset potentials of CNT samples based on 3-5 measurements against tube size or the

number of walls. The CNTs loading was 0.025 mg cm^{-2}. The electrocatalystic activity of CNTs for OER strongly depends on the characteristics of CNTs (i.e., OD and the number of walls). The activities for the OER of CNTs-2, CNTs-3 and CNTs-4 are significantly higher compared with those of CNTs-1, CNTs-5, CNTs-6 and CNTs-7. For the reaction on the CNTs-1, the onset potential is 1.75±0.01 V and the current is 5.9±1.7 mA cm^{-2} measured at 1.8 V. When the average number of walls increase to 3 with a corresponding increase of tube size, i.e., OD=3.8 nm (e.g., CNTs-3), the onset potential is shifted to a lower potential 1.64±0.01 V and the current density significantly increased to 56±4.7 mA cm^{-2} at 1.8 V, almost 10 times higher than that measured on SWNTs, CNTs-1. However, with a further increase in the number of walls (or the tube size), the activity for OER decreases again. For example, for CNTs-5 with an average 7 walls and OD = 5.1 nm, the onset potential increased again to 1.73±0.02 V and current density at 1.8 V dropped significantly to 28.7±2.7 mA cm^{-2}. In the case of large outer diameter MWNTs (CNTs-7), the onset potential is around 1.78±0.01 V and current density at 1.8 V is only 1.6±1.8 mA cm^{-2}. Most significantly, the activity of CNTs for OER follows distinctive volcano type dependence on the size (Fig.3.7 B) or on the number of walls of CNTs (Fig.3.7 C). The most active CNTs for the OER in alkaline solution are the ones mainly with 2-7 walls and with a diameter in the range of 2-5 nm (Fig. 3.7 B and C).

The TOF calculated at 1.8 V (*vs*. RHE) for CNTs with different number of wall and 50% Pt-C are presented in Fig. 3.7 D. The results show that the TOF increase from 0.01 s^{-1} for CNTs-1 to 1.34 s^{-1} for CNTs-2 and reach the maximum of 2.0 s^{-1} for CNT-4 which is about twice of 50% Pt/C with a TOF number of 0.954 s^{-1}. As the number of wall increase, the TOF decreases to 1.6 s^{-1} for the CNTs-5, and the TOF reach 0.67 s^{-1} for CNTs-6 when the number of walls is over 12. Similar distinctive volcano type

dependence of TOF on number of wall further demonstrate that the most active CNTs for the OER in alkaline solution are the ones mainly with 2-7 walls and with a diameter in the range of 2-5 nm.

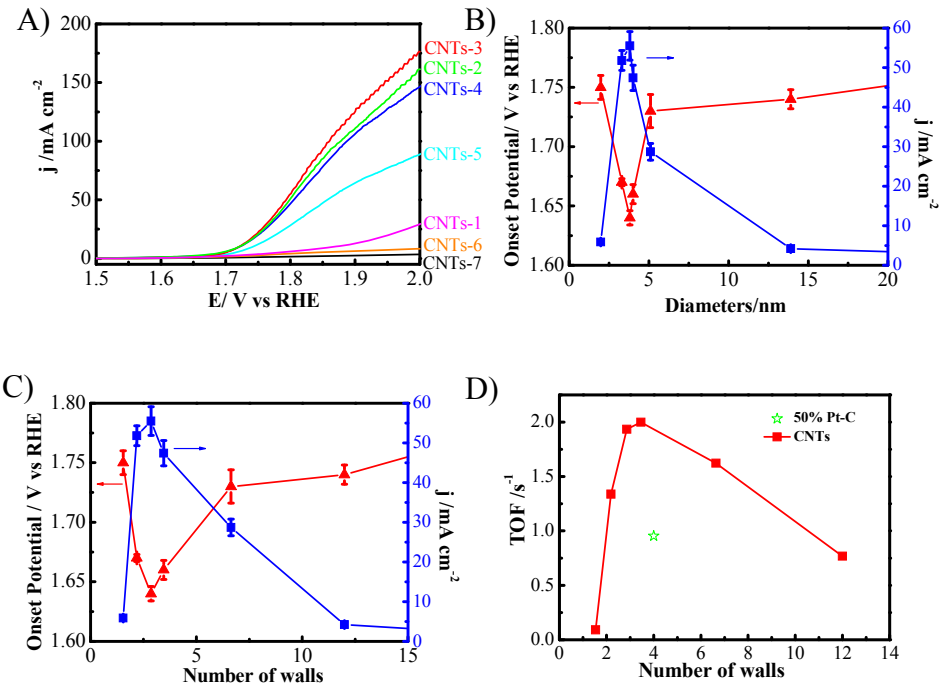

Figure 3.7. A) LSV of OER for CNTs measured in 1M KOH at scan rate of 1 mV s^{-1} with rotating rate of 2000 rpm; plots of current density measured at 1.8 V vs RHE and onset potential as a function of B) outer diameter (OD) and C) number of walls of CNTs; D) the calculated TOF vs number of walls for different CNTs at potential of 1.8 V vs RHE. The catalyst and CNTs loading was 0.025 mg cm^{-2}.

For the purpose of comparison, the activities of activated carbon, graphite, 20%Ru/C, 50%Pt/C catalysts were measured for OER in alkaline solution under identical conditions and the results are given in Fig. 3.8 together with the results on CNT-3 and CNTs-4. CNTs-3 and CNTs-4 have a lower onset potential and significantly higher current density, as compared with 50% Pt/C, activated carbon and graphite. For example, the current density of 56±4.7 mA cm^{-2} at a potential of 1.8 V for the OER on CNTs-3 is 10 times that of 50% Pt/C (5.6±2.1 mA cm^{-2}) and activated carbon

(5.8±3.2 mA cm^{-2}), and almost 100 times that of graphite (0.6±1.2 mA cm^{-2}). The BET surface area of activated carbon and graphite is 651 and 679 m^2 g^{-1}, respectively, similar to that of CNTs-3 samples (643 m^2 g^{-1}, Table 3.1). This indicates that high electrocatalytic activity of CNTs-3 for OER is not due to the high surface area. The onset potential of CNTs-3 for OER is 1.64±0.01 V, which is similar with that for Pt/C. The state-of-the-art Ru/C catalysts exhibited lowest onset potential of 1.58±0.02 V, indicating the better activity of Ru/C. However, the current density at higher potential is still significantly lower than that measured on CNTs-3 and CNTs-4 might because of the super conductivity of CNTs.

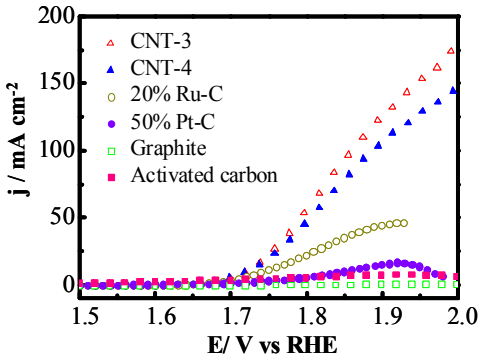

Figure 3.8. Linear scans voltammetry of selected CNTs, activated carbon, graphite, 20% Ru-C and 50% Pt-C for OER in 1M KOH at a scan rate of 1 mV s^{-1} with rotating rate of 2000 rpm. The catalyst and CNTs loading was 0.025 mg cm^{-2}.

The electrocatalytic activity of the CNTs for OER was further investigated by chronopotetiometry at different current density with CNTs loading of 0.1 mg cm^{-2}, measured at a rotating rate of 2000 rpm. The results are shown in Fig.3.9 A. The potentials for CNTs-2, CNTs-3, CNTs-4 and CNTs-5 to deliver a current density of 2, 5, 10, 20 and 50 mA cm^{-2} are significantly lower than that of CNTs-1, CNTs-6 and CNTs-7. For example, the potentials for CNTs-3 to achieve a current density of 2, 5, 10, 20 and 50 mA cm^{-2} are 1.64, 1.65, 1.68, 1.7 and 1.76 V respectively. On the other hand the potentials for MWNTs, CNTs-6 to achieve a current density of 2, 5, 10, 20

and 50 mA cm^{-2} are 1.74, 1.87, 1.95, 2.4 and 2.6 V, substantially higher than that observed on CNTs-3. These results further demonstrate that the electrocatalytic activity of CNTs-2, CNTs-3, CNTs-4 and CNTs-5 for OER is superior to CNTs-1, CNTs-6 and CNTs-7. The electrocatalytic activity of CNTs composed of between 2-7 concentric tubes and an outer diameter of 2-5 nm is also comparable with the active transition metal oxides [29, 30]. For example, the mass specific current density for OER on CNTs-3 is 100 A g^{-1} (i.e., 10 mA cm^{-2} on CNTs-3 with CNT loading of 0.1 mg cm^{-2}) at η = 0.45 V (1.68 V vs RHE), which is significantly better than 20 A g^{-1} reported on $NiMoO_4$ catalysts supported on Ni [30] and is comparable with 120 A g^{-1} for OER observed on the nitrogen-doped carbon materials under the same η [25]. Pristine CNTs are inherently very stable and highly conductive, an essential requirement as practical electrocatalysts for water oxidation reactions.

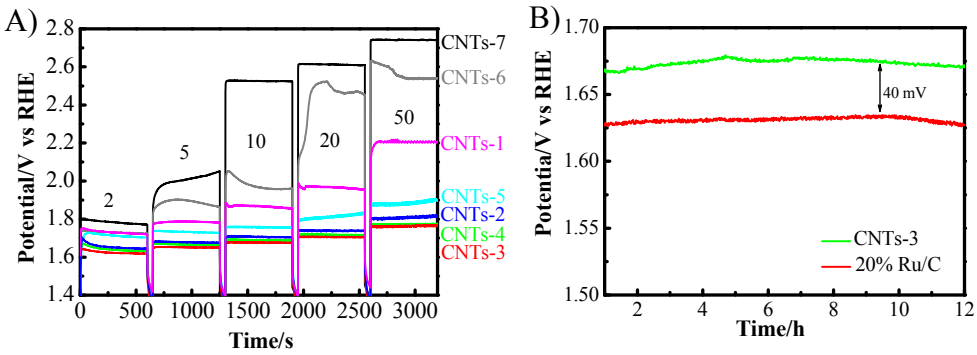

Figure 3.9. Chronopotentiometry of CNTs in 1 M KOH solution at different current density (mA cm^{-2}). The CNTs loading was 0.1 mg cm^{-2} and the rotating rate was 2000 rpm. Numbers are the current density in mA cm^{-2}.

The stability of CNTs-3 was also compared with 20% Ru/C at current density of 10 mA cm^{-2} with CNTs loading of 0.1 mg cm^{-2} (Fig.3.9 B). The potential to achieve 10 mA cm^{-2} for CNTs-3 is around 1.675 V, which is 40 mV higher than 20% Ru/C. Ru/C has a lower onset potential and the increase loading for long-term stability testing will significantly increase the current density, hence Ru/C can achieve a current density of

10 mA cm^{-2} at lower potential compared with CNTs-3. As the increase of time, the potentials to delivery a current density of 10 mA cm^{-2} for both CNTs-3 and Ru/C are remain stable after 12 h, demonstrating pristine CNTs are stable and of potential application as practical electrocatalysts for water oxidation reactions.

3.3.3 Kinetics of OER on CNTs

Figure 3.10 A is the Tafel plots for the OER on CNTs measured in 1M KOH with catalysts loading of 0.025 mg cm^{-2}. For OER, dual Tafel slopes were exhibited by the CNTs-2, CNTs-3, CNTs-4 and CNTs-5 catalysts, with a Tafel slope close to ~60 mV dec^{-1} at low η and ~120 mV dec^{-1} at high η. The dual Tafel slopes at low and high η regions were also reported for the OER on Pt and cobalt electrodes in alkaline solutions [3, 31, 32]. For the reaction on Ru/C, Tafel slope was 50 mV dec^{-1} at low η, similar to the Tafel slopes observed on metal oxide catalysts such as NiO_x and (Ni, Co)O_x [33, 34]. On the other hand, for the OER on CNTs-1, CNTs-6 and CNTs-7, the observed Tafel slope is ~140 mV dec^{-1}, substantially higher than that for the reaction on CNTs-2, CNTs-3, CNTs-4, CNTs-5 and Ru/C. The Tafel slope of ~60 mV dec^{-1} observed for the OER on CNTs-2, CNTs-3, CNTs-4, and CNTs-5 indicates the facile initial discharge of an OH^- ion on the surface of the outer walls of CNTs, as predicted for the first electron transfer step at the metal or metal hydroxide active site in the alkaline solution on metal and metal oxide-based catalysts [31, 34, 35]. The very high Tafel slope, ~140 mV dec^{-1} observed for the reaction on CNTs-1, CNTs-6 and CNTs-7 simply implies that the energy barrier for the electron transfer associated with the discharge of OH^{-1} species on the SWNTs and MWNTs is very high. This is evidently supported by the extremely low activity of SWNTs and MWNTs for the OER in alkaline solutions.

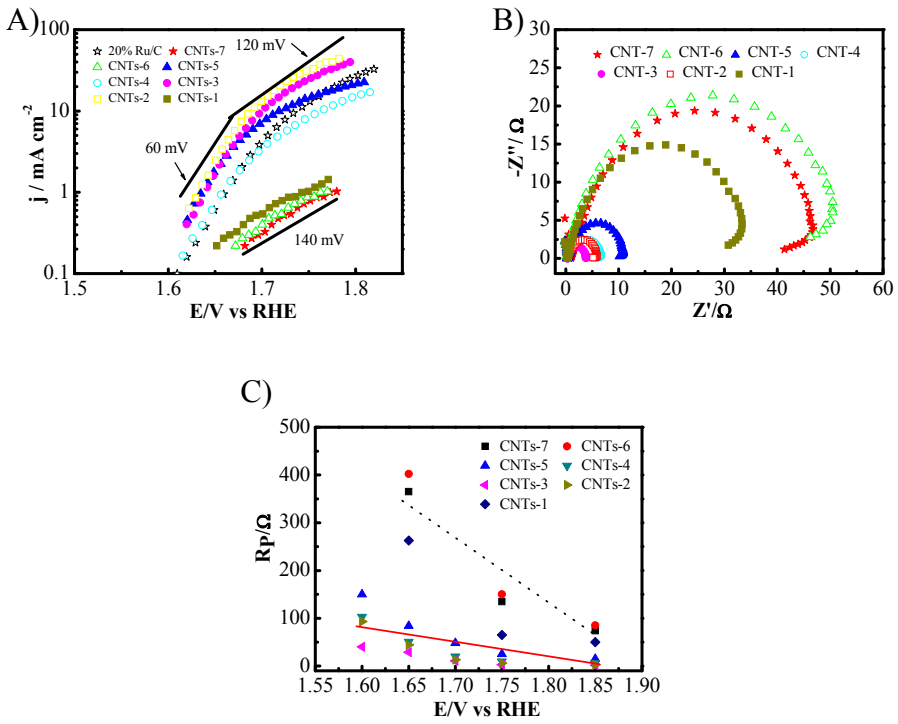

Figure 3.10. A) Tafel plots for OER on CNTs and 20% Ru/C catalysts, B) impedance spectra for the reaction on CNTs, measured at 1.65 V, and C) electrode polarization resistance, R_P of CNTs as a function of applied potential. The tests were conducted in 1M KOH solution with catalyst loading of 0.025 mg cm^{-2}.

The electrochemical impedance responses for the OER on CNTs are characterized by a single and depressed arc (Fig.3.10 B), similar to that reported for the reaction on nickel and cobalt electrode [31, 34]. The electrode polarization resistance, R_P is related to the kinetics of the interfacial charge transfer process. R_P for OER measured at a dc bias of 1.65 V (η = 0.42 V) on CNTs composed of between 2-7 concentric tubes and an outer diameter of 2-5 nm is in the range of 3.6-6.1 Ω cm^2, substantially smaller than 33 Ω cm^2 to 55 Ω cm^2 measured on CNTs-1, CNTs-6 and CNTs-7. And the R_p of CNTs composed of between 2-7 concentric tubes and an outer diameter of 2-5 nm are much less sensitive to the applied dc bias, indicating the high activity of the CNTs for the OER (Fig.3.10 C). These results again indicate the much lower energy barrier

for OER on CNTs-2, CNTs-3, CNTs-4 and CNTs-5, as compared to the reaction on CNTs-1, CNTs-6 and CNTs-7, consistent with the results from LSV and Tafel slope.

3.3.4. Electrocatalytic activity of CNTs

Wang et al showed recently that the trace metal elements in the heteroatom-doped graphene are responsible for the catalytic ORR observed [36]. In the present study, the amount of trace metal impurities (i.e., Co, Fe, Mo, Ni) in the as-received CNTs samples are typically in the range of 0.63% for CNTs-1 to 3.45% for CNTs-3 (see Table 3.2). After HCl treatment, the total trace metal impurities are reduced to 1.3% for CNTs-2, 1.1% for CNTs-3, and 0.44% for CNTs-1. The presence of the trace metal impurities after the HCl treatment is mainly due to the fact that milder purification treatment was used in this study to avoid the adverse structural modification of CNTs associated with harsh oxidation treatment [37]. As shown in Fig.3.5 and 3.6, significant reduction in the trace metal impurities has little effect on the electrocatalytic activity of the selected CNTs for the OER in alkaline solutions. The activity of CNTs-3 for OER is almost 10 times higher than that measured on CNTs-1 while the content of trace metal impurities of CNTs-3 is 1.1%, about 2.5 times higher than 0.44% on CNTs-1. The activity of MWNTs, CNTs-7, is 35 times lower than that of CNTs-3, but the trace metal content of CNTs-7 is 0.95%, close to that of CNTs-3 (Table 3.2). These results indicate that the presence of trace metal impurities is not responsible for the huge difference of activities between CNTs samples.

Having identified that there is a clear maximum in the catalytic activity of CNTs as a function of increasing size or number of walls, it is important to consider whether there is a rationale for this observed behavior. As a starting point, the energetics of functionalization of CNTs as a function of diameter has been extensively examined

for a variety of substituents. For example, it is well documented that processes such as the chemisorption of hydrogen on the outside surface of SWNTs is exothermic for small diameters, due to the release of strain, and becomes less favorable as the index, n, of the armchair nanotube (n,n) increases [38, 39]. Based on these, it might be expected that the initial reaction of hydroxide, i.e., the discharge of OH^{-1} species and other mechanistic steps that involve adsorption or attachment of OH^{-1} species to the outside of the tubes, are most favorable and therefore fastest for CNTs of smallest diameter. Therefore it might be expected that the rate would diminish with increasing CNT size. While this is in accord with the limiting behavior observed for larger diameters, it fails to explain why CNTs with outer diameter 2-5 nm are far more effective than in the single walled CNTs with smaller size.

The electron transport properties of CNTs can play an important role in the charge transfer processes for the OER. The electric properties of SWNTs are sensitive to the size and chirality of the tubes. In theory, nearly one-third of the SWNTs are metallic or semi-metallic and the other two-thirds are semiconducting [40]. The absorption of OH^- and intermediate species, such as OOH^*, could have a significant effect on the electronic state of the outer wall of SWNTs as it is well known that covalent sidewall functionalization of SWNTs can drastically change the electronic states of nanotubes near the Fermi level [41]. The covalent functionalization associated with the purification of CNTs could disrupt the π-electron system, causing the loss of the optical and electrical properties of SWNTs. The combined effect of dominant semiconducting properties and variation of electronic states by absorption of OH^- and other species could be responsible for the low activity of the SWNTs (i.e., CNTs-1) for OER and fuel cell reactions.

Unlike SWNTs, the presence of inner walls could increase the number of conducting

channels and create the possibility of interactions between the different walls. Fujisawa et al. studied the electrical properties of SWNTs and DWNTs and showed experimentally that the conduction mechanism strongly depends on the total fraction of metallic inner and outer tubes within the DWCNT samples, and the inner tubes contribute significantly to the electronic transport properties of DWNTs [42]. The outer wall can also serve as a protective barrier to prevent endohedral reactions, potentially allowing the inner-tube to retain its electronic properties [43]. This indicates the possibility of the separation of functionality of the outer wall and inner-tubes for the OER on DWNTs; the outer wall provides reaction sites for the adsorption and dissociation of OH^-, OOH^*, species, while the intact inner-tube serves as the electronic conducting pathway for the charge transfer process of the reaction, assuming there is a reasonable distribution of conducting and semi-conducting tubes for both outer wall and inner tubes. The electron transfer between the outer wall and inner tube could occur by electron tunneling, similar to the electron tunneling through thin oxide films as proposed by Damjanovic et al for the OER on Pt [44]. This hypothesis explains why double/triple-walled CNTs-2, CNTs-3 and CNTs-4 are far more effective than single-walled CNTs-1.

As the number of walls/layers increases, other issues could adversely affect the electrocatalytic activity of CNTs. Li et al studied the transparency-conductance performance of SWNTs, DWNTs and MWNTs, and found that DWNTs have better performance in this regard [45]. This was explained by the fact that SWNTs contain many semi-conducting nanotubes, while MWNTs materials absorb more photons per nanotube due to the large mass density. In the case of OER, the driven force for the electron transfer or tunneling between the outer wall and inner tubes is the applied dc bias, *i.e.*, the η. As the number of walls/layers increases, the dc bias between the outer

wall and the nearest inner tube would diminish due to the distribution of the dc bias across each layer. Thus, the electron transfer or tunneling from the outer surface to the inner tubes could become less favourable as the number of walls/layers increases. This appears to be supported by the reduced activity of CNTs-4 and CNTs-5 as compared to CNTs-2 and CNTs-3 due to the increased number of walls and the very high Tafel slope and high R_P for the OER on multi-walled CNTs-6 and CNTs-7.

3.4 Conclusion

Here we demonstrated, for the first time, that the electrocatalytic activity of CNTs for the OER of water electrolysis in alkaline solutions shows a distinctive volcano-dependence on the size and/or number of walls of CNTs. CNTs with OD around 2-5 nm and 2-7 walls have excellent activity, fast kinetics and much lower energy barrier for OER in alkaline solutions, as compared with the SWNTs (i.e., CNTs-1) and MWNTs (i.e., CNTs-6 and CNTs-7). For example, the activity of TWCNTs (i.e., CNTs-3) measured at 1.8 V (*vs*. RHE) for OER is ~10 times higher than that observed on SWNTs and 35 times higher than that on MWNTs. The Tafel slope for the reaction on CNTs with OD around 2-5 nm and 2-7 walls is ~60 mV dec^{-1}, substantially lower than ~200 mV dec^{-1} for the reaction on SMCNTs and MWNTs, i.e., CNTs-1, CNTs-6 and CNTs-7. Such CNTs are also very active as compared to commercial 50% Pt/C and 20% Ru/C in alkaline solution. Substantial work needs to be done to fundamentally understand the reasons for the volcano-type dependence of the activity of CNTs for the OER in alkaline solution. Preliminary results indicate that there may exist a dual functionality of CNTs with specific number of walls; the outer wall provides reaction sites for the absorption and dissociation of OH^-, OOH^*, species, while the intact inner-tube serves as the effective electronic conducting pathway for

the charge transfer process of the reaction via electron tunneling between the outer wall and inner tubes. However, such dual functionality of the CNTs for OER diminishes as the number of walls increases most likely due to the reduced driving force (i.e., the dc bias) across the walls or layers of CNTs for the electron tunneling between the outer wall and inner tubes.

Acknowledgment

This research was supported by the Australian Research Council *Discovery Project Funding Scheme* (project number: DP120102325, DP120104932 and DP0986999), and the Major International (Regional) Joint Research Project of the National Natural Science Foundation of China (51210002), as well as access to resources at iVEC and NCI.

References:

1. J. R. McKone, N. S. Lewis and H. B. Gray, *Chem. Mat.*, 2014, 26, 407-414.
2. T. J. Meyer, *Nature*, 2008, 451, 778-779.
3. V. I. Birss and A. Damjanovic, *J. Electrochem. Soc.*, 1987, 134, 113-117.
4. T. Reier, M. Oezaslan and P. Strasser, *Acs Catalysis*, 2012, 2, 1765-1772.
5. D. V. Esposito, S. T. Hunt, Y. C. Kimmel and J. G. Chen, *Journal of the American Chemical Society*, 2012, 134, 3025-3033.
6. J. C. Cruz, V. Baglio, S. Siracusano, V. Antonucci, A. S. Arico, R. Ornelas, L. Ortiz-Frade, G. Osorio-Monreal, S. M. Duron-Torres and L. G. Arriaga, *International Journal of Electrochemical Science*, 2011, 6, 6607-6619.
7. E. Rasten, G. Hagen and R. Tunold, *Electrochimica Acta*, 2003, 48, 3945-3952.
8. A. Di Blasi, C. D'Urso, V. Baglio, V. Antonucci, A. S. Arico, R. Ornelas, F. Matteucci, G. Orozco, D. Beltran, Y. Meas and L. G. Arriaga, *Journal of Applied Electrochemistry*, 2009, 39, 191-196.
9. T. Takashima, K. Hashimoto and R. Nakamura, *Journal of the American Chemical Society*, 2012, 134, 1519-1527.
10. W. Y. Yuan, P. K. Shen and S. P. Jiang, *Journal of Materials Chemistry A*, 2014, 2, 123-129.
11. R. N. Singh, D. Mishra, Anindita, A. S. K. Sinha and A. Singh, *Electrochem. Commun.*, 2007,

9, 1369-1373.

12. J. Wu, Y. Xue, X. Yan, W. Yan, Q. Cheng and Y. Xie, *Nano Research*, 2012, 5, 521-530.

13. F. Jiao and H. Frei, *Angewandte Chemie International Edition*, 2009, 48, 1841-1844.

14. C. R. Davidson, G. Kissel and S. Srinivasan, *Journal of Electroanalytical Chemistry*, 1982, 132, 129-135.

15. M. W. Louie and A. T. Bell, *Journal of the American Chemical Society*, 2013, 135, 12329-12337.

16. R. D. L. Smith, M. S. Prévot, R. D. Fagan, S. Trudel and C. P. Berlinguette, *Journal of the American Chemical Society*, 2013, 135, 11580-11586.

17. J. Suntivich, K. J. May, H. A. Gasteiger, J. B. Goodenough and Y. Shao-Horn, *Science*, 2011, 334, 1383-1385.

18. D. Eder, *Chemical Reviews*, 2010, 110, 1348-1385.

19. F. M. Toma, A. Sartorel, M. Iurlo, M. Carraro, S. Rapino, L. Hoober-Burkhardt, T. Da Ros, M. Marcaccio, G. Scorrano, F. Paolucci, M. Bonchio and M. Prato, *Chemsuschem*, 2011, 4, 1447-1451.

20. M. Gong, Y. Li, H. Wang, Y. Liang, J. Z. Wu, J. Zhou, J. Wang, T. Regier, F. Wei and H. Dai, *Journal of the American Chemical Society*, 2013, 135, 8452-8455.

21. Y. Xiang, S. Lu and S. P. Jiang, *Chem. Soc. Rev.*, 2012, 41, 7291-7321.

22. X. Lu and C. Zhao, *J. Mater. Chem. A*, 2013, 1, 12053-12059.

23. F. Li, B. Zhang, X. Li, Y. Jiang, L. Chen, Y. Li and L. Sun, *Angewandte Chemie-International Edition*, 2011, 50, 12276-12279.

24. K. P. Gong, F. Du, Z. H. Xia, M. Durstock and L. M. Dai, *Science*, 2009, 323, 760-764.

25. Y. Zhao, R. Nakamura, K. Kamiya, S. Nakanishi and K. Hashimoto, *Nature Communications*, 2013, 4.

26. U. J. Kim, C. A. Furtado, X. M. Liu, G. G. Chen and P. C. Eklund, *Journal of the American Chemical Society*, 2005, 127, 15437-15445.

27. M. S. Dresselhaus, G. Dresselhaus, R. Saito and A. Jorio, in *Carbon Nanotubes: Quantum Cylinders of Graphene*, eds. S. Saito and A. Zettl, Elsevier Science Bv, Amsterdam, 2008, DOI: 10.1016/s1572-0934(08)00004-8, pp. 83-108.

28. R. Saito, M. Hofmann, G. Dresselhaus, A. Jorio and M. S. Dresselhaus, *Adv. Phys.*, 2011, 60, 413-550.

29. C. C. L. McCrory, S. Jung, J. C. Peters and T. F. Jaramillo, *Journal of the American Chemical Society*, 2013, 135, 16977-16987.

30. R. N. Singh, M. R. Awasthi and A. S. K. Sinha, *J. Solid State Electrochem.*, 2009, 13, 1613-1619.

31. M. E. G. Lyons and M. P. Brandon, *International Journal of Electrochemical Science*, 2008, 3, 1425-1462.

32. A. Damjanovic, *Electrochim. Acta*, 1992, 37, 2533-2539.

33. L. Trotochaud, J. K. Ranney, K. N. Williams and S. W. Boettcher, *J. Am. Chem. Soc.*, 2012,

134, 17253-17261.

34. M. E. G. Lyons and M. P. Brandon, *International Journal of Electrochemical Science*, 2008, 3, 1386-1424.

35. R. L. Doyle, I. J. Godwin, M. P. Brandon and M. E. G. Lyons, *Physical Chemistry Chemical Physics*, 2013, 15, 13737-13783.

36. L. Wang, A. Ambrosi and M. Pumera, *Angew. Chem.-Int. Edit.*, 2013, 52, 13818-13821.

37. Z. Q. Tian, S. P. Jiang, Y. M. Liang and P. K. Shen, *J. Phys. Chem. B*, 2006, 110, 5343-5350.

38. H. Cheng, G. P. Pez and A. C. Cooper, *J. Am. Chem. Soc.*, 2001, 123, 5845-5846.

39. A. Bilic and J. D. Gale, *Journal of Physical Chemistry C*, 2008, 112, 12568-12575.

40. R. Saito, M. Fujita, G. Dresselhaus and M. S. Dresselhaus, *Appl. Phys. Lett.*, 1992, 60, 2204-2206.

41. J. J. Zhao, H. K. Park, J. Han and J. P. Lu, *J. Phys. Chem. B*, 2004, 108, 4227-4230.

42. K. Fujisawa, K. Komiyama, H. Muramatsu, D. Shimamoto, T. Tojo, Y. A. Kim, T. Hayashi, M. Endo, K. Oshida, M. Terrones and M. S. Dresselhaus, *Acs Nano*, 2011, 5, 7547-7554.

43. C. Shen, A. H. Brozena and Y. H. Wang, *Nanoscale*, 2011, 3, 503-518.

44. A. Damjanovic, V. I. Birss and D. S. Boudreaux, *J. Electrochem. Soc.*, 1991, 138, 2549-2555.

45. Z. R. Li, H. R. Kandel, E. Dervishi, V. Saini, A. S. Biris, A. R. Biris and D. Lupu, *Appl. Phys. Lett.*, 2007, 91.

Chapter 4: Beneath the Surface: the Role of Inner Tubes on the Electrocatalytic Activity of Pristine Carbon Nanotubes in Alkaline Solutions

4.1 Introduction

CNTs are seamless cylinders composed of one or more curved layers of graphene with either open or closed ends, and have been extensively studied as catalysts supports[1-3] for its unique properties such as large specific surface area, excellent chemical and mechanical properties and high electrical conductivity. Noble metal based nanoparticles (NPs) supported on CNTs have been intensively studied as highly effective electrocatalysts for the most important electrochemical energy conversion and storage reactions such as ORR,[4-6] OER[7] and HER.[8, 9] Base metal oxides or hydroxides, such as Co_3O_4/CoO,[2, 10] nickel-iron layered double hydroxides,[7] perovskites,[11] and Mn-Co spinels[12] are also supported or encapsulated into CNTs or doped CNTs as effective and stable catalysts for ORR, OER or HER.

It is widely known that the electrocatalytic activity for ORR and water splitting reactions can be enhanced through doping carbon materials with heteroatoms such as N,[13, 14] B[15] and S.[16] The incorporation of electron-accepting nitrogen atoms in the conjugated carbon plane provides a four-electron pathway for the ORR on CNTs with enhanced performance.[17] Waki et al. found that the formation of topological defects on the MWNTs through oxidation by refluxing in sulfuric acid and concentrated nitric

acid followed by annealing in argon at high temperature can significantly enhance the activity for ORR in acid solution.[18] Tian et al. reported high activity and stability for OER and ORR on N-doped graphene/SWNTs hybrid.[19] B-doped graphene also demonstrated good electrocatalytic activity for HER.[20] Pristine CNTs have been evaluated as ORR catalysts in alkaline solutions and ORR on CNTs proceeds through two electron process with formation of H_2O_2.[21] However, it is generally believed that pristine CNTs without nitrogen-doping would have little electrocatalytic activity since the active sites of edge plane exposure alone are far too low for the electrochemical reactions such as ORR.[21-24]

We recently discovered that CNTs composed of 2-7 concentric tubes or walls have very high electrochemical activities for the OER in alkaline solutions as compared with typical SWNTs and MWNTs.[25] The results indicate that the number of walls of CNTs plays a vital role in the electrocatalytic activities of CNTs for ORR. However, *is this a reaction specific activity or this is a more general and intrinsic property of CNTs with 2-7 walls?* To answer this fundamental and important question, we studied the electrochemical activities of pristine CNTs as a function of number of walls for OER, HER and ORR in alkaline solutions. The results demonstrate that CNTs composed of 2-7 concentric tubes not only show a significantly better activity for the electrochemical oxidation reaction like OER, but also have a much higher activity for the electrochemical reduction reactions such as HER and ORR as compared to typical SWNTs and MWNTs.

4.2 Experimental

4.2.1 Materials

CNTs with different number of walls and diameters were obtained from commercial sources including Nanostructured & Amorphous Materials, Inc., USA, Beijing Dk Nano Technology Co. Ltd and Shenzhen Nano, China. The as-received CNTs were purified as reported in chapter 3.[25]

4.2.2 Characterization

The electrochemical measurements were conducted in a three-electrode cell with a Luggin capillary, using a Gamery Reference 3000 Potentiostat. The tip of the Luggin capillary was placed 3 mm beneath the working electrode. The working electrode was prepared as follows that in chapter 3. The ohmic potential drop between the working electrode and the tip of the Luggin capillary was estimated by measuring the impedance value at the frequency of 30 kHz. A Pt wire and SCE were used as the counter and reference electrodes, respectively. Potentials in the present study were given versus RHE reference electrode ($E_{RHE} = E_{\text{vs SCE}} + E_{SCE} + 0.059\times pH$, where $E_{SCE} = 0.247$V vs RHE at 20 ^{o}C).

For OER, HER and ORR the linear scan voltammetry was conducted at a sweep rate of 10 mV s^{-1} at stirring rate of 1600 rpm with catalysts loading of 0.025 mg cm^{-2}. For studying OER and HER, the electrolyte solution was saturated with N_2, and for ORR studying, the electrolyte was bubbled with O_2. Tafel plots were recorded at a sweep rate of 1 mV s^{-1} with the electrode initially conditioned at a potential of 0.65 V (vs. SCE) for 5 min before the potential scan. Tafel plots were IR corrected.

4.3 Results and Discussion

4.3.1 Electrocchemical survey of CNTs

Fig. 4.1 shows the CV of the CNTs measured in 1 M KOH solution. All potentials in the present study were given versus RHE reference electrode. Three typical electrochemical active regions were observed, which are corresponding to OER at 1.5-2.5 V, ORR region at 0.2-0.8 V and HER at -0.3 to -0.5 V. The electrocatalytic activity of CNTs depends strongly on the properties of CNTs. For OER, CNTs-2 and CNTs-3 show significantly higher activity compared to CNTs-1, CNTs-6 and CNTs-7. Similar trends can also be observed for HER and ORR. The results show that electrocatalytic activities of CNTs for OER, HER and ORR are related to the nature of CNTs.

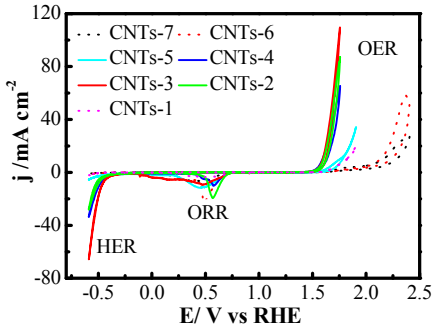

Figure 4.1. Cyclic voltammetry curves of CNTs measured at scan rate of 10 mV s^{-1} with catalyst loading of 0.025 mg cm^{-2} in 1 M KOH solution without stirring.

4.3.2 Electrochemical activity for OER

The electrocatalytic activity of CNTs for OER, ORR and HER was studied separately using LSV in 1 M KOH solution. Fig. 4.2 A shows the LSV of OER on CNTs. The electrocatalytic activity for OER varies significantly with the CNTs. The best activity was obtained on three walled CNTs, CNTs-3, achieving lowest onset potential of 1.64 V and highest current density of 160 mA cm^{-2} at 1.8 V. In the case of SWNTs, CNTs-

1, the onset potential for OER is 1.75 V and the current density at 1.8 V is 9.6 mA cm^{-2}, 16 times lower than 160 mA cm^{-2} measured on CNTs-3. Poor performance was also observed on MWNTs. In the case of CNTs-7, the onset potential is 1.78 V and current density at 1.8 V is only 3.6 mA cm^{-2}, which is about 44 times smaller than that of CNTs-3. CNTs-2, CNTs-4 and CNTs-5 also show significantly higher activity for the OER as compared to CNTs-1, CNTs-6 and CNTs-7. Most significantly, the electrocatalytic activity (e.g., the current density) of CNTs for OER follows a distinctive volcano-shaped dependence on the number of walls of CNTs (Fig. 4.2 B). The most active CNTs for the OER in alkaline solution are the ones mainly with 2-7 walls.

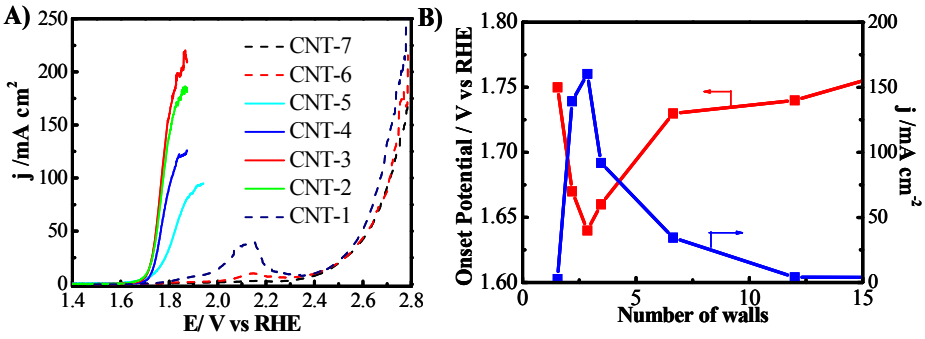

Figure 4.2. (A) LSV curves of OER and (B) corresponding plots of current density measured at 1.8 V and onset potential as a function of number of walls of CNTs. The scan rate is 0.01 V s^{-1} at rotating rate of 1600 rpm.

The Tafel slope of ~60 mV dec^{-1} (Fig. 3.11 A) observed for the OER on CNTs-2, CNTs-3, CNTs-4, and CNTs-5 is consistent with the rate determine steps (RDS) for OER involveing a chemical step (Eq.2) subsequent to the first electron transfer step (Eq.1)[26-29]

$$CNT + OH^- \rightarrow CNT\text{-}OH + e \quad (1)$$

$$CNT\text{-}OH + OH^- \rightarrow CNT\text{-}O^- + H_2O \quad (2)$$

The very high Tafel slope, ~140 mV dec^{-1} observed for the reaction on CNTs-1, CNTs-6 and CNTs-7 simply implies that the energy barrier for the electron transfer associated with the discharge of OH^{-1} species on the SWNTs and MWNTs is higher than CNTs-2, CNTs-3, CNTs-4, and CNTs-5. And the RDS on CNTs-1, CNTs-6 and CNTs-7 is limited by the first electron transfer step with the adsorption of one OH^- (Eq (1))[26, 27].

4.3.3 Electrochemical activity for HER

The CNTs composed of between 2-7 concentric tubes also show significantly better activities for HER as compared with SWNTs and MWNTs. CNTs-3 shows the highest activity for HER with onset potential of -0.48 V and current density of 21.0 mA cm^{-2} measured at -0.6 V (Fig.4.3 A). On the other hand, OER on CNTs-1 and CNTs-7 exhibits much lower activity. In the case of CNTs-7, the onset potential is -0.582 V, more than 100 mV more negative than -0.48 V for the HER on CNTs-3. The current density at -0.6 V is 1.3 mA cm^{-2}, 16 times lower than 21.0 mA cm^{-2} measured on CNTs-3. The electrocatalytic activity of CNTs for HER is also characterized by a distinctive volcano-shaped dependence on the number of walls (Fig.4.3 B).

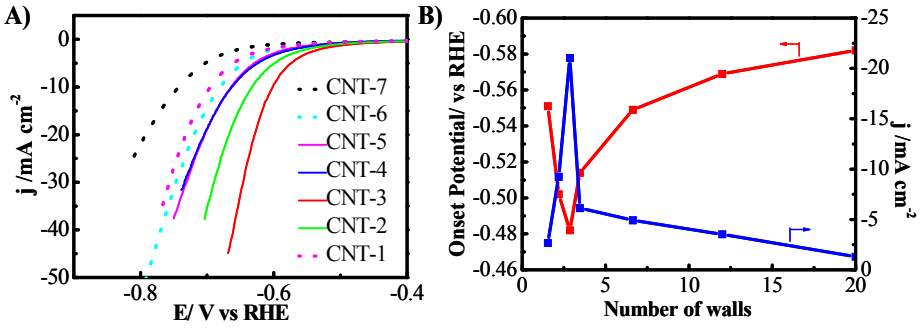

Figure 4.3. (A) LSV curves of HER and (B) corresponding plots of current density measured at -0.6 V and onset potential as a function of number of walls of CNTs. The scan rate is 0.01 V s^{-1} at rotating rate of 1600 rpm.

Fig. 4.4 shows the Tafel regions of HER on CNTs electrodes. The Tafel slopes are 230, 180, 170, 175, 198, 260 and 310 mV dec^{-1} for CNTs-1 to CNTs-7 respectively. The lower Tafel slope of CNTs-3 is consistent with the higher activity for HER on CNTs compared with other types of CNTs. In the case of HER in alkaline solution, the high Tafel slope of OER can be illustrated on the basis of dual barrier model where the charge transfer reaction has to surmount two energy barriers as follow

$$CNT + H_2O \rightarrow CNT\text{-}H^+ + OH^- \quad (3)$$

$$CNT\text{-}H^+ + e \rightarrow CNT\text{-}H \quad (4)$$

The HER on CNTs in alkaline firstly involves the deprotonation of H_2O to form OH^- and H^+, and then secondly involves the reaction of H^+ with an electron on the CNTs surface.

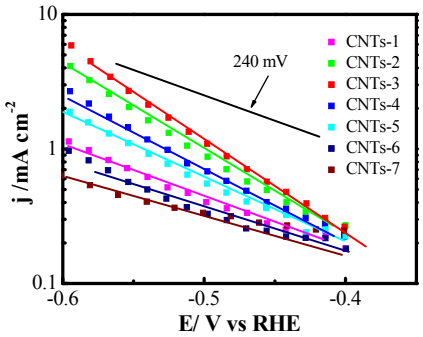

Figure 4.4. Tafel plots for HER on CNTs. The tests were conducted in 1M KOH solution with catalyst loading of 0.025 mg cm^{-2} and stirring rate of 1600 rpm.

4.3.4 Electrochemical activity for ORR

Similar to that observed on OER and HER, the number of walls of CNTs also have significant influence on the ORR. Both the half-wave potential and the current density measured at 0.8 V indicate that CNTs-2 and CNTs-3 have the best activity for ORR (Fig 4.5 A). The half-wave potential for ORR on CNTs-2 and CNTs-3 electrode is

0.78 V, 60-70 mV more positive as compared with CNTs-1 and CNTs-7. The current density for ORR on CNTs-2 and CNTs-3 is 0.93 mA cm^{-2} at 0.8 V, which is 7.2 and 8.2 times of that measured on CNTs-1 and CNTs-7, respectively. The electrocatalytic activity of CNTs for ORR as measured by the current density shows identical volcano-type relationship as a function of number of walls (Fig.4.5 B), similar to that observed for OER and HER.

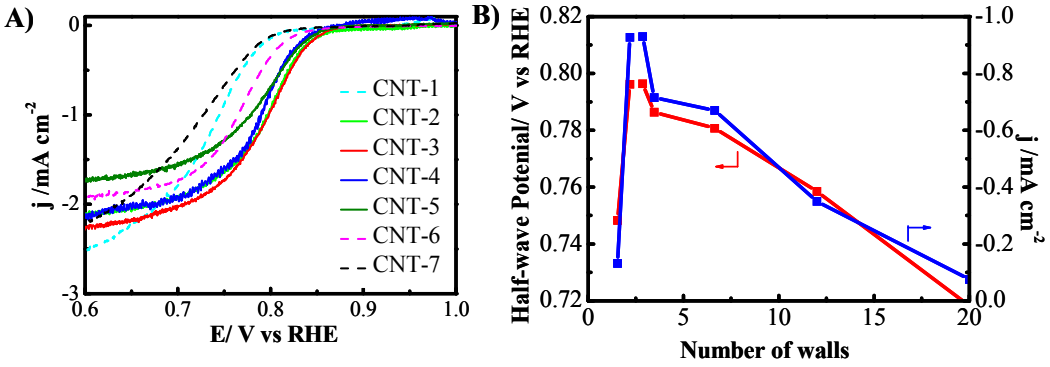

Figure 4.5. (A) LSV curved of ORR in O_2-saturated 1M KOH and (B) corresponding plots of current density measured at 0.8 V and half-wave potential as a function of number of walls of CNTs. LSV curves were measured in 1M KOH solution at scan rate of 10 mV s^{-1} with rotating rate of 1600 rpm and CNTs loading was 0.025 mg cm^{-2}.

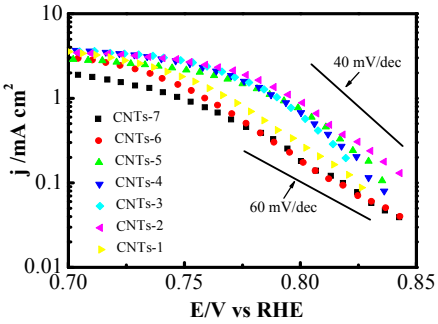

Figure 4.6. Tafel slope for ORR on CNTs in O_2-saturated 1 M KOH solution with a scan rate of 1 mV s^{-1}. The tests were conducted in 1M KOH solution with catalyst loading of 0.025 mg cm^{-2} and stirring rate of 1600 rpm.

The Tafel slopes of CNTs for ORR in Fig. 4.6 are consistent with the activity and reveal the electron transfer number. CNTs-3 has a lowest overpotential and highest

current density around 0.7-0.85 V, hence a Tafel slope of 44 mV dec^{-1} obtained, indicating the ORR on CNTs-3 is limited by the second electron transfer process. For CNTs-2, CNTs-4 and CNTs-5, the Tafel slopes calculated are 50, 48 and 51 mV dec^{-1} respectively. However the Tafel slopes for CNTs-1, CNTs-6 and CNTs-7 are 54, 56 and 59 mV dec^{-1}, which is approaching 60 mV dec^{-1} indicating the ORR on CNTs-1, CNTs-6 and CNTs-7 involve loss of one electron subsequently limited by a chemical steps. These results demonstrate that ORR on CNTs-2, CNTs-3 and CNTs-4 is a 2 electron transfer oxygen reduction process, and the ORR is limited by the second electron transfer process (Eq. 7) following (Eq. 5). However, the Tafel slope of approaching 60 mV dec^{-1} is consistent with the ORR on CNTs-1, CNTs-6 and CNTs-7 is probably limited by the chemical binding of H_2O to from HO_2 (ads) (Eq. 6) following (Eq. 5).

$$CNT + O_2 + e \rightarrow CNT\text{-}O_2^- \quad (5)$$

$$2CNT\text{-}O_2^- + H_2O \rightarrow 2CNT\text{-}HO_2^- + O_2 + OH^- \quad (6)$$

$$CNT\text{-}O_2^- + H_2O + e \rightarrow CNT\text{-}HO_2^- + OH^- \quad (7)$$

4.3.5 Comparison of electrochemical activity of CNTs with Pt/C

Fig. 4.7 compares the electrocatalytic activity of best performed CNTs, CNT-3 and commercial Pt/C catalysts in a 1 M KOH solution. The results show that the electrocatalytic activity of CNTs-3 for OER is significantly higher than Pt/C. For OER on Pt/C, the onset potential is 1.63 V and the current density at 1.8 V is 15 mA cm^{-2}, significantly lower than 160 mA cm^{-2} for the reaction on CNTs-3. On the other hand, Pt/C shows a much better activity for HER and ORR. The half wave potential for ORR and the onset potentials for HER are 0.9 V and 0 V respectively, which is significantly positive, as compared with 0.863 V and -0.48 V measured on CNTs-3. These results in turn indicates that CNTs with 2-7 walls have an excellent

electrocatalytic activity for electrochemical oxidation reactions like OER, but relatively poor electrocatalytic activity for the electrochemical reduction reactions such as HER and ORR in alkaline solutions, as compared to Pt/C catalysts.

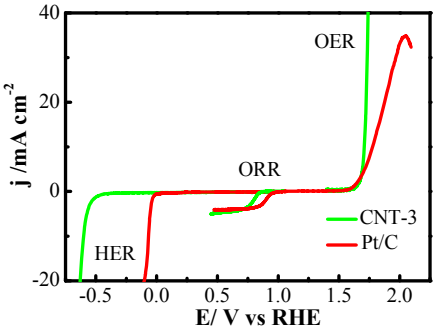

Figure 4.7. LSV curves of CNTs-3 and 20% Pt/C electrocatalysts, measured at scan rate of 10 mV s^{-1} in 1 M KOH solution without stirring. ORR was measured in O_2-saturated 1M KOH solution. Pt and CNTs-3 catalyst loading was 0.025 mg cm^{-2}.

4.3.6 Electrochemical chemistry of CNTs

The results identified that there is a clear maximum in the catalytic activity of CNTs for OER, HER and ORR as a function of number of walls or size of CNTs. The electrocatalytic activities of CNTs with number of walls of 2-7, i.e., CNTs-2, CNTs-3, CNTs-4 and CNTs-5 are significantly higher than typical SWNTs and MWNTs, i.e., CNTs-1, CNTs-6 and CNTs-7 for OER, ORR and HER. Such distinctive volcano-type dependence of electrocatalytic activity of CNTs is not related to the specific surface area nor the surface defects or size of CNTs. For example, the BET surface area of CNTs-1 is 651 m^2 g^{-1}, similar to 679 and 643 m^2 g^{-1} of CNTs-2 and CNTs-3 (Table 3.1). However, CNTs-2 and CNTs-3 show much higher activity for OER, ORR and HER when compared with CNTs-1 (Fig.4.2, 4.3 and 4.5). Both theoretical and experimental investigations have indicated that the affinity of CNTs with water

molecule or OH group increases with decreasing the diameter of CNTs due to the increased misalignment of π-orbitals.[30-32] Therefore, the increased electrocatalytic activity from CNTs-1 to CNTs-3 cannot be ascribed to the increase of size of CNTs. Though the surface defects of MWNTs such as CNTs-6 and CNTs-7 are significantly higher as compared to CNTs-2 and CNTs-3 (e.g., the I_D/I_G ratio of CNTs-6 and CNTs-7 is 2.5-2.86, much higher than 0.51-0.76 of CNTs-2 and CNTs-3), CNT-6 and CNTs-7 show the lowest catalytic activity for OER, HER and ORR.

The distinctive volcano-shaped dependence on CNTs also cannot be explained based on the presence of some impurities after the purification treatment. Rather milder purification treatment was used in this study in order to avoid the adverse structural modification of CNTs associated with harsh oxidation treatment.[33] However, as shown for the ORR,[25] significant reduction in the trace metal impurities has little effect on the electrocatalytic activity of the selected CNTs (Fig. 3.6). For example, the activity of MWNTs, CNTs-7, is 44 times lower than that of CNTs-3, but the trace metal content of CNTs-7 is 0.95%, close to that of CNTs-3 (Table 3.2). Thus, the substantially increased catalytic activity of CNTs with 2-7 walls cannot be contributed to the surface defects of CNTs as well as the trace metal impurities. Therefore we argue that the distinctive volcano-shaped activity curves for OER, HER and ORR on CNTs are a clear indication of an intrinsic property of CNTs and the critical role of inner tubes on the electrocatalytic activity of CNTs.

The exact mechanism for the high electrocatalytic activity of CNTs with 2-7 walls is not clear at this stage. However, the most likely reason for the high activity of double walled CNTs and three walled CNTs (i.e., CNTs-2, CNTs-3 and CNTs-4) as compared to SWNTs (i.e, CNTs-1) is the effective separation of the functionality of the outer wall and inner tubes; the outer wall provides reaction sites for the adsorption

and dissociation of OH^-_{ads}, $O_{2,ads}$, O_{ads} species for the electrochemical reactions, while the protected inner-tubes serve as the effective electronic conducting pathway for the charge transfer process of the reaction. Fujisawa et al. studied the electrical properties of SWNTs and DWNTs and showed experimentally that the inner tubes contribute significantly to the electronic transport properties of DWNTs.[34] Li et a synthesized carbon nanotube-graphene complexes through partially unzipping few outer walls of CNTs and attributed the observed high activity for ORR as the results of its high activity sites of the abundant edges and defects of the unzipped outer walls and the less damaged and electrically conducting inner tubes.[35] The effective electron transfer between the outer wall and inner tubes could occur by electron tunneling under the electrochemical polarization driving force, similar to the electron tunneling through thin oxide films as proposed by Damjanovic et al for the OER on Pt.[36] Fig. 4.8 shows schematically the role of the effective electron transfer between outer wall and inner tubes on the OER, HER and ORR on DWNTs.

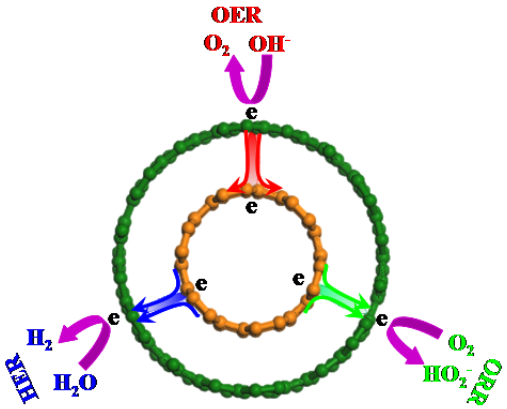

Figure 4.8. Schematic of electron transfer pathway for OER, HER and ORR through electron tunneling effect on DWNTs.

Evidently, such separation of the functionality and electron transfer between the outer wall and inner tubes would not be possible for SWNTs. The proposed mechanism

implies that the electron transfer between the outer wall and inner tubes would strongly depend on the distribution of the driven force, the applied polarization potential across the inner tubes. Thus, in the case of MWNTs, the driving force of polarization potential for the electron transfer or tunneling between the outer wall and inner tubes would decrease with the increase in the number of inner tubes. Thus, the electron transfer or tunneling between the outer surfaces to the inner tubes could become less favourable as the number of walls/layers increases. This hypothesis explains why double/triple-walled CNTs-2, CNTs-3 and CNTs-4 are far more active for the electrochemical reactions than MWNTs, CNTs-6 and CNTs-7.

In alkaline conditions, the OER, ORR and HER can be written as follows: [21, 37, 38]

OER: $4OH^- \rightarrow O_2 + 2H_2O + 4e$ (8)

ORR: $O_2 + H_2O + 2e \rightarrow HO_2^- + OH^-$ (9)

HER: $H_2O + 2e \rightarrow H_2 + 2OH^-$ (10)

The electrochemically active species for OER is OH^-, while for ORR and HER, it is O_2 and H_2O molecules, respectively. The origin of the overpotential or barrier of an electrochemical reaction can be directly linked to the proton and/or electron transfer to the adsorbed reaction species bonded to the surface of the electrocatalysts, which in turn depends on the interaction energy between the species and catalyst surface. As shown by Norskov et al. for the ORR, Pt is very close to optimum and metals that have either stronger or weaker bonding of oxygen than Pt are poor ORR catalysts.[39] The interaction energy of water with CNT surface is very weak due to the inert nature of pristine CNTs and the extension of the nanotubes have modest effect on the interaction energies.[40] The weak bonding of water molecules indicates that barrier for HER would be large. This is evidently confirmed by the very high Tafel slopes of 170-310 mV dec^{-1} for HER on CNTs under the conditions of the present study (Fig.

4.4), which is substantially higher than 74 mV dec^{-1} observed on Co[38] and 75 mV dec^{-1} on Pt in alkaline solutions.[41] ORR on CNTs is similar to that on glassy carbon and characterized by two-electron transfer process with the formation of hydrogen peroxide intermediates (Fig.4.6). In the case of OER in alkaline solutions, the discharge of the OH^- species would be relatively easy due to the high affinity of OH^- ions on CNTs, and hence, kinetically OER is more favourable on the surface of the CNTs[25] as compared to ORR and HER.

As shown above, the electrocatalytic activity of pristine CNTs is substantially different for OER, ORR and HER in alkaline solution, but shows remarkably identical volcano curves as a function of number of concentric tubes or walls. This shows that such volcano-type dependence of the electrocatalytic activity of CNTs is not related to the interaction energies between the reactive species and the surface of CNTs or surface active sites. This in turn implies that the nature of such volcano curves is originated from the effect of inner tubes on the electron charge transfer via the tunneling effect, very different from origin of the well know volcano curves for the ORR and HER as reported by Norskov.[39, 42] Such inner tube effect of CNTs deserves a further comment that promotion effect of inner tubes could lead to the development of new electrocatalysts for electrochemical energy conversion and storage technologies.

4.4 Conclusion

Here, CNTs with wide range of number of walls were studied for OER, HER and ORR in alkaline solution. The electrocatalytic activity of CNTs for the OER in general is substantially higher than HER and ORR, as compared to Pt/C catalysts. Despite the substantial differences in electrocatalytic activity, CNTs show almost

identical distinctive volcano-shaped dependences on the number of walls for OER, HER and ORR. CNTs with 2-7 walls have significantly higher electrochemical activity than typical SWNTs and MWNTs. The much better activity of CNTs with 2-7 walls is most likely due to the separation of functionality of outer wall and inner tubes and the fast electron transfer between the outer wall and inner tube through electron tunneling. The universal volcano-shaped dependence of the electrocatalytic activity of CNTs as a function of number of walls clearly demonstrates that the high activity of CNTs with 2-7 walls is an intrinsic property of CNTs beyond the active or defect sites on the surface of CNTs. The finding explores a new possibility to develop highly active and stable electrocatalysts by manipulating the quantum effect of CNTs.

Acknowledgement

The project was supported by the Australian Research Council *Discovery Project* funding scheme (project number: DP120102325 & DP120104932).

References

1. D. Eder, *Chemical Reviews*, 2010, 110, 1348-1385.
2. J. Wu, Y. Xue, X. Yan, W. Yan, Q. Cheng and Y. Xie, *Nano Research*, 2012, 5, 521-530.
3. F. M. Toma, A. Sartorel, M. Iurlo, M. Carraro, S. Rapino, L. Hoober-Burkhardt, T. Da Ros, M. Marcaccio, G. Scorrano, F. Paolucci, M. Bonchio and M. Prato, *Chemsuschem*, 2011, 4, 1447-1451.
4. J. Zhang, S. Tang, L. Liao, W. Yu, J. Li, F. Seland and G. M. Haarberg, *Journal of Power Sources*, 2014, 267, 706-713.
5. B. P. Vinayan and S. Ramaprabhu, *Nanoscale*, 2013, 5, 5109-5118.
6. S. Y. Wang, X. Wang and S. P. Jiang, *Langmuir*, 2008, 24, 10505-10512.
7. M. Gong, Y. Li, H. Wang, Y. Liang, J. Z. Wu, J. Zhou, J. Wang, T. Regier, F. Wei and H. Dai, *Journal of the American Chemical Society*, 2013, 135, 8452-8455.
8. M. H. Miles and M. A. Thomason, *J. Electrochem. Soc.*, 1976, 123, 1459-1461.
9. R. Bashyam and P. Zelenay, *Nature*, 2006, 443, 63-66.
10. Y. Liang, H. Wang, P. Diao, W. Chang, G. Hong, Y. Li, M. Gong, L. Xie, J. Zhou, J. Wang, T. Z. Regier, F. Wei and H. Dai, *Journal of the American Chemical Society*, 2012, 134, 15849-15857.

11. K. Miyazaki, K.-i. Kawakita, T. Abe, T. Fukutsuka, K. Kojima and Z. Ogumi, *Journal of Materials Chemistry*, 2011, 21, 1913-1917.
12. A. Zhao, J. Masa, W. Xia, A. Maljusch, M.-G. Willinger, G. Clavel, K. Xie, R. Schlögl, W. Schuhmann and M. Muhler, *Journal of the American Chemical Society*, 2014, 136, 7551-7554.
13. Z. Chen, D. Higgins, H. Tao, R. S. Hsu and Z. Chen, *Journal of Physical Chemistry C*, 2009, 113, 21008-21013.
14. Y. Zhao, R. Nakamura, K. Kamiya, S. Nakanishi and K. Hashimoto, *Nat Commun*, 2013, 4.
15. L. Yang, S. Jiang, Y. Zhao, L. Zhu, S. Chen, X. Wang, Q. Wu, J. Ma, Y. Ma and Z. Hu, *Angewandte Chemie-International Edition*, 2011, 50, 7132-7135.
16. Q. Shi, F. Peng, S. Liao, H. Wang, H. Yu, Z. Liu, B. Zhang and D. Su, *J. Mater. Chem. A*, 2013, 1, 14853-14857.
17. K. Gong, F. Du, Z. Xia, M. Durstock and L. Dai, *Science*, 2009, 323, 760-764.
18. K. Waki, R. A. Wong, H. S. Oktaviano, T. Fujio, T. Nagai, K. Kimoto and K. Yamada, *Energy & Environmental Science*, 2014, 7, 1950-1958.
19. G.-L. Tian, M.-Q. Zhao, D. Yu, X.-Y. Kong, J.-Q. Huang, Q. Zhang and F. Wei, *Small*, 2014, 10, 2251-2259.
20. B. R. Sathe, X. Zou and T. Asefa, *Catalysis Science & Technology*, 2014, 4, 2023-2030.
21. I. Kruusenberg, N. Alexeyeva and K. Tammeveski, *Carbon*, 2009, 47, 651-658.
22. I. Kruusenberg, N. Alexeyeva, K. Tammeveski, J. Kozlova, L. Matisen, V. Sammelselg, J. Solla-Gullon and J. M. Feliu, *Carbon*, 2011, 49, 4031-4039.
23. S. Kundu, T. C. Nagaiah, W. Xia, Y. M. Wang, S. Van Dommele, J. H. Bitter, M. Santa, G. Grundmeier, M. Bron, W. Schuhmann and M. Muhler, *Journal of Physical Chemistry C*, 2009, 113, 14302-14310.
24. R. Kannan, U. Bipinlal, S. Kurungot and V. K. Pillai, *Phys. Chem. Chem. Phys.*, 2011, 13, 10312-10317.
25. Y. Cheng, C. W. Xu, L. C. Jia, J. D. Gale, L. L. Zhang, C. Liu, P. K. Shen and S. P. Jiang, *Appl. Catal. B-Environ.*, 2015, 163, 96-104.
26. R. L. Doyle, I. J. Godwin, M. P. Brandon and M. E. G. Lyons, *Physical Chemistry Chemical Physics*, 2013, 15, 13737-13783.
27. Y. Surendranath and D. G. Nocera, in *Progress in Inorganic Chemistry*, John Wiley & Sons, Inc., 2011, DOI: 10.1002/9781118148235.ch9, pp. 505-560.
28. D. K. Bediako, Y. Surendranath and D. G. Nocera, *Journal of the American Chemical Society*, 2013, 135, 3662-3674.
29. Y. Surendranath, M. W. Kanan and D. G. Nocera, *Journal of the American Chemical Society*, 2010, 132, 16501-16509.
30. D. A. Britz and A. N. Khlobystov, *Chem. Soc. Rev.*, 2006, 35, 637-659.
31. Z. F. Chen, W. Thiel and A. Hirsch, *ChemPhysChem*, 2003, 4, 93-+.

32. S. Niyogi, M. A. Hamon, H. Hu, B. Zhao, P. Bhowmik, R. Sen, M. E. Itkis and R. C. Haddon, *Accounts of Chemical Research*, 2002, 35, 1105-1113.
33. Z. Q. Tian, S. P. Jiang, Y. M. Liang and P. K. Shen, *J. Phys. Chem. B*, 2006, 110, 5343-5350.
34. K. Fujisawa, K. Komiyama, H. Muramatsu, D. Shimamoto, T. Tojo, Y. A. Kim, T. Hayashi, M. Endo, K. Oshida, M. Terrones and M. S. Dresselhaus, *Acs Nano*, 2011, 5, 7547-7554.
35. Y. Li, W. Zhou, H. Wang, L. Xie, Y. Liang, F. Wei, J. C. Idrobo, S. J. Pennycook and H. Dai, *Nat Nanotechnol*, 2012, 7, 394-400.
36. A. Damjanovic, V. I. Birss and D. S. Boudreaux, *J. Electrochem. Soc.*, 1991, 138, 2549-2555.
37. S. P. Jiang, Z. G. Lin and A. C. C. Tseung, *J. Electrochem. Soc.*, 1990, 137, 764-769.
38. S. P. Jiang and A. C. C. Tseung, *J. Electrochem. Soc.*, 1991, 138, 1216-1222.
39. J. K. Norskov, J. Rossmeisl, A. Logadottir, L. Lindqvist, J. R. Kitchin, T. Bligaard and H. Jonsson, *J. Phys. Chem. B*, 2004, 108, 17886-17892.
40. P. Schyman and W. L. Jorgensen, *Journal of Physical Chemistry Letters*, 2013, 4, 468-474.
41. B. V. Tilak and C. P. Chen, *Journal of Applied Electrochemistry*, 1993, 23, 631-640.
42. J. K. Norskov, T. Bligaard, A. Logadottir, J. R. Kitchin, J. G. Chen, S. Pandelov and J. K. Norskov, *J. Electrochem. Soc.*, 2005, 152, J23-J26.

Chapter 5: Oxygen Evolution Reaction on Pristine Carbon Nanotubes: Kinetics and Mechanism

5.1 Introduction

Water splitting is greatly constrained by the high overpotentials and sluggish of OER [1-3] because it is thermodynamically and kinetically unfavorable for removing of four electrons to form oxygen-oxygen double bond [3-5]. RuO_2 and IrO_2-based electrodes are considered as the-state-of-the-art catalysts for OER due to their relatively low redox potentials (ca. 1.39 and 1.35V vs. RHE respectively) and high conductivity[3, 6, 7]. However, the poor stability in base (generally suffering slow dissolution in alkaline solution) and the high price of RuO_2 and IrO_2-based catalysts are the main obstacles that hinder their application[1, 8]. Hence base metals were incorporated with noble metals to reduce the cost and improve the OER activity[9-12]. Pyrochlore-type and delafossite-type oxides containing precious metal, with general formula $A_2[B_{2-x}A_x]O_{7-y}$, A=Pb or Bi, B=Ru or Ir, $0<x<1$ and $0<y<0.5$, have demonstrated outstanding activity towards OER [11, 13-15]. Base metal (Co, Fe, Ni, Mn) based oxides[16-18] or hydroxides layers[19-21] and spinels[22], perovskites[23-25] generally outperform precious metal materials in terms of overpotential and stability as well as being lower cost in alkaline solution[26, 27]. Among them, Ni-Fe double oxides or hydroxides are known as one of the best non-noble systems for OER in alkaline solution and the activity are comparable to that of RuO_2 and IrO_2[18, 28-32]. The efficiency of OER catalysts is still

one of the main barriers for the viability of energy storage via water-splitting even though huge amount of efforts were devoted.

CNTs are intensively studied as catalysts supports for ORR [33-36], fuel oxidation [37-39] and water splitting[40, 41] for its unique properties such as large specific surface area, excellent mechanical and electrical properties. Carbon nanotube-metal hybrids for OER are attracting increasing interests recently [29, 42]. Wu et al. synthesized a hybrid consisting of Co_3O_4 nanocrystals supported on SWNTs via a simple self-assembly approach. The Co_3O_4/SWNTs hybrid electrode for the OER exhibits enhanced catalytic activity as well as superior stability under neutral and alkaline conditions compared with unsupported Co_3O_4[43]. Ultrathin nickel-iron layered double hydroxide nanoplates supported on oxidized MWNTs achieved a current density of 10 A g^{-1} at η = 0.228 V in 1.0 M KOH with catalysts loading of 0.25 mg cm^{-2} [29]. Polyoxometalates (POM) supported on CNTs exhibit enhanced activity for oxygen evolution from water under dark or illuminated conditions[44]. Recently, metal free OER catalysts are attracting increasing interests. Zhao et al showed that nitrogen-doped carbon material for oxygen evolution in alkaline media, and the material generated a current density of 10 mA cm^{-2} at the overpotential of 0.38 V, comparable to those of iridium and cobalt oxide catalysts and the authors claim these catalysts are the best among the non-metal oxygen evolution electrocatalyst. The electrochemical and physical studies indicate that the high oxygen evolution activity of the nitrogen/carbon materials is from the pyridinic-nitrogen- or/and quaternary-nitrogen-related active sites[45]. Tian et al. reported N-doped graphene/single walled CNTs hybrid for both ORR and OER[46]. Borghei et al. synthesized a high catalytic activity nitrogen-containing FWCNTs (N-FWCNTs) with low nitrogen content (~0.5 at.%) by pyrolysis of few-walled CNTs (FWCNTs) with polyaniline at high temperatures, and the resulting N-FWCNTs

showed remarkable electrocatalytic activity for ORR, HER and hydrogen peroxide decomposition compared to larger multi-walled nanotubes[47]. However, it is generally believed that pristine CNTs without nitrogen-doping or supported metal or metal oxide nanoparticles (NPs) would have little electrocatalytic activity for the water oxidation reactions. In chapter 3, We demonstrated that CNTs composed of 2-7 concentric tubes with an OD of 2-5 nm have very high electrochemical activities for the OER in alkaline solutions compared with typical single walled CNTs and multi walled CNTs, and we propose that the difference OER activity of different CNTs is because of the electron transfer tunneling effect between the outer wall and the inner tubes[48]. Here, various CNTs are selected and the detailed electro-kinetics of OER on CNTs was studied in acid, neutral buffer and alkaline solutions, and the mechanism of OER was divulged.

5.2 Experimental

5.2.1 Materials

CNTs with different number of walls and diameters were obtained from commercial sources including Nanostructured & Amorphous Materials, Inc., USA, Beijing Dk Nano technology Co., LTD, China and Shenzhen Nano, China. The as-received CNTs were purified follow the procedure in chapter 3[48]. The purified CNTs were dried and collected for further test. KOH (Sigma-Aldrich), $KHPO_4$ (Sigma-Aldrich), KH_2PO_4 (Sigma-Aldrich), Nafion solution (Sigma-Aldrich, 5% in isopropanal and water) were received and used without further treatment.

5.2.2 Characterization

The electrochemical measurements were conducted in a typical three electrode cell with a Luggin capillary. The tip of the Luggin capillary was placed 3 mm beneath the working electrode. The ohmic potential drop between the working electrode and the tip of the Luggin capillary was estimated by measuring the electrode resistance at 30 kHz[49]. A Pt wire and SCE were used as the counter and reference electrodes, respectively. All potentials in the present study except specified were given versus RHE reference electrode ($E_{RHE}= E_{SCE} + 0.245 + 0.059pH$). The cyclic voltammetry (CV) were conducted at 10 mV s^{-1} in the potential range between 0-1.25 V (vs. SCE) in 1.0 M KOH, 0-2 V (vs. SCE) in 0.5 M H_2SO_4 and neutrual solution (pH 7 buffer solutions). IR-corrected Tafel plots were recorded at a sweep rate of 1 mV s^{-1} with the electrode initially conditioned at current density of 0.5 mA cm^{-2} for 5 min before the potential scan[50]. The pH dependence studies were carrying out in 0.5 M buffer solution (in the pH range of 1-13, 0.4 M $KHPO_4$ and 0.1 M KH_2PO_4 mixture, the pH slightly adjusted by adding 2 M KOH solution) with the addition of KNO_3 to keep the ionic strength as 1.0 M, and the studies in alkaline solution and acid solution were carry out with addition of KNO_3 to keep the ionic strength as 1.0 M without buffer solution when the concentration of acid or alkaline are less than 1.0 M, pure H_2SO_4 and KOH solution were used when the concentration equal or over 1.0 M. The reaction order was obtained by current density at fixed potential (in low overpotential region, 1.3 V vs SCE in acid and neutral solutions, and 0.7 V vs SCE for 10^{-3} to 1.0 M KOH solutions and 0.6 V vs SCE for 2-10.0 M KOH solutions). All the electrochemical tests mentioned above were conducted on a rotating disk electrode with a rotation rate of 1600 rpm to avoid the formation of bubbles from the evolved O_2 at the electrode surface, and the catalyst loading is 0.025 mg cm^{-2}.

5.3 Results and discussion

5.3.1 OER activity of CNTs in acid, neutral and alkaline solutions

Fig. 5.1 shows the cyclic voltammetry curves of CNTs measured in 0.5 M H_2SO_4, neutral and 1.0 M KOH solution at scan rate of 10 mV s^{-1} with a mass loading of 0.005 mg and stirring rate of 1600 rpm. The results indicate that CNTs-2, CNTs-3 and CNTs-4 have a lower onset potential and higher current density at lower overpotential compared with conventional single walled CNTs (CNTs-1) and multi walled CNTs (CNTs-7) in alkaline, neutral as well as acid solution. For example, the onset potentials are observed around 1.75 V in 0.5 M H_2SO_4 solutions for CNTs-2, CNTs-3 and CNTs-4, and the current density significantly increase around 2.0 V, and the onset potential for OER is observed around 1.9 V for CNTs-1 and CNTs-6, which is much higher than that of CNTs-2, CNTs-3 and CNTs-4. In neutral condition, the onset potential is around 1.9 V for CNTs-2, CNTs-3 and CNTs-5 lower than that of CNTs-1, CNTs-6 and CNTs-7 which are observed around 2.0-2.05 V. The OER activities of CNTs in 1.0 M KOH is significantly higher than that observed in acid and neutral solutions. In 1.0 M KOH solution, the OER starts around 1.65 V for CNTs-2, CNTs-3 and CNTs-4, and the current densities quickly rise around 1.65-1.7 V. While the OER on CNTs-1 and CNTs-6 and CNTs-7 is commenced around 1.75 V, but an increase of current densities are only observed when the potential is over 2.2 V, demonstrated the activity for OER on CNTs-2, CNTs-3 and CNTs-4 are significantly higher than that of CNTs-1, CNTs-6 and CNTs-7, consistent with the reported results[48]. More interesting, the activity of CNTs for OER follows a volcano type dependence on the number of walls/OD of CNTs in all conditions and the most active CNTs for the OER are the ones with 2-8 walls and with a diameter in the range of 2-5 nm.

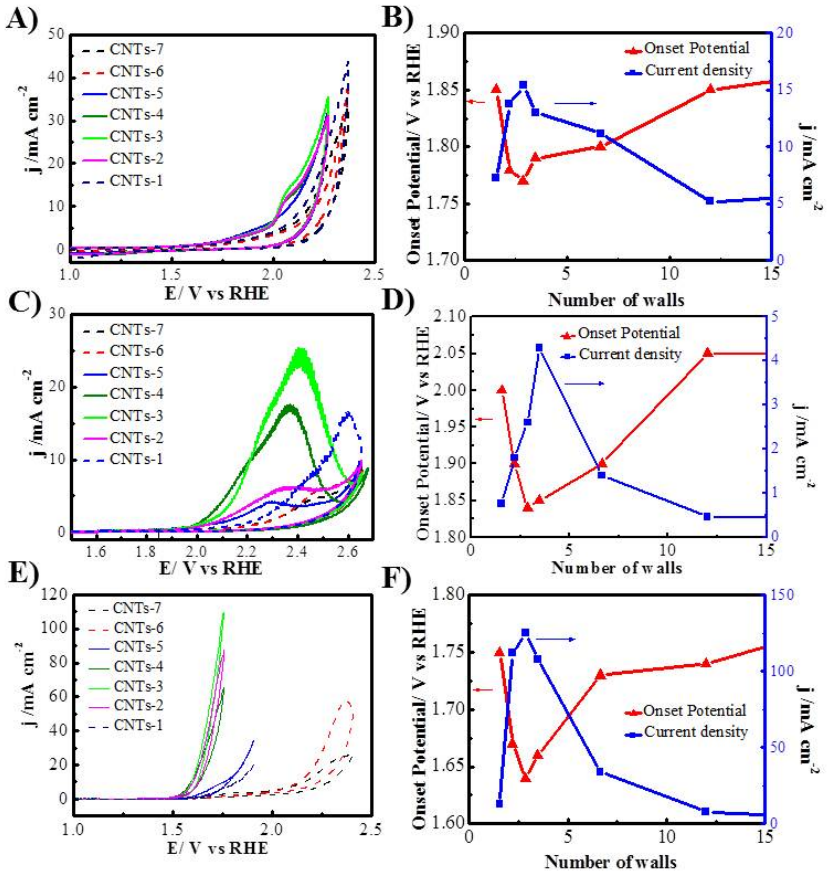

Figure 5.1. A) cyclic voltammetry of OER for CNTs measured in A) 0.5 M H_2SO_4, C) pH 7 buffer solution, E) 1.0 M KOH, and plots of current density measured as a function of number of walls of CNTs in B) 0.5 M H_2SO_4 measured at 2.1 V, D) pH 7 buffer solution measured at 2.1 V, F) 1M KOH measured at 1.7 V. The catalyst loading are 0.025 mg cm^{-2}, the stirring rate is 1600 rpm, and the scan rate is 10 mV s^{-1}.

5.3.2 The pH dependant activity of CNTs

The activities of CNTs for OER have been found to be critically related to the pH of the solution. Fig. 5.2 show the potential to achieve an OER current density of 0.5 mA cm^{-2} for CNTs-1, CNTs-3, CNTs-4 and CNTs-7 catalysts for OER in solutions with pH ranging from 0-14. The results indicate that the potentials to achieve a current density of 0.5 mA cm^{-2} change with the pH, and the trends of different CNTs are similar, and the potential for CNTs-3 and CNTs-4 are much lower than that of CNTs-

1 and CNTs-7 under all conditions. The potentials are in the range of 1.9-2.05 V in 0.8 M H_2SO_4 and slightly decrease to 1.85-1.97 V with the increase of pH in the range of 0 to 4. Then the potentials increase gradually from 1.85 to 2.05 V for CNTs-3 and CNTs-4 and 1.97 to 2.17 V for CNTs-1 and CNTs-6 when the solution pH increases from pH=4 to 9.35. Around pH=10, the potentials start to drop as the increase of pH, and the potentials to delivery a current density of 0.5 mA cm^{-2} are around 1.65 V for CNTs-3 and CNTs-4, 1.75 V for CNTs-1 and CNTs-6 at pH 14 (1.0 M KOH solutions), indicating the increase in the electrocatalytic activity of the catalysts for OER with the increase of the concentration of OH^- (C_{OH}). These results demonstrate that the OER activity on CNTs is sensitive to the C_{OH}.

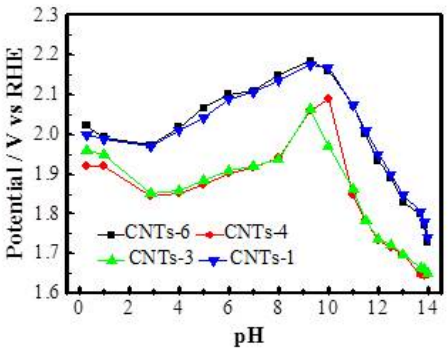

Figure 5.2. The potential to achieve a current density of 0.5 mA cm^{-2} in the whole pH range from 0 to 14. The catalyst loading are 0.025 mg cm^{-2} and the stirring rate is 1600 rpm.

Table 5.1 Kinetics parameters of CNTs-1, CNTs-3, CNTs-4 and CNTs-6 under different conditions

Materials	Parameters	Acid	Neutral	alkaline		
				10^{-3}-0.1	0.1-1	2-10
CNTs-1	Tafel slope (mV/dec)	240	204	240	120	60
	Reaction order	0	0.03	0.5	1	1
CNTs-2	Tafel slope (mV/dec)	240	204	110	58	45
	Reaction order	0	0.13	1	1	2
CNTs-4	Tafel slope (mV/dec)	240	204	110	63	47
	Reaction order	0	0.09	1	1	2
CNTs-6	Tafel slope (mV/dec)	240	204	240	120	60
	Reaction order	0	0.03	0.5	1	1

5.3.3 Tafel slope and reaction order

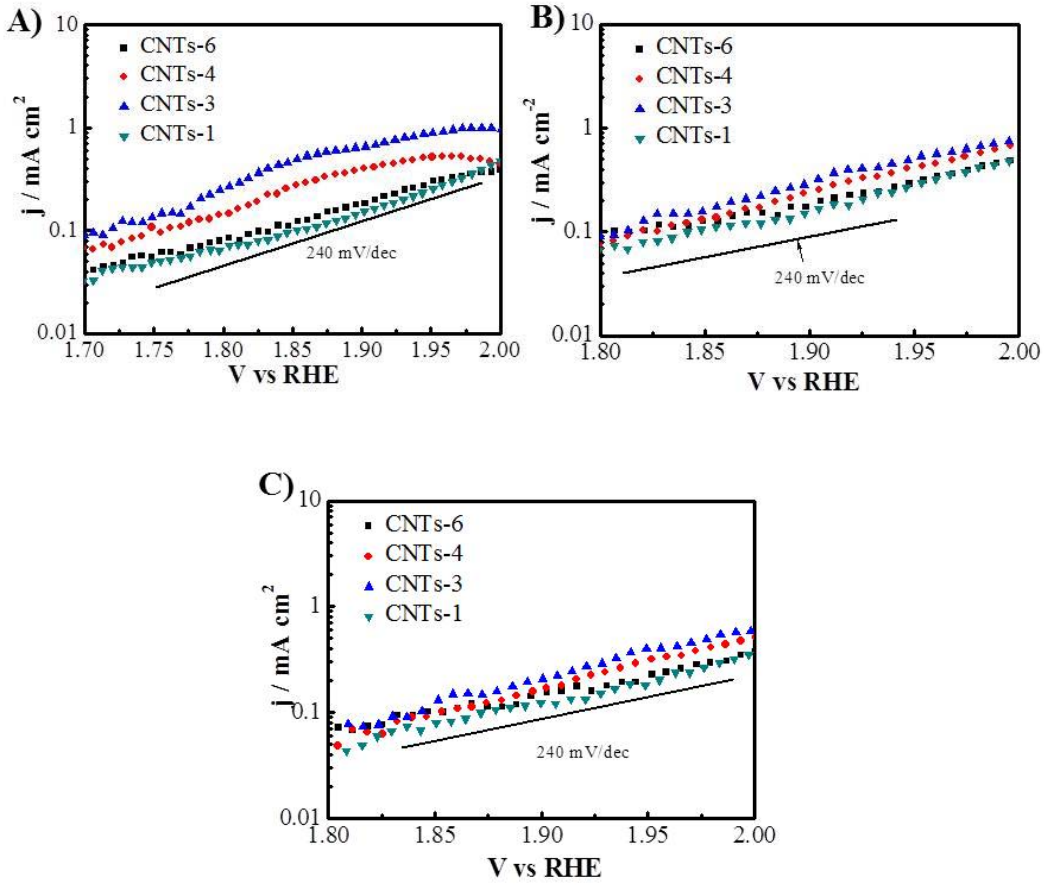

Figure 5.3. Tafel plots for OER on CNTs-1, CNTs-3, CNTs-4 and CNTs-6 in H_2SO_4 solutions. A) 1.0 M, B) 0.5 M, and C) 0.1 M.

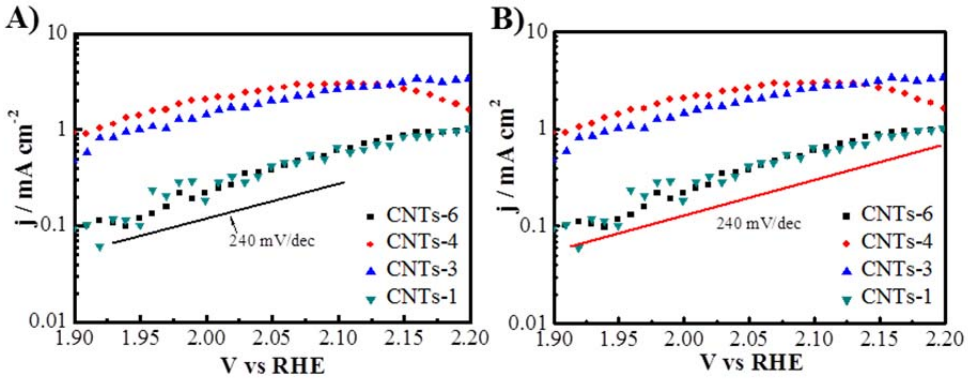

Figure 5.4. Tafel plots for OER on CNTs-1, CNTs-3, CNTs-4 and CNTs-6 in buffer solution A) pH 7 and B) pH 8.

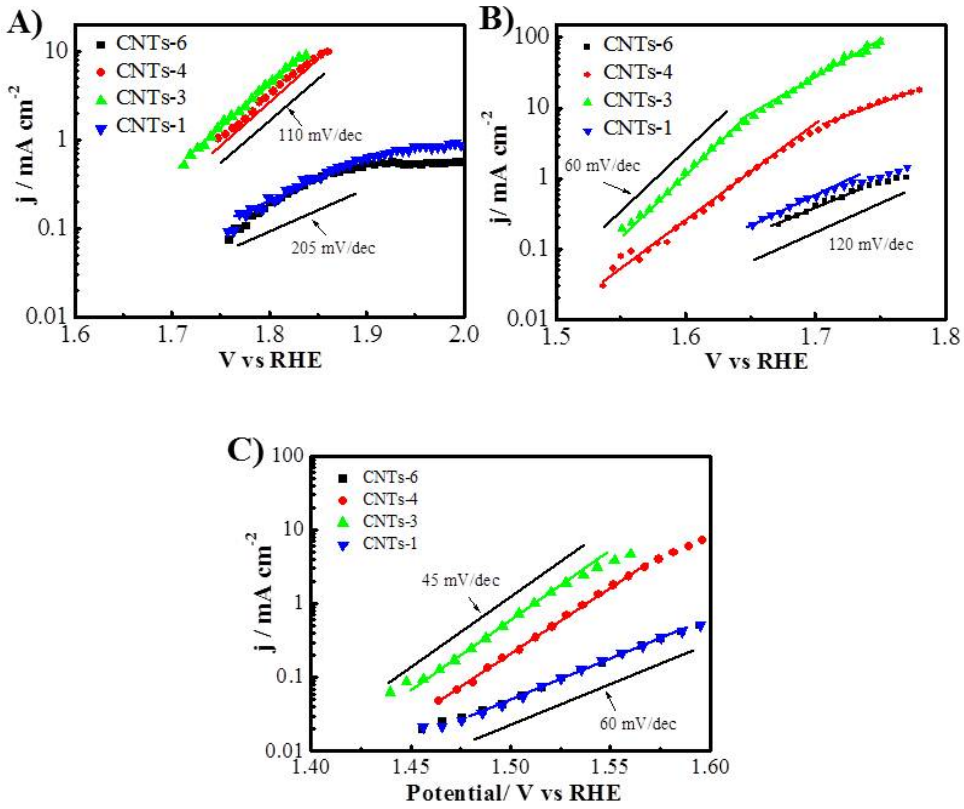

Figure 5.5. Tafel plots for OER on CNTs-1, CNTs-3, CNTs-4 and CNTs-6 in A) 0.01 M, B) 1.0 M and C) 10.0 M KOH solutions

The Tafel behavior, especially the Tafel-slope, is an important kinetic parameter to reveal changes in the apparent OER mechanism. The effects of solution pH/OH^- concentration on the rate determine steps were also investigated. The steady state polarization for OER on CNTs-1, CNTs-3, CNTs-4 and CNTs-6 was evaluated as function of potential in acid, neutral and alkaline solutions with stirring rate of 1600 rpm. A high ionic strength was maintained with 1.0 M ions by adding KNO_3 to avoid diffusing double layer effects [50-52]. The Tafel slopes of CNTs for OER in acid and neutral solution closes to 240 mV dec^{-1} (Fig. 5.3 and 5.4), indicating the low activity and slow kinetic of OER on CNTs in both acid and neutral solutions. The Tafel slopes are very sensitive to the C_{OH}, and a significant decrease of Tafel slope was observed

as the increase of the C_{OH}. A Tafel slope of 110 mV dec^{-1} was obtained for CNTs-3 and CNTs-4 in 0.001 M KOH solutions, significantly lower than that of CNTs-1 and CNTs-6 (205 mV/dec) at same condition (Fig. 5.5 A), revealed the difference of rate determine step (RDS) on different type of CNTs. As the concentration of KOH increase to 1.0 M, a Tafel slope of 60 mV dec^{-1} at lower overpotential and a Tafel slope approaching 120 mV dec^{-1} at higher overpotential were observed on CNTs-3 and CNTs-4, and a Tafel slope of 120 mV dec^{-1} was observed on CNTs-1 and CNTs-6 (Fig. 5.5B). The Tafel slopes decreased to around 40 mV dec^{-1} for CNTs-3 and CNTs-4 and 60 mV dec^{-1} for CNTs-1 and CNTs-6 in 10.0 M KOH solutions, indicating the increase of activity (Fig. 5.5C). The results suggest the nature of the rate determine step (RDS) is highly related with the C_{OH} in solution. A Tafel slope of 120 mV dec^{-1} in 0.001 M KOH implying the rate of OER is limited by the first electron transfer step. The Tafel slope of 40 mV dec^{-1} in 10.0 M KOH indicates the second electron transfer step is the rate-determining step. The Tafel slope of 60 mV dec^{-1} predicting the OER involves a chemical step subsequent to the first electron transfer step in 1.0 M KOH solution[4, 53].

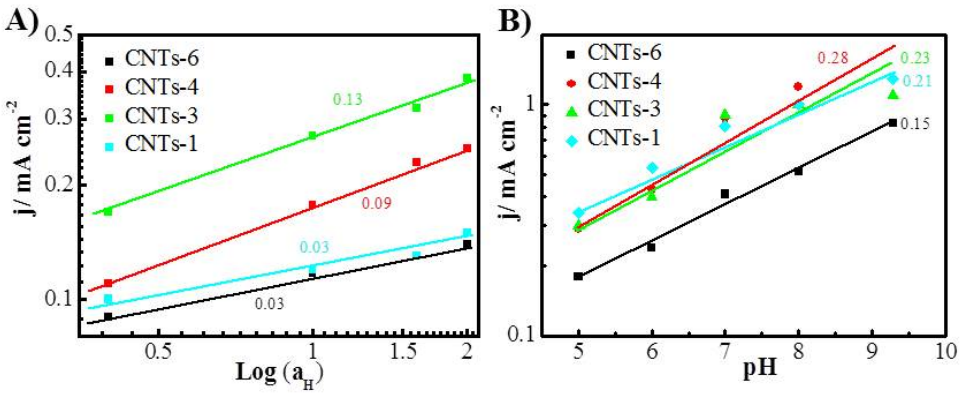

Figure 5.6. Reaction order for OER on CNTs-1, CNTs-3, CNTs-4 and CNTs-6 in A) 0.1-1.0 M H_2SO_4, obtained at 1.3 V vs SCE and B) pH 5-7 buffer solutions, obtained 1.3 V vs SCE.

The dependence of reaction rate on OH^- or H^- strength was investigated by controlled potential electrolysis at lower overpotentials regions. KNO_3 was added to each

solution to preserve a constant ionic strength of 1.0 M when the pH adjusted from 0-14 to eliminate the diffuse double layer effects[50], and buffer solution were prepared when the reaction order acquired in under pH 4-8. In acid solutions, the reaction order in H^+ activity is 0.13, 0.09, 0.03 and 0.03 for CNTs-3, CNTs-4, CNTs-1 and CNTs-6 respectively (Fig. 5.6 A), yielded an approaching zeroth-order dependence on proton. These results demonstrated that the activity of CNTs is not sensitive to the change of H^+ concentration over the range of 0.4-2 M. The reaction order is about 0.2 for the CNTs in neutral buffer solutions as show in Fig. 5.6 B. In alkaline solutions, the reaction order is close to integer and varies with the change of OH^- concentration. For CNTs-1 and CNTs-6, two typical reaction order were observed with a number of approaching 0.5 when the OH^- in the range of 10^{-3} to 0.1 M and a number approaching to 1 when the OH^- in the range of 0.1-10.0 M (Fig. 5.7 A and B), which is consistent with the change of Tafel slope with OH^- concentrations, indicating the different kinetics and RDS steps for OER. Similar phenomenon was obtained for CNTs-3 and CNTs-4. A reaction order of 1 was obtained when the OH^- concentration in the range of 10^{-3} to 1.0 M, and a reaction order of 2 were observed with OH^- range from 2-10.0 M (Fig. 5.7 C-E). The change of reaction order indicating the mechanistic change of OER on CNTs with the OH^- concentration, consistent with the change of Tafel slopes.

The change of OER mechanism was also supported by the OH^-/pH dependence of steady-state electrode potential at constant current density of 0.5 mA cm^{-2} (Fig. 5.8). Fig. 5.8 A shows the OH^-/pH dependence of potential (əE/ əpH) over the pH range of 4-8, a slope of around 30 mV/pH was obtained, indicating the activity decrease with the increase of pH. Fig. 5.8 B shows that OH^-/pH dependence of potential ($əE/əa_{OH^-}$) over the OH^- concentration of 10^{-3} to 1.0 M, in the case of CNTs-1 and CNTs-6, a slope approaching -120 mV/pH was obtained. While a change of $əE/əa_{OH^-}$ were

observed for CNTs-3 and CNTs-4, a slope of -120 mV/pH were observed over the OH^- concentration of 10^{-3} to 10^{-2} M and a slope of -56 mV/pH over the OH^- concentration of 0.01-1M, further demonstrated the change of OER mechanisms.

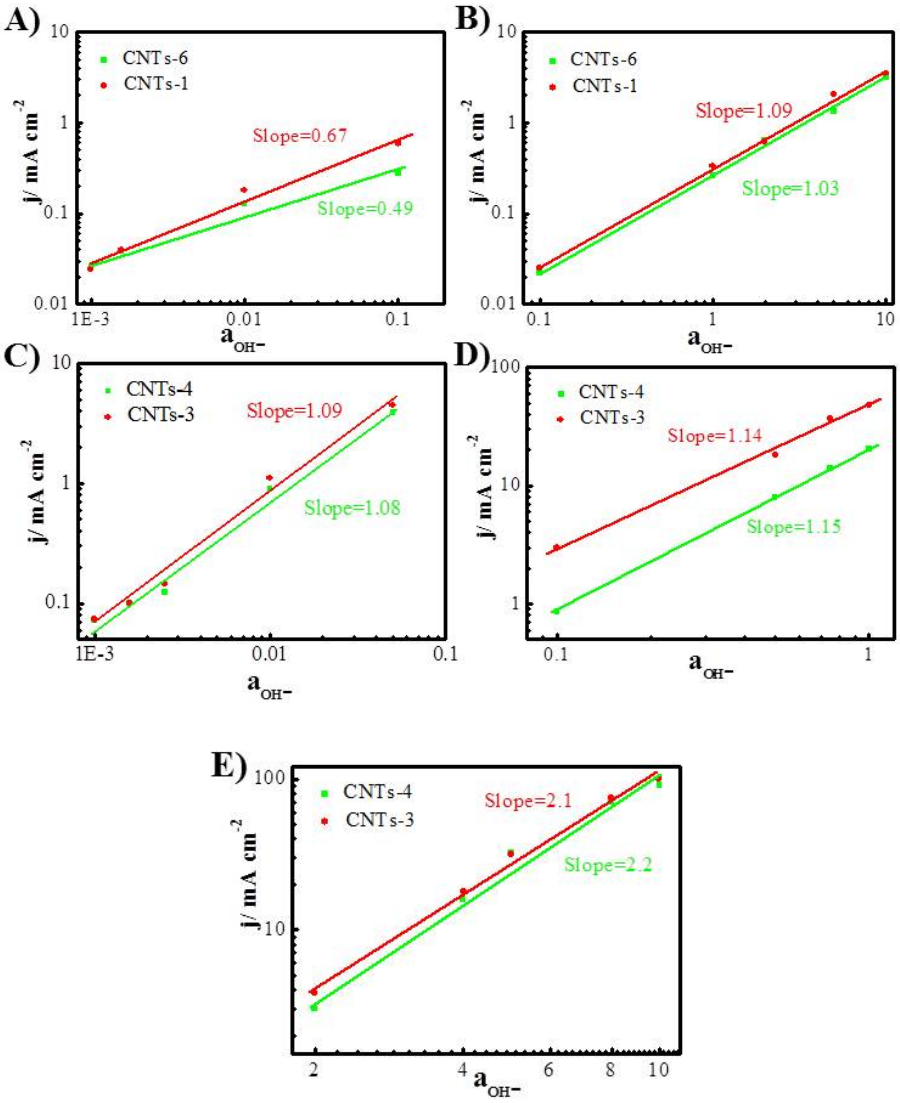

Figure 5.7. Reaction order for OER in alkaline solutions. A) 10^{-3} -0.1 M KOH solutions, obtained at 0.8 V vs SCE; B) 0.1-10.0 M KOH solutions for CNTs-1 and CNTs-6, obtained at 0.7 V vs SCE; C) 10^{-3} -0.1 M KOH solutions, obtained at 0.8 V vs SCE; D) 0.1-1.0 M KOH solutions, obtained at 0.7 V vs SCE, E) 2-10.0 M KOH solutions, obtained at 0.6 V vs SCE.

5.3.4 Oxygen evolution reaction mechanism

Tafel slope behavior describing the effect of potential, E, or overpotential, η, on steady-state current density, along with experimentally determined reaction orders, forms the basic mechanistic analysis of OER on CNTs. The Tafel slope and the reaction order were summarized in Table 5.1. All the CNTs show very high Tafel slope approaching 240 mV dec^{-1} with a zeroth reaction order dependence on proton for OER in acid and neutral conditions. The OER kinetics is sensitive to the C_{OH}, and CNTs composed of between 2-7 concentric tubes show significantly lower Tafel slopes and higher reaction order at same alkaline conditions. A Tafel slope closing to 40 mV dec^{-1} and a reaction order of 2 were obtained under 2-10 mol L^{-1} KOH solutions for CNTs composed of between 2-7 concentric tubes (CNTs-3 and CNTs-4), while a Tafel slope of 60 mV dec^{-1} and reaction order of 1 were observed for typical single walled CNTs and multi walled CNTs, CNTs-6 and CNTs-1 respectively, at the same condition. A 120 mV dec^{-1} Tafel slope and reaction order of 1 were recorded under 10^{-3}-10^{-1} M KOH, pH 11-13, for CNTs-3 and CNTs-4, compared with a Tafel slope of 240 mV dec^{-1} and a reaction order of 0.5 for CNTs-1 and CNTs-6. These results demonstrate the kinetics varies with different types of CNTs and also pH/C_{OH} revealing the OER mechanism on CNTs. The reaction order at constant potential $(\partial E/\partial \log j)_{pH}$ and constant current density $(\partial E/ \partial pH)_j$ are related to the Tafel slope and can be expressed as follow:

$$\left(\frac{\partial E}{\partial pH}\right)_j = -\left(\frac{\partial \log j}{\partial pH}\right)_E \left(\frac{\partial E}{\partial \log j}\right)_{pH} \quad (1)$$

For example, substituting $(\partial E/ \partial pH)_j$ = -56 mV/pH (Fig. 5.6 B) and $(\partial E/ \partial \log j)_{pH}$ = 60 mV dec^{-1} (the Tafel slope in Fig.5.6 D) into eq. 1 gives the $(\partial \log j/ \partial a_{OH^-})_E$ = 1. These

are also supported by the results obtained in neutral solution and OH^- ranging from 10^{-3} to 1.0 M, revealing the self-consistency of kinetics parameters.

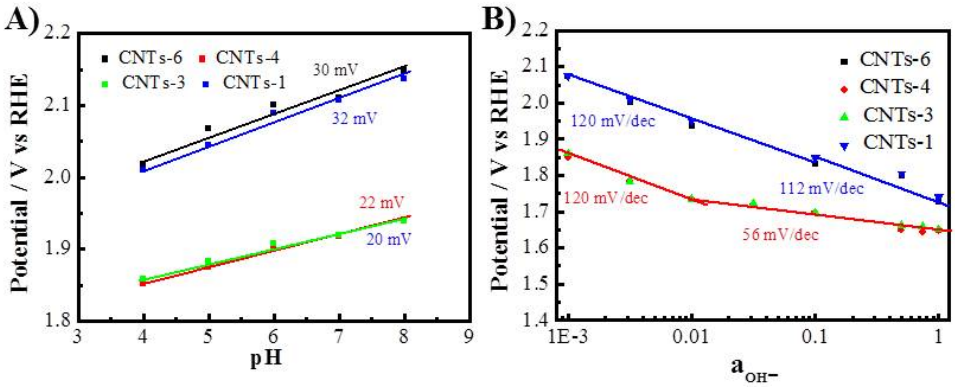

Figure 5.8. pH or a_{OH^-} dependence of steady-state electrode potential at constant current density (0.5 mA cm^{-2})

Extensive mechanistic studies have been performed to study the OER on Pt surface under acidic and alkaline solutions. The proposed reaction for the OER under acidic conditions involves water binding to the surface and irreversible removal of one electron and one proton to form platinum hydroxides, yield a Tafel slope of 117 mV/dec. In alkaline conditions, the rate-determine step involves the removal of one proton and one electron from platinum hyoxides to form a surface oxide species (Tafel slope of 46 mV/dec) [52, 54-56]. The shift in mechanism across a wide pH range is attributed to the kinetic facility of oxidizing hydroxide relative to water [52, 55, 57]. The shift of mechanism in acid and alkaline solution was also observed on Rh, Pt-Rh surface, where a Tafel slope of 60 and 120 mV dec^{-1} were obtained in acid solution and a Tafel slope of 40 and 40 mV dec^{-1} observed in alkaline solutions respectively[53]. However, Ir and Ru elctrode exhibits a Tafel slope of 40 mV dec^{-1} both in acid and alkaline solutions [53, 58], which is because Ir and Ru are considered the best catalysts for splitting H_2O molecules. Recently, D. G. Nocera group reported a functionally stable manganese oxide oxygen evolution catalyst in acid, neutral and alkaline

conditions, in the alkaline pH regime, a ~60 mV dec^{-1} Tafel slope and first-order dependence on proton concentration were observed, whereas the OER in acid conditions exhibited a quasi-infinite Tafel slope of 653 ± 166 mV dec^{-1} and zeroth-order dependence on proton concentration. The results reflect two competing mechanisms: a one-electron one-proton pathway that is dominant under alkaline conditions and a Mn^{3+}disproportionation process, which predominates under acidic conditions. At neutral pH, competition between these two mechanisms resulted in a half-order dependence on proton concentration and Tafel slopes that are intermediate to those observed for the limiting acidic and alkaline regimes[59].

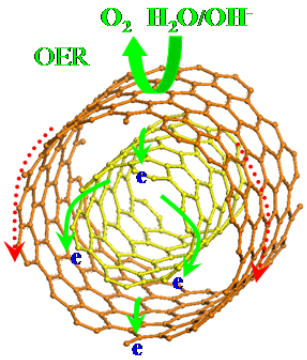

Figure 5.9. Schematic of electron transfer pathway for OER through tunneling effect on CNTs

Table 5.1. Onset potential and current density of CNTs in acid, neutral and alkaline solutions. The current density is obtained at 2.1 V vs RHE in acid and neutral conditions, and 1.7 V in alkaline.

Materials	Parameters	Acid	Neutral	alkaline
CNTs-1	Onset potential	1.85	2	1.75
	Current density	7.3	0.76	13
CNTs-2	Onset potential	1.78	1.9	1.67
	Current density	13.74	1.8	112
CNTs-3	Onset potential	1.77	1.84	1.64
	Current density	15.4	2.6	125
CNTs-4	Onset potential	1.79	1.85	1.66
	Current density	13	4.3	108
CNTs-5	Onset potential	1.8	1.9	1.73
	Current density	11.2	1.4	34
CNTs-6	Onset potential	1.85	2.05	1.74
	Current density	5.2	0.46	8
CNTs-7	Onset potential	1.87	2.05	1.78
	Current density	6.06	0.47	3

For CNTs, Tafel slope of approaching 240 mV dec^{-1} in acid and neutral conditions indicate the electron transfer cannot take place. The Tafel slope is significantly higher than that on Rh, Ir, Pt and Pt-Rh in acid conditions, which exhibit Tafel slope of 60, 40, 120 and 120 mV dec^{-1} respectively[53], and also substantially higher than the-art-of-the-state non-noble catalysts, CoPi (60 mV dec^{-1}) and NiBi (30 mV dec^{-1}), in neutral conditions[50, 52]. The slope much greater than 120 mV dec^{-1} are classified as quasi-infinite and are consistent with an initial rate determine chemical step[59]. In acid or neutral conditions, the deprotonation of H_2O molecule must be realized before the H_2O evolves to molecule O_2. For Rh, Ir, Pt and Pt-Rh electrodes, the deprotonation of H_2O is facile due to the available of high active valence electrons, hence it is kinetic favorable for OER in acid. On pure CNTs surface, the deprotonation of H_2O is not facile because a free energy of 89.96 kJ/mol is required[60].

For OER on CNTs, charging of the interface involves the accumulation the accumulation of OH^- species to form electrical double layer. The defects or the trace metal on the CNTs surface might play a role for the activity of the CNTs, however, the exclusively better activities of CNTs-2, CNTs-3 and CNTs-4 compared with CNTs-1, CNTs-6 and CNTs-7 in all conditions (Table 5.2) are mainly contribute to the different electron transfer pathway in the CNTs. For DWNTs and FWCNTs, the presence of inner tubes could increase the number of conducting channels and the discharged electron can transfer into the inner walls through tunneling effects driven by the applied potential, which create the separation of electron and discharged intermediates (Fig. 5.9). Li et a synthesized carbon nanotube-graphene complexes through partially unzipping few outer walls of CNTs and attributed the observed high activity for ORR as the results of its high activity sites of the abundant edges and defects of the unzipped outer walls and the less damaged and electrically conducting

inner tubes [65]. Borghei et al. synthesized a high catalytic electrochemical active nitrogen-containing FWCNTs (N-FWCNTs) with low nitrogen content（～0.5 at.%), and the resulting N-FWCNTs showed remarkable electrocatalytic activity for ORR, HER and hydrogen peroxide decomposition compared to larger multi-walled nanotubes[47]. These results all demonstrate the excellent electron transfer properties of the inner tubes of DWNTs and FWCNTs attribute to the excellent activity for modified CNTs. Here, the outer wall can serve as a protective barrier to prevent endohedral reactions, potentially allowing the inner-tube to retain its electronic properties [66], which reveals the possibility of the separation of functionality of the outer wall and inner-tubes for the OER on DWNTs and FWCNTs[48]. The electron transfer between the outer wall and inner tube could occur by electron tunneling, similar to the electron tunneling through thin oxide films as proposed by Damjanovic et al for the OER on Pt [67]. The electronic properties of SWNTs is disrupted due to the absorption of OH^- and intermediate species, such as OH* and OOH^* [68]. On the other hand, the discharged electron must transfer between the C=C bonds on SWNTs, and this obviously will lead to the combine of electrons with the discharged OH, O and OOH intermediates even without considering the proportion of semi-conducting SWNTs existed[69], hence decrease the efficiency of OER on SWNTs (Fig. 5.9). This hypothesis explains why double/triple-walled CNTs-2, CNTs-3 and CNTs-4 are far more effective than single-walled CNTs-1 in all conditions, and also supported by the OER kinetics parameter in this study. While as the increase of number of walls for typical large diameter MWNTs, the driving force for the electron transfer or tunneling effect between the outer wall and inner tubes, η, would diminish due to the distribution of the dc bias across each layer. Thus, the electron transfer or tunneling from the outer surface to the inner tubes could become less favourable as the number of walls/layers increases.

5.4 Conclusion

Small diameter CNTs composed of between 2-7 concentric tubes and with an OD of 2-5 nm are demonstrated better catalysts for OER compared with typical single walled CNTs and multi walled CNTs, CNTs-1, CNTs-6 and CNTs-7. Here the CNTs were studied at different pH, and the kinetics and mechanism are revealed. The results demonstrated that CNTs that composed of between 2-7 concentric tubes and with an OD of 2-5 nm show significantly higher activity in acid, neutral and alkaline solutions, and the activity of the CNTs for OER is closely related with the C_{OH} groups. The OER is limited by the deprotonation of water in acid and neutral conditions, and the C_{OH} play a vital role in OER on all the CNTs. OER on CNTs composed of between 2-7 concentric tubes and with an OD of 2-5 nm in alkaline solution show higher kinetics and enhanced activities. A Tafel slope closing to 40 mV dec^{-1} and a reation order of 2 was obtained under 5-10 mol L^{-1} KOH solution for CNTs-3 and CNTs-4, indicating the OER on these small diameter CNTs involves the discharge of two electron followed by the RDS. While a Tafel slope of 60 mV dec^{-1} and reaction order of 1 were observed for typical single walled CNTs and multi walled CNTs, CNTs-6 and CNTs-1 at the same condition, revealing the OER involves a chemical step subsequent to the first electron transfer step. And a 120 mV dec^{-1} Tafel slope and reaction order of 1 were recorded under lower concentration of KOH solution for CNTs-3 and CNTs-4 (10^{-3}-10^{-1} M KOH, pH 11-13), illustrating that OER is limited by the first electron transfer steps. The different kinetics and OER on different CNTs further demonstrate the proposed tunneling effect. The finding provide an area to develop a new class of advanced OER catalysts based on pure carbon, rather than metals or metal oxides.

Acknowledgment

This research was supported by the Australian Research Council *Discovery Project Funding Scheme* (project number: DP120102325, DP120104932 and DP0986999), and the Major International (Regional) Joint Research Project of the National Natural Science Foundation of China (51210002), as well as access to resources at iVEC and NCI

References

1. D. Pletcher and X. Li, *International Journal of Hydrogen Energy*, 2011, 36, 15089-15104.
2. F. M. Toma, A. Sartorel, M. Iurlo, M. Carraro, P. Parisse, C. Maccato, S. Rapino, B. Rodriguez Gonzalez, H. Amenitsch, T. Da Ros, L. Casalis, A. Goldoni, M. Marcaccio, G. Scorrano, G. Scoles, F. Paolucci, M. Prato and M. Bonchio, *Nature Chemistry*, 2010, 2, 826-831.
3. H. Dau, C. Limberg, T. Reier, M. Risch, S. Roggan and P. Strasser, *Chemcatchem*, 2010, 2, 724-761.
4. R. L. Doyle, I. J. Godwin, M. P. Brandon and M. E. G. Lyons, *Physical Chemistry Chemical Physics*, 2013, 15, 13737-13783.
5. I. C. Man, H.-Y. Su, F. Calle-Vallejo, H. A. Hansen, J. I. Martínez, N. G. Inoglu, J. Kitchin, T. F. Jaramillo, J. K. Nørskov and J. Rossmeisl, *Chemcatchem*, 2011, 3, 1159-1165.
6. J. C. Cruz, V. Baglio, S. Siracusano, V. Antonucci, A. S. Arico, R. Ornelas, L. Ortiz-Frade, G. Osorio-Monreal, S. M. Duron-Torres and L. G. Arriaga, *International Journal of Electrochemical Science*, 2011, 6, 6607-6619.
7. A. Di Blasi, C. D'Urso, V. Baglio, V. Antonucci, A. S. Arico, R. Ornelas, F. Matteucci, G. Orozco, D. Beltran, Y. Meas and L. G. Arriaga, *Journal of Applied Electrochemistry*, 2009, 39, 191-196.
8. A. Ursua, L. M. Gandia and P. Sanchis, *Proceedings of the Ieee*, 2012, 100, 410-426.
9. R. Forgie, G. Bugosh, K. C. Neyerlin, Z. C. Liu and P. Strasser, *Electrochemical and Solid State Letters*, 2010, 13, D36-D39.
10. M. H. Miles, E. A. Klaus, B. P. Gunn, J. R. Locker, W. E. Serafin and S. Srinivasan, *Electrochimica Acta*, 1978, 23, 521-526.
11. H. S. Horowitz, H. H. Horowitz and J. M. Longo, *Journal of the Electrochemical Society*, 1981, 128, C131-C131.
12. M. Carmo, D. L. Fritz, J. Merge and D. Stolten, *International Journal of Hydrogen Energy*, 2013, 38, 4901-4934.

13. H. S. Horowitz, J. M. Longo and H. H. Horowitz, *Journal of the Electrochemical Society*, 1983, 130, 1851-1859.
14. P. F. Carcia, R. D. Shannon, P. E. Bierstedt and R. B. Flippen, *Journal of the Electrochemical Society*, 1980, 127, 1974-1978.
15. P. F. Carcia, R. D. Shannon, R. B. Flippen and P. E. Bierstedt, *Journal of the Electrochemical Society*, 1979, 126, C326-C326.
16. C. Bocca, A. Barbucci, M. Delucchi and G. Cerisola, *International Journal of Hydrogen Energy*, 1999, 24, 21-26.
17. C. Iwakura, A. Honji and H. Tamura, *Electrochimica Acta*, 1981, 26, 1319-1326.
18. L. Trotochaud, J. K. Ranney, K. N. Williams and S. W. Boettcher, *Journal of the American Chemical Society*, 2012, 134, 17253-17261.
19. R. L. Doyle and M. E. G. Lyons, *Physical Chemistry Chemical Physics*, 2013, 15, 5224-5237.
20. D. Cibrev, M. Jankulovska, T. Lana-Villarreal and R. Gomez, *International Journal of Hydrogen Energy*, 2013, 38, 2746-2753.
21. R. L. Doyle and M. E. G. Lyons, *Journal of the Electrochemical Society*, 2013, 160, H142-H154.
22. F. Cheng, J. Shen, B. Peng, Y. Pan, Z. Tao and J. Chen, *Nature Chemistry*, 2011, 3, 79-84.
23. K. J. May, C. E. Carlton, K. A. Stoerzinger, M. Risch, J. Suntivich, Y. L. Lee, A. Grimaud and Y. Shao-Horn, *J. Phys. Chem. Lett.*, 2012, 3, 3264-3270.
24. S. Raabe, D. Mierwaldt, J. Ciston, M. Uijttewaal, H. Stein, J. Hoffmann, Y. M. Zhu, P. Blochl and C. Jooss, *Adv. Funct. Mater.*, 2012, 22, 3378-3388.
25. A. Grimaud, K. J. May, C. E. Carlton, Y.-L. Lee, M. Risch, W. T. Hong, J. Zhou and Y. Shao-Horn, *Nat Commun*, 2013, 4.
26. J. Rosen, G. S. Hutchings and F. Jiao, *Journal of the American Chemical Society*, 2013, 135, 4516-4521.
27. D. U. Lee, B. J. Kim and Z. W. Chen, *J. Mater. Chem. A*, 2013, 1, 4754-4762.
28. E. Potvin and L. Brossard, *Materials Chemistry and Physics*, 1992, 31, 311-318.
29. M. Gong, Y. Li, H. Wang, Y. Liang, J. Z. Wu, J. Zhou, J. Wang, T. Regier, F. Wei and H. Dai, *Journal of the American Chemical Society*, 2013, 135, 8452-8455.
30. M. W. Louie and A. T. Bell, *Journal of the American Chemical Society*, 2013, 135, 12329-12337.
31. C. C. L. McCrory, S. Jung, J. C. Peters and T. F. Jaramillo, *Journal of the American Chemical Society*, 2013, 135, 16977-16987.
32. R. D. L. Smith, M. S. Prévot, R. D. Fagan, S. Trudel and C. P. Berlinguette, *Journal of the American Chemical Society*, 2013, 135, 11580-11586.
33. D. C. Higgins, D. Meza and Z. Chen, *The Journal of Physical Chemistry C*, 2010, 114, 21982-21988.

34. J. Zhang, S. Tang, L. Liao, W. Yu, J. Li, F. Seland and G. M. Haarberg, *Journal of Power Sources*, 2014, 267, 706-713.
35. W. Yang, Y. Wang, J. Li and X. Yang, *Energy & Environmental Science*, 2010, 3, 144-149.
36. B. P. Vinayan and S. Ramaprabhu, *Nanoscale*, 2013, 5, 5109-5118.
37. C. Hu, Y. Cao, L. Yang, Z. Bai, Y. Guo, K. Wang, P. Xu and J. zhou, *Applied Surface Science*, 2011, 257, 7968-7974.
38. Y. Cheng and S. P. Jiang, *Electrochimica Acta*, 2013, 99, 124-132.
39. Y. Cheng, C. Xu, P. K. Shen and S. P. Jiang, *Applied Catalysis B: Environmental*, 2014, 158–159, 140-149.
40. H.-Y. Wang, F.-M. Wang, Y.-Y. Wang, C.-C. Wan, B.-J. Hwang, R. Santhanam and J. Rick, *The Journal of Physical Chemistry C*, 2011, 115, 8439-8446.
41. H. Kim and S. H. Moon, *Carbon*, 2011, 49, 1491-1501.
42. Y. Cheng, C. Liu, H.-M. Cheng and S. P. Jiang, *ACS Applied Materials & Interfaces*, 2014, 6, 10089-10098.
43. J. Wu, Y. Xue, X. Yan, W. Yan, Q. Cheng and Y. Xie, *Nano Research*, 2012, 5, 521-530.
44. F. M. Toma, A. Sartorel, M. Iurlo, M. Carraro, S. Rapino, L. Hoober-Burkhardt, T. Da Ros, M. Marcaccio, G. Scorrano, F. Paolucci, M. Bonchio and M. Prato, *Chemsuschem*, 2011, 4, 1447-1451.
45. Y. Zhao, R. Nakamura, K. Kamiya, S. Nakanishi and K. Hashimoto, *Nat Commun*, 2013, 4.
46. G.-L. Tian, M.-Q. Zhao, D. Yu, X.-Y. Kong, J.-Q. Huang, Q. Zhang and F. Wei, *Small*, 2014, 10, 2251-2259.
47. M. Borghei, P. Kanninen, M. Lundahl, T. Susi, J. Sainio, I. Anoshkin, A. Nasibulin, T. Kallio, K. Tammeveski, E. Kauppinen and V. Ruiz, *Applied Catalysis B: Environmental*, 2014, 158–159, 233-241.
48. Y. Cheng, C. Xu, L. Jia, J. D. Gale, L. Zhang, C. Liu, P. K. Shen and S. P. Jiang, *Applied Catalysis B: Environmental*, 2015, 163, 96-104.
49. M. E. G. Lyons and S. Floquet, *Physical Chemistry Chemical Physics*, 2011, 13, 5314-5335.
50. D. K. Bediako, Y. Surendranath and D. G. Nocera, *Journal of the American Chemical Society*, 2013, 135, 3662-3674.
51. Y. Surendranath and D. G. Nocera, in *Progress in Inorganic Chemistry*, John Wiley & Sons, Inc., 2011, DOI: 10.1002/9781118148235.ch9, pp. 505-560.
52. Y. Surendranath, M. W. Kanan and D. G. Nocera, *Journal of the American Chemical Society*, 2010, 132, 16501-16509.
53. A. Damjanovic, A. Dey and J. O. M. Bockris, *Journal of the Electrochemical Society*, 1966, 113, 739-746.
54. B. E. Conway and T. C. Liu, *Langmuir*, 1990, 6, 268-276.
55. V. I. Birss and A. Damjanovic, *Journal of the Electrochemical Society*, 1987, 134, 113-117.

56. V. I. Birss, A. Damjanovic and P. G. Hudson, *Journal of the Electrochemical Society*, 1986, 133, 1621-1625.
57. A. Damjanovic, A. Dey and J. O. M. Bockris, *Electrochimica Acta*, 1966, 11, 791-814.
58. T. Reier, M. Oezaslan and P. Strasser, *Acs Catalysis*, 2012, 2, 1765-1772.
59. M. Huynh, D. K. Bediako and D. G. Nocera, *Journal of the American Chemical Society*, 2014, 136, 6002-6010.
60. M. W. Palascak and G. C. Shields, *The Journal of Physical Chemistry A*, 2004, 108, 3692-3694.
61. R. E. Meyer, *Journal of the Electrochemical Society*, 1960, 107, 847-853.
62. M. S. Abdel-Aal and A. A. Hermas, *Journal of Applied Electrochemistry*, 2000, 30, 339-345.
63. M. E. G. Lyons and M. P. Brandon, *International Journal of Electrochemical Science*, 2008, 3, 1425-1462.
64. M. E. G. Lyons and M. P. Brandon, *International Journal of Electrochemical Science*, 2008, 3, 1386-1424.
65. Y. Li, W. Zhou, H. Wang, L. Xie, Y. Liang, F. Wei, J.-C. Idrobo, S. J. Pennycook and H. Dai, *Nat Nano*, 2012, 7, 394-400.
66. C. Shen, A. H. Brozena and Y. H. Wang, *Nanoscale*, 2011, 3, 503-518.
67. A. Damjanovic, V. I. Birss and D. S. Boudreaux, *J. Electrochem. Soc.*, 1991, 138, 2549-2555.
68. J. J. Zhao, H. K. Park, J. Han and J. P. Lu, *J. Phys. Chem. B*, 2004, 108, 4227-4230.
69. R. Saito, M. Fujita, G. Dresselhaus and M. S. Dresselhaus, *Applied Physics Letters*, 1992, 60, 2204-2206.

Chapter 6: Phthalocyanines Functionalized Carbon Nanotubes for Photo-electrochemical Water Oxidation

6.1 Introduction

Dye sensitized photo-electrochemical systems have attracted intensive interests due to its outstanding features such as high efficiency, promising stability, flexibility, and low-cost for investment and fabrication[1-3]. Normally, dye sensitized photo-electrochemical systems are comprised of three essential components: efficient light-harvesting sensitizer; stable charge-separating units which normally are meso-structured wide band gap metal oxide semiconductors, and compatible donor-acceptor[3-5]. The nanocrystalline semiconductors, that provides the light absorption, charge collection and diffusion, are playing the vital role in dye sensitized photo-electrochemical systems. The key breakthrough is the use of mesoporous TiO_2 electrode supported with monolayer of a molecular sensitizer[6], in which the photo-excited dyes inject electrons into the conduction band of the TiO_2 electrode under illumination, and then the dyes are regenerated by the electron donor in the electrolyte[3]. Nanostructured metal oxides such as TiO_2[7-9], Fe_2O_3[10, 11], SnO_2[9, 12, 13] and ZnO[9, 14, 15] have been intensively investigated for developing dye sensitized photo-electrochemical devices.

One of the major bottlenecks in dye sensitized photo-electrochemical systems is the poor transport of photo-generated electrons across semiconductor network, which lead

to high electron-hole recombination and low overall energy conversion efficiency. An appealing concept is introduction of CNTs to direct the photo-generated electrons flow and assist in charge injection and extraction. Porphyrin and SWNT were assembled as three-dimensional arrays onto nanostructured SnO_2 films by an electrophoretic deposition method. Femtosecond transient absorption studies confirm photo-induced electron transfer between excited H_4P^{2+} and SWNT, and PEC effect observed with SWNT and porphyrin assembly demonstrates CNTs are able to promote both charge separation and charge transport[16]. Recently, Li et al. also demonstrated the application of direct synthesized CNTs networks films as a hole collector for perovskite solar cells, the solar cell performance is improved due to the enhanced hole extraction and reduced electron-hole recombination[17]. Li et al. demonstrated that the semiconducting SWNTs exhibit a much better photo-catalytic effect when cooperated with TiO_2 compared with typical MWNTs[18]. Several mechanisms were proposed to explain the enhancement of the photo-catalytic properties of CNTs-semiconductor composites. Hoffmann et al. proposed that the CNTs can transfer the photo-generated electron through the carbon nanotube hence enhance the charge separation[19]. Wang et al. claimed that CNTs act as sensitizers and transfer the electron to the conduction band of semiconductor such as TiO_2, allowing formation of superoxide radicals[20]. Unfortunately, the function of CNTs is still remaining controversial and unexplored.

It is generally believed that pristine CNTs without PEC catalysts would not have any activity for water splitting under UV or visible light because the band gaps of CNTs are too small to split water molecules. Here we reported, for the first time, that pristine CNTs with 2-7 number of walls functionalized with dyes such as zinc phthlocyanine (ZnPc) show significantly high PEC activity for water splitting without

incorporating with semiconductor oxides, as compared with dye-functionalized conventional SWNTs and MWNTs under identical test conditions, despite the fact that dyes have no PEC activity on their own. The fundamental reasons for the dye-functionalized CNTs with 2-7 inner tubes are the effective electron-hole separation ability of the CNTs with 2-7 inner tubes via the electron tunneling mechanism under the influence of electrochemical polarization potential driving force.

6.2 Experimental

6.2.1 Materials

CNTs with different number of walls and diameters were obtained from commercial sources including Nanostructured & Amorphous Materials, Inc., USA, Beijing Dk Nano technology Co., LTD, China and Shenzhen Nano, China. The as-received CNTs were purified following the procedure reported[21]: 50 mg CNTs were dispersed in 50 mL HCl acid (30 wt %) before ultrasonicated for 1 h. The dispersion was separated and the sludge dispersed in another 50 mL HCl acid (30 wt %), followed by stirring overnight. The CNTs pellets were collected and transferred into Teflon digestion tank and another 10 mL HCl acid were added and digested at 120 ^{o}C overnight. After the digestion, the CNTs were washed by fresh HCl, and then washed by 5 mol L^{-1} HNO_3 for 3 times before washed by DI water for 3 times. The purified CNTs were dried and collected for further test. After purification, the total amount of Fe, Co, Mo and Ni elements are substantially reduced to less than 1.3 % as confirmed by the ICP-OES and thermogravimetry analysis. Zinc Phthalocyanine (Sigma-Aldrich, denoted as ZnPc, Schematic 6.1), KOH (Sigma-Aldrich), Nafion solution (Sigma-Aldrich, 5% in isopropanol and water) and F-doped SnO_2 coated glass (FTO, R_Ω 8 Ω cm^{-1}, Pilkington glass, USA) were received and used without further treatment.

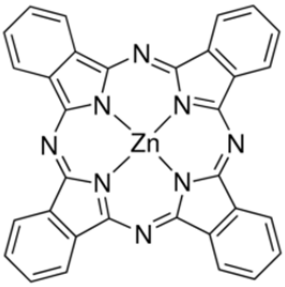

Schematic 6.1. Molecular structure of zinc phthalocyanine, ZnPc.

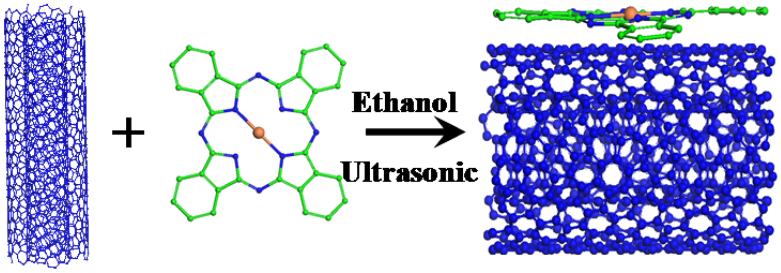

Schematic 6.2. Functionalized the CNTs with Zinc Phthlocyanine

6.2.2 Synthesis of ZnPc/CNTs

Pristine CNTs (20 mg) were sonicated in 50 mL ethanol in the presence of 0.6 mg mL^{-1} ZnPc for 2 h, and the dispersions were stirred overnight before filtered and dried in vacuum oven at 71 ^{o}C (Schematic 6.2). The product was noted as ZnPc/CNT-n.

The ZnPc/CNTs solutions were deposited on transparent conducting glass substrates F-doped SnO_2 coated glass, FTO (R_Ω 8 Ω cm^{-1}, Pilkington glass (USA)). FTO conductive glasses with dimension of 20×25×2 mm (width/length/thickness) were ultrasonically cleaned for 15 minutes in acetone, ethanol and acetone sequentially. After rinsing, the FTO glasses were blow-dried by nitrogen. ZnPc/CNTs (10 mg) were dispersed in 5 mL of ethanol nafion mixture (Ethanol: Nafion 9:1) to form a homogeneous ink solutions, then were deposited onto the conductive side of the FTO glasses according to the following procedure: (1) pipetting 100 µL of the CNT solution into the FTO glass and drying for 20 min, (2) repeating this process 5 times

to get a desirable thickness. The loading of the catalysts were kept constant for all the samples of 1 mg cm^{-2}.

6.2.3 Characterization

Thermo gravimetric (Q5000, USA) analysis (TGA) was performed to investigate the loading of ZnPc under air flow upon equilibration at 100 °C for 15 min, followed by a ramp of 10 °C min^{-1} up to 800°C. The FT-IR spectra were recorded from KBr disks using a Perkin-Elmer Spectrum GX FT-IR/Raman Spectrometer with a spectral resolution of 4 cm^{-1}. The UV-vis analysis absorbance was measured by UV-visible Spectrophotometer (JASCO, V-670).The X-ray photoelectron spectroscopy (XPS) measurements were carried out on a XPS apparatus (Kratos AXIS Ultra DLD) with a pass energy of 40 eV, the XP spectra are referenced to the Si 2p feature of the substrates at a binding energy of 99.8 eV. Distributions of ZnPc on CNT-1, CNT-3 and CNT-7 were further studied high angle annular dark field STEM and elemental mapping on Titan G2 60-300 at 80 kV.

The PEC behavior of different samples was tested according to the following procedure[23]. An aqueous solution of KOH (1 M) was used as electrolyte for all the photocurrent measurements. The schematic structure of photo-electrochemical cell is presented in Schematic 6.3. The photocurrent measurements were carried out in a three electrode cell with Pt as counter electrode and Ag/AgCl as the reference electrode. The deposited films were employed as the working electrode. The photocurrent value of different samples was obtained by subtracting the dark current from the light current at a given potential. Therefore, the synthesized photoanodes were individually exposed to a 500 W xenon lamp based solar simulator (ABET Technologies Sun 2000). The light intensity was calibrated and the measured light

intensity was 100 mW cm^{-2}. The photo voltage of the open circuit was measured in two separate modes: light-off (dark) and light-on (bright).

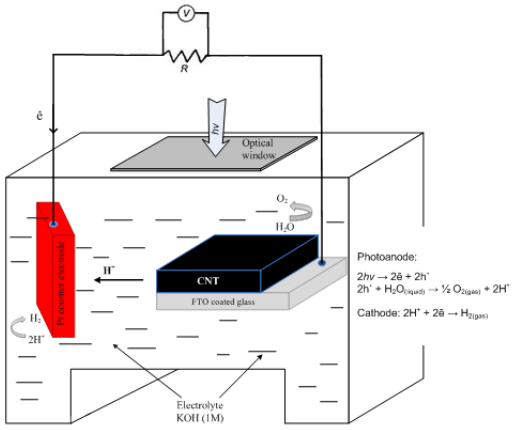

Schematic 6.3. Structure of the photo-electrochemical cell.

6.3 Results and discussion

6.3.1 Chracterization of ZnPc/CNTs

CNTs used in this study were obtained commercially and were clarified into seven groups, depending on the number of walls. Before use, CNTs were purified to remove the metallic catalysts used in the synthesis of CNTs, using conventional acid treatment methods[21]. Figure 3.1-3.4 is the TEM micrographs and Raman spectra of pristine CNTs after the purification treatment. The average diameter and number of walls were calculated based on the TEM images and summarized in chapter 3 [21]. Briefely, CNT-1 is mainly composed of SWNTs (~79%) with average outer diameter (OD) of ~1.97 nm. CNT-2 consists of 65% DWNTs and 23% triple-walled CNTs (TWNTs) with average OD of 3.3 nm. CNT-3 is mainly TWNTs (51 %) and DWNTs (25%) with average OD of 3.8 nm. CNT-4 is similar with that of CNT-3 with 57% TWNTs and average OD of 4.0 nm. CNT-5 consists of 3-10 walls with average number of walls of seven and OD in the range of 4-6 nm. CNT-6 and CNT-7 are

typical MWNTs with number of walls over 12 and 20, and OD of 13.9 nm and 35.2 nm, respectively. The Raman spectra show that the intensities of the *G* band (~1590 cm^{-1}) and *G'* band (~2700 cm^{-1}) decrease with an increasing number of walls and OD. The ratio of the intensity of the *D* band near 1300 cm^{-1} to the *G* band around 1590 cm^{-1}, I_D/I_G is 0.155, 0.51, 0.76, 0.94, 1.35, 2.50 and 2.86 for CNT-1; CNT-2, CNT-3, CNT-4, CNT-5, CNT-6 and CNT-7, respectively. The pristine CNTs are further characterized by X-ray photoelectron spectroscopy (XPS) (Fig. 6.1), and only C and O were detected from the pristine CNTs. No metal peaks were observed indicating that there is only trace amount of metal impurities in CNTs. This is consistent with the ICP results (Table 3.2), which demonstrate that there are 0.44%, 1.38%, 1.1%, 0.77%, 0.66%, 0.42% and 0.95% metal impurities in CNT-1 to CNT-7 respectively. The amount of defects such as C-O, C=O and C-OO were calculated through decovolution of the C 1s peaks, and the results in show that the defects (C-O, C=O and C-OO) in the CNTs varies with CNTs and the amounts are in the range of 4.17 to 8.33 at% (which means 100 C atoms, there are 4.17-8.33 C atoms are C-O, C=O and C-OO, Fig. 6.2 and Table 6.1), consistent with the results reported[24].

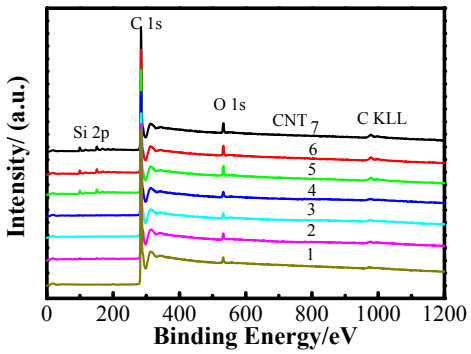

Figure 6.1. XPS survey spectra for pristine CNTs.

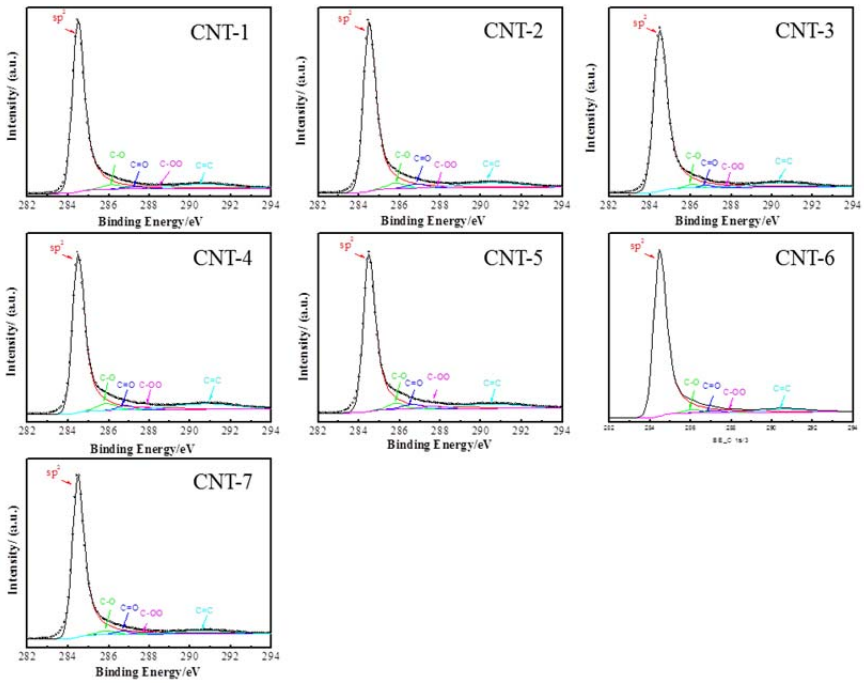

Figure 6.2. XPS core-level spectra of C 1s of different CNTs.

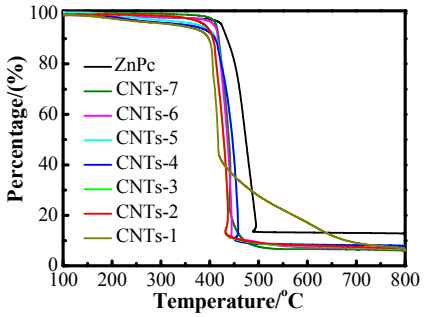

Figure 6.3. TG analysis of ZnPc and ZnPc/CNTs.

Table 6.1. XPS peaks position and the percentage of surface concentration of C, O, Zn and N.

Materials		CNT-1	CNT-2	CNT-3	CNT-4	CNT-5	CNT-6	CNT-7	ZnPc
Defects (XPS)		6.16	4.17	8.16	8.33	7.91	4.77	6.79	-
Zn2p	3/2	1021. 6	1022.1	1021.9	1021.9	1022.1	1022.1	1022.0	1022.5
	1/2	1044.6	1045.1	1045.0	1045.0	1045.2	1045.2	1045.0	1045.5
N 1s		398.7	398.7	398.7	398.7	398.7	398.7	398.7	399.3
		-	-	-	-	-	-	-	401.4
N%		4.35	6.17	5.86	5.85	5.98	4.50	4.58	-
C%		93.26	90.80	91.73	92.01	90.08	92.43	92.42	-
O%		1.64	2.15	1.50	1.27	2.97	2.33	2.22	-
Zn%		0.75	0.88	0.91	0.87	0.97	0.74	0.78	-

CNTs were functionalized with dyes, ZnPc, by simply dispersing the CNTs and dyes in ethanol with the assistance of untrsonication. The loading of dye assembled on CNTs was confirmed by TGA (Fig. 6.3). Figure 6.4 dispalys the elemental mapping using EDS coupled with STEM on ZnPc-functionalized CNT-1, CNT-3 and CNT-7. Combining with EDS spectra obtained from mapping area (Fig. 6.5), the results clearly demonstrate that Zn and N are homogenously distributed on the CNTs surface, indicating that ZnPc is successfully supported onto the CNTs surface, forming ZnPc/CNTs.[25]

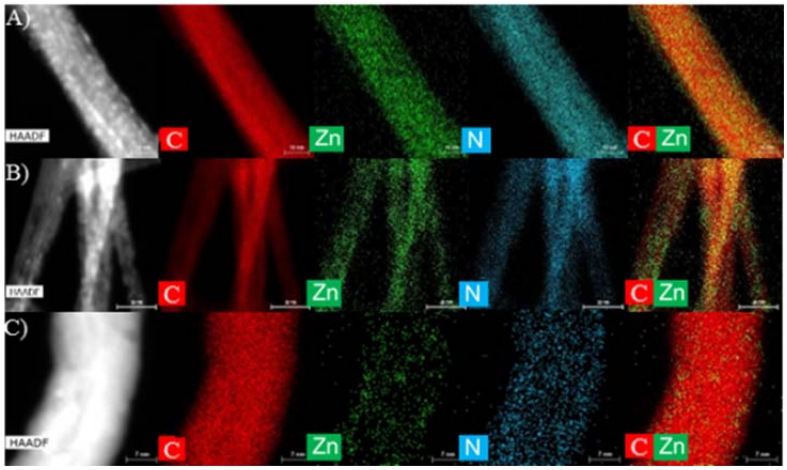

Figure 6.4. The HAADF-STEM-EDS mapping images of A) ZnPc/CNT-1 (Bar = 10 nm); B) ZnPc/CNT-3 (Bar =20 nm); and C) ZnPc/CNT-7 (Bar = 7 nm).

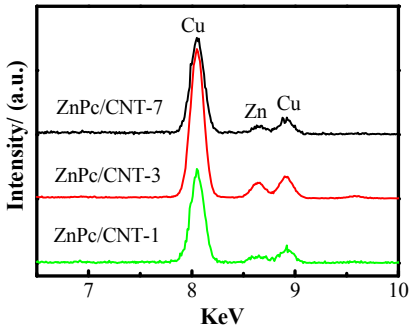

Figure 6.5. The EDS spectra obtained from HAADF-STEM-EDS mapping images of ZnPc/CNT-1, ZnPc/CNT-3 and ZnPc/CNT-7. The Cu is from the grid.

The interaction between dye and CNTs was further studied by FTIR and XPS. Fig. 6.6A is the FTIR spectra of ZnPc/CNTs. For pure ZnPc, intense IR active bands were observed between 400 and 1650 cm^{-1}, which are consistent with the results reported[26, 27]. In the case of ZnPc/CNTs, corresponding peaks from ZnPc were also detected, indicating that CNTs were functionalized by ZnPc. The IR spectra results show that the intensity ratio at 725 cm^{-1} and 1384 cm^{-1} increase significantly from 0.9 on ZnPc to 1.2-2.4 for ZnPc/CNTs, revealing the increase of the out-of-plane bending for C-H and C-N-C bonds and/or the reduction of Zn-N, C-N stretching and C-H and C-N-C in-plane bending,[28] demonstrated that ZnPc is immobilized onto the CNT carbon plane through π-π stacking.[29]

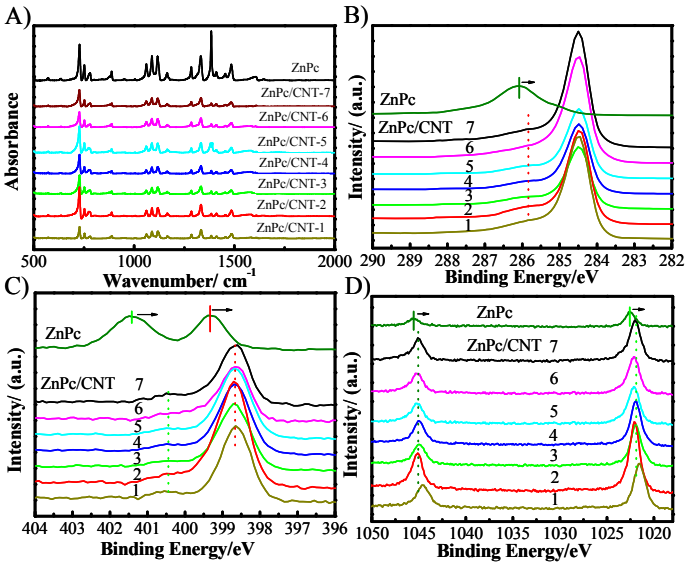

Figure 6.6. A) FTIR spectra of the ZnPc and ZnPc functionalized CNTs, and XPS core level for ZnPc functionalized CNTs and ZnPc B) C 1s; C) N 1s; D) Zn 2p.

Figure 6.6 B-D is the typical XPS core level spectra of the C 1s, N 1s and the Zn 2p peaks for ZnPc and ZnPc/CNTs. The N 1s peak of ZnPc is compose of two small peaks around 401.4 and 399.3 eV, corresponding to protonated and deprotonated nitrogen respectively. After functionalized onto the CNTs, the peaks for N 1s are

negatively shift by more than 1 eV to around 398.7 eV, and only one peak was observed, which indicates a substantial chemical change and the occurrence of charge transfer from CNT to the N species of ZnPc. Similar shifts of the Zn 2p spectrum are also observed from pure ZnPc and its functionalized CNTs. In the case of pure ZnPc, the Zn 2p3/2 and Zn 2p1/2 were obtained at 1022.5 and 1045.5 eV respectively. However, the peaks of Zn 2p3/2 and Zn 2p1/2 are significantly negatively shift by 0.5-0.9 eV to around 1022 eV and 1045 eV respectively after the ZnPc was functionalized onto the CNTs surface. The negatively shift of N 1s and Zn 2p indicates the donation of electron from CNTs to the ZnPc, indicating that ZnPc acts as a p-type dopant to positively charge carbon atoms in the nanotube carbon plane.

6.3.2 Photo-elctrochemical properties of ZnPc/CNTs

Figure 6.7 shows the UV-visible diffuse reflectance spectra of pristine CNTs and the ZnPc/CNTs. The absorbance of pristine CNTs is very low with an absorption threshold around 200-350 nm in the ultraviolet (UV) region of solar radiation (Fig. 6.7 A). The absorbance of ZnPc is around 200-250 nm and 650-700 nm (Fig. 6.7 B), which is consistent with the results reported[30]. In the case of ZnPc/CNTs, absorbance range increases significantly to 200-350 nm with substantially increased intensity. Absorption peaks around 665 nm were also observed for ZnPc/CNTs which corresponds to the long wavelength absorption band of ZnPc[30]. The intensity of absorbance of ZnPc/CNTs shows an interesting volcano curves as a function of number of walls of CNTs with the highest absorbance observed on ZnPc-functionalized CNTs with three walls, ZnPc/CNT-4 (Fig. 6.7 C).

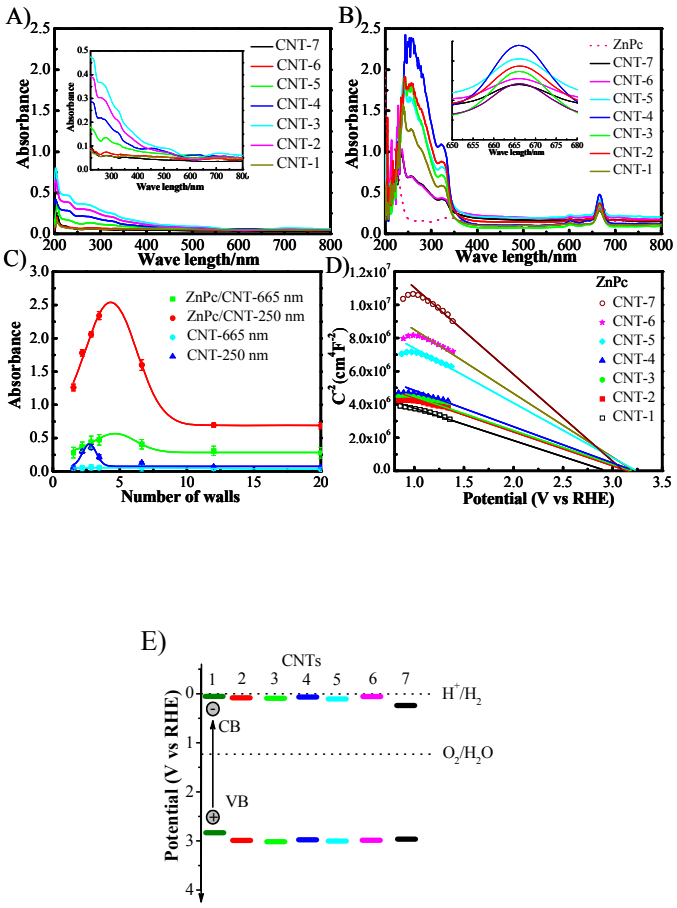

Figure 6.7. The UV-vis spectra of A) pristine CNTs; B) ZnPc/CNTs; and C) the absorbance of pristine CNTs and ZnPc/CNTs at 250 nm and 665 nm; D) Mott-Schottky plots for ZnPc/CNTs according to impedance measurements, the flat-band potentials are obtained from the intercepts of the extrapolated lines; and E) Band positions of ZnPc/CNTs according to the band gaps and flat-band potentials obtained from c. CB, conduction band; VB, valence band.

The band gaps were calculated from the UV-visible spectra, based on solid band theory following the equation $(\alpha h\nu)=A(h\nu-E_g)^m$.[31] The band gap is 2.07 eV, close to the reported number of 1.97 eV[32]. The band gaps of ZnPc/CNTs are in the range of 2.5 to 3.1 eV (Fig. 6.8), significantly larger than that of ZnPc dye. The flat-band potentials were obtained from the intercepts of the extrapolated lines from the Mott-Schottky plots (Fig. 6.7 D) and the negative slopes of Mott-Schottky plots indicate that ZnPc/CNTs are p-type semiconductor. The flat-band potentials of ZnPc/CNTs

were calculated in the range of 2.8 to 3.3 V, which lie above the oxygen-evolution potential, 1.23 V vs RHE (Fig. 6.7 E). Thus the high occupied molecule orbit (HOMO) of ZnPc/CNTs is in the range of 0.0 to 0.4 V, located close to the hydrogen-evolution potential, 0.0 V vs RHE. And the low unoccupied molecule orbit (HOMO) lies above the oxygen evolution potential. The position of the LUMO and HOMO of ZnPc/CNTs implies that photo water splitting can take place on ZnPc/CNTs with the additional electrochemical polarization potential.

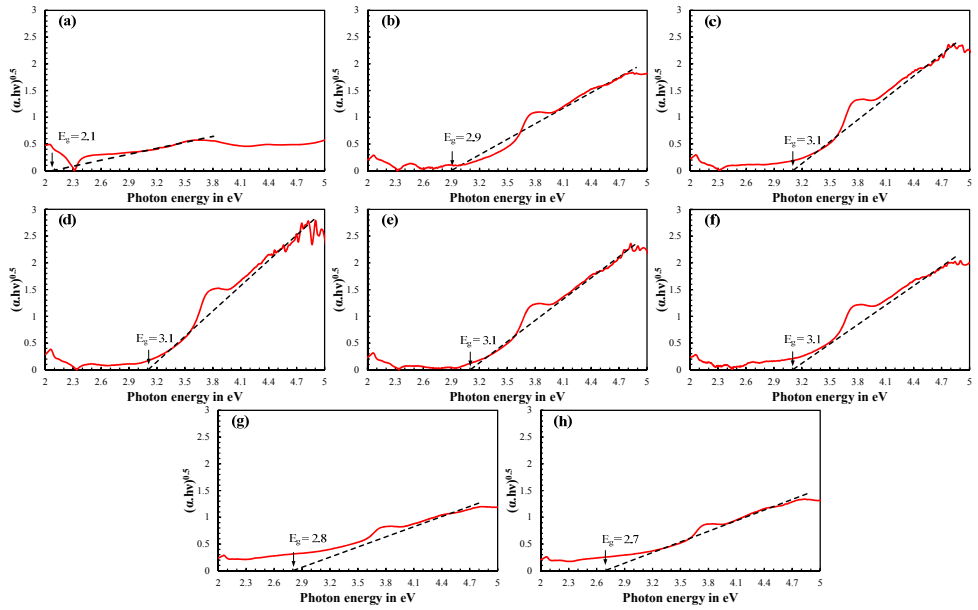

Figure 6.8. Band gap (Eg) calculation for ZnPc and ZnPc/CNTs, a) ZnPc, b) ZnPc/CNT-1, c) ZnPc/CNT-2, d) ZnPc/CNT-3, e) ZnPc/CNT-4, f) ZnPc/CNT-5, g) ZnPc/CNT-6, h) ZnPc/CNT-7.

LSV were conducted to study pristine CNTs and ZnPc/CNTs for PEC water oxidation in 1 M KOH solution under dark and illumination. In the case of pristine CNTs, the photocurrent densities are very low, less than 0.005 mA cm^{-2} (Fig. 6.9 A), indicating that pristine CNTs alone are not PEC catalysts for water oxidation. Functionalized CNTs with ZnPc show significantly high photocurrent densities especially for the water oxidation reaction on ZnPc-fuctionalized CNT-2, CNT-3, CNT-4 and CNT-5. For example, the photocurrent density of ZnPc/CNT-4 at 1.2 V is 0.32 mA cm^{-2},

which is about 3.6 times of that measured on ZnPc/CNT-1 (0.09 mA cm^{-2}) and an order of magnitude higher than on ZnPc/CNT-7 (0.02 mA cm^{-2}). The onset potential for photo-electrochemical water oxidation on ZnPc/CNT-2, ZnPc/CNT-3, ZnPc/CNT-4 and ZnPc/CNT-5 is ~1.03 V versus RHE, ~0.16 V lower than 1.18 V measured on ZnPc/CNT-6, ZnPc/CNT-7, and also ~ 0.21 V lower than the thermodynamic electrochemical potential of 1.23 V versus RHE for electrochemical water oxidation. The photocurrent densities significantly increase with the increase of applied potential, and most importantly the photocurrent densities of ZnPc/CNTs also show characteristic volcano curves as a function of number of walls ((Fig. 6.9 C)), identical to the absorbance curve. The results clearly indicate that the PEC activity of dye-functionalized CNTs with number of 2-7 walls for water oxidation reaction is significantly higher than dye-functionalized SWNTs and MWNTs. In the case of CNT-1, mainly SWNTs, the onset potential is 1.05 V, 0.13 V lower than that of ZnPc/CNT-6, ZnPc/CNT-7 which is likely because of the semiconductors properties of SWNTs which lead to preferential band gap[18, 33] and/or the small amount of DWNTs in this sample.

The PEC activities of the ZnPc/CNTs are further demonstrated by the on-off curves conducted at potential of 1.2 V (Fig. 6.9 E). The difference of on-off current density is the photo-current density of ZnPc/CNTs and represents the PEC activity of ZnPc/CNTs. The photo-current densities of ZnPc functionalized CNT-2, CNT-3 and CNT-4 are around 0.22, 0.22 and 0.28 mA cm^{-2} respectively, which is significantly higher than that of ZnPc functionalized CNT-1, CNT-6 and CNT-7, with a photocurrent density of 0.11, 0.07 and 0.05 mA cm^{-2} respectively, consistent with the volcano shape activity obtained from LSV results.

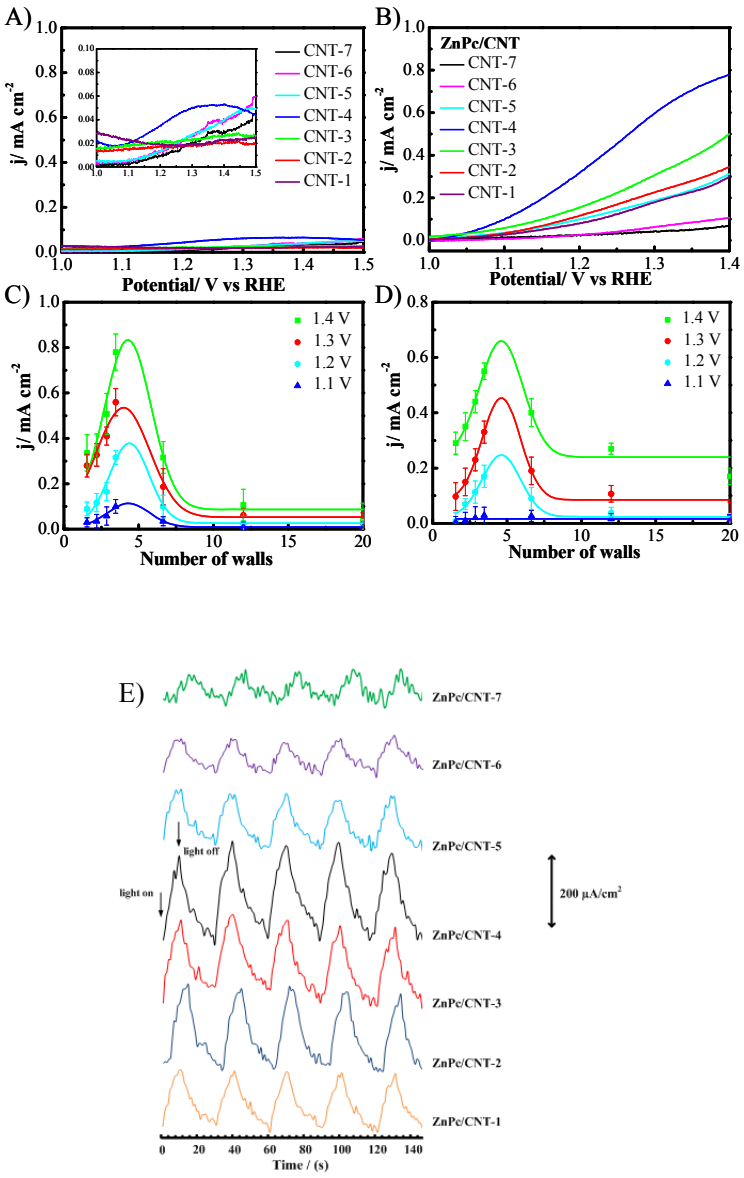

Figure 6.9. Photo-current density of A) pristine CNTs and B) ZnPc functionalized CNTs, C) the current density of ZnPc/CNTs vs number of walls at different potential D) photocurrent density at different voltages of CoPc/CNTs; E) the on-off curves of ZnPc/CNTs. Catalysts loading is 1 mg cm^{-2}.

6.3.3 Electron separation through tunneling effect

ZnPc can interact with the carbon plane of the CNTs through π-π interaction[34, 35], and act as a p-type dopant to the electron rich CNTs, however, the XPS results indicate the interactions of the ZnPc with different types of CNTs are similar (Table 6.1).

CNTs have been demonstrated to improve light harvesting capabilities (excitation generation) and/or to facilitate charge transport due to the excellent electrical conductivity of CNTs, hence reducing the chance of electron-hole recombination[36-38]. It is intriguing that the absorbance of UV-vis spectra and photo electrochemical activity of water oxidation exhibits remarkably identical volcano dependence with the number of walls. This volcano-type activity is not related with the loading of ZnPc on the CNTs surface due to the loadings of ZnPc are similar on different CNTs. The band gap of ZnPc/CNT-7 (2.7 eV) is 0.4 eV smaller than that of ZnPc/CNT-4 (3.1 eV), and the band-edge position for conduction band is similar, however, the PEC water oxidation ability of ZnPc/CNT-7 is far less than that of ZnPc/CNT-4. Besides, the ZnPc/CNT-1 exhibit preferable band gap and edge position for photo-electrochemical water splitting compared with ZnPc/CNT-4, while, the photo-activity of ZnPc/CNT-1 is only about one third of ZnPc/CNT-4. These results indicate that volcano-type activity is not related to the differences of band gaps of ZnPc/CNTs. Moreover, the difference does not result from the defects of the CNTs nor the metal impurities in the CNTs. Shota et al. studied the energy conversion efficiency of ZnPc attached on the caps of SWNT using density functional theory (DFT), shows that the charge separation mechanism observed at the interface is not changed qualitatively by the presence and absence of metallic cluster at the open end of (6,6) CNT.[39] In our case, the defects in CNT-2 is about 4.17 at%, similar with that of CNT-7 with a number of 4.77 at%, and the trace metal content of CNT-7 is 0.95%, close to 1.38% of CNT-2, while the photocurrent density of ZnPc/CNT-2 is about 4 times of ZnPc/CNT-6.

In our dye-functionalized CNTs system, the PEC water oxidation starts with the activation of dye (light-harvesting antennae system) by absorbing photons creating holes and photo-activated electrons. Next the electrons inject into the CNTs (charge-

separating units), and the holes accept the electron from OH^- (electron donor) to create O_2 provided the electrons and holes are not recombined. The kinetic competition between electron-hole recombination and water oxidation is a key consideration for the development of efficient photocatalysts for solar driven water splitting[40-43]. Hence it is rational to propose that the significant difference of the photocurrent density for water oxidation results from the charge separation pathway of different types of CNTs.

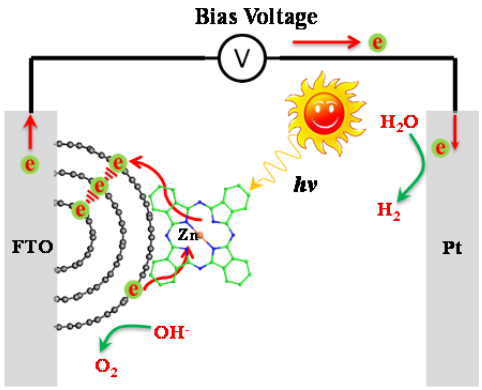

Schematic 6.4. Schematic of dye functionalized CNTs for PEC water oxidation via electron tunneling effect.

The electric properties of SWNTs are sensitive to the size and chirality of the tubes. In theory, nearly one-third of the SWNTs are metallic or semi-metallic and the other two-thirds are semiconducting[44]. Due to the semiconductor properties of SWNTs in CNT-1, the electrons can be stored in SWNTs leave the hole with enough life time for water oxidation[45] and the band gap and band-edge position of ZnPc/CNT-1 is proved more suitable for PEC water splitting[18], hence creating enhanced photocurrent for ZnPc/CNT-1 compared with typical MWNTs with number of walls over 10. Unlike SWNTs, the presence of inner walls could increase the number of conducting channels and create the possibility for electrons and holes separation. Here, the photo activated electron injection and the applied dc bias provide the driving force for the

electron transfer between the outer wall and inner tube through electron tunneling when the distance is small enough. This is consistent with that all the dye functionalized carbon nanotube requiring additional voltage to achieve high photocurrent generation. Hence the photo-generated electrons are entrapped in the inner tubes which effectively improve the electron-hole separation to generate free charge carriers and avoid electron-hole recombination. Then allows the electron transferring through the inner tubes endows the holes with enough lifetimes to combine with OH^- for oxygen generation (Schematic 6.4). This hypothesis explains why double/triple-walled CNT-2, CNT-3 and CNT-4 are more effective for photo oxidation than single-walled CNT-1. As the number of walls/layers increases, the driven force created by photo activated electron injection and dc bias for the tunneling effect between the outer wall and inner tubes will diminish due to the distribution of the driving force across each layer, hence higher onset potential and lower photo-current densities are observed. It is noticeable that the number of inner tubes in the range of 2-7 are effective for the electron-hole separation through the tunneling effect due to the distance between the outer walls and inner tube for these CNTs is in the range of effective tunneling effect distance (order of 10 angstroms)[46, 47]. Thus, electron-hole separation could be less favorable for large diameter MWNTs because the number of walls/layers increases would significantly reduce the tunneling effect. These explain why typical large diameter MWNTs exhibit significantly lower activity for photo-electrochemical water splitting.

6.4 Conclusion

In this paper, ZnPc functionalized CNTs were developed through noncovalent functionalization and the results demonstrate that ZnPc were successfully loaded onto the surface of the CNTs with loading around 60%. The dye functionalized CNTs

show significantly enhanced UV-vis absorbance and enhanced photo-current density for water oxidation in 1 KOH solution. The photo-currents and the UV-vis absorbance show a universal volcano shape as function of number of walls. The results demonstrate that the volcano shapes of the dye functionalized CNTs is not because of the defects or impurities in CNTs or the band gap of the CNTs, revealing the favorable electron separation ability of CNTs with 2-7 inner tubes through tunneling effects, which alleviate the hole-electron recombination. Our results open new opportunity to toward designing flexible and robust catalysts for developing high efficient photocatalyts by incorporating CNTs composed of between 2-7 concentric tubes with semiconductors or dyes.

Acknowledgement

The author would like to thanks Amir Memar for testing the photo-electrochemical activity and the UV-vis spectra.

References

1. M. Gratzel, *Nature*, 2001, 414, 338-344.
2. A. Hagfeldt and M. Grätzel, *Accounts of Chemical Research*, 2000, 33, 269-277.
3. A. Hagfeldt, G. Boschloo, L. Sun, L. Kloo and H. Pettersson, *Chemical Reviews*, 2010, 110, 6595-6663.
4. D. G. Nocera, *Accounts of Chemical Research*, 2012, 45, 767-776.
5. *Nat Photon*, 2012, 6, 136-137.
6. B. O'Regan and M. Gratzel, *Nature*, 1991, 353, 737-740.
7. J. T. Park, W. S. Chi, S. J. Kim, D. Lee and J. H. Kim, *Sci. Rep.*, 2014, 4.
8. F. Sauvage, F. Di Fonzo, A. Li Bassi, C. S. Casari, V. Russo, G. Divitini, C. Ducati, C. E. Bottani, P. Comte and M. Graetzel, *Nano Letters*, 2010, 10, 2562-2567.
9. P. Tiwana, P. Docampo, M. B. Johnston, H. J. Snaith and L. M. Herz, *Acs Nano*, 2011, 5, 5158-5166.
10. H. Niu, S. Zhang, Q. Ma, S. Qin, L. Wan, J. Xu and S. Miao, *RSC Advances*, 2013, 3, 17228-17235.

11. M. Sethupathy, P. Pandey and P. Manisankar, *Journal of Applied Polymer Science*, 2014, 131, n/a-n/a.

12. H. J. Snaith and C. Ducati, *Nano Letters*, 2010, 10, 1259-1265.

13. A. Birkel, Y.-G. Lee, D. Koll, X. V. Meerbeek, S. Frank, M. J. Choi, Y. S. Kang, K. Char and W. Tremel, *Energy & Environmental Science*, 2012, 5, 5392-5400.

14. X. Zhang, Y. Liu and Z. Kang, *ACS Applied Materials & Interfaces*, 2014, 6, 4480-4489.

15. A. Omar, H. Abdullah, S. Shaari and M. R. Taha, *Journal of Materials Research*, 2013, 28, 1753-1760.

16. T. Hasobe, S. Fukuzumi and P. V. Kamat, *The Journal of Physical Chemistry B*, 2006, 110, 25477-25484.

17. Z. Li, S. A. Kulkarni, P. P. Boix, E. Shi, A. Cao, K. Fu, S. K. Batabyal, J. Zhang, Q. Xiong, L. H. Wong, N. Mathews and S. G. Mhaisalkar, *Acs Nano*, 2014, 8, 6797-6804.

18. N. Li, Y. Ma, B. Wang, Y. Huang, Y. Wu, X. Yang and Y. Chen, *Carbon*, 2011, 49, 5132-5141.

19. M. R. Hoffmann, S. T. Martin, W. Choi and D. W. Bahnemann, *Chemical Reviews*, 1995, 95, 69-96.

20. W. Wang, P. Serp, P. Kalck and J. L. Faria, *Journal of Molecular Catalysis A: Chemical*, 2005, 235, 194-199.

21. Y. Cheng, C. Xu, L. Jia, J. D. Gale, L. Zhang, C. Liu, P. K. Shen and S. P. Jiang, *Applied Catalysis B: Environmental*, 2015, 163, 96-104.

22. Y. Lin, S. Zhou, S. W. Sheehan and D. Wang, *Journal of the American Chemical Society*, 2011, 133, 2398-2401.

23. A. Memar, W. R. W. Daud, S. Hosseini, E. Eftekhari and L. J. Minggu, *Solar Energy*, 2010, 84, 1538-1544.

24. V. Datsyuk, M. Kalyva, K. Papagelis, J. Parthenios, D. Tasis, A. Siokou, I. Kallitsis and C. Galiotis, *Carbon*, 2008, 46, 833-840.

25. G. Bottari, G. de la Torre, D. M. Guldi and T. Torres, *Chemical Reviews*, 2010, 110, 6768-6816.

26. D. R. Tackley, G. Dent and W. Ewen Smith, *Physical Chemistry Chemical Physics*, 2000, 2, 3949-3955.

27. C. Murray, N. Dozova, J. G. McCaffrey, S. FitzGerald, N. Shafizadeh and C. Crepin, *Physical Chemistry Chemical Physics*, 2010, 12, 10406-10422.

28. G. S. S. Saini, S. Singh, S. Kaur, R. Kumar, V. Sathe and S. K. Tripathi, *Journal of Physics-Condensed Matter*, 2009, 21.

29. J. D. Correa and W. Orellana, *Physical Review B*, 2012, 86, 125417.

30. A. Ogunsipe and T. Nyokong, *Journal of Molecular Structure*, 2004, 689, 89-97.

31. J. Tauc, R. Grigorovici and A. Vancu, *physica status solidi (b)*, 1966, 15, 627-637.

32. S. Senthilarasu, S. Velumani, R. Sathyamoorthy, A. Subbarayan, J. A. Ascencio, G. Canizal, P. J. Sebastian, J. A. Chavez and R. Perez, *Appl Phys A*, 2003, 77, 383-389.

33. M. Gong, T. A. Shastry, Y. Xie, M. Bernardi, D. Jasion, K. A. Luck, T. J. Marks, J. C. Grossman, S. Ren and M. C. Hersam, *Nano Letters*, 2014, 14, 5308-5314.

34. C. Ehli, C. Oelsner, D. M. Guldi, A. Mateo-Alonso, M. Prato, C. Schmidt, C. Backes, F. Hauke and A. Hirsch, *Nature chemistry*, 2009, 1, 243-249.

35. F. Würthner, *Chemical communications*, 2004, 1564-1579.

36. A. C. Dillon, *Chemical Reviews*, 2010, 110, 6856-6872.

37. K. Woan, G. Pyrgiotakis and W. Sigmund, *Advanced Materials*, 2009, 21, 2233-2239.

38. G. D. M. R. Dabera, K. D. G. I. Jayawardena, M. R. R. Prabhath, I. Yahya, Y. Y. Tan, N. A. Nismy, H. Shiozawa, M. Sauer, G. Ruiz-Soria, P. Ayala, V. Stolojan, A. A. D. T. Adikaari, P. D. Jarowski, T. Pichler and S. R. P. Silva, *Acs Nano*, 2012, 7, 556-565.

39. S. Ono, R. Kuwahara and K. Ohno, *J. Appl. Phys.*, 2014, 116, 054305.

40. F. Le Formal, S. R. Pendlebury, M. Cornuz, S. D. Tilley, M. Grätzel and J. R. Durrant, *Journal of the American Chemical Society*, 2014, 136, 2564-2574.

41. F. M. Pesci, A. J. Cowan, B. D. Alexander, J. R. Durrant and D. R. Klug, *The Journal of Physical Chemistry Letters*, 2011, 2, 1900-1903.

42. M. Barroso, S. R. Pendlebury, A. J. Cowan and J. R. Durrant, *Chemical Science*, 2013, 4, 2724-2734.

43. A. J. Cowan, C. J. Barnett, S. R. Pendlebury, M. Barroso, K. Sivula, M. Grätzel, J. R. Durrant and D. R. Klug, *Journal of the American Chemical Society*, 2011, 133, 10134-10140.

44. R. Saito, M. Fujita, G. Dresselhaus and M. S. Dresselhaus, *Appl. Phys. Lett.*, 1992, 60, 2204-2206.

45. A. Kongkanand and P. V. Kamat, *Acs Nano*, 2007, 1, 13-21.

46. C. Li, E. T. Thostenson and T.-W. Chou, *Applied Physics Letters*, 2007, 91, -.

47. N. Hu, Y. Karube, C. Yan, Z. Masuda and H. Fukunaga, *Acta Materialia*, 2008, 56, 2929-2936.

Chapter 7: One-Step Synthesized Metal-Carbon Nanotubes Network Hybrids as Highly Efficient Catalysts for Oxygen Evolution Reaction of Water Splitting

7.1 Introduction

Hydrogen production from water splitting driven by renewable energy is an attractive environmentally friendly pathway for renewable energy storage. However, the efficiency of the photo- or electro-chemical water splitting is greatly constraint by the high overpotentials of OER.[1] The state-of-the-art OER catalysts such as precious metals based RuO_2, IrO_2 and their combinations are not economically viable due to their high price and scarcity.[2-6] There are extensive research activities on the non-precious metal oxide based materials as electrocatalysts, including nickel, iron and cobalt based oxides/hydroxides,[3, 7-11] spinels,[12] and perovskites.[13-14] The results indicate that high specific surface area is beneficial for the electrochemical activity of OER catalysts. There are various synthesis methods to achieve nanoscaled OER catalysts with high surface area, including electrodeposition,[15-17] sol-gel,[18] solution cast,[11] and hydrothermal precipitation.[19] Metal oxide thin films are also attractive due to the high surface area and high mobility of electrons through the nanometer scale thin-film to reach the supported electrode.[9, 20-21] However, large scale fabrication of thin and crack-free film electrodes within a few nanometers is a challenging issue for their practical application.

Another strategy is to incorporate the oxides with high surface area and conductive carbon materials. The carbon material not only significantly increases the conductivity of the oxides or hydroxides based electrocatalysts, but also can enhances the stability of the nanostructured catalysts.[22] CNTs and graphene have attracted extensive attention as catalyst supports for OER due to high mechanical strength, excellent electrical conductivities, and superior chemical stability.[23] Wu et al.[24] prepared Co_2O_3 particles supported on SWNTs and yielded a current density of 66 A g^{-1} at η = 0.37 V in 1 M KOH solution, significantly better than unsupported Co_2O_3 nanocrystals. Cobalt oxide nanoparticles (NPs) supported on oxidized multi-walled CNTs was reported to exhibit an onset potential of 1.51 V vs. RHE and a current density of 10 mA cm^{-2} (40 A g^{-1}) at η = 0.39 V in 0.1 M KOH.[19] Co_3O_4 nanocrystals grown on reduced graphene oxide (Co_3O_4/N-rmGO) exhibits a current density of 10 mA cm^{-2} (10 A g^{-1}) at overpotential of ~0.31 V in 1 M KOH solution with catalyst 1 mg cm^{-2} loaded onto Ni foam[25]. Manganese oxide supported onto CNTs show high activity and stability for water splitting in neutral conditions[26]. We demonstrated most recently that graphene supported MnO_2 nanowires have a much higher electrocatalytic activity for the OER in alkaline solutions than that of Pt/C catalysts.[27] However, preparation of CNT or graphene supported metal catalysts generally involves multi-synthesis steps and is difficulty to control and scale up.

CNTs are demonstrated the road of nanomaterials towards industry due to the widely applications.[28-29] Chemical vapor deposition and arc-discharge are widely applied to grow high quality CNTs with commercially viable quantities on metal catalysts, such as such as Ni, Fe, Co, Pd, Ag, Pt, etc. or mixtures of Co, Fe and Ni.[28, 30-31] For example, as early as in 1998, we demonstrated the synthesis of high quality SWNTs with a yield of tens of milligrams per batch using a floating catalysts CVD method.[32]

Industrial-scale production of SWNTs is also possible using layered double hydroxides as catalysts.[33] The CNTs produced are usually involve multi physical or chemical purification steps due to the CNTs inevitably contain carbonaceous impurities (e.g. amorphous carbon, graphite and carbon NPs) and catalyst particles[28]. Hence, it would be much more commercially viable to synthesize CNTs-metal hybrids in one-time for catalysts application. Here we fabricate metallic NPs embedded CNTs (M-CNTs) hybrid catalysts by directly growing CNTs on transition metal catalysts using arc-discharge and chemical vapor deposition (CVD) techniques. The results demonstrate that one-step synthesized hybrid catalysts have excellent activity and superior stability for OER in alkaline solutions.

7.2 Experimental

7.2.1 One-step synthesis of Metallic NPs embedded CNTs hybrids

The metal-CNT hybrids synthesized by arc-discharge and CVD techniques are denoted as M-CNT-Arc and M-CNT-CVD, respectively. The M-CNT-Arc samples were prepared by a hydrogen arc discharge method, the details are described previously.[34] Briefly, a mixture of 2.6 at.% Ni, 0.7 at.% Fe, 0.7 at.% Co, and graphite powder were used as the anode, hydrogen was used as the buffer gas, and electric arc was operated under a dc mode between the anode and a pure graphite cathode. After discharge for a few minutes, high yield web-like substance, which consists of CNTs and metallic NPs, were collected between the cathode and the upper chamber wall.

The M-CNT-CVD samples were prepared by a floating catalyst CVD method.[35] Typically, 99 wt.% ferrocene and 1 wt.% sulfur serve as the catalyst precursor and growth promoter, respectively. They were carried into the reaction zone by 2000 sccm

H_2 and 3 sccm CH_4 to grow SWNTs at 1100 ^oC, thin films of SWNTs with metallic NPs embedded were then collected at downstream of the quartz tube reactor.

Metallic NP catalysts embedded in the M-CNTs network hybrids were separated from the CNTs networks by calcinations of M-CNTs-Arc and M-CNTs-CVD at 500 ^oC for 1 h to decompose the carbon materials. The composition of metal catalysts was analyzed using ICP (ICP-OES PerkinElmer, Optima 7300 DV). In addition, the metal oxide-CNTs were also prepared by mechanically mixing $NiCoFeO_x$ and FeO_x with pure DWNTs and SWNTs, respectively, and the metal oxide loading (MO_x:CNTs ratio) was kept the same with that of corresponding M-CNTs hybrids. Briefly, 30 mg DWNTs were mixed with 35.4 mg $NiCoFeO_x$ to form $NiCoFeO_x$-DWNTs catalysts and 30 mg SWNTs were mixed 86 mg FeO_x to form FeO_x-SWNTs catalysts. The mixture were ground in mortar and dispersed in 50 mL ethanol solution, followed by mixing under ultrasonication treatment for 15 min. The mixed catalysts were filtered and dried at 70 ^oC in vacuum oven.

7.2.2 Characterization

Thermogravimetric analysis (TG, Q5000) was conducted to measure the content of carbon materials in the M-CNTs hybrids. Scanning electron microscopy with 5 keV and X-ray energy dispersion spectroscopy with 15 keV (SEM, NEON 40EsB) were applied to examine the microstructure and element distribution of M-CNTs hybrid. The morphology of the catalysts was characterized using a transmission electron microscope (TEM JEOL3000) operating at 200 kV. The structure was identified with X-ray diffractometer (XRD, Rigaku D/MAX RINT 2500) operated at 40 kV and 30 mA with Cu K_α in the range of 20-90^o. The Raman spectra were recorded in air at room temperature using a Perkin-Elmer GX FT-IR/Raman spectrometer with a back-

scattered configuration and equipped with an Nd: YAG laser at 1064 nm as its light source for Raman.

The electrochemical measurements were conducted in a three electrode cell with a Luggin capillary. The tip of the Luggin capillary was placed 3 mm beneath the working electrode. Generally, 4 mg of the as-prepared catalyst was ultrasonically mixed in a Nafion solution (4 mL, Ethanol:Nafion=9:1, Nafion 520, DuPont, USA) to form a homogeneous ink. 5 μL of the catalyst ink was pipetted onto the surface of a GCE and dried in air. The diameter of GCE was 5 mm. Without specification, the catalyst loading was 0.025 mg cm^{-2}. The ohmic potential drop between the working electrode and the tip of the Luggin capillary was estimated by measuring the electrode resistance at 30 kHz. A Pt wire and SCE were used as the counter and reference electrodes, respectively. All potentials in the present study were given versus RHE reference electrode ($E = E_{SCE} + 0.247 + 0.059pH$, here 0.247 V is the potential for SCE at 20 ^{o}C).

The ESA was estimated from the non-faradaic capacitive current associated with electrochemical double-layer capacitance of the catalytic surface from scan rate dependence of cyclic voltammograms (CVs).[36-37] The CVs were obtained at a scan rate of 10 mV s^{-1} in the potential range between -1.5-0.6 V (vs. SCE). The LSV was conducted at a scan rate of 1 mV s^{-1} in the potential range between 0-1 V (vs. SCE) and the system was stabilized after 10 cycles. IR-corrected Tafel plots were recorded at a scan rate of 1 mV s^{-1} with the electrode initially conditioned at potential of 0.65 V (vs. SCE) for 5 min before the scan.[38] The chronopotentiometry was conducted at different current density with catalysts loading of 0.1 mg cm^{-2}, using a Gamry Reference 3000 Potentiostat. Except the measurement of ESA, all the electrochemical tests were conducted on a rotating disk electrode with a rotation rate of 1600 rpm in

order to minimize the interference of the bubbles formed at the electrode surface. For comparison, a commercial Ru/C (20 wt% Ru on Vulcan carbon black from Premetek Co.) was also investigated for OER under identical conditions.

The effect of pH on the activity of M-CNTs hybrid catalysts was studied by LSV in KNO_3 solution using scanning rate of 10 mV s^{-1} under static conditions. pH of the solution was adjusted with the addition of 1 M KOH or H_2SO_4 (the ionic strength was kept at 1 M). The pH of the solution was not buffered to avoid influences from the specific adsorption of multivalent anions.[39]

7.3 Results and discussion

7.3.1. Characterization of M-CNTs hybrids

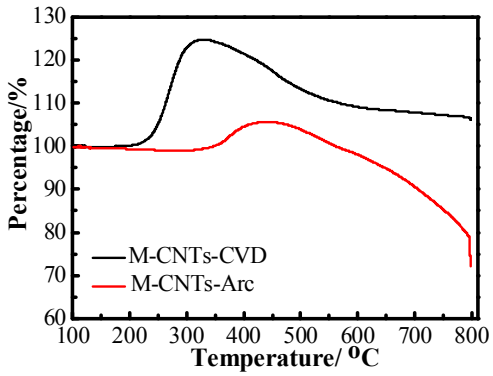

Figure 7.1. TGA curves of M-CNTs-Arc and M-CNTs-CVD hybrid catalysts.

Fig. 7.1 is the TGA curves of the as-synthesized M-CNTs-Arc and M-CNTs-CVD hybrids. The increasing of weight around 350-500 and 200-400 °C for M-CNTs-Arc and M-CNTs-CVD, respectively, is due to the oxidation of metal catalysts. Carbon

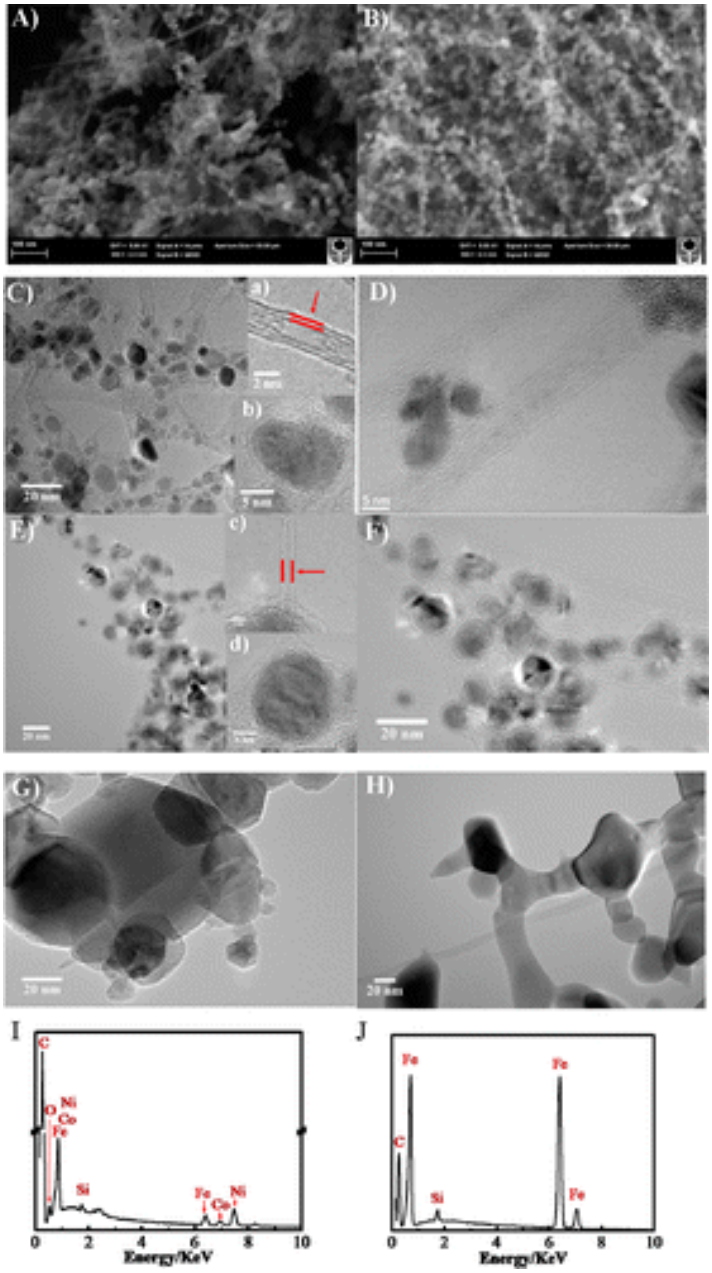

Figure 7.2. SEM images of A) M-CNTs-Arc; B) M-CNTs-CVD; and TEM images of C and D) M-CNTs-Arc, the inset a) is a DWCNT and b) is the metal core with graphite shell; E and F) M-CNTs-CVD, the inset c) is a SWCNT and d) is the metal core with graphite shell; G) $NiCo_{0.16}Fe_{0.34}O_x$; H) FeO_x. EDS spectra of I) M-CNTs-Arc; J) M-CNTs-CVD.

supports decompose at temperatures around 500-800 ^{o}C for M-CNTs-Arc and 350-650 ^{o}C for M-CNTs-CVD. The content of carbon supports was estimated to be 45.9±3% in M-CNTs-Arc and 25.8±2.8% in M-CNTs-CVD. This indicates that metal

catalyst embedded was 54.1 and 74.2% for M-CNTs-Arc and M-CNTs-CVD, respectively. The composition of metal catalysts separated from M-CNTs-Arc as analyzed by ICP consists of 35.7±0.2% Ni, 12.1±0.15% Fe and 5.7±0.12% Co. Thus the atomic ratio of Ni:Co:Fe of the metal catalysts in M-CNTs-Arc is 1:0.16:0.34, giving the catalyst formula $NiCo_{0.16}Fe_{0.34}$ in metallic form and $NiCo_{0.16}Fe_{0.34}O_x$ in oxidized form. In the case of M-CNTs-CVD, as expected, only Fe was detected, indicating the calcinated catalyst is FeO_x. The BET surface area of M-CNTs-Arc, M-CNTs-CVD, $NiCo_{0.16}Fe_{0.34}O_x$ and FeO_x is 166.5, 88.5, 38.3 and 36.8 $m^2\ g^{-1}$, respectively.

Fig. 7.2 is the SEM and HRTEM micrographs of metal NP embedded CNTs hybrid catalysts. The SEM images indicate that both M-CNTs-Arc and M-CNTs-CVD have a porous structure with metal particle connected by interconnected CNTs or CNTs bundles (Fig. 7.2 A and B). The metal-CNTs hybrids produced by arc-discharge and CVD show an interesting core-shell like structure, in which metal NPs core is encapsulated by a graphite shell and connected by CNTs network (Fig. 7.2 C-F). M-CNTs-Arc exhibits a metal core with an average size ~6.7 nm and a 1-3 nm thick graphite or amorphous carbon shell, which is connected mainly by DWNTs (see insets in Fig. 7.2 C and D). The diameter of DWNTs is ~3 nm. In the case of hybrid catalysts synthesized by CVD, M-CNTs-CVD, and the size of metal core is ~11.0 nm surrounded by a 1.5-2.5 nm thick graphite shell. The core-shell structures are mainly connected by SWNTs with size around 2 nm (insets in Fig.7.2 E and F), consistent with previous study.[40] The $NiCo_{0.16}Fe_{0.34}O_x$ and FeO_x metal oxide catalysts obtained from the M-CNTs hybrids were also characterized by TEM (Fig. 7.2 G and H). The average size of the $NiCo_{0.16}Fe_{0.34}O_x$ metal oxides and FeO_x catalysts is 38.2 nm and 34.8 nm, respectively. The large size of the metal catalysts is mainly due to the

sintering and aggregation of the metal catalysts during the decomposition treatment at 500°C. The EDS spectra confirm the existence of Ni, Fe and Co for M-CNTs-Arc (Fig. 7.2 I), while in the case of M-CNTs-CVD, the metal catalysts only contain Fe (Fig. 7.2 J).

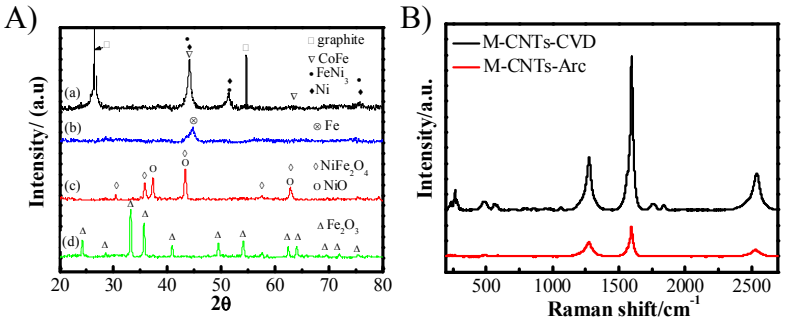

Figure 7.3. A) XRD patterns of M-CNTs-Arc (a), M-CNTs-CVD (b), $NiCo_{0.16}Fe_{0.34}O_x$ (c) and FeO_x (d); B) Raman spectra of M-CNTs-Arc and M-CNTs-CVD.

Fig. 7.3 A is the XRD spectra of M-CNTs-Arc and M-CNTs-CVD, as well as the separated metal oxide catalysts. For M-CNTs-Arc, the high intensity peak around 26.5° and 54.7° is from CNTs and graphite. The peaks around 44.1°, 51.3° can be attributed to $FeNi_3$, FeNi or CoFe alloy. In the case of M-CNTs-CVD, the peak at 44.6° is related to metallic Fe, consistent with the EDS analysis. This indicates that M-CNTs-CVD is composed of metallic Fe nanoparticle core. However, no peak around 26.5 ° was observed probably due to the lower content of graphite and CNTs in the sample. Fe_2O_3 was detected after calcination of M-CNTs-CVD hybrids. The XRD spectra also indicate $NiCo_{0.16}Fe_{0.34}O_x$ is mainly composed of NiO and $NiFe_2O_4$. No Co based oxides were detected probably due to the small amount of Co and the formation of alloy with Fe and Ni.

Fig. 7.3 B is the Raman spectra obtained from M-CNTs-Arc and M-CNTs-CVD. The peak around 1270 cm^{-1}, 1590 cm^{-1} and 2540 cm^{-1} are corresponding to the D band, G band and the second order G′ band of typical CNTs. The I_D/I_G is calculated as 1.01

and 0.57 for CNTs produced by arc-discharge and CVD, respectively. In the case of M-CNTs-CVD, the high intensity radial breathing mode (RBM) observed around 100-300 cm^{-1} is typical for SWNTs,[41-43] indicating that the encapsulated Fe particles are mainly collected by SWNTs, consistent with the HRTEM results. However, the largely depressed RBM and increased I_D/I_G ratio observed for M-CNTs-Arc indicates the presence of DWNTs[44] between the encapsulated $NiCo_{0.16}Fe_{0.34}$ in the case of M-CNTs-Arc catalysts.

7.3.2. Electrochemical analysis

Fig. 7.4 is the CV of M-CNTs-Arc, M-CNTs-CVD, $NiCo_{0.16}Fe_{0.34}O_x$ and FeO_x, measured at scan rate of 10 mV s^{-1} in 1 M KOH solution. The catalyst loading was 0.025 mg cm^{-2}. In the case of M-CNTs-Arc hybrid catalysts, the oxidation and reduction potential change with the cycling time (Fig. 7.4 A). The oxidation peak potential is 1.43 V for the 1st cycle and decreases to 1.4 V after 11th cycles. And the increase of the area for the redox couple with cycling is attributed to the increasing passivation of $NiCo_{0.16}Fe_{0.34}$ into Ni and Co hydroxides and oxyhydroxides during cycling.[7, 20-21] The redox potential at 1.4 and 1.3 V is most likely associated with the transformation between $Ni(OH)_2$ and NiOOH in alkaline electrolyte.[1, 20-21, 45] Similar to M-CNTs-Arc, the redox potentials of $NiCo_{0.16}Fe_{0.34}O_x$ redox peaks occur at potentials of 1.4 and 1.32 V. However, the area of the redox reaction is much smaller than that of M-CNTs-Arc due to the smaller surface area and low electronic conductivity.[46] In the case of M-CNTs-CVD, the passivation of metallic Fe to Fe(Ⅱ)/Fe(Ⅲ) oxides/hydroxides occur at potential between -0.1 and 0.3 V (Fig. 7.4 B).[47,45]

The ESA for the M-CNTs hybrid catalysts was estimated from the electrochemical double-layer capacitance (C_{DL}) of the catalytic surface (here we use a general specific capacitance C_s = 0.040 mF cm^{-2} to estimate the ESA for carbon proposed by McCrory et. al.[36]). The C_{DL} is calculated based on the plot of i_c as a function of the scan rate ν, yielding a straight line with a slope equal to C_{DL} ($i_c = \nu C_{DL}$) (Fig. 7.4C). Based on the slopes, the ESA is 23.4, 16.4, 5.7 and 6.0 m^2 g^{-1} for M-CNTs-Arc, M-CNTs-CVD, $NiCo_{0.16}Fe_{0.34}O_x$ and FeO_x, respectively. The ESA of the catalysts is substantially smaller than the corresponding BET surface area (see Table 7.1).

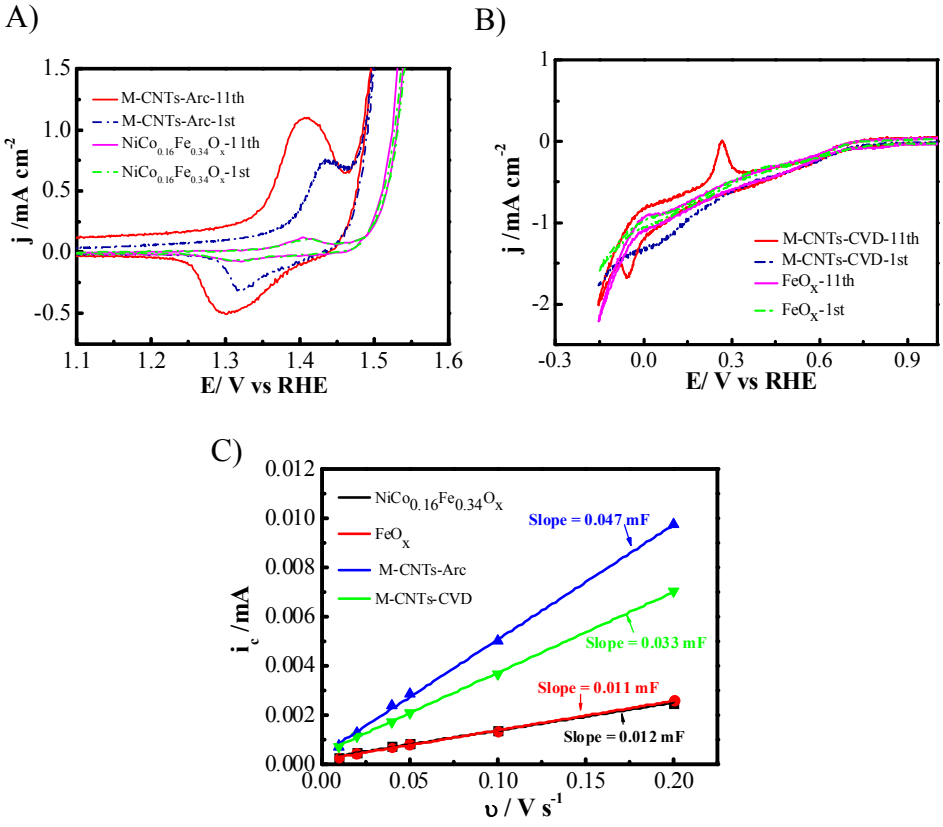

Figure 7.4. CV of A) M-CNTs-Arc and $NiCo_{0.16}Fe_{0.34}O_x$, B) M-CNTs-CVD and FeO_x in 1 M KOH solution with scan rate of 10 mV s^{-1} and catalysts loading of 0.025 mg cm^{-2} at a rotating rate of 1600 rpm; C) the anodic charging currents measured at -0.05 V vs SCE plotted as a function of scan rate, the determined double-layer capacitance of the catalysts is taken as the average value of the slope of the linear fits to the data.

Table 7.1 Physical and electrochemical properties of the catalysts materials studied.

CNTs	M-CNTs-Arc	M-CNTs-CVD	$NiCo_{0.16}Fe_{0.34}O_x$	FeO_x	Ru/C
BET surface area /m^2 g^{-1}	166.5	88.5	38.3	36.8	-
I_D/I_G	1.01	0.57	-	-	-
ESA / m^2 g^{-1}	23.4	16.4	5.6	6.0	-
Onset potential / V	1.48	1.55	1.55	1.60	1.58
$j_{g,\ \eta=0.47\ V}$ / mA cm^{-2}	196	56	18	3.2	8
$j_{s,\ \eta=0.47\ V}$ / mA cm^{-2}	32.8	13.4	11.8	2.2	-
Tafel slope / mV dec^{-1}	34	34		74	50

[#] The onset potential, j, and Tafel slope measured in 1 M KOH solution with rotating speed of 1600 rpm. j_g is the geometric area based current density and j_s is the specific electrochemically active surface area (ESA) based current density.

7.3.3 Electrocatalytic activity for OER

Fig. 7.5A is the LSV for OER on M-CNTs-Arc, M-CNTs-CVD, $NiCo_{0.16}Fe_{0.34}O_x$, FeO_x and 20%Ru/C catalysts, measured at scan rate of 1 mV s^{-1} in 1 M KOH solutions. The catalyst loading was 0.025 mg cm^{-2}. M-CNTs-Arc hybrid catalysts show the best activity for OER. The onset potential of M-CNTs-Arc is 1.48 V, which is 100 and 70 mV lower than that of 20% Ru/C (1.58 V) and M-CNTs-CVD (1.55 V), respectively. The current density measured at 1.7 V (η=0.47 V) is 196 mA cm^{-2} for M-CNTs-Arc, which is 3.6 times of that of M-CNTs-CVD (54 mA cm^{-2}) and 20 times of 20% Ru/C (10 mA cm^{-2}). The metal catalysts separated from the M-CNTs hybrids show a much lower activity for OER. The onset potential for OER on $NiCo_{0.16}Fe_{0.34}O_x$ and FeO_x is 1.55 and 1.60 V, respectively, 70 and 50 mV higher than that of the corresponding M-CNTs-Arc and M-CNTs-CVD hybrid catalysts, respectively. The current density at 1.7 V is 18 and 3.2 mA cm^{-2} for the reaction on $NiCo_{0.16}Fe_{0.34}O_x$ and FeO_x, much lower than that of the corresponding M-CNTs-Arc and M-CNTs-CVD. The much lower activity of separated metal catalysts is partially due to the significant sintering and growth of the metallic catalysts during the high temperature decomposition treatment.

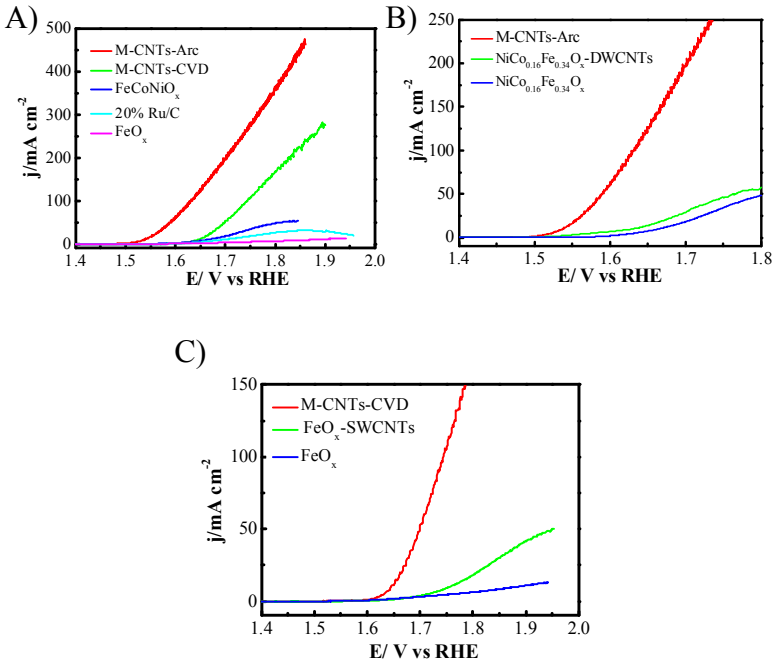

Figure 7.5. LSV of A) M-CNTs-Arc, M-CNTs-CVD, $NiCo_{0.16}Fe_{0.34}O_x$, FeO_x and Ru/C; B) M-CNTs-Arc, $NiCo_{0.16}Fe_{0.34}O_x$-DWNTs and $NiCo_{0.16}Fe_{0.34}O_x$; C) M-CNTs-CVD, FeO_x-SWNTs and FeO_x. The LSV was measured in 1 M KOH solution with scan rate of 1 mV s^{-1} and catalysts loading of 0.025 mg cm^{-2} at a rotating rate of 1600 rpm.

To separate the surface area effect from the intrinsic catalytic activity of the hybrid catalysts, we calculated the specific catalysts activity based on the EAS of the catalysts. The ESA specific activity of M-CNTs-Arc, M-CNTs-CVD, $NiCo_{0.16}Fe_{0.34}O_x$ and FeO_x was calculated to be 32.8, 13.4, 11.8 and 2.2 mA cm^{-2} at potential of 1.7 V in 1M KOH, respectively. This indicates that high electrocatalytic activity of M-CNTs-Arc and M-CNTs-CVD as compared to the corresponding metal core catalysts is not completely due to the high surface areas of the former.

The electrochemical activity of mechanically mixed $NiCoFeO_x$-DWNTs and FeO_x-SWNTs were also tested by LSV in 1 M KOH solution under identical conditions, and the results are shown in Fig. 7.5 B and C. The results indicate that the mechanically mixed $NiCoFeO_x$-DWNTs and FeO_x-SWNTs catalysts show slightly

higher electrochemical activity for OER as compared with corresponding $NiCoFeO_x$ and FeO_x metal catalysts, but still significantly lower than that of one-step synthesized M-CNTs-Arc and M-CNTs-CVD catalysts. For example, for the reaction on $NiCoFeO_x$-DWNTs, the onset potential is 1.52 V, ~30 mV lower than that on $NiCo_{0.16}Fe_{0.34}O_x$, but still 40 mV higher than that on M-CNTs-Arc. The current density measured at 1.7 V is 35 mA cm^{-2}, about twice of that on $NiCo_{0.16}Fe_{0.34}O_x$ (18 mA cm^{-2}), however it is only 17.8% of 196 mA cm^{-2} obtained for the OER on M-CNTs-Arc. The much lower electrocatalytic activity of the mechanically mixed metal oxide-CNTs as compared to the one-step synthesized M-CNTs hybrids indicates that there might be a synergistic effect between encapsulated metal catalysts. And the interconnected carbon materials including CNTs, graphite or/and graphene, are responsible for the lower onset potential and significantly higher current density for OER.

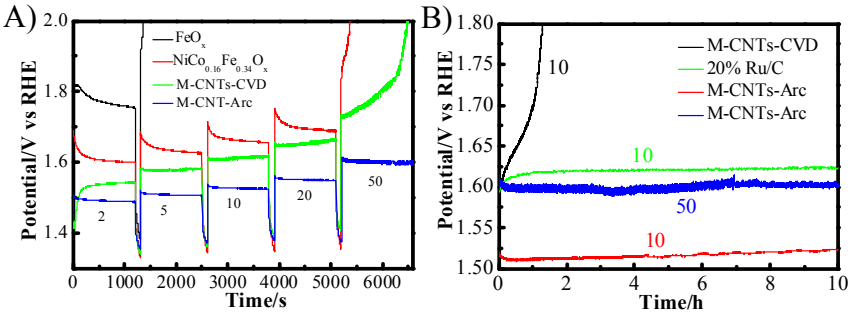

Figure 7.6. A) Chronopotentiometry of M-CNTs-Arc, M-CNTs-CVD, $NiCo_{0.16}Fe_{0.34}O_x$, and FeO_x in 1 M KOH solution; B) the long-term stability measured at current density of 10 mA cm^{-2} and 50 mA cm^{-2} measured in 1 M KOH solution. The catalyst loading was 0.1 mg cm^{-2} and the rotating rate was 1600 rpm. Numbers are current density in mA cm^{-2}.

Fig. 7.6 A shows the chropotentiometry curves at different current densities for the OER on M-CNTs-Arc, M-CNTs-CVD, $NiCo_{0.16}Fe_{0.34}O_x$ and FeO_x measured in 1 M KOH. The catalyst loading was 0.1 mg cm^{-2}. The potential to achieve a current

density of 2, 5, 10, 20 and 50 mA cm^{-2} for M-CNTs-Arc is 1.488, 1.506, 1.524, 1.550, 1.595 V, respectively. For the reaction on $NiCo_{0.16}Fe_{0.34}O_x$, the potential at a current density of 2, 5, 10 and 20 mA cm^{-2} is 1.596, 1.629, 1.658 and 1.685 V, considerably higher than that observed on M-CNTs-Arc. In the case of M-CNTs-CVD, the potential to achieve 2, 5, 10, 20 and 50 mA cm^{-2} is 1.542, 1.581, 1.615, 1.655 and 1.725 V, respectively, higher than that of M-CNTs-Arc under the same current loads. Also, at a current density of 50 mA cm^{-2}, the potential for OER on M-CNTs-CVD is not stable, the potential increased rapidly from 1.725 V to over 2 V after testing for 20 min. This indicates that M-CNTs-CVD hybrids have a much lower stability for OER as compared to M-CNTs-Arc hybrids. In addition, FeO_x is not able to achieve a current density of 5 mA cm^{-2}. This indicates that the electrocatalytic activity of FeO_x is much lower than that of $NiCo_{0.16}Fe_{0.34}O_x$.

The durability of M-CNTs-Arc, M-CNTs-CVD and Ru/C for OER was determined using controlled-current electrolysis in 1 M KOH (Fig 7.6 B). The catalyst material was held at a constant current density of 10 mA cm^{-2} for 10 h at a rotation rate of 1600 rpm, while the operating potential was measured as a function of time. For M-CNTs-Arc, the potential at 10 mA cm^{-2} is 1.52 V (η =0.29V) at the t=0, and the changes in the potential during the stability test are very small. After 10 h continuous operation, the potential to deliver 10 mA cm^{-2} is 1.524 V (η =0.294V), very close to the potential before the test. This indicates excellent stability of the M-CNTs-Arc hybrid catalysts. In the case of 20% Ru/C catalysts, the potential to achieve 10 mA cm^{-2} is 1.585 V (η =0.355 V) when t=0, increases to 1.625 V (η =0.395 V) after tested for 5 h and then remains stable around 1.625 V. However, the stability of M-CNTs-CVD hybrids is very poor. The potential to deliver a current density of 10 mA cm^{-2} rises from 1.6 V at t=0 to 1.8 V at t=1 h. The M-CNTs-CVD is completely

decomposed after 2 h operation and the electrolyte solution turned brownish most likely due to the dissolution of Fe. The outstanding stability of the M-CNTs-Arc was also further confirmed by testing at current density of 50 mA cm^{-2} in 1 M KOH. The results show that the potential to achieve 50 mA cm^{-2} (500 A g^{-1}) is 1.595 V (η =0.365 V) and the potential remained the same after test for 10 h, indicating that the M-CNTs-Arc is also very stable at high current densities.

McCrory et al recently studied the benchmarking heterogenous electrocatalysts prepared by electrodeposition for OER in 1 M KOH with rotating rate of 1600 rpm.[36] The overpotentials for achieving a current density of 10 mA cm^{-2} for IrO_x, $NiFeO_x$, $CoFeO_x$, $NiCoO_x$, CoO_x, $NiLaO_x$, $NiCuO_x$, NiO_x, and $NiCeO_x$ films are 0.32, 0.35, 0.37, 0.38, 0.39, 0.41, 0.41, 0.42 and 0.43V, respectively. Liang et al showed that Co_3O_4 nanocrystals grown on reduced graphene oxide (Co_3O_4/N-rmGO) exhibits a current density of 10 mA cm^{-2} (or 1 A g^{-1}) at η = ~0.31 V in 1 M KOH solution with catalyst loading of 1 mg cm^{-2}.[25] Ultrathin nickel-iron layered double hydroxide nanoplates supported on oxidized MWNTs was reported to achieve a current density of 10 A g^{-1} at η = 0.228 V in 1 M KOH with catalysts loading of 0.25 mg cm^{-2}.[11] In the present study, the M-CNTs-Arc hybrid catalyst achieved a current density of 10 mA cm^{-2} (or 100 A g^{-1}) at η = 0.29 V (i.e., 1.524 V vs RHE) in 1 M KOH with catalyst loading of 0.1 mg cm^{-2}. This indicates that M-CNTs-Arc hybrids are among the most active non-precious metal OER catalysts. The results demonstrate that M-CNTs hybrid produced by arc-discharge technique using $NiCo_{0.16}Fe_{0.34}$ metal catalysts is a promising catalyst with high activity and superior long-term stability for OER in alkaline solutions.

7.3.4 Effect of pH

The activity of M-CNTs for OER has been found to be critically related to the pH of the solution. Fig.7.7 shows the effect of pH on the OER activity for M-CNTs-Arc and M-CNTs-CVD. The variation trend for the onset potential and current density for M-CNTs-CVD and M-CNTs-Arc with pH is similar. The onset potentials for OER on M-CNTs-CVD and M-CNTs-Arc hybrids electrodes increased from ～1.7 V at pH=2.11 to ～2.2 V at pH=10, then decreased sharply to ～1.5 V when the pH was above 11 (Fig.7.7 C). The current densities of M-CNTs measured at 1.7 V are low in the pH range of 1-10. However, a dramatic increase were observed when pH increased to 12-14, reaching current density of 180 and 55 mA cm^{-2} at pH=13.6 for M-CNTs-CVD and M-CNTs-Arc, respectively (Fig. 7.7D). The different behavior of M-CNTs as a function of pH of the electrolytes indicates that fundamentally different mechanisms exist for OER under acidic, neutral and basic conditions. The reason for such drastic change of the reaction activity of the M-CNTs hybrid catalysts for OER as a function of solution pH is not clear at this stage. One possible reason may be related to the significant role of the surface electrochemistry of hydrous oxide, formed in acidic, neutral and basic conditions on the electrodes of transition metals due to their amphoteric nature.[7-8, 48] Takashima et. al. found that the OER overpotential for manganese oxide increase from 0.5 V to 0.7 V when the pH increased from 4 to 8, but sharply decreased to 0.48 V at pH ≥ 9, and proposed that the pH dependence of onset potential and current density might be due to the surface charge caused by OH^- species.[49] At low pH, the M-CNTs-Arc and M-CNTs-CVD are protonated and thus positively charged. At high pH, they would act as acids, adsorbing OH^- or donating protons and thus becoming negatively charged. The lower onset potential is expected in basic solution than those in acidic/neutral solution because of the highly charged

metal ions with excess hydroxide ions are active sites for oxygen evolution and oxygen species such as M-O$^-$ is easier to donate electrons in alkaline solution than that in acid or neutral solution with positively charged species.[49]

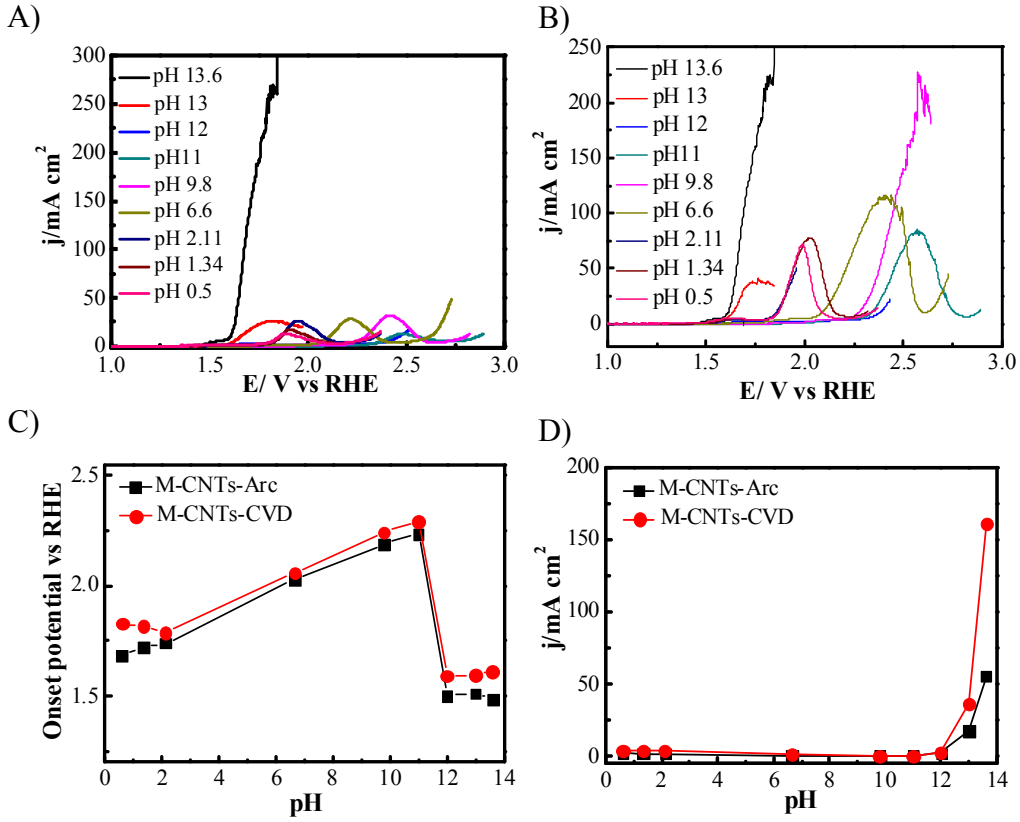

Figure 7.7. LSV of A) M-CNTs-Arc and B) M-CNTs-CVD under different pH solutions for OER, measured at scan rate of 10 mV s^{-1}; C) Plots of onset potential as function of pH; and D) plots of current density measured at 1.7 V vs. RHE as function of pH.

Fig. 7.8 is the Tafel slope plots for OER on M-CNTs-Arc and M-CNTs-CVD hybrids, measured in 1 M KOH solution at scanning rate of 1 mV s^{-1}. The Tafel slope of M-CNTs-Arc is 34 mV dec^{-1}, lower than 50 mV dec^{-1} obtained on the $NiCo_{0.16}Fe_{0.34}O_x$ metal catalysts (Fig. 7.8 A). For the OER on hydrous NiO, Lyons et al reported the Tafel slope of 40-60 mV dec^{-1} at low overpotentials.[8, 50] In the case of M-CNTs-CVD, the Tafel slope is 34 mV dec^{-1}, also lower than 77 mV dec^{-1} measured on FeO_x. The lower Tafel slopes observed on M-CNTs as compared to that on metal oxide catalysts indicate an increase of electron transfer for OER,[11, 20-21] an indication of the

synergistic effect of graphitic shell and CNTs network on the electrocatalytic activity of metal NPs catalyst. The reaction order plots with respect to OH^- activity (log I vs log a_{OH^-} at a given value) of M-CNTs-Arc were also constructed based on the polarization data in 0.5, 1 and 2 M KOH solution (Fig. 7.8C). A reaction order of 0.97 was obtained, indicating that the OER follows first-order kinetics with respect to the OH^- concentration. However, the reaction order was not obtained for M-CNTs-CVD because of the poor stability of the catalysts, which result in the non-linear function of logI and log a_{OH^-}.

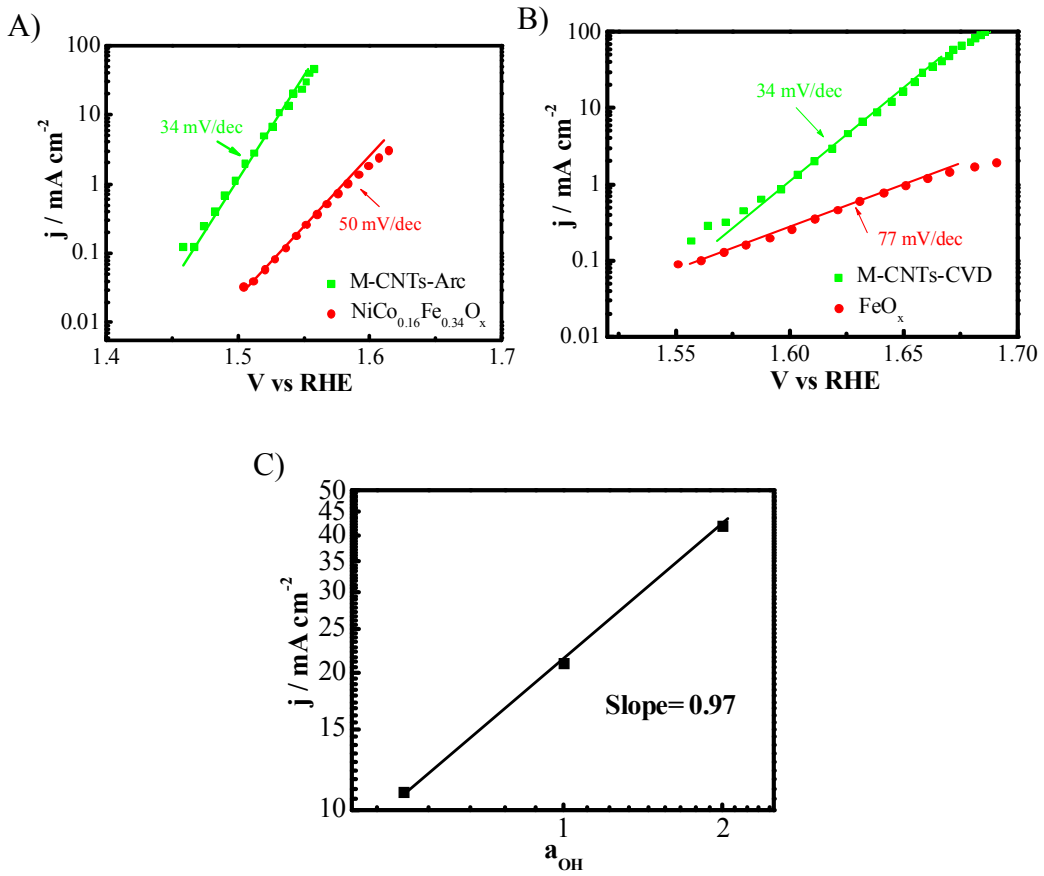

Figure 7.8. Tafel plots for oxygen evolution in 1 M KOH solutions at A) M-CNTs-Arc and $NiCo_{0.16}Fe_{0.34}O_x$; B) M-CNTs-CVD and FeO_x; C) plots of reaction order for OER on M-CNTs-Arc.

The Tafel slope of CNTs for OER under stirring condition was also investigated in 1 M, 0.1 M and 0.01 M KOH solutions and the results are shown in Fig. 7.9. For M-

CNTs-Arc, the Tafel slope recorded is 74 mV dec^{-1} in 0.01M KOH solution. However, the Tafel slope is around 34 mV dec^{-1} when the concentration of KOH of solution in the range of 0.1-1 M KOH. In the case of M-CNTs-CVD, a Tafel slope of 34, 41 and 89 mV dec^{-1} was obtained at in 1 M, 0.1 M and 0.01 M KOH solution respectively, indicating that the rate determine step (RDS) is influenced by the concentration of KOH.

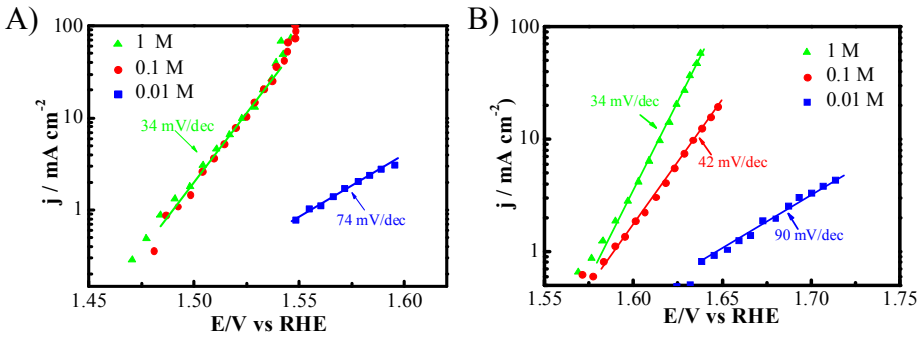

Figure 7.9. Tafel plots for oxygen evolution at A) M-CNTs-Arc and B) M-CNTs-CVD electrode measured in 1 M, 0.1 M and 0.01 M KOH solutions.

The significant dependence of OER activity on pH demonstrates that OH^- is playing a critical role in OER on M-CNTs hybrid catalysts. As shown in Fig. 7.3A, the transformation of $NiCo_{0.16}Fe_{0.34}$ into $NiCo_{0.16}Fe_{0.34}$-OOH (M-OOH) occurs before the oxygen evolution. Thus, the initial steps of OER are the absorption of OH^- on M-CNTs-Arc, forming M-CNTs-$NiCo_{0.16}Fe_{0.34}$-OOH.[8, 45] The surface-enhanced Raman spectroscopy also provides evidences of formation of MOOH intermediates for Ni[51] and NiFe oxides.[20] A Tafel slope of 34 mV dec^{-1} with a reaction order of ~1.0 for M-CNTs-Arc indicates that oxygen evolution on M-OOH begins with absorbing OH^- as a fast step and the subsequent electrochemical interaction between the surface adsorbed intermediate and OH^-.[45, 47] The rate determining step is most likely the formation of metal oxide or metal oxo species, as shown by Lyons et al.[45, 47, 50]

The superiority of M-CNTs-Arc hybrids catalysts can be attributing to the following reasons. Firstly, $NiCo_{0.16}Fe_{0.34}$ and its oxides are superior catalysts for OER as compared with that of Fe and FeO_x in the case of M-CNTs-CVD. Secondly, the M-CNTs hybrids produced by arc-discharge using $NiCo_{0.16}Fe_{0.34}$ catalysts are connected mainly by DWNTs networks, and the encapsulated $NiCo_{0.16}Fe_{0.34}$ with graphite enhances the activity and stability for OER. For M-CNTs-CVD, metal catalysts are interconnected via SWNTs networks, which generally contains large amount of semiconductor.[52-54] The excellent conductivity of DWNTs would provide a better path way for electron charge transfer during OER, as compared to SWNTs.

7.4 Conclusion

Here we, for the first time, reported a simple, scalable and commercial viable one-step synthesis method to fabricate metal-CNTs network hybrid catalysts using arc-discharge and CVD techniques for OER catalysis. The metal-CNTs hybrids synthesized by arc-discharge technique with $NiCo_{0.16}Fe_{0.34}$ catalysts (M-CNTs-Arc) and the CVD technique with Fe catalysts have significantly higher electrocatalytic activity for OER in alkaline solutions as compared with corresponding bare metal oxides or supported catalysts. The as-synthesized M-CNTs-Arc catalysts show low onset potential (1.48 V), significantly high activity and super stability for OER. The M-CNTs-Arc hybrids produced the highest activity for OER in alkaline solutions, achieving 100 A g^{-1} at $\eta = 0.29$ V, and 500 A g^{-1} at $\eta = 0.37$ V. And the Tafel slope of 34 mV dec^{-1} with a reaction order of ~1.0 for M-CNTs-Arc indicates that oxygen evolution on M-CNTs-Arc is mainly limited by the formation of metal oxide or metal oxo species. The excellent activity and durability of the M-CNTs-Arc network hybrids is most likely due to the synergistic effect between the encapsulated metal

catalysts and the interconnected CNTs. These results provide a new way and open an area to further advance the catalysts for OER.

Acknowledgement

We would like to acknowledge Mr Jin Zhang for the measurement of the BET surface area of M-CNTs hybrids and Mr Lei Zhang for the assistance of ICP operation. The project is supported by the Australian Research Council *Discovery Project funding scheme* (project number: DP120104932). The authors also acknowledge the facilities, and the scientific and technical assistance of the Australian Microscopy & Microanalysis Research Facility at the Centre for Microscopy, Characterisation & Analysis, and the University of Western Australia, a facility funded by the University, State and Commonwealth Governments. The author would like to thanks Prof. Huiming Chen and Prof. Chang Liu for providing the materials.

References:

1. Y. Surendranath and D. G. Nocera, in *Progress in Inorganic Chemistry*, John Wiley & Sons, Inc., 2011, DOI: 10.1002/9781118148235.ch9, pp. 505-560.
2. A. Ursua, L. M. Gandia and P. Sanchis, *Proceedings of the Ieee*, 2012, 100, 410-426.
3. D. Pletcher and X. Li, *International Journal of Hydrogen Energy*, 2011, 36, 15089-15104.
4. Y.-H. Fang and Z.-P. Liu, *Journal of the American Chemical Society*, 2010, 132, 18214-18222.
5. M. E. G. Lyons and L. D. Burke, *Journal of the Chemical Society, Faraday Transactions 1: Physical Chemistry in Condensed Phases*, 1987, 83, 299-321.
6. M. E. G. Lyons and S. Floquet, *Physical Chemistry Chemical Physics*, 2011, 13, 5314-5335.
7. M. E. G. Lyons and M. P. Brandon, *International Journal of Electrochemical Science*, 2008, 3, 1425-1462.
8. M. E. G. Lyons and M. P. Brandon, *International Journal of Electrochemical Science*, 2008, 3, 1386-1424.
9. L. Trotochaud, J. K. Ranney, K. N. Williams and S. W. Boettcher, *Journal of the American Chemical Society*, 2012, 134, 17253-17261.
10. D. Cibrev, M. Jankulovska, T. Lana-Villarreal and R. Gomez, *International Journal of Hydrogen Energy*, 2013, 38, 2746-2753.

11. M. Gong, Y. Li, H. Wang, Y. Liang, J. Z. Wu, J. Zhou, J. Wang, T. Regier, F. Wei and H. Dai, *Journal of the American Chemical Society*, 2013, 135, 8452-8455.
12. M. Hamdani, R. N. Singh and P. Chartier, *International Journal of Electrochemical Science*, 2010, 5, 556-577.
13. J. O. Bockris and T. Otagawa, *J. Phys. Chem.*, 1983, 87, 2960-2971.
14. A. N. Jain, S. K. Tiwari, R. N. Singh and P. Chartier, *Journal of the Chemical Society, Faraday Transactions*, 1995, 91, 1871-1875.
15. E. B. Castro and C. A. Gervasi, *International Journal of Hydrogen Energy*, 2000, 25, 1163-1170.
16. E. B. Castro, C. A. Gervasi and J. R. Vilche, *Journal of Applied Electrochemistry*, 1998, 28, 835-841.
17. M. D. Merrill and R. C. Dougherty, *The Journal of Physical Chemistry C*, 2008, 112, 3655-3666.
18. Y. Lee, J. Suntivich, K. J. May, E. E. Perry and Y. Shao-Horn, *The Journal of Physical Chemistry Letters*, 2012, 3, 399-404.
19. X. Lu and C. Zhao, *J. Mater. Chem. A*, 2013, 1, 12053-12059.
20. M. W. Louie and A. T. Bell, *Journal of the American Chemical Society*, 2013, 135, 12329-12337.
21. R. D. L. Smith, M. S. Prévot, R. D. Fagan, S. Trudel and C. P. Berlinguette, *Journal of the American Chemical Society*, 2013, 135, 11580-11586.
22. X. Zou, J. Su, R. Silva, A. Goswami, B. R. Sathe and T. Asefa, *Chem. Commun.*, 2013, 49, 7522-7524.
23. Q. Liu, J. T. Jin and J. Y. Zhang, *Acs Applied Materials & Interfaces*, 2013, 5, 5002-5008.
24. J. Wu, Y. Xue, X. Yan, W. Yan, Q. Cheng and Y. Xie, *Nano Research*, 2012, 5, 521-530.
25. Y. Liang, Y. Li, H. Wang, J. Zhou, J. Wang, T. Regier and H. Dai, *Nat Mater*, 2011, 10, 780-786.
26. K. Mette, A. Bergmann, J.-P. Tessonnier, M. Hävecker, L. Yao, T. Ressler, R. Schlögl, P. Strasser and M. Behrens, *Chemcatchem*, 2012, 4, 851-862.
27. W. Y. Yuan, P. K. Shen and S. P. Jiang, *Journal of Materials Chemistry A*, 2014, 2, 123-129.
28. Q. Zhang, J.-Q. Huang, W.-Z. Qian, Y.-Y. Zhang and F. Wei, *Small*, 2013, 9, 1237-1265.
29. M. F. L. De Volder, S. H. Tawfick, R. H. Baughman and A. J. Hart, *Science*, 2013, 339, 535-539.
30. J. Prasek, J. Drbohlavova, J. Chomoucka, J. Hubalek, O. Jasek, V. Adam and R. Kizek, *Journal of Materials Chemistry*, 2011, 21, 15872-15884.
31. C. Liu and H. M. Cheng, *Materials Today*, 2013, 16, 19-28.
32. H. M. Cheng, F. Li, G. Su, H. Y. Pan, L. L. He, X. Sun and M. S. Dresselhaus, *Appl. Phys. Lett.*, 1998, 72, 3282-3284.

33. M. Q. Zhao, Q. Zhang, X. L. Jia, J. Q. Huang, Y. H. Zhang and F. Wei, *Adv. Funct. Mater.*, 2010, 20, 677-685.
34. C. Liu, H. T. Cong, F. Li, P. H. Tan, H. M. Cheng, K. Lu and B. L. Zhou, *Carbon*, 1999, 37, 1865-1868.
35. B. Yu, C. Liu, P. X. Hou, Y. Tian, S. S. Li, B. L. Liu, F. Li, E. I. Kauppinen and H. M. Cheng, *J. Am. Chem. Soc.*, 2011, 133, 5232-5235.
36. C. C. L. McCrory, S. Jung, J. C. Peters and T. F. Jaramillo, *Journal of the American Chemical Society*, 2013, 135, 16977-16987.
37. J. D. Benck, Z. Chen, L. Y. Kuritzky, A. J. Forman and T. F. Jaramillo, *Acs Catalysis*, 2012, 2, 1916-1923.
38. D. K. Bediako, Y. Surendranath and D. G. Nocera, *Journal of the American Chemical Society*, 2013, 135, 3662-3674.
39. A. Imanishi, T. Okamura, N. Ohashi, R. Nakamura and Y. Nakato, *J. Am. Chem. Soc.*, 2007, 129, 11569-11578.
40. B. Yu, C. Liu, P.-X. Hou, Y. Tian, S. Li, B. Liu, F. Li, E. I. Kauppinen and H.-M. Cheng, *Journal of the American Chemical Society*, 2011, 133, 5232-5235.
41. U. J. Kim, C. A. Furtado, X. M. Liu, G. G. Chen and P. C. Eklund, *Journal of the American Chemical Society*, 2005, 127, 15437-15445.
42. M. S. Dresselhaus, G. Dresselhaus, R. Saito and A. Jorio, in *Carbon Nanotubes: Quantum Cylinders of Graphene*, eds. S. Saito and A. Zettl, Elsevier Science Bv, Amsterdam, 2008, DOI: 10.1016/s1572-0934(08)00004-8, pp. 83-108.
43. R. Saito, M. Hofmann, G. Dresselhaus, A. Jorio and M. S. Dresselhaus, *Adv. Phys.*, 2011, 60, 413-550.
44. K. Fujisawa, K. Komiyama, H. Muramatsu, D. Shimamoto, T. Tojo, Y. A. Kim, T. Hayashi, M. Endo, K. Oshida, M. Terrones and M. S. Dresselhaus, *Acs Nano*, 2011, 5, 7547-7554.
45. R. L. Doyle, I. J. Godwin, M. P. Brandon and M. E. G. Lyons, *Physical Chemistry Chemical Physics*, 2013, 15, 13737-13783.
46. R. B. Rakhi, W. Chen, D. Cha and H. N. Alshareef, *Advanced Energy Materials*, 2012, 2, 381-389.
47. R. L. Doyle and M. E. G. Lyons, *J. Electrochem. Soc.*, 2013, 160, H142-H154.
48. M. E. G. Lyons and M. P. Brandon, *International Journal of Electrochemical Science*, 2008, 3, 1463-1503.
49. T. Takashima, K. Hashimoto and R. Nakamura, *Journal of the American Chemical Society*, 2012, 134, 1519-1527.
50. M. E. G. Lyons, R. L. Doyle, I. Godwin, M. O'Brien and L. Russell, *J. Electrochem. Soc.*, 2012, 159, H932-H944.
51. B. S. Yeo and A. T. Bell, *The Journal of Physical Chemistry C*, 2012, 116, 8394-8400.
52. P. R. Bandaru, *Journal of Nanoscience and Nanotechnology*, 2007, 7, 1239-1267.

53. M. C. Hersam, *Nat Nano*, 2008, 3, 387-394.
54. H. Liu, Y. Feng, T. Tanaka, Y. Urabe and H. Kataura, *The Journal of Physical Chemistry C*, 2010, 114, 9270-9276.

Chapter 8: Effect of Nitrogen-containing Functionalization on the Electrocatalystic Activity of PtRu Nanoparticles Supported on Carbon Nanotubes for Methanol Oxidation of Fuel Cells

8.1. Introduction

Fuel cells are expected to play a key role in our future energy economy due to the limited fossil fuel reserves and the increasing energy demand[1, 2]. DMFCs, a device anticipated to serve as a power source for mobile application, have been extensively studied due to its advantages, such as high energy density (methanol has 17900 kJ/L), relatively quick start-up, rapid response to varying loading, and safe for storage and transportation[3, 4]. However, the sluggish kinetic rates for methanol oxidation inhibit the large-scale production of cost-effective and highly efficient DMFCs[3]. Intensified researches have been conducted all over the world to develop the active and stable electrocatalysts for methanol oxidation, particularly in the area of binary alloy catalysts, such as PtRu[5], Pt-Os[6], Pt-Sn[7], Pt-W[6] and Pt-Mo[8]. Among these, the PtRu alloy catalyst system is widely accepted as one of the most promising anode catalysts for DMFC [9, 10]. In order to enhance the dispersion of metal nanoparticles (NPs) and thus to increase the utilization and efficiency of the precious metal, PtRu alloy supported onto high surface area carbon supports, including carbon blacks, mesoporous carbon[11, 12], carbon nanofibers [13], and CNTs [5, 14], were investigated. Particularly, CNTs have received wide attention on their application as catalysts

support in fuel cell due to their large specific surface area, high electronic conductivity, and excellent chemical stability[15-18].

Owing to the chemical inert of pristine CNTs, homogenous binding sites are required to introduce onto the surface of the CNTs through surface-functionalization in order to obtain high dispersion of metal NPs on CNTs[19, 20]. The most common covalent functionalization is via the aggressive oxidation treatment in a mixture of HNO_3/H_2SO_4 solution, introducing the carbonyl groups (-COOH) onto the surface of CNTs [21, 22]. However, the acid oxidation method inevitably causes some structural damage of CNTs and introduces large amount of defects; consequently disrupts the delocalized electron system and results in loss of their electronic conductivity and corrosion resistance [4, 23]. Non-covalent functionalization of CNTs by surfactants[4, 23], aromatic compounds[5], polymers or polyelectrolytes [23-27] and biomolecules [28] has attracted great interest due to the advantages of providing high density of anchoring site without damage the intrinsic property of CNTs. A variety of polyelectrolyte and solvents such as poly(diallyldimethylammonium chloride) (*PDDA*)[29, 30], polypyrrole (PPY)[31], PEI[26], polyaniline (PANI) [27], phenanthroline[32], hydroxyquinoline[7], 1-aminopyrene (1-AP)[5], tetrahydrofuran (THF) [33], have been employed to functionalize CNTs as catalysts supports. Non-colvant fuctionalization by polyelectrolytes and solvent significantly improves the distribution and electrocatalytic activity of Pt and Pt based alloy NPs on CNTs or graphene [7, 24, 27, 29, 30, 32, 34]. The electrocatalytic activity of Pt NPs is also affected by the nature of non-covalent functionalization. Wang et al investigated the effect of polyelectrolytes on the electronic structure of Pt NPs on polymers functionalized on CNTs[35]. The spectroscopic and electrochemical characterization as well as DFT calculation reveal that polyanions with electron-rich functional groups would donate electrons to Pt atoms which cause an increase in the

electron density around Pt atoms and downshift d-band center of Pt resulting in a weaker chemisorptions of oxygen-containing species (e.g., CO) enhancing the electrocatalystic activity of Pt NPs[35].

It is of significant importance to understand the influence of the polyelectrolyte and/or solvent on the morphology, distribution and electrocatalytic activity of the Pt-based NPs supported on CNTs in order to develop better and more efficient catalysts for fuel cells. Here, polymers such as poly (diallyldimethylammonium chloride) (PDDA) and PEI, and solvents such as 1-aminopyrene (AP) and terahydrofuran (THF) were selected to functionalize the CNTs as supports for PtRu NPs. PDDA is water-soluble quaternary ammonium strong cationic polyelectrolyte while PEI is one of the most popular amino-rich highly hydrophilic cationic polyelectrolyte for fuel cell applications [26, 33, 36, 37]. AP and THF have been shown to be effective in functionalization of CNTs [5, 33, 38]. The results clearly indicate that the electrocatalystic activity depends strongly on the composition and structure of the functionalization agents and functionalization agents with ammonium or amino groups are particularly effective to enhance the activity of the PtRu NPs for the MOR of fuel cells.

8.2 Experimental

8.2.1 Functionalization of CNTs

Materials used in this experiment include sulfuric acid (99.5%, Fluka), nitric acid (65%, Fluka), ethanol (Sigma-Aldrich), methanol (Sigma-Aldrich), CNTs (multi-walled CNTs, Shenzhen Nano, China), hexachloroplatinic(IV) acid (Sigma-Aldrich), ruthenium chloride (Sigma-Aldrich), ethylene glycol (Sigma-Aldrich), Nafion solution (5% in isoproponal and water), PDDA (molecular weight over 100000), PEI (molecular weight ~1300, Sigma-Aldrich), AP (molecular weight 217, Sigma-

Aldrich), THF (molecular weight 72, Sigma-Aldrich). All the chemicals were used without further purification. Fig. 8.1 shows the structure of the functionalization agents used in the present study.

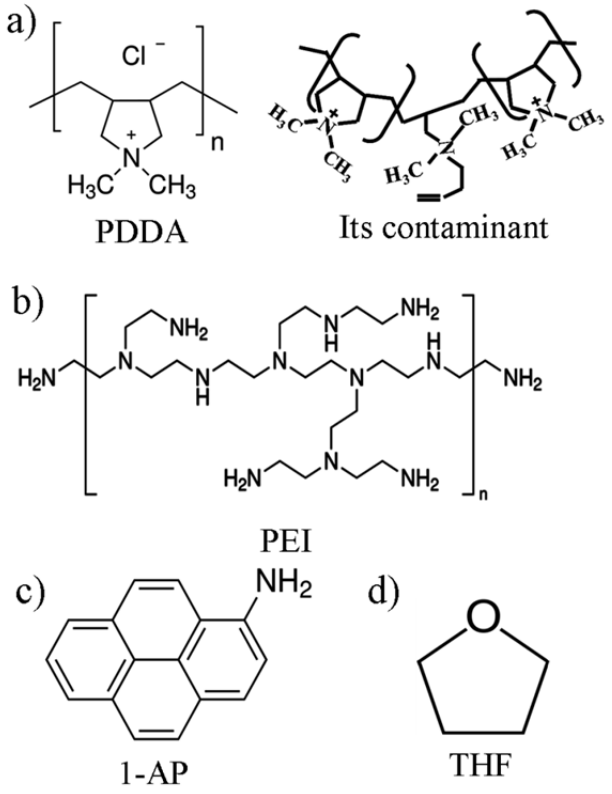

Figure 8.1. Molecular structure of functionalization agents used in the present study.

CNTs functionalized by PDDA and PEI were synthesized as follow: 200 mg pristine CNTs were ultrasonicated in 400 mL ultrapure water (resistivity 18.2 MΩ cm) for 1 h in presence of 0.5 wt% PDDA or PEI and stirred overnight. During the PDDA functionalization process, 2 g NaCl was added in order to promote the PDDA functionalization [24, 26]. The functionalized CNTs were washed with ultrapure water for several times to remove the excess PDDA or PEI. The products were noted as PDDA-CNTs and PEI-CNTs respectively. For AP functionalization, 200 mg pristine CNTs were dispersed in 100 mL ethanol with ultrasound for 1 h in the presence of 20 mg of AP, then stirred overnight for 12 h and filtrated using nylon membrane, followed by

washing for several times with ethanol to remove the excess AP. The product was noted as AP-CNTs. In the case of THF functionalization, 200 mg of pristine CNTs were dispersed in 100 mL THF with ultrasound for 1 h, and then stirred for overnight and filtrated using nylon membrane. The product was noted as THF-CNTs. For comparison, CNTs were also functionalized by a conventional acid oxidation treatment following the procedure reported elsewhere[26]. In this method, 200 mg of CNTs were treated in 200 mL of a mixed acid solution (H_2SO_4:HNO_3 in 1:1 v/v), followed by refluxing at 140 ^oC for 4 h. The obtained solution was then diluted with 2 L of deionized water to reduce the acidity of the solution, followed by filtration. The acid-treated CNTs are denoted as AO-CNTs. The as-functionalized CNTs were dried in vacuum oven at 70^oC for 24 h.

8.2.2 Synthesis of PtRu/CNTs electrocatalysts

To prepare PtRu/CNTs, 30 mg PDDA, PEI, AP and THF functionalized CNTs and AO-CNTs were firstly ultrasonicated in 50 mL ethylene glycol (EG) solution for 30 min respectively before the addition of approximate amount of H_2PtCl_6 and $RuCl_3$ with Pt:Ru ratio of 1:1[5]. The solution was controlled at a pH of slightly less than 7 (e.g., pH 6.5) to maintain a weak acidity. The beaker was then placed in a microwave oven and heated for 2 min, followed by stirring overnight under pH 3-4. The solution was then filtered using a nylon filter membrane and washed for several times. The obtained catalysts were dried in a vacuum oven at 70^oC for 24 h. The metal loading on CNTs was controlled at 40 wt%. The products were noted as PtRu/PDDA-CNTs, PtRu/PEI-CNTs, PtRu/AP-CNTs, PtRu/THF-CNTs and PtRu/AO-CNTs.

8.2.3 Characterization

Thermo gravimetric (Q5000, USA) analyses (TGA) were performed to investigate the loading of PDDA, PEI, AP and THF under air flow upon equilibration at 100 °C for 15 min, followed by a ramp of 10 °C min^{-1} up to 800°C. And PtRu loading were also tested using TGA under air upon equilibration at 100 °C for 15 min, followed by a ramp of 10 °C min^{-1} up to 800°C. The Raman spectra were recorded in air at room temperature using a Perkin–Elmer GX Raman spectrometer with a back-scattered configuration and equipped with a Nd:YAG laser at 1064 nm as its light source for Raman. Distributions of PtRu NPs on MWCNT were characterized using a transmission electron microscope (JEOL JEM-2000EX, Japan) with operating at 200 kV. Here, the mean sizes of the PtRu NPs were obtained by measuring 250 randomly chosen particles in the TEM images. The products were identified with X-ray diffractometer (XRD, Rigaku D/MAX RINT 2500) operated at 40 kV and 30 mA with Cu Ka (l = 1.5406 A˚) in the range of 20-90^{o}. The X-ray photoelectron spectroscopy (XPS) measurements were carried out on a XPS apparatus (ESCALAB 250, Thermo-VG Scientific Ltd.). The Pt:Ru ratio of as obtained catalysts was further confirmed by Inductively Coupled Plasma (ICP-OES, IRIS Intrepid Ⅱ XSP,USA). The solution for ICP analysis were prepared as follow: All the PtRu catalysts were burned in TG pan, and the solid were collected and digested in PTFE digestion tank using microwave dissolver (SINEO, HDS-8G) with 10 mL aqua regia (the procedure was set as: 150 ^{o}C, 5 min; 180 ^{o}C, 5 min; 200 ^{o}C, 10 min; 230 ^{o}C, 20 min).

The electrochemical measurements were conducted in a standard electrochemical cell using a Princeton potentiostat（Versastat3，USA）. Generally, 4 mg of the catalyst was ultrasonically mixed in 4 mL of ethanol nafion mixture (with Ethnol: Nafion 9:1) to form a homogeneous ink, followed by dropping 10 μL of the catalyst ink onto the

surface of a glass carbon electrode (GCE). The diameter of GCE was 4 mm. Pt foil (3.0 cm^2) and Ag/AgCl (saturated KCl) electrodes were used as the counter and reference electrodes, respectively. All potentials in the present study were given versus Ag/AgCl (saturated KCl) electrode. The electrochemical active area of PtRu/CNTs were measured in a nitrogen-saturated 0.5 M H_2SO_4 solution at a scan rate of 50 mV s^{-1} and the elelctrocatalytic activity for the MOR was measured in a nitrogen-saturated 0.5 M H_2SO_4 + 1.0 M CH_3OH solution at a scan rate of 50 mV s^{-1}. The Pt metal loading was kept at 2 μg. The tests were conducted at 25^oC.

The CO-stripping was performed in a nitrogen-saturated 0.5 M H_2SO_4 solution. First, the solution was bubbled with ultrapure N_2 for 15 min, then CO was adsorbed by flowing 0.5% CO in N_2 at a flow rate of 50 ml min^{-1} through the working electrode compartment by keeping the potential at −0.12 V versus Ag/AgCl reference electrode for 30 min, followed by bubbling N_2 for 30 min by keeping the potential at the same value. The potential was scanned from 0 to 1.0 V at a scan rate of 50 mV s^{-1}.

8.3 Results and Discussion

8.3.1 TGA and Raman spectra analysis of functionalized CNTs

Table 8.1. The loading of functionalization agents, PtRu NPs and decomposition temperature of functionalized CNTs and the Raman I_D/I_G ratio.

Electrocatalysts	Agent loading (%)	PtRu loading (%)	Decomposition temperature (^oC)	Raman I_D/I_G
PDDA	3.5	37.0	550-690	2.85
PEI	3.0	37.1	550-705	2.9
AP	1.0	38.0	550-695	2.7
THF	1.0	38.0	550-670	3.1
AO	-	36.1	400-620	3.6
CNTs	-	-	550-680	3.1

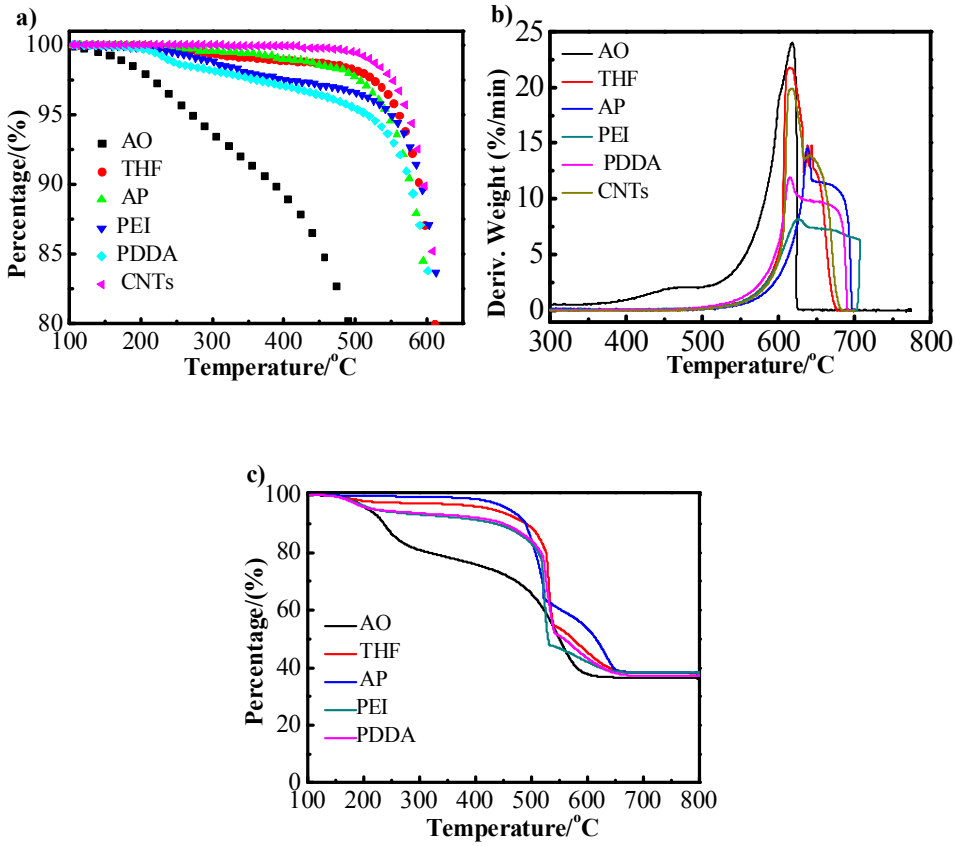

Figure 8.2. TGA curves of A) CNTs, PDDA-CNTs, PEI-CNTs, AP-CNTs, THF-CNTs and AO-CNTs, B) differential TGA curves, showing the decomposition of CNTs and functionalized CNTs under air flow, C) PtRu supported on PDDA-CNTs, PEI-CNTs, AP-CNTs, THF-CNTs and AO-CNTs under air flow.

The loadings of PDDA, PEI, AP and THF on CNTs and PtRu on functionalized CNTs were analyzed by TGA method and the results are shown in Fig. 8.2. The loading of the functionalization agents was determined from the weight loss around 400 ^{o}C. The loading of PDDA and PEI on CNTs is 3.5 wt% and 3.0 wt%, respectively, and it is ~1 wt% AP and THF assembled onto CNTs (Fig. 8.2 A). The low loading of AP and THF is probably due to their much smaller molecule weight. The decomposition temperature of CNTs is also affected by the functionalization. The decomposition temperatures of PDDA, PEI and AP functionalized CNTs are around 550-690, 550-705, 550-695 ^{o}C respectively, higher than 550-680 ^{o}C of pristine CNT (Fig. 8.2B).

This indicates that PDDA, PEI and AP wrapped on CNTs surface improve the thermal stability of CNTs. On the other hand, the decomposition of THF-CNTs slightly shifts to lower temperature (550-670^{o}C) as compared to that of pristine CNTs. This may be because of the extra oxygen atoms assembled on the surface of CNTs by THF functionalization (Fig. 8.1). AO-CNTs starts to lose weight at temperatures as low as 200 ^{o}C and its decomposition temperature is around 400-620 ^{o}C, significantly lower than pristine CNTs. This indicates that acid oxidation treatment reduces the thermal stability of CNTs probably due to the structural damage of CNTs by acid treatment.

The loading of PtRu NPs on CNTs was also obtained from TGA (Fig. 8.2 C). The PtRu loading supported on PDDA-CNTs, PEI-CNTs, AP-CNTs, THF-CNTs and AO-CNTs are 37.0, 37.1, 38.0, 38.0 and 36.1 wt%, respectively. The measured PtRu loading is close to the design loading 40 wt%. The PtRu ratios of as-synthesized catalysts were also analyzed by ICP, and the Pt:Ru ratio supported on PDDA-CNTs, PEI-CNTs, AP-CNTs and THF-CNTs is 0.94:1, 1.01:1, 1.02:1 and 0.97:1, respectively. The loading of functionalization agents, PtRu NPs and decomposition temperature of functionalized CNTs are summarized in Table 8.1.

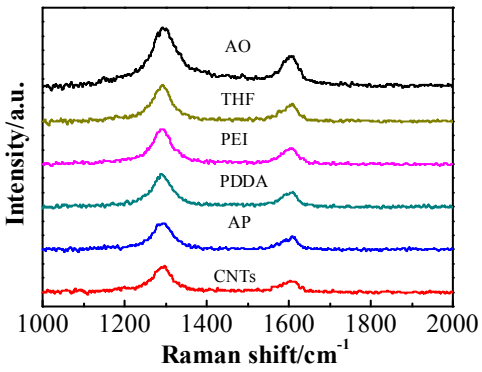

Figure 8.3. Raman spectroscopy of pristine CNTs, PDDA-CNTs, PEI-CNTs, AP-CNTs, THF -CNTs CNTs and AO-CNTs.

Fig. 8.3 is the Raman spectra of the pristine CNTs and functionalized CNTs. The relative intensity ratio of the D (near 1300 cm^{-1}) to G (in the 1580-1600 cm^{-1} region) band (I_D /I_G) is used as probes of CNT wall integrity (Table 8.1) [39]. The calculated I_D/ I_G value for pristine CNTs is 3.1. For AO-CNTs, the I_D/I_G ratio is 3.6, significantly higher than pristine CNTs, which demonstrates that acid oxidation treatment brings significant number of defects on the surface of CNTs and result in an increase of disordered sp^2 carbon material[40, 41]. The values of I_D/I_G of PDDA, PEI, AP and THF functionalized CNTs are 2.85, 2.9, 2.7 and 3.1, respectively. The results indicate that PDDA, PEI and AP functionalized MWCNT have fewer defects as compared to AO-CNTs most likely due to the self-assembly and wrapping of PDDA, PEI and AP which enhances the stability of the CNTs with fewer defects. The I_D/I_G ratio of THF-CNTs is almost the same as pristine CNTs and the reason is most likely related to the weak interaction between THF and CNTs. The improved structural stability of PDDA, PEI and AP functionalized CNTs appears to be consistent with the thermal stability of the corresponding functionalized CNTs.

8.3.2 TEM, XRD and XPS analysis of PtRu/CNTs catalysts

Fig. 8.4 shows the TEM images and the corresponding histograms of the particle sizes distribution of PtRu NPs on functionalized CNTs. In the case of PtRu/AO-CNTs, the dispersion of PtRu NPs is relatively poor with a large number of aggregates and the average particle size of PtRu NPs is ~4.2 nm (Fig. 8.4 E). In the case of PtRu NPs supported on PDDA-CNTs, PEI-CNTs, AP-CNTs and THF-CNTs, the distribution of PtRu NPs is significantly better than that supported on AO-CNTs. The average particle sizes of PtRu NPs supported on PDDA-CNTs, PEI-CNTs, AP-CNTs and THF-CNTs are ~3.13, ~2.98, ~2.94 and ~3.28 nm (Fig. 8.3 A-D), respectively.

PDDA, PEI, AP and THF functionalized CNTs are far more effective catalyst supports for Pt-based NPs as compared to the conventional acid-oxidized CNTs.

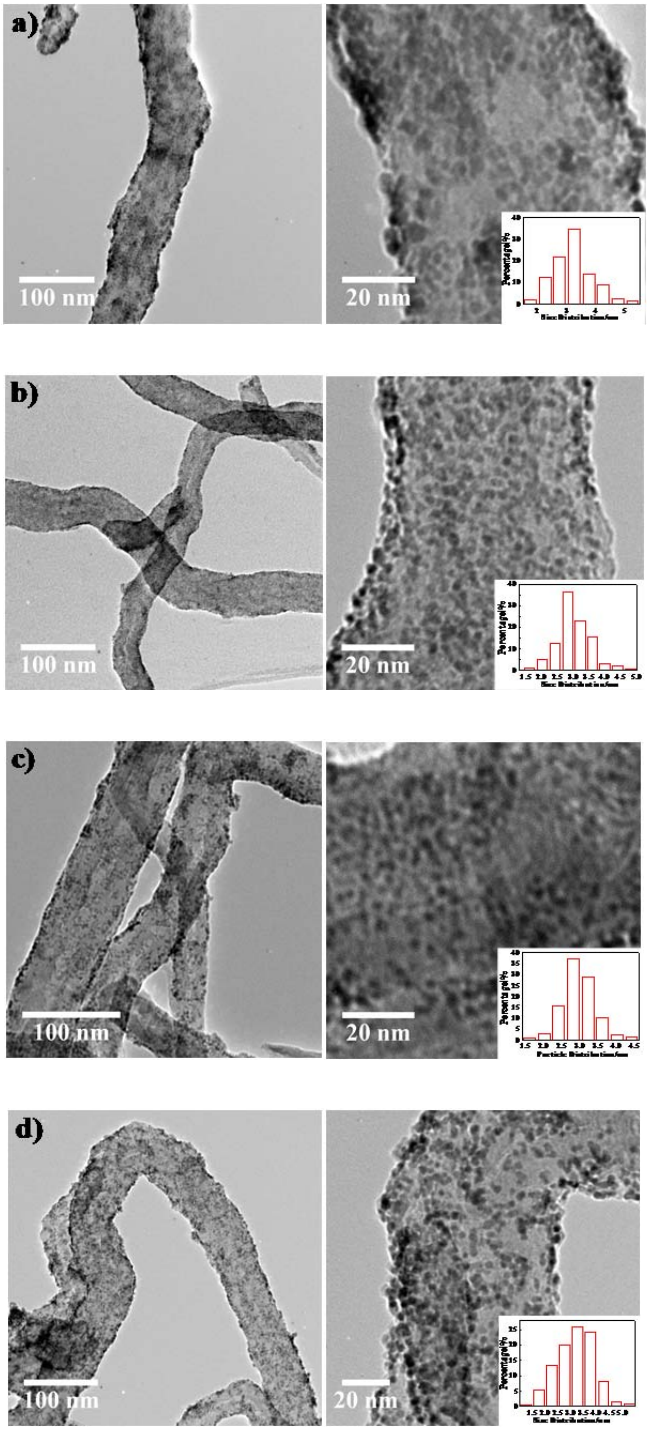

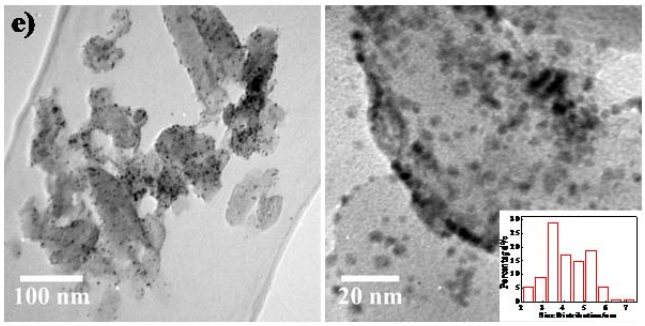

Figure 8.4. TEM images of (a) PtRu/PDDA-CNTs, (b) PtRu/PEI-CNTs, (c) PtRu/AP-CNTs, (d) PtRu/THF-CNTs and (e) PtRu/AO-CNTs. Left image is the low magnification TEM and right image is the corresponding high resolution TEM. The insert is the histograms of particle size distribution

The morphology and particle size distribution of PtRu NPs appears to be affected by the functionalization agents. The PtRu NPs supported on PEI-CNTs, AP-CNTs and THF-CNTs show better dispersion as compared to that on PDDA-CNTs. PDDA used in the present study has a high molecular weight around 100,000, and can interact with the CNTs surface through π-π interaction due to the presence of unsaturated contaminant in the PDDA chain through aligned configuration, helical wrapping, and peseudohelical organization[42, 43]. The presence of 2-3% of the unsaturated contaminant is formed during the polymerization of the monomer. The presence of some agglomeration of PtRu NPs on PDDA-CNTs (Fig. 8.3A) indicate that the orbital overlap through π-π transition via the 2-3% unsaturated contaminant in the PDDA chain may not be sufficient to cover the whole surface of the CNTs, leading to the relatively lower density of PtRu NPs when compared with that PtRu supported on PEI and AP functionalized CNTs.

In the case of THF functionalized CNTs, THF interacts with the CNTs through the σ-π interaction between the π bonds of CNTs and the σ bonds of cyclopentanes of THF[33]. However, the interaction between THF and CNTs would be relatively weak due to the small molecular weight and the weak σ-π interaction. This may explain the

fact that PtRu NPs supported on THF-CNTs have a relatively larger average particle size (3.28 nm) as compared with that supported on PDDA-CNTs, PEI-CNTs as well as AP-CNTs.

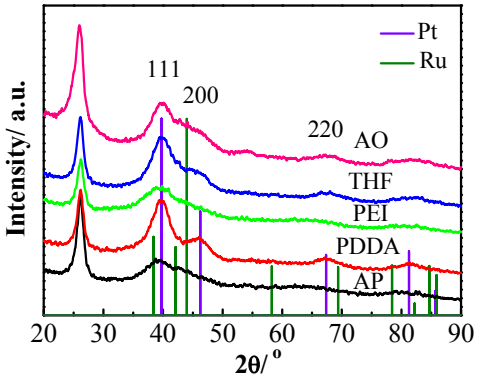

Figure 8.5. XRD patterns of PtRu/PDDA-CNTs, PtRu/PEI-CNTs, PtRu/AP-CNTs, PtRu/THF-CNTs and AO-CNTs.

Fig. 8.5 is the XRD spectra of the as-synthesized PtRu catalysts supported on functionalized CNTs. The high peak near 2θ of 26° originates from the graphitic carbon of CNTs. The XRD results show the presence of broad diffraction peaks at 39.6° and 46.3°, which can be assigned to Pt(111) and Pt(200) and consistent with the face-centered cubic (fcc) structure of platinum[44]. No recognizable Ru hexagonal close-packed (hcp) structure or RuO_2 tetragonal phase was observed in all the samples, suggesting that Ru was mostly incorporated into the Pt fcc lattice and formed Pt-Ru bimetallic alloy (reference: PtRu NPs Supported on Ozone-Treated Mesoporous Carbon Thin Film As Highly Active Anode Materials for Direct Methanol Fuel Cells). For crystallites with a size less than 5 nm, the spread of measured intensities becomes so large that neighboring reflections Pt(111) and Pt(200) start overlapping in amplitude rather than intensity[45]. The XRD patterns show that PtRu supported on PDDA-CNTs, THF-CNTs and AO-CNTs have higher peaks of Pt(111), which indicate increased crystallinity and relatively larger particle sizes of

PtRu NPs supported on PDDA and THF functionalized CNTs. The relatively lower intensity and overlapping of the neighboring reflections of Pt (111) and Pt (200) for PtRu NPs supported on PEI and AP functionalized CNTs indicates PtRu NPs supported on PEI and AP functionalized CNTs have a smaller average particle size, which are consistent with the results obtained from the TEM data.

Table 8.2. Relative concentration and ratio of Pt/Ru and BE of Pt obtained from XPS spectra of PtRu NPs supported on AP, PDDA, PEI and THF functionalized CNTs.

Species	Relative concentration (%)				Species	Relative concentration (%)			
	AP	PDDA	PEI	THF		AP	PDDA	PEI	THF
Pt(0)	42.3	43.3	44	44.2	Ru(0)	46.1	37.6	79.4	55.6
Pt(II)	32.4	32.4	33.8	32	Ru(IV)	35.2	36.8	10.3	33.3
Pt(IV)	25.3	24.1	22	23.9	Ru(IV) (hydrate)	18.7	25.6	10.3	11.1
	Pt:Ru ratio by ICP					Pt:Ru ratio by XPS			
	1.02:1	0.94:1	0.101:1	0.97:1		1.04:1	0.85:1	1.01:1	0.89:1
	Binding Energy, eV					Binding Energy, eV			
	AP	PDDA	PEI	THF		AP	PDDA	PEI	THF
$Pt4f_{7/2}$	75.08	74.85	75.08	74.85	$Ru3p_{3/2}$	485.8	486.5	485.8	485.2
$Pt4f_{5/2}$	71.8	71.5	71.8	71.5	$Ru3p_{1/2}$	463.5	464.2	463.5	463.1

XPS was employed to analyze the composition of PtRu supported on functionalized CNTs and the results are shown in Fig. 6 and Table 8.2. XPS peak deconvolution of Pt 4f and Ru 3p reveal metallic Pt(0), Pt(II) and Pt(IV) on the PtRu NPs on functionalized CNTs are in the range of 42.3-44.2%, 32-33.8% and 22-25.3% (Table 8.2), indicating that the distribution of Pt(0), Pt(II) and Pt(IV) species is similar for the PtRu catalysts studied. However, the binding energy of Pt is affected by the functionalization agent. Pt4f binding energy of PtRu NPs in PtRu/PEI-CNTs and PtRu/AP-CNTs shifted +0.23 eV as compared with that in PtRu/PDDA-CNTs and PtRu/THF-CNTs (Fig. 8.6 C). The change of the binding energy of Pt4f is most likely due to the electron transfer between Pt and amino groups in the PtRu/PEI-CNTs and PtRu/AP-CNTs catalysts, similar to that observed in Pt NPs supported on polypyrrole carbon black[46] and in Au clusters stabilized by poly(N-vinyl-2-pyrrolidone) [47]. In the

case of Ru, there is more metallic Ru (0) observed for PtRu supported on PEI-CNTs (79.4%). Relatively high Ru (0) was also observed for PtRu supported on THF (55.6%) and AP (46.1%) functionalized CNTs. For PtRu/PDDA-CNTs; it is of 37.6% Ru (0).

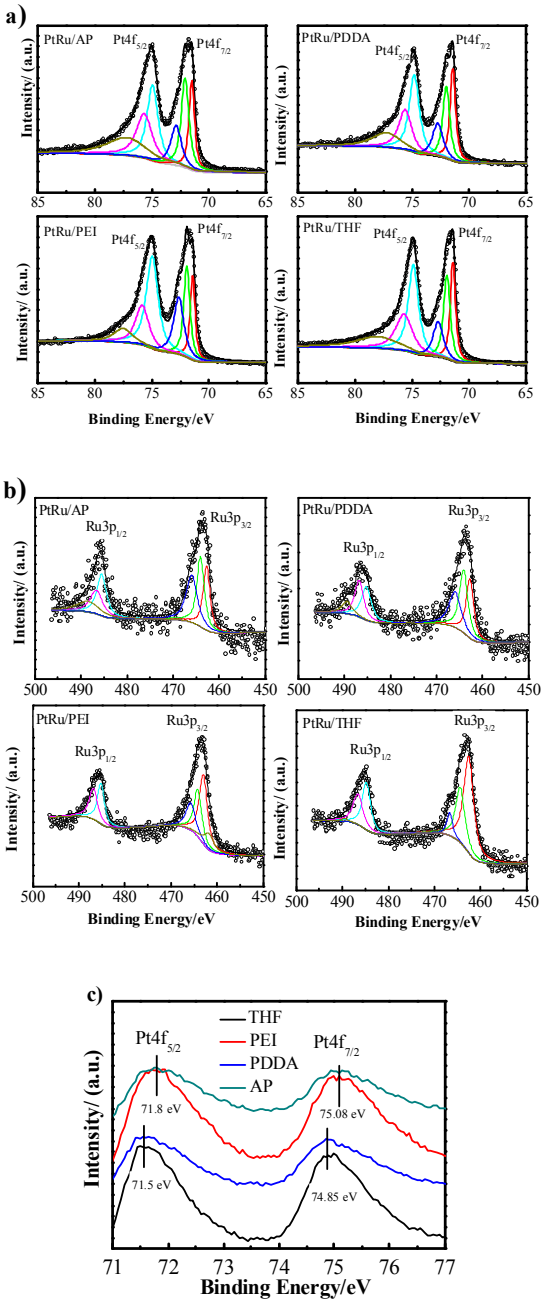

Figure 8.6. XPS core-level spectra for Pt 4f and Ru 3p regions of PtRu supported on AP, PDDA, PEI and THF functionalized CNT

As shown in Table 8.2, the Pt:Ru ratio obtained from XPS is 1.04:1, 0.85:1, 1.01:1 and 0.89:1 for PtRu supported on AP, PDDA, PEI and THF functionalized CNTs, respectively. The results show that PtRu supported on AP and PEI functionalized CNTs present an idea alloy surface with Pt:Ru ratio closing 1:1. While, the composition of Ru for PtRu supported on PDDA and THF functionalized CNTs is slightly higher than that obtained from ICP. Though the average NPs size of the prepared PtRu catalysts are in the range of 2.9-3.2 nm, the XPS results would enhance the composition of atoms in the surface region rather than those of more internal atoms[48]. Thus the XPS data presented here could be regard as near-surface composition somewhat coupled with bulk composition[48, 49]. Hence, the concentration of Ru on the particle surface for PtRu supported on PDDA and THF functionalized CNTs is slightly higher than Pt.

8.3.3 Electrocatalystic activity for CO stripping and methanol oxidation reaction

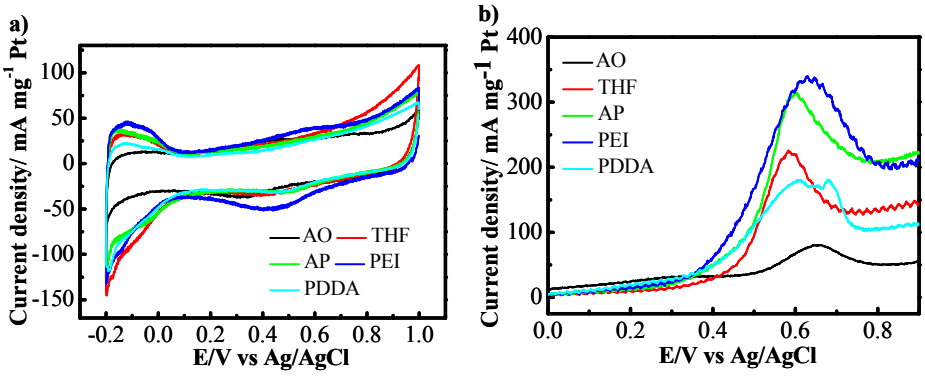

Figure 8.7. Cyclic voltammograms of PtRu/PDDA-CNTs, PtRu/PEI-CNTs, PtRu/AP-CNTs, PtRu/THF-CNTs and PtRu/AO-CNTs in (a) N_2-saturated 0.5 M H_2SO_4 and (b) in a CO-saturated 0.5 M H_2SO_4 solution

Fig. 8.7 A is the cyclic voltammograms (CVs) for PtRu/CNTs catalysts in a nitrogen-saturated 0.5 M H_2SO_4 solution with a sweep rate of 50 mV s^{-1}. The peaks in the

potential region -0.199-0.092 V are associated with the hydrogen adsorption process in the anodic scan[50]. The coulombic charge for hydrogen desorption (Q_H) was used to calculate the active platinum surface of the electrodes. The value of Q_H was calculated as the mean value between the amounts of charge exchanged during the electro-adsorption and desorption of H_2 on Pt sites minus the contribution of ''double layer'' charge. The electrochemical surface area (ESA) of PtRu NPs supported on the functionalized CNTs is listed in the Table 8.3. The values of ESA for PtRu NPs supported on PDDA, PEI, AP, THF and acid functionalized CNTs are 123.3, 141.4, 132.4, 126.2 and 62.3 $m^2\ g^{-1}_{Pt}$ respectively. The results indicate the ESA of PtRu supported on PDDA, PEI, AP and THF functionalized CNTs are quiet similar but more than 98-127% higher than that for PtRu NPs supported on AO-CNTs.

Polyelectrolyte and solvent functionalization also enhances the activity of PtRu NPs for the CO oxidation reaction (Fig. 8.7 B). In the case of PtRu/PEI-CNT and PtRu/AP-CNTs, the peak current density for CO oxidation is 335 and 306 mA mg^{-1}_{Pt} with the same onset potential at 0.35 V and similar peak potential (around 0.59 and 0.63V respectively). On the other hand, the CO oxidation peak is positively shifted to a high potential (0.67 V) for PtRu/ PDDA-CNTs. This may be because PDDA is able to draw electron from Pt atoms and increase the d-band center resulting in a strong chemisorption of CO species[35]. PtRu/THF-CNTs show relatively poor activity for CO oxidation with an onset potential of 0.4V and peak current density of only 204 mA mg^{-1}_{Pt} around 0.58 V. The electrocatalystic activity of PtRu supported on AO-CNTs for CO oxidation is very poor, showing a peak current density of 76 mA mg^{-1}_{Pt} at 0.66 V.

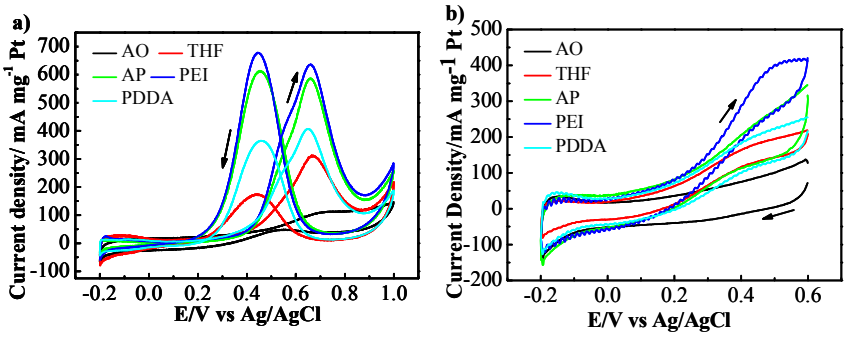

Figure 8.8. Cyclic voltammograms of (a) in N_2-saturated 0.5M H_2SO_4 + 1.0M CH_3OH from -0.2 to 1.0 V, (b) in N_2-saturated 0.5M H_2SO_4 + 1.0M CH_3OH from -0.2 to 0.6 V (c) the comparison of peak current density and current density at 0.4 V for methanol oxidation. The scanning rate was 50 mV s^{-1}.

Fig. 8.8 the activity for methanol oxidation of PtRu NPs supported on functionalized CNTs in a 0.5 M H_2SO_4 + 1.0 M CH_3OH solution at sweeping rate of 50 mV s^{-1}. The electrocatalystic activity of the Pt based electrocatalysts can be assessed by the forward peak current density. The peak current density for the MOR on PtRu/AO-CNTs is 110 mA mg^{-1}_{Pt}, significantly lower than that observed for the reaction on PtRu supported on non-covalent functionalized CNTs (Fig. 8.8 A). This again demonstrates that non-covalent functionalized CNTs are better supports for PtRu NPs, consistent with the data reported elsewhere[5, 24]. The best performance was obtained on PtRu NPs supported on PEI-CNTs and AP-CNTs, achieving a forward peak current of 635 and 585 mA mg^{-1}_{Pt}, which are significantly better than 440 and 425 mA mg^{-1}_{Pt} measured on PtRu/PDDA-CNTs and PtRu/THF-CNTs, respectively. Considering the working state of DMFCs, the current density around 0.3, 0.4 and 0.5 V were also compared with the scan from -0.2 to 0.6 V and the results were presented in Fig. 8.8 B, and the current density and onset potential current density are also given in Table 8.3. The current density observed around 0.3, 0.4 and 0.5 V show a similar trend with peak current density. For example, the current density at 0.4 V is 291, 202, 182 and

158 mA mg^{-1}_{Pt} for PtRu supported on PDDA, PEI, AP and THF functionalized CNTs, which is significantly higher than that of PtRu/AO-CNTs.

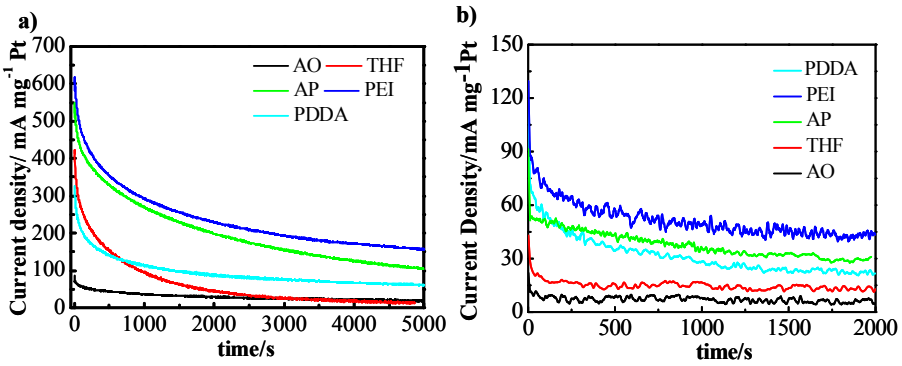

Figure 8.9. Chronoamperometry of PtRu/PDDA-CNTs, PtRu/PEI-CNTs, PtRu/AP-CNTs, PtRu/THF-CNTs and PtRu/AO-CNTs measured in a 0.5 M H_2SO_4 + 1.0M CH_3OH solution under a cell voltage of a) 0.6V, b) 0.4 V.

Fig. 8.9 shows chronoamperometry curves of the PtRu NPs supported on functionalized CNTs, measured in a solution of 0.5 M H_2SO_4 + 1.0 M CH_3OH at a constant potential of 0.6 V and 0.4 V. The oxidation current decrease rather rapidly initially for all the catalysts studied and the decay is most likely due to the poisoning of intermediate species, such as CO_{ads}, CH_3OH_{ads}, $COOH_{ads}$, and CHO_{ads} formed during the MOR [51, 52]. In the case of 0.6 V, which is similar with the extreme working condition of DMFCs, PtRu/PEI-CNTs, PtRu/AP-CNTs and PtRu/PDDA-CNTs reached a relatively stable current density of 160, 106 and 80 mA mg^{-1}_{Pt} respectively after initial current decay. For the reaction on PtRu/THF-CNTs and PtRu/AO-CNTs, the current is 16 and 18 mA mg^{-1}_{Pt} after polarized for 5000 s. The results from the chronoamperometry at 0.4 V show a similar trend with that at 0.6 V (Fig. 8.9 B). These results indicate that PtRu NPs supported on PEI, AP and PDDA functionalized CNTs have a much higher stability as compared to that on THF-CNTs and AO-CNTs.

Table 8.3. Particle Size, electrochemical surface area, peak current density of PtRu supported on functionalized CNTs for methanol oxidation reaction.

Electrocatalysts	Particle size (nm)	ESA (m^2 g^{-1}Pt)	Onset potential (mV)	Peak current (mA mg^{-1}Pt)	Current density (mA mg^{-1}Pt)		
					0.3V	0.4V	0.5V
PDDA	3.13	123.3	250	440	115	182	214
PEI	2.98	141.4	200	635	152	291	375
AP	2.94	132.5	200	585	121	202	276
THF	3.28	126.2	250	425	105	158	195
AO	4.2	62.3	500	110	52	75	100

8.3.4 Effect of functionalization agents

The present study shows that the composition and structure of the functionalization agents play an important role in the electrocatalystic activity of PtRu NPs for the MOR. The much better dispersion and smaller particle size of PtRu supported on non-covalent functionalized CNTs by PDDA, PEI, AP and THF as compared to that supported on acid functionalized CNTs clearly indicates that non-covalent functionalization is very effective to introduce uniformly distributed binding sites on CNTs with no detrimental effect on the intrinsic properties of CNTs. The TGA and Raman analysis demonstrate that non-covalent functionalization enhance the thermal and structural stability of CNTs in particular for the functionalization agents with strong intermolecular force or interaction with the CNTs, e.g., through π-π stacking between the functionalization agents and CNTs. In the case of weak intermolecular force between the functionalization agent like THF and CNTs, the non-covalent functionalization enhances the dispersion of PtRu NPs but has little effect on the thermal and structural stability of CNTs.

The superior of the non-covalent functionalization is also supported by the much higher electrocatalytic activity of PtRu NPs on PDDA, PEI, AP and THF functionalized CNTs as compared to that on AO-CNTs (Fig. 8.8 A). PtRu NPs

supported on PEI, AP, PDDA and THF functionalized CNTs show a significantly higher peak current density (635-425 mA mg^{-1}_{Pt}) than 110 mA mg^{-1}_{Pt} measured on PtRu/AO-CNTs. Most important observation in the present study is the significant dependence of the electrocatalystic stability of the PtRu NPs on the nature of the functionalization agents. The PtRu NPs on PDDA, PEI and AP functionalized CNTs show a much better stability (160 to 80 mA mg^{-1}_{Pt} at 0.6 V after polarized for 5000 s and 60 to 25 mA mg^{-1}_{Pt} at 0.4 V after 2000 s polarization) as compared to that supported on THF-CNTs. The current density measured at 0.6 V after polarized for 5000 s for the reaction on PtRu/THF-CNTs is 16 mA mg^{-1}_{Pt}, close to 18 mA mg^{-1}_{Pt} measured on PtRu/AO-CNTs. This indicates that THF functionalization has no enhance effect on the stability of PtRu electrocatalysts towards the poisoning of the reaction intermediates. The best results were obtained on PtRu/PEI-CNTs with highest activity and stability for the MOR (see Table 8.3). On the other hand, XPS analysis shows that the differences in the PtRu ratio or the electronic states of the PtRu NPs supported on functionalized CNTs are very small (Table 8.2).

PEI and AP contain amino groups while PDDA is a water-soluble quaternary ammonium polyelectrolyte. THF is an oxygen-containing heterocycle with five-membered rings and no nitrogen-containing groups. The electronegativity difference between carbon and oxygen makes the C-O bond moderately polar. PEI is a cationic polymer with repeating unit composed of the amine group and two carbon aliphatic CH_2CH_2 spacer (Fig. 8.1). The assembly of the PEI on CNTs would be strong due to the high molecular weight and the electrostatic attraction between the positively charged PEI and negatively charge CNTs, resulting in the attachment of large amount of N-containing amine group on the outer surface of CNTs. PDDA is also a cationic polymer with N-containing repeating unit, but the π-π interaction with

the CNTs surface primarily occurs through the 2-3% of unsaturated contaminant in the PDDA chain [42, 43]. This may limit the attachment of N-containing functional groups to the surface of CNTs. The lower density of attached N-groups on the CNTs surface may also contribute to the relatively poor dispersion of PtRu NPs on PDDA-CNTs (Fig. 8.4 A). In the case of 1-AP, the interaction with CNTs is via π-π stacking. However, due to the bulk size of benzene rings, the attached nitrogen functional groups on the surface of CNTs would be expected to be smaller than that of PEI but higher than that of PDDA. Fig. 8.10 shows schematically the assembly of PEI, 1-AP and PDDA on the outer wall surface of CNTs. The high density of N-containing functional groups assembled on CNTs in the case of PEI and 1-AP is consistent with the +0.23 eV positive shift of Pt4f BE of PtRu NPs supported on PEI and AP functionalized CNTs as compared to that supported on PDDA-CNTs (Fig.8.6 C).

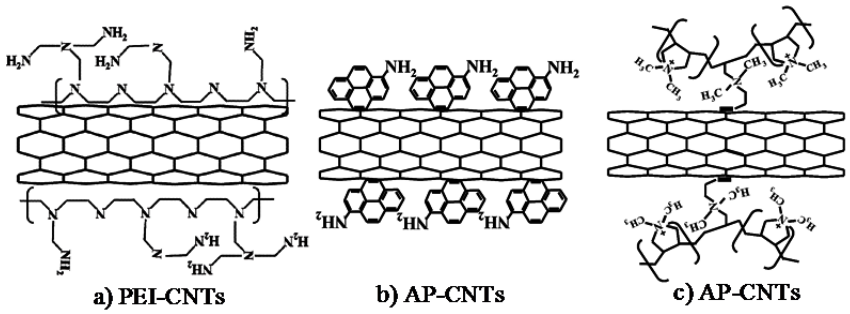

Figure 8.10. Schematic of the assembly of PEI, 1-AP and PDDA on the surface of CNTs.

It has been shown that the doped carbon materials by nitrogen, boron, phosphorus and sulfur have high electrocatalystic activity, high durability and high tolerance towards poisoning of the fuel cell reactions[53-58]. Doping with heteroatoms can modulate the structure, electronic and physicochemical properties of carbon materials like CNTs. For example, for the N-doped electron rich CNTs, the π electrons of carbon can be activated by the conjugation with the lone-pair electrons of N dopants, and the O_2 can be effectively reduced on the neighboring positively charged carbon atoms [59].

Nitrogen doped CNTs and graphene also enhance the activity of Pt and PtRu NPs for the MOR [60-62]. Incorporation of nitrogen into carbon supports also improves the stability of PtRu NPs for the MOR as shown by Olsen et al[63]. The electron-rich dopants such as nitrogen are beneficial for the breaking the electroneutrality of the sp^2 carbon to create charged sites for the adsorption of oxygen species and promote the MOR and ORR[46, 64]. N-containing functionalization agents such as PEI and 1-AP would have higher amino-containing functional groups assembled on the CNTs as compared with that of PDDA, as schematically shown in Fig. 8.10. The positive shift of the BE of Pt4f in the case of PtRu NPs supported on PEI and 1-AP functionalized CNTs indicates the strong interaction between N-containing functional groups assembled on CNTs and PtRu NPs, most likely due to the electron donating of large number of nitrogen-containing functional group assembled on CNTs. In the case of PDDA-CNTs, the electron donating effect of limited quaternary ammonium group assembled on the CNTs surface may be reduced by the electron drawing of cationic PDDA. This may explain the no change in BE of Pt4f for PtRu/PDDA-CNTs (Fig. 8.6 C). The nitrogen in the amino functional groups of the attached functionalization agents can activate the π electrons of CNTs supports and promotes the MOR, similar to that observed for the N-doped carbon materials like CNTs and graphene [59-62]. The promotion effect of nitrogen in the functionalization agents is evidently supported by the high activity and stability of PtRu supported on PEI and 1-AP functionalized CNTs and in less degree on PDDA functionalized CNTs, as compared with THF and AO functionalized CNTs. The results in the present study indicate the strong dependence of the activity and stability of PtRu NPs on the distribution and density of N-containing functional groups assembled on the surface of CNTs in the following order:

PtRu/PEI-CNTs > PtRu/AP-CNTs > PtRu/PDDA-CNTs >> PtRu/THF-CNTs ~ PtRu/AO-CNTs

THF contains no nitrogen and thus, despite the initial high activity of PtRu/THF-CNTs for the MOR, its resistance toward the poisoning of intermediate species such as CO of the MOR is very low as the assembled THF offers no promotion effect for the MOR, similar to that of PtRu/AO-CNTs (Fig. 8.9).

8.4 Conclusion

In this work, the effect of nitrogen-containing functionalization was studied on PtRu NPs supported on PDDA, PEI, AP and THF functionalized CNTs. PtRu NPs with particle size around 3 nm and similar Pt/Ru ratio were successfully synthesized onto the functionalized CNTs. Non-covalent functionalization by polyelectrolytes or solvents is far more effective to uniformly assembly PtRu NPs on CNTs and enhances the thermal and structural stability of CNTs as compared with the conventional acid functionalized CNTs. PtRu catalysts supported on PEI-CNTs and 1-AP-CNTs and in less extent on PDDA-CNTs exhibited much higher electrocatalytic activity and stability toward the MOR as compared to that on THF-CNTs and AO-CNTs. The fundamental reason for the high electrocatalytic activity of PtRu NPs on PEI, 1-AP and in less extend on PDDA functionalized CNTs is the strong interaction between the electron rich nitrogen of the functional group of the functionalization agents and CNTs, indicated by the positive shift of the BE of Pt4f. The strong interaction of electron-rich nitrogen of the functional groups could activate the π electrons of carbon and promote the electrocatalytic activity and stability of PtRu catalysts, similar to that reported on nitrogen-doped carbon materials. The results indicate that the

functionalization agents with ammonium or amino groups are particularly effective to enhance the activity of the PtRu NPs for the MOR of fuel cells.

Acknowledgement

This work was supported by the Australian Research Council (DP120102325 & DP120104932) and the Major International (Regional) Joint Research Project of NNSFC (51210002), China. The authors acknowledge the facilities, scientific and technical assistance of the Curtin University Electron Microscope Facility and Curtin X-Ray Laboratory, both of which are partially funded by the University, State and Commonwealth Governments.

References:

1. M. K. Debe, *Nature*, 2012, 486, 43-51.
2. A. Manthiram, A. V. Murugan, A. Sarkar and T. Muraliganth, *Energy & Environmental Science*, 2008, 1, 621-638.
3. X. Zhao, M. Yin, L. Ma, L. Liang, C. Liu, J. Liao, T. Lu and W. Xing, *Energy & Environmental Science*, 2011, 4, 2736-2753.
4. Y. L. Hsin, K. C. Hwang and C.-T. Yeh, *Journal of the American Chemical Society*, 2007, 129, 9999-10010.
5. S. Wang, X. Wang and S. P. Jiang, *Langmuir*, 2008, 24, 10505-10512.
6. K. Sundmacher, *Industrial & Engineering Chemistry Research*, 2010, 49, 10159-10182.
7. C. Hu, Y. Cao, L. Yang, Z. Bai, Y. Guo, K. Wang, P. Xu and J. Zhou, *Applied Surface Science*, 2011, 257, 7968-7974.
8. O. Guillen-Villafuerte, R. Guil-Lopez, E. Nieto, G. Garcia, J. L. Rodriguez, E. Pastor and J. L. G. Fierro, *International Journal of Hydrogen Energy*, 2012, 37, 7171-7179.
9. V. Neburchilov, J. Martin, H. Wang and J. Zhang, *Journal of Power Sources*, 2007, 169, 221-238.
10. A. Chen and P. Holt-Hindle, *Chemical Reviews*, 2010, 110, 3767-3804.
11. C. Arbizzani, S. Beninati, F. Soavi, A. Varzi and M. Mastragostino, *Journal of Power Sources*, 2008, 185, 615-620.
12. F. A. Viva, M. M. Bruno, M. Jobbágy and H. R. Corti, *The Journal of Physical Chemistry C*, 2011, 116, 4097-4104.

13. M. Tsuji, M. Kubokawa, R. Yano, N. Miyamae, T. Tsuji, M.-S. Jun, S. Hong, S. Lim, S.-H. Yoon and I. Mochida, *Langmuir*, 2006, 23, 387-390.
14. J. Prabhuram, T. S. Zhao, Z. K. Tang, R. Chen and Z. X. Liang, *The Journal of Physical Chemistry B*, 2006, 110, 5245-5252.
15. Y. Kuang, Y. Cui, Y. Zhang, Y. Yu, X. Zhang and J. Chen, *Chemistry-a European Journal*, 2012, 18, 1522-1527.
16. D. Eder, *Chemical Reviews*, 2010, 110, 1348-1385.
17. M. F. L. De Volder, S. H. Tawfick, R. H. Baughman and A. J. Hart, *Science*, 2013, 339, 535-539.
18. Q. Zhang, J.-Q. Huang, W.-Z. Qian, Y.-Y. Zhang and F. Wei, *Small*, 2013, 9, 1237-1265.
19. L. J. Meng, C. L. Fu and Q. H. Lu, *Prog. Nat. Sci.*, 2009, 19, 801-810.
20. A. Hirsch and O. Vostrowsky, in *Functional Molecular Nanostructures*, ed. A. D. Schluter, Springer-Verlag Berlin, Berlin, 2005, vol. 245, pp. 193-237.
21. M. A. Herrero and M. Prato, *Mol. Cryst. Liquid Cryst.*, 2008, 483, 21-32.
22. B. H. Wu, D. Hu, Y. J. Kuang, Y. M. Yu, X. H. Zhang and J. H. Chen, *Chem. Commun.*, 2011, 47, 5253-5255.
23. C. Y. Hu, Y. J. Xu, S. W. Duo, R. F. Zhang and M. S. Li, *J. Chin. Chem. Soc.*, 2009, 56, 234-239.
24. S. Wang, S. P. Jiang and X. Wang, *Nanotechnology*, 2008, 19.
25. K. R. Reddy, B. C. Sin, K. S. Ryu, J.-C. Kim, H. Chung and Y. Lee, *Synthetic Metals*, 2009, 159, 595-603.
26. Y. Cheng and S. P. Jiang, *Electrochimica Acta*, 2013, 99, 124-132.
27. H.-Y. Lee, W. Vogel and P. P.-J. Chu, *Langmuir*, 2011, 27, 14654-14661.
28. G. N. Ostojic, J. R. Ireland and M. C. Hersam, *Langmuir*, 2008, 24, 9784-9789.
29. S. Wang, X. Wang and S. P. Jiang, *Physical Chemistry Chemical Physics*, 2011, 13, 7187-7195.
30. D. Wang, S. Lu and S. P. Jiang, *Chem. Commun.*, 2010, 46, 2058-2060.
31. V. Selvaraj and M. Alagar, *Electrochemistry Communications*, 2007, 9, 1145-1153.
32. Z. Bai, Y. Guo, L. Yang, L. Li, W. Li, P. Xu, C. Hu and K. Wang, *Journal of Power Sources*, 2011, 196, 6232-6237.
33. D. Wang, S. Lu and S. P. Jiang, *Electrochimica Acta*, 2010, 55, 2964-2971.
34. S. Wang, S. P. Jiang, T. J. White, J. Guo and X. Wang, *Journal of Physical Chemistry C*, 2009, 113, 18935-18945.
35. S. Wang, F. Yang, S. P. Jiang, S. Chen and X. Wang, *Electrochemistry Communications*, 2010, 12, 1646-1649.
36. J. Li, W. Yang, H. Zhu, X. Wang, F. Yang, B. Zhang and X. Yang, *Talanta*, 2009, 79, 935-939.
37. S.-C. Yi, C. Y. Jung and W. J. Kim, *Materials Research Bulletin*, 2011, 46, 2433-2440.

38. Z. Lin, L. Ji, W. E. Krause and X. Zhang, *Journal of Power Sources*, 2010, 195, 5520-5526.
39. U. J. Kim, C. A. Furtado, X. M. Liu, G. G. Chen and P. C. Eklund, *Journal of the American Chemical Society*, 2005, 127, 15437-15445.
40. G. Zhang, S. Sun, D. Yang, J.-P. Dodelet and E. Sacher, *Carbon*, 2008, 46, 196-205.
41. Y.-C. Chiang, W.-H. Lin and Y.-C. Chang, *Applied Surface Science*, 2011, 257, 2401-2410.
42. D.-Q. Yang, J.-F. Rochette and E. Sacher, *The Journal of Physical Chemistry B*, 2005, 109, 4481-4484.
43. C. Caddeo, C. Melis, L. Colombo and A. Mattoni, *Journal of Physical Chemistry C*, 2010, 114, 21109-21113.
44. E. Antolini and F. Cardellini, *Journal of Alloys and Compounds*, 2001, 315, 118-122.
45. E. A. Baranova, Y. Le Page, D. Ilin, C. Bock, B. MacDougall and P. H. J. Mercier, *Journal of Alloys and Compounds*, 2009, 471, 387-394.
46. S. Zhang, H. Wang, N. Zhang, F. D. Kong, H. Liu and G. P. Yin, *J. Power Sources*, 2012, 197, 44-49.
47. H. Tsunoyama, N. Ichikuni, H. Sakurai and T. Tsukuda, *J. Am. Chem. Soc.*, 2009, 131, 7086-7093.
48. F. Bensebaa, N. Patrito, Y. Le Page, P. L'Ecuyer and D. Wang, *Journal of Materials Chemistry*, 2004, 14, 3378-3384.
49. K. C. Park, I. Y. Jang, W. Wongwiriyapan, S. Morimoto, Y. J. Kim, Y. C. Jung, T. Toya and M. Endo, *Journal of Materials Chemistry*, 2010, 20, 5345-5354.
50. A. Pozio, M. De Francesco, A. Cemmi, F. Cardellini and L. Giorgi, *Journal of Power Sources*, 2002, 105, 13-19.
51. T. H. M. Housmans, A. H. Wonders and M. T. M. Koper, *The Journal of Physical Chemistry B*, 2006, 110, 10021-10031.
52. P. Ferrin and M. Mavrikakis, *Journal of the American Chemical Society*, 2009, 131, 14381-14389.
53. Y. G. Chen, J. J. Wang, H. Liu, M. N. Banis, R. Y. Li, X. L. Sun, T. K. Sham, S. Y. Ye and S. Knights, *Journal of Physical Chemistry C*, 2011, 115, 3769-3776.
54. S. J. J. Jiang, L. Zhu, Y. W. Ma, X. Z. Wang, J. G. Liu, J. M. Zhu, Y. N. Fan, Z. G. Zou and Z. Hu, *J. Power Sources*, 2010, 195, 7578-7582.
55. D. C. Higgins, D. Meza and Z. W. Chen, *Journal of Physical Chemistry C*, 2010, 114, 21982-21988.
56. D. S. Yu, Q. Zhang and L. M. Dai, *J. Am. Chem. Soc.*, 2010, 132, 15127-15129.
57. Y. K. Zhou, K. Neyerlin, T. S. Olson, S. Pylypenko, J. Bult, H. N. Dinh, T. Gennett, Z. P. Shao and R. O'Hayre, *Energy & Environmental Science*, 2010, 3, 1437-1446.
58. Y. Zheng, Y. Jiao, L. Ge, M. Jaroniec and S. Z. Qiao, *Angew. Chem.-Int. Edit.*, 2013, 52, 3110-3116.
59. B. Shan and K. Cho, *Chem. Phys. Lett.*, 2010, 492, 131-136.

60. R. Chetty, S. Kundu, W. Xia, M. Bron, W. Schuhmann, V. Chirila, W. Brandl, T. Reinecke and M. Muhler, *Electrochimica Acta*, 2009, 54, 4208-4215.
61. G. Wu, R. Swaidan, D. Li and N. Li, *Electrochimica Acta*, 2008, 53, 7622-7629.
62. B. Xiong, Y. K. Zhou, Y. Y. Zhao, J. Wang, X. Chen, R. O'Hayre and Z. P. Shao, *Carbon*, 2013, 52, 181-192.
63. T. S. Olson, A. A. Dameron, K. Wood, S. Pylpenko, K. E. Hurst, S. Christensen, J. B. Bult, D. S. Ginley, R. O'Hayre, H. Dinh and T. Gennett, *J. Electrochem. Soc.*, 2013, 160, F389-F394.
64. T. Maiyalagan, B. Viswanathan and U. Varadaraju, *Electrochem. Commun.*, 2005, 7, 905-912.

Chapter 9: New Core-Shell Structured $PtRuCo_x$ Nanoparticles Supported on Carbon Nanotubes as Highly Active and Durable Electroctalysts for Direct Methanol Fuel Cells

9.1 Introduction

Direct methanol fuel cells (DMFCs) have been extensively studied as promising energy conversion devices due to the fact that methanol fuel has a high energy density (17900 kJ/L) and is safe for storage and transportation.[1-2] However, the sluggish kinetic rates for MOR are significant hurdles for the large-scale production of cost-effective and highly efficient DMFCs. To date, platinum based catalysts have been considered the efficient catalysts for DMFCs. Unfortunately, MOR on Pt-based electrocatalysts is limited by the significant poisoning of reaction intermediate species such as CO.[3-4] Intensified research has been conducted all over the world in the development of active and stable electrocatalysts for MOR, particularly in the area of binary alloy catalysts such as, PtRu,[5-7] PtOs,[8] PtSn,[9] PtW,[8] PtPd,[10] PtPb[11-12] and PtMo.[13] Among these, PtRu catalysts are considered as the best anode catalysts for DMFC.[8, 14] Sustaining efforts are made to pursuit Pt based catalysts with high electrochemical activity, long-term durability and low cost both for cathode and anode in the past decades.[1, 15-16] Many techniques have been developed to manipulate and control the morphology,[17] shape,[18-19] structure,[20-21] composition[9, 22] of the electrocatalysts by alloying Pt with other transition metals and optimizing supports to achieve high activity. Enhanced activity has also been achieved through uniformly

dispersing PtRu nanoparticles (NPs) on carbon nanomaterials such as carbon naotubes, mesoporous carbon or graphene.[4-5, 23-24] The performance of PtRu for MOR can also be enhanced by incorporating the PtRu with metal oxides including MnO_2,[25] TiO_2,[26] SnO_2,[27] MoO_x,[28] WO_3[29] and Fe_2O_3.[30] However, it remains challenging to develop MOR catalysts with high activity and long-term stability.

Research recently focuses on the manipulation of nanoparticle structure in order to optimize the catalyst activity without increasing the loading of Pt.[31-32] The dealloying of less noble elements from Pt based alloy NPs is a useful strategy to create high active surface area alloy that exhibits a Pt skeleton surface, or a highly coordinated pure Pt skin.[33-34] Another strategy is to control the distribution of Pt in the particle to form core-shell,[20, 31, 35-36] or Pt skin structure[32, 37] to alter the binding energy and to enhance the catalyst performance. The core-shell structured NPs with monolayer or several layers of precious group metals on non-precious group metals core is of great interest to reduce the Pt loading and to increase the activity by tuning the activity of the shell metal through interactions with the core, and at the same time the Pt shell can protect the core metal from corrosion and result in higher long-term stability.[31, 35-36, 38-40] Pt-Ru core-shell NPs were shown to have enhanced activity for DMFCs.[41-43] Thermal annealing can lead to the segregation Pt atoms to the surface in controlled atmosphere.[40, 44] For example, annealing the PtNi NPs resulted in a Pt-skeleton-type surface structure with improved activity.[32] $PtCu_3$ prepared by heat-treatment and dealloying shows improved activity and stability for the O_2 reduction reaction.[45] Pt_3Co NPs synthesized using an impregnation reduction method and annealed at 400 ^oC and 700 ^oC under H_2 atmosphere led to the formation of ordered Pt_3Co intermetallic cores with a 2-3 atomic-layer-thick platinum shell, exhibiting over 200% increase in mass activity and over 300% increase in specific activity for the O_2

reduction reaction when compared with the disordered Pt_3Co alloy NPs as well as Pt/C.[46]

To the best of our knowledge, there appears to be no report on the combining of dealloying and annealing through manipulating and controling the PtRu NPs to simultaneously achieves enhanced activity and stability for MOR. Here, we developed a method to design carbon nanotube supported PtRu skinned $PtRuCo_x$ core-shell NPs via successive dealloying and annealing treatment. The prepared $PtRuCo_x$ catalysts exhibit enhanced activity and excellent stability for MOR of DMFCs.

9.2 Experimental

9.2.1 Materials

Materials used in this experiment include sulfuric acid (99.5%, Fluka), nitric acid (65%, Fluka), ethanol (Sigma-Aldrich), methanol (Sigma-Aldrich), MWNTs (Shenzhen Nano, China), H_2PtCl_6 (Sigma-Aldrich), $RuCl_3$ (Sigma-Aldrich), $Co(NO_3)_2$ (Sigma-Aldrich), ethylene glycol (Sigma-Aldrich), Nafion solution (5% in isoproponal and water), poly(ethyleneimine) (PEI, molecular weight ~1300, Sigma-Aldrich), and PtRu/C (60 wt% PtRu/C, Alfa Aesar). All the chemicals were used without further purification.

9.2.2 Synthesis of $PtRuCo_x$/CNTs electrocatalysts

The procedures to synthesize PtRuCo catalysts supported on PEI-fucntionalized CNTs via dealloy and annealing was presented in Fig. 9.1. Pristine CNTs (200 mg) was sonicated in 400 mL Milli-Q water in the presence of 0.5 wt% PEI for 1 h, then the dispersion was stirred for overnight, filtrated using nylon membrane and washed for several times to remove the excess PEI. The obtained solid was then dried in

vacuum oven for 24 h at 71 ^{o}C. The product was noted as PEI-CNTs. PEI-CNTs (100 mg) was first ultrasonicated in 150 mL ethylene glycol (EG) solution for 60 min before the addition of approximate amount of H_2PtCl_6, $RuCl_3$ and $Co(NO_3)_2$ with atomic ratio of Pt:Ru:Co = 1:1:1. The solution was controlled at a pH of slightly less than 7 (e.g., pH 6.5) to maintain a weak acidity and was bubbled with pure N_2 for 15 min. The beaker was then placed in a microwave oven (1000 W) and heated for 4 min, followed by stirring overnight under pH 3-4. The solution was filtered using a nylon filter membrane and washed for several times. The as-synthesized catalysts were noted as PtRuCo. Dealloying of PtRuCo was carried out by mixing 50 mg PtRuCo in 50mL 1:1 HNO_3 and ultra-sonicated for 5 min. After the acid treatment, the PtRuCo catalysts were annealed at 200, 300, 350, 400, 450, and 500℃ under argon flow for 1 h. In this paper, the assembled PtRuCo NP alloy is denoted as PtRuCo, PtRuCo after dealloying is denoted as $PtRuCo_x$, $PtRuCo_x$ after annealed at different temperature is denoted as $PtRuCo_x$-T, e.g. $PtRuCo_x$ after annealed at 450℃ is denoted as $PtRuCo_x$-450. For comparison, PtRuCo without dealloying was annealed at 450 ^{o}C and was denoted as PtRuCo-450.

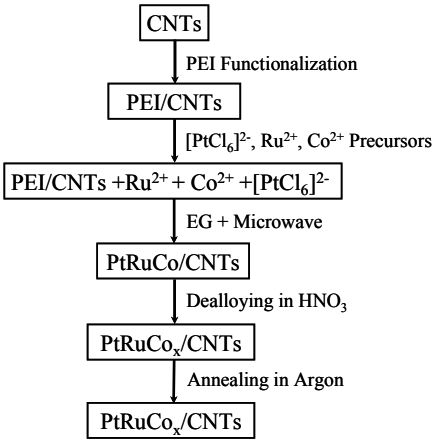

Figure 9.1. Procedure of the synthesis of core-shell structured $PtRuCo_x$ NPs supported on PEI-functionalized CNTs.

9.2.3 Characterization

Microstructures of PtRuCo, $PtRuCo_x$ and $PtRuCo_x$-T catalysts supported on CNT were characterized using a high resolution TEM transmission electron microscope (TEM JEOL3000) with operating at 300 kV. The products were identified with X-ray diffractometer (XRD, Rigaku D/MAX RINT 2500) operated at 40 kV and 30 mA with Cu Ka (l = 1.5406 A˚) in the range of 20-90^o. The X-ray photoelectron spectroscopy (XPS) measurements were carried out on a XPS apparatus (ESCALAB 250, Thermo-VG Scientific Ltd.) with photon energy of 1450 eV. The Pt:Ru:Co ratio of the catalysts was also analyzed by Inductively Coupled Plasma (ICP-OES, IRIS Intrepid Ⅱ XSP,USA). The solution for ICP analysis were prepared as follow: PtRuCo catalysts were burned in thermal gravimetric pan, and the solid were collected and digested in polytetrafluoroethylene (PTFE) digestion tank using microwave dissolver (SINEO, HDS-8G) with 10 mL aqua regia (the procedure was set as: 150 ^{o}C, 5 min, 180 ^{o}C, 5 min, 200 ^{o}C, 10 min, 230 ^{o}C, 20 min). And the $PtRuCo_x$-450 was further studied high angle annular dark field STEM and elemental mapping on Titan G2 60-300 at 80 kV.

The electrochemical measurements were conducted in a standard electrochemical cell using a Princeton potentiostat (Versastat3，USA). Generally, 4 mg of the catalyst was ultrasonically mixed in 4 mL of ethanol nafion mixture (with Ethnol: Nafion 9:1) to form a homogeneous ink, followed by dropping certain amount of the catalyst ink onto the surface of a glassy carbon electrode (GCE). The diameter of GCE was 4 mm. The Pt loading is controlled at 0.01 mg cm^{-2}. Pt foil (3.0 cm^2) and Ag/AgCl (saturated KCl) electrodes were used as the counter and reference electrodes, respectively. Potentials in the present study were given versus Ag/AgCl reference electrode. The electrochemical active surface area (ESA) was measured in a N_2-saturated 0.5 M

H_2SO_4 solution at a scan rate of 0.05 V s^{-1} and the elelctrocatalytic activity and stability for the MOR was measured in a N_2-saturated 0.5 H_2SO_4 + 1.0 M CH_3OH solution at a scan rate of 0.05 V s^{-1}. The microstructure stability were performed by cyclic voltammetry in the potential window of -0.2-1.0 V in N_2-saturated 0.5 M H_2SO_4 + 1.0 M CH_3OH solution. For the purpose of comparison, the structural stability of conventional 60%PtRu/C from Alfa Aesar was also measured under the same test conditions.

The CO-stripping was performed in a N_2-saturated 0.5 M H_2SO_4 solution. First, 0.5 M H_2SO_4 solution was bubbled with pure N_2 for 15 min, then CO was adsorbed by flowing 0.5% CO in N_2 at a flow rate of 50 ml min^{-1} through the working electrode compartment by keeping the potential at -0.12 V versus Ag/AgCl for 30 min, followed by switching the gas to N_2 for 30 min by keeping at the same potential. The potential was then scanned from 0.0 to 1.0 V at a scan rate of 0.05 V s^{-1}.

9.3 Results and discussion

9.3.1 TEM, XRD and XPS analysis

Fig. 9.2 is the high resolution TEM micrographs of PtRuCo and $PtRuCo_x$ NPs annealed at different temperatures. PtRuCo alloy NPs were uniformly deposited onto the PEI functionalized CNTs, and the average size of the alloy catalysts is 2.4±0.5 nm (Fig. 9.2A). The particle sizes distribution is symmetrical with 82% of the NPs in the range of 1.6-2.5 nm. The Fast Fourier Transform (FFT) analysis of a PtRuCo alloy particle show that atomic plane distance is 0.22 nm, which is consistent with the parameter (0.22-0.23 nm) reported for PtRu alloy particles,[47-48] indicating that the alloying of Co has no effect on the PtRu alloy lattice parameters. After dealloying treatment, the average size of $PtRuCo_x$ is decreased to 2.1±0.4 nm, and NPs with sizes

less than 2.3 nm is about 89% due to the corrosion of surface cobalt from the alloy particles (Fig. 9.2 B). Atomic plane distance of 0.23 and 0.2 nm detected by the FFT analysis of $PtRuCo_x$ is due to the deviation of the smaller Co atoms from the Pt fcc lattice and might expose Ru lattice, hence decrease the alloy degree of NPs. Oezaslan et al[49] studied the size-dependent morphology of dealloyed bimetallic catalysts and found that nanopores or hollows were not observed in dealloyed Pt-Co and Pt-Cu NPs with size less than 5 nm due to the high surface energy of voids of small particles and the rapid annihilation process of vacancies by highly mobile low coordinated Pt surface atoms. Same could also be true for the dealloyed $PtRuCo_x$ NPs due to the small size.

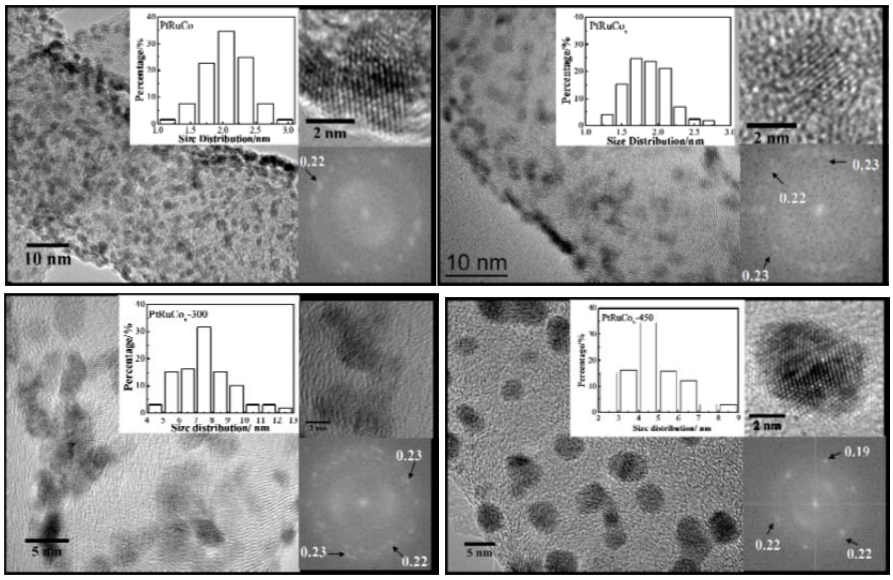

Figure 9.2. TEM micrographs, histogram and Fast Fourier Transform (FFT) images of A) PtRuCo, B) $PtRuCo_x$, C) $PtRuCo_x$-300, and D) $PtRuCo_x$-450.

After annealed at 300 ^oC, the $PtRuCo_x$ catalysts were characterized by branched nanodendrites (average size of 8.1±1.7 nm) with diameter of 2-4 nm (Fig. 9.2C). This indicates that thermal treatment has a great influence on the morphology of the dealloyed $PtRuCo_x$ NPs due to the coalescence and agglomeration of dealloyed NPs. With the increase of the annealing temperature to 450 ^oC, the $PtRuCo_x$ shows multiple

planar-twinned NPs with average particle size of 4.2±0.7 nm (Fig. 9.2D). No branched nanodendrites were observed. The atomic plane distance was 0.22 nm and 0.19 nm and the decrease in the atomic plane distance indicates the increase of the crystallinity of $PtRuCo_x$ as compared to that annealed at 300°C.[32, 50]

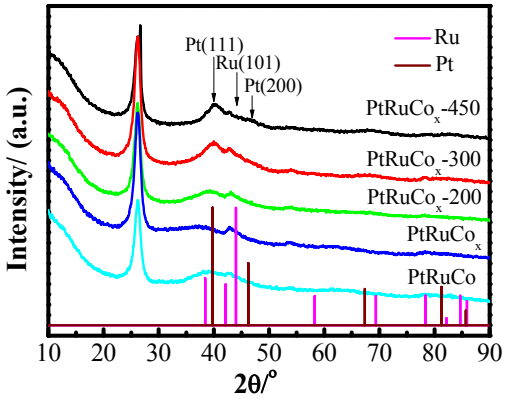

Figure 9.3. XRD patterns of PtRuCo, $PtRuCo_x$, $PtRuCo_x$-200, $PtRuCo_x$-300 and $PtRuCo_x$-450.

X-ray diffraction (XRD) measurements were used to identify the crystalline structures of PtRuCo, $PtRuCo_x$ and $PtRuCo_x$-T, and the results are shown in Fig. 9.3. An overlapping and collapse of peaks between 2Θ = 35 to 46° might be because of the formation of small size PtRuCo alloy. Sun et al claimed that reducing the diameter of Pt NPs down to around 1 nm would lead to a collapse in the crystalline structure based on the combined experimental and computational studies.[51] The peak for Pt (111) was observed at 2Θ= 39.5° for PtRuCo, and the peak shifted to 37.9° after dealloying. The lattice diameter is 0.3942 nm for PtRuCo and 0.4170 nm for $PtRuCo_x$. These results indicate the increase of d-spacing and expansion of the lattice constant due to the dealloying or corrosion of the smaller Co atoms from the Pt fcc lattice. The increase of the peak intensity near Ru (101) and the decrease in the intensity of Pt (111) peak of $PtRuCo_x$ could be due to the reduced alloy degree and crystallinity of PtRuCo after dealloying. The intensity of the Pt(111) peak of the

$PtRuCo_x$ increases with the annealing temperature, indicating the increase of crystallinity. With the increase of temperature, the peaks of Pt (111) are shifted to higher 2Θ values. For example, the peak for Pt (111) was observed at 2Θ of 39.5 and 40.1^o for $PtRuCo_x$-300 and $PtRuCo_x$-450, and the lattice parameters also changed to 0.3913 and 0.3891 nm, respectively. These results demonstrated the decrease of lattice space (lattice shrinking) after annealing. On the other hand, the peak intensity around Ru(101) decreases with the increase of annealing temperature and almost disappeared after annealing at 450 ^{o}C. This indicates the reconstruction of the $PtRuCo_x$ NPs and the most Ru is incorporated into the Pt (111) lattice to form an intermetallic alloy phase.

Table 9.1. Particle size, electrochemical surface area, peak current density of PtRuCo, $PtRuCo_x$ and $PtRuCo_x$ annealed at different temperatures.

Electrocatalyst	Particle size (nm)	Lattice parameter (nm)	ESA (m^2/g Pt)	Onset potential (V)	Peak Current density for MOR (A g^{-1}Pt)	CO onset potential (V)
PtRuCo	2.4	0.3942	60.5	0.3	360	0.522
$PtRuCo_x$	2.1	0.4170	110.5	0.22	608	0.400
$PtRuCo_x$-200	-	0.3992	116.7	0.22	750	0.390
$PtRuCo_x$-300	8.1	0.3913	70.2	0.22	905	0.380
$PtRuCo_x$-350	-	-	-	0.22	910	-
$PtRuCo_x$-400	-	-	-	0.22	945	-
$PtRuCo_x$-450	4.2	0.3885	67.9	0.22	1017	0.280
$PtRuCo_x$-500	-	-	-	0.22	890	-
PtRuCo-450	-	-	53.1	0.22	809	-

XPS spectra reveal more information on the near surface composition of PtRuCo and $PtRuCo_x$ NPs. Fig. 9.4A show the XPS survey spectra of PtRuCo, $PtRuCo_x$, $PtRuCo_x$-300, $PtRuCo_x$- 450, and Fig. 9.4B-C show the XPS core-level spectra for Pt4f, Ru3p and Co2p regions, respectively. The binding energy (BE) of $Pt4f_{7/2}$ and $Pt4f_{5/2}$ was observed at 71.6 and 74.9 eV for PtRuCo, and was positively shifted by 0.76 eV (72.32 eV) and 0.46 eV (75.4 eV), respectively for $PtRuCo_x$ after dealloying. The increase in BE is due to the presence of higher oxidation state components (eg. PtO) resulted from the HNO_3 treatment. The $Ru3p_{1/2}$ and $Ru3p_{3/2}$ peaks were observed at

485.9 and 463.3 eV for PtRuCo, and 487.0 and 464.3 eV for $PtRuCo_x$ (Fig. 9.4C). The peak for Co2p was observed at 782.5 eV for PtRuCo, however, the Co2p peak disappeared after dealloying most likely due to the depletion of surface Co atoms and the low concentration of Co in the $PtRuCo_x$ NPs (Fig. 9.4D). Annealing treatment changes the binding energy for Pt4f and Ru3p. For example, the BE was observed at 71.6 and 75.0 eV for $Pt4f_{7/2}$ and $Pt4f_{5/2}$ for $PtRuCo_x$ annealed at 450°C, $PtRuCo_x$-450, which is similar with that of PtRuCo. BE of $Ru3p_{1/2}$ and $Ru3p_{3/2}$ is at 485 and 462.5 eV for $PtRuCo_x$-450, respectively, which is slightly lower than that of PtRuCo, indicating the increase of metallic Ru concentration.

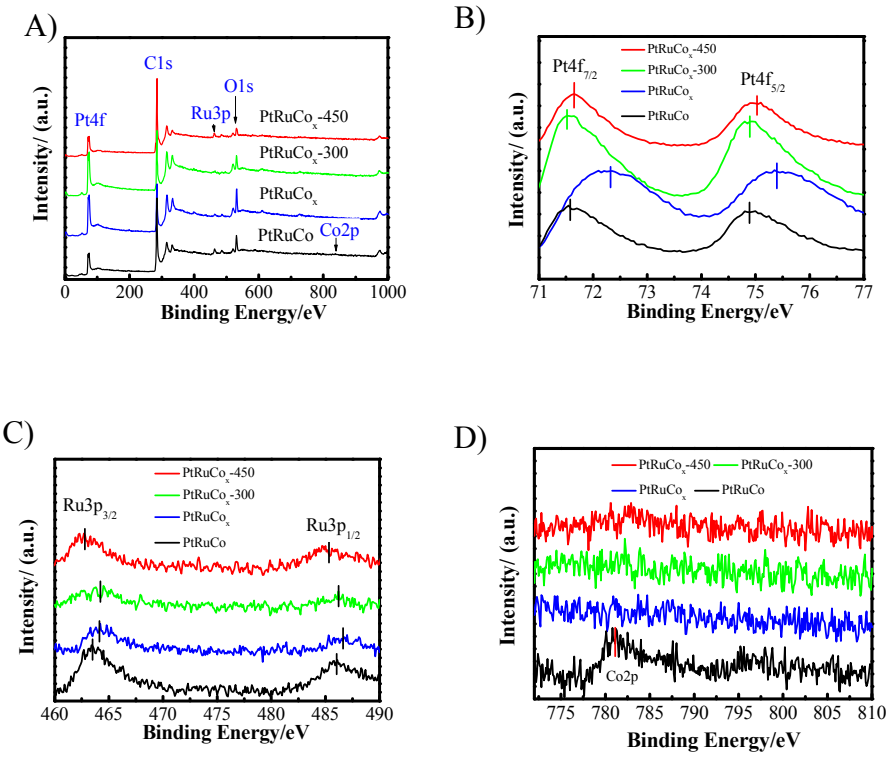

Figure 9.4. A) XPS patterns of PtRuCo, $PtRuCo_x$, $PtRuCo_x$-300, $PtRuCo_x$-450, and core-level spectra for B) Pt4f regions, C) Ru3p regions, D) Co2p regions.

Fig. 9.5 shows the peak deconvolution of Pt4f of the PtRuCo and $PtRuCo_x$ annealed at different temperatures. The metallic Pt(0) decreased from 45.2% to 38.4% after dealloying of PtRuCo most likely due to the HNO_3 acid treatment, which oxidize

metallic Pt(0) to Pt(IV) and Pt(II) (Fig. 9.5A). After annealed at 300 ^{o}C, $PtRuCo_x$-300, the proportion of metallic Pt(0) increase from 38.4% to 45.2% without change in the Pt:Ru ratio. With further increase of the annealing temperature to 450 ^{o}C, metallic Pt(0) increased to 50.1%, which might because of the segregation of Pt to the surface and the reduction of Pt oxides. Similar trend were also observed for Ru(0), Ru (II) and Ru (IV) (hydrate) species on the $PtRuCo_x$ after the annealing (Fig. 9.5B). A significantly decrease of Ru(0) and increase of Ru(IV) indicate the formation of RuO_2 after PtRuCo was dealloyed in HNO_3 solution. Annealing treatment under argon atmosphere reduces the ruthenium oxides and increases the metallic Ru(0) species from 6% for $PtRuCo_x$ to 50.8% for $PtRuCo_x$-450. The BE values and element distribution of the catalysts are summarized in Table 9.2.

Table 9.2. Relative concentration and binding energy of Pt and Ru species and the Pt/Ru composition ratios obtained from XPS and ICP analysis of PtRuCo, $PtRuCo_x$, $PtRuCo_x$-300 and $PtRuCo_x$-450.

Species	Relative concentration (%)			
	PtRuCo	$PtRuCo_x$	$PtRuCo_x$-300	$PtRuCo_x$-450
Pt(0)	45.2	38.4	45.2	50.1
Pt(II)	32.8	33.7	30.6	36.5
Pt(IV)	22.0	27.9	24.2	13.4
Ru(0)	28.3	6.6	32.2	50.8
Ru(IV)	40.9	59.1	42.6	29.6
Ru(IV) (hydrate)	30.8	34.3	25.2	19.6
	Binding energy (eV)			
$Pt4f_{5/2}$	74.9	75.4	74.9	75.0
$Pt4f_{7/2}$	71.6	72.3	71.6	71.6
$Ru3p_{3/2}$	463.4	464.4	464.6	462.5
Ru $3p_{1/2}$	485.9	486.9	486.2	485.0
Pt:Ru:Co ratio (XPS)	1:1.15:0.27	1:0.56:0	1:0.56:0	1:1.01:0
Pt:Ru:Co ratio (ICP)	1:0.98:1.05	1:0.97:0.48	1:0.97:0.48	1:0.97:0.48

The composition of PtRuCo and $PtRuCo_x$ annealed at different temperatures was analyzed by ICP and XPS. The Pt:Ru:Co ratio of PtRuCo alloy NPs is 1:0.98:1.05 based on the ICP analysis, which is close to the targeted PtRuCo ratio of 1:1:1. This indicates the facile synthesis method of the self-assembly of multi-component Pt, Ru, Co precursor compositions onto the PEI functionalized CNTs. However, the XPS

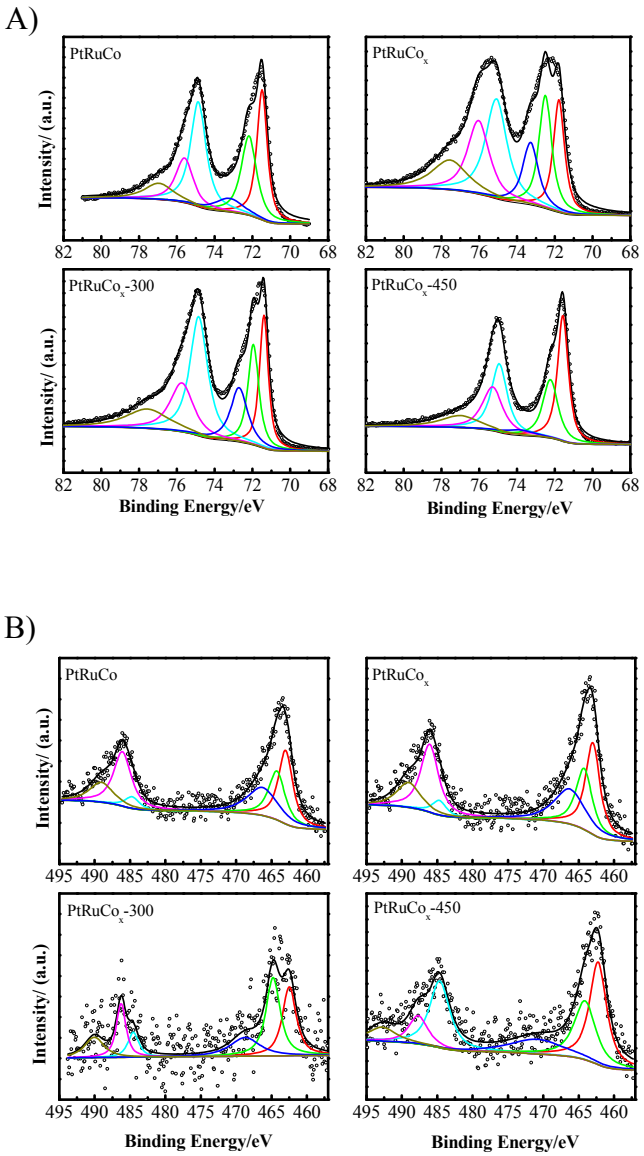

Figure 9.5. Peak deconvolution of A) Pt 4f, B) Ru 3p for PtRuCo, PtRuCo$_x$, PtRuCo$_x$-300, PtRuCo$_x$-450 from the XPS measurement.

analysis shows that the PtRuCo alloy NPs have a composition of Pt:Ru:Co = 1:1.15:0.27, very different from 1:0.98:1.05 of the ICP data in terms of the cobalt content. The significant difference in the atomic ratio of ICP and XPS data indicates that the XPS data obtained from photon energy of 1450 eV could be regard as near-surface composition.[52-55] This indicates the PtRuCo alloy NPs have a PtRu-rich surface and Co-rich core. After dealloying treatment, no Co was detect by XPS for

$PtRuCo_x$ (Fig. 9.4D), indicating the chemical dealloying completely leaches out the surface base metal Co. The Pt:Ru:Co ratio is 1:0.56:0 from XPS, also very different from the 1:0.91:0.48 ratio obtained from ICP. This indicates that $PtRuCo_x$ NPs may be characterized by a Co-free PtRu-skinned shell structure. After annealing the $PtRuCo_x$ at 300 ^oC, the Pt:Ru:Co ratio is 1:0.56:0 from XPS data, almost the same as that obtained from $PtRuCo_x$. In the case of $PtRuCo_x$-450, the Pt:Ru:Co ratio changed to 1:1.01:0 based on the XPS data, indicating surface restructuring of $PtRuCo_x$ NPs annealed at 450 ^oC. The XPS and ICP results indicate that subsequent dealloying and annealing treatment of PtRuCo alloy NPs would lead to the formation of the core-shell nanostructures with Co-rich core and PtRu shell.

In order to prove the core-shell nanostructures with Co-rich core and PtRu shell, elemental mapping using EDS coupled with STEM were carried out for PtRuCo-450. Fig. 9.6 shows the HAADF/STEM images and EDS elemental mapping of Pt, Ru and Co of NPs supported on CNTs. Fig. 9.6 A demenstarated that all three elements, Pt, Ru and Co, were detected for all the particles and the Pt, Ru and Co distributions are overlapped together. No single element particle was observed demonstrating homogenous alloy particles were form. The PtRuCo alloy particles are further explored by the elemental mapping and line scan of single PtRuCo nanoparticle. Fig. 9.6 B shows one typical PtRuCo NPs for $PtRuCo_x$-450. The distribution areas of Pt and Ru are similar to the size of PtRuCo NPs, while the distribution of Co is small than the particle size and the Co is enriched in the core of the particles. The line scan profile (Fig. 9.6 B inserted) intensity indicate that Pt and Ru follows the same trend, however, the higher intensity of Co only observed at the core of the PtRuCo nanoparticle. These results directly demonstrate that the PtRuCo form a ~1 nm thick Co free PtRu shell and a Co rich PtRuCo core.

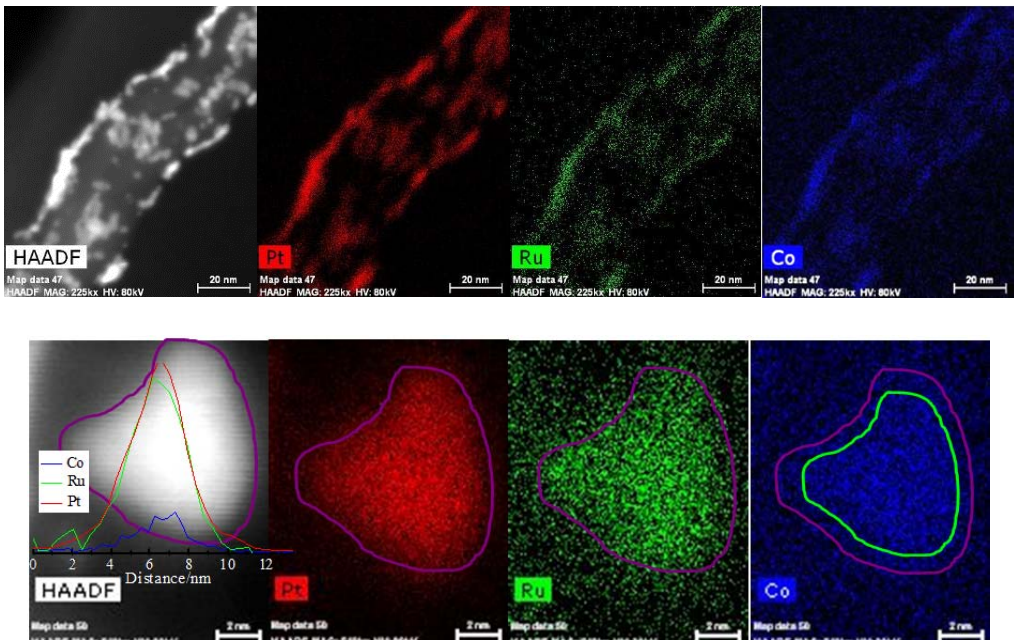

Figure 9.6. The HAADF-STEM-EDS mapping images of $PtRuCo_x$-450 particles.

9.3.2 Electrochemical surface area and CO stripping

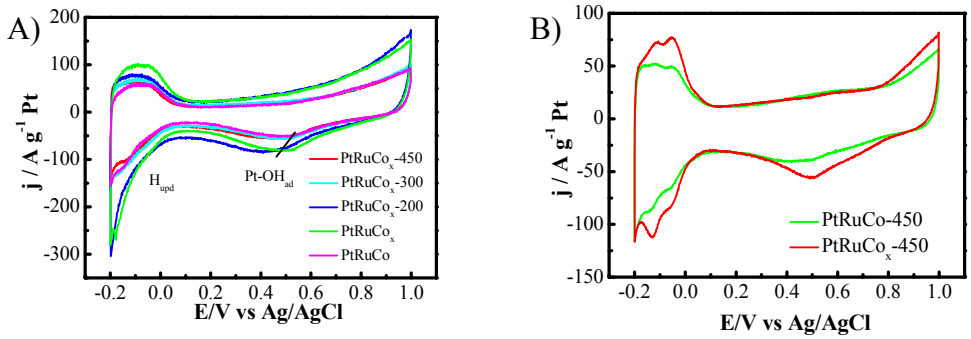

Figure 9.7. Cyclic voltammograms of A) PtRuCo, $PtRuCo_x$, and $PtRuCo_x$-T, B) Comparison of PtRuCo and $PtRuCo_x$ annealed at 450 ^oC in N_2-saturated 0.5 M H_2SO_4 solution. The scan rate was 0.05 V s^{-1}.

The electrochemical surface area (ESA) of the obtained catalyst were calculated through the area of the hydrogen adsorption and desorption peak after correcting for the double layer charging current from the CVs measured in 0.5 M H_2SO_4 solutions, and the results are shown in Fig. 9.7. The calculated ESA is given in Table 9.2. Dealloying of PtRuCo alloy NPs can significantly increase the ESA for the catalysts.

As shown in Fig. 9.7 and Table 9.2, the ESA of $PtRuCo_x$ is 110.5 m^2 g^{-1}_{Pt}, which is about 1.8 times larger than that of PtRuCo alloy NPs (ESA=60.5 m^2 g^{-1}_{Pt}). Dealloying of less noble metal Co can expose the underneath Pt to the surface which lead to the increased ESA. The depletion of surface cobalt elements of $PtRuCo_x$ is consistent with the TEM, XRD and XPS results. After annealing at 200 ^oC for 1 h, the ESA slightly decreased to 106 m^2 g^{-1}_{Pt}. When the annealing temperature was increased to 300 ^oC, the ESA was dramatically reduced to 70 m^2 g^{-1}_{Pt} most likely due to the aggregation of small nanoclusters and the formation of nanodendrites (Fig. 9.2 C). In the case of $PtRuCo_x$ annealed at 450 ^oC, $PtRuCo_x$-450, ESA is 63.9 m^2 g^{-1}_{Pt}, which is slightly higher than 60.5 m^2 g^{-1}_{Pt} of the original PtRuCo NPs. However, direct annealing of PtRuCo alloy NPs without the dealloying treatment will result in the substantial decrease in the ESA. As shown in Fig. 9.7B, the ESA of PtRuCo alloy NPs annealed at 450^oC is 53.1 m^2 g^{-1}_{Pt}, lower than 63.9 m^2 g^{-1}_{Pt} obtained on $PtRuCo_x$ dealloyed NPs annealed at 450^oC.

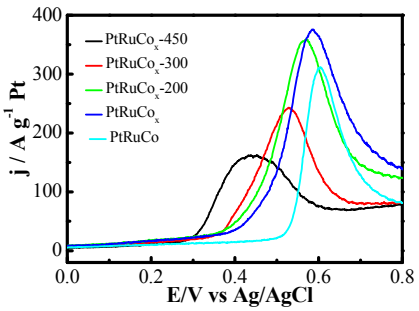

Figure 9.8. CO-stripping of PtRuCo, $PtRuCo_x$, and $PtRuCo_x$-T, measured in CO saturated 0.5 M H_2SO_4 solution at a scan rate of 0.05 V s^{-1}.

Fig. 9.8 is the CO-stripping curves of PtRuCo, $PtRuCo_x$ and $PtRuCo_x$-T, measured in CO saturated 0.5 M H_2SO_4. For the CO oxidation reaction, PtRuCo shows a sharp oxidation peak at 0.604 V and an onset potential at 0.522 V. Both the onset and peak

potentials are negatively shifted to 0.4 V and 0.684 V on $PtRuCo_x$, indicated the increased activity of the $PtRuCo_x$ for CO oxidation, as compared to PtRuCo alloy catalysts. Annealing of $PtRuCo_x$ at 200 ^oC did not change the onset and peak potentials for the CO oxidation. However, for the reaction on $PtRuCo_x$ annealed at 450 ^oC, $PtRuCo_x$-450, there is a significant negative shift of the onset and peak potentials to 0.28 V and 0.42 V, respectively, indicating the significantly enhanced electrocatalystic activity of the $PtRuCo_x$-450 for the CO oxidation. Ochal et al. proposed that the CO stripping voltammetry can be used as a diagnostic tool for determination of surface composition of PtRu NPs, and their results show the CO oxidation on PtRu (1:1) alloy NPs started at 0.31 V with peak potential at ~0.65 V, while for PtRu core-shell structure, the onset potential for CO oxidation was observed at 0.28 V with the peak potential at ~0.4 V,[35] in excellent agreement with the CO stripping results on the $PtRuCo_x$-450 catalysts of this study. The CO oxidation behavior observed on $PtRuCo_x$-450 is similar with the result reported for PtRu core-shell structured electrocatalysts,[35, 45, 56] which indirectly demonstrate the formation of PtRu-rich skin on the surface of $PtRuCo_x$-450 NPs, consistent with the HAADF-STEM-EDS results.

9.3.3 Methanol oxidation reaction

Fig. 9.9 is the cyclic voltammetry for the MOR on PtRuCo, $PtRuCo_x$ and $PtRuCo_x$-T and PtRuCo-450 measured in 0.5 M H_2SO_4 + 1.0 M CH_3OH solution. The Pt loading was 0.01 mg cm^{-2}. The PtRuCo, $PtRuCo_x$ and $PtRuCo_x$-450 and PtRuCo-450 show the typical polarization curves for MOR.[5, 57-59] The peak current density of the forward scan indicates the electrocatalystic activity of the catalysts for the MOR. PtRuCo alloy NPs catalysts show the peak current density of 360 A g^{-1}_{Pt} at 0.65 V and onset potential of 0.3 V. After dealloying, $PtRuCo_x$ NPs catalysts show the peak

current density of 608 A g^{-1}_{Pt} at 0.65 V, which is 1.7 times of that before dealloying. The onset potential for MOR is 0.22 V, 80 mV lower than of PtRuCo. The electroactivity is further improved after annealing and the electrocatalystic activity of the $PtRuCo_x$ increases with the annealing temperature with the optimum results achieved for the $PtRuCo_x$ annealed at 450°C (Fig. 9.8B). For the MOR on $PtRuCo_x$-450, the peak current density at 0.63 V is 1017 A g^{-1}_{Pt} and the onset potential is 0.22 V. The electrocatalystic activity of $PtRuCo_x$-450 is 2.8 times of PtRuCo and 1.7 times of $PtRuCo_x$, despite the fact that the ESA of $PtRuCo_x$ is 110.5 m^2 g^{-1}_{Pt}, higher than 63.9 m^2 g^{-1}_{Pt} of $PtRuCo_x$-450. The peak current density for the reaction on PtRuCo-450 is 809 A g^{-1}_{Pt}, also higher than that of $PtRuCo_x$ electrocatalysts. This indicates that the PtRu skinned PtRuCo core structure obtained by successive dealloying and annealing can significantly enhances the electrocatalytic activity for MOR.

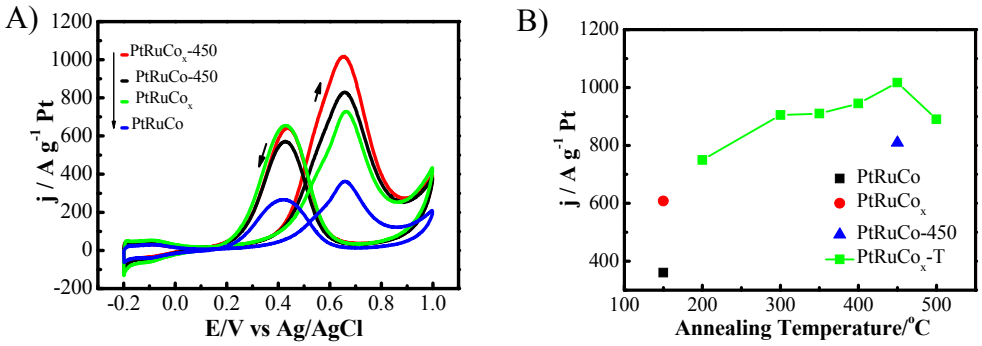

Figure 9.9. (A) cyclic voltammetric curves of the methanol oxidation reaction on PtRuCo, $PtRuCo_x$, $PtRuCo_x$-450 and PtRuCo-450 in an N_2-saturated 0.5 M H_2SO_4 + 1.0 M CH_3OH solution with the scanning rate of 0.05 V s^{-1}, and B) the change of peak forward current density of catalysts treated at different conditions.

The superior activity of $PtRuCo_x$ annealed at 450 °C, $PtRuCo_x$-450 was further confirmed by the chronoamperometry (CA) data recorded in a 0.5 M H_2SO_4 + 1.0 M CH_3OH solution at a constant potential of 0.6 and 0.4 V at room temperature for a

period of 5000 s (Fig. 9.10). For comparison, the activity of a commercial PtRu/C (60% PtRu, Alfa Aesar) was also tested. The oxidation current decreased continuously for all the catalysts studied due to the poisoning of intermediate species, such as CO_{ads}, CH_3OH_{ads}, $COOH_{ads}$, and CHO_{ads} formed during the MOR.[60] For the reaction measured at 0.6 V (Fig. 9.10A), the current density drops dramatically from 354 A g^{-1}_{Pt} to 37 A g^{-1}_{Pt} after polarized for 5000 s in the case of PtRuCo. After dealloying, the stability of the $PtRuCo_x$ is slightly improved, reaching 96 A g^{-1}_{Pt} at the end of the test. The best performance was obtained on $PtRuCo_x$ NPs catalysts annealed at 450 ^oC, $PtRuCo_x$-450. After polarization at 0.6 V for 5000 s, the current density is 234 A g^{-1}_{Pt}, 1.6 times higher of 145 A g^{-1}_{Pt} measured on conventional PtRu/C catalysts. Similar stability behavior was also observed for the electrocatalysts polarized under 0.4 V (Fig. 9.10B), a more realistic potential for the practical application of electrocatalysts for methanol fuel cells.[2, 61-62] After 5000 s polarization, the current density for $PtRuCo_x$-450 is 40 A g^{-1}_{Pt}, which is 5 and 2.7 times of PtRuCo (8 A g^{-1}_{Pt}) and $PtRuCo_x$ (15 A g^{-1}_{Pt}), respectively, and 1.6 times of PtRu/C (25 A g^{-1}_{Pt}). The superior performance stability of $PtRuCo_x$-450 NP catalysts is consistent with its high activity for the CO oxidation, as shown in Fig. 9.8.

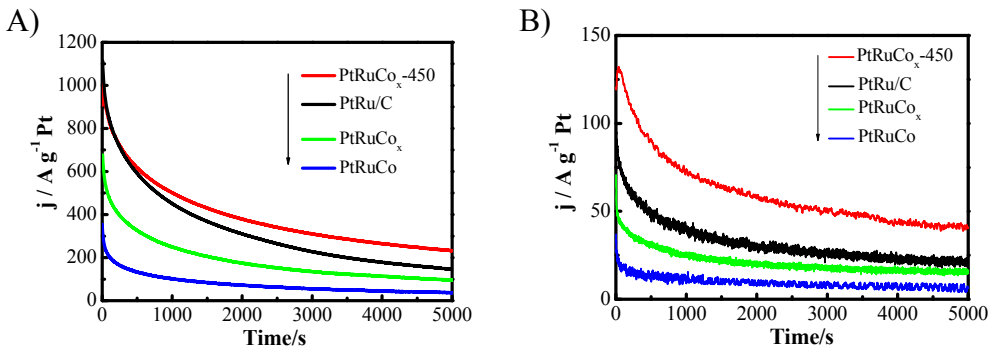

Figure 9.10. Chronoamperometry curves for the MOR reaction on PtRuCo, $PtRuCo_x$, $PtRuCo_x$-450, and PtRu/C, measured in a 0.5 M H_2SO_4 + 1.0 M CH_3OH solution at (A) 0.6 V and (B) 0.4 V for a period of 5000 s.

The microstructural stability of Pt-based electrocatalysts is a critical parameter for the durability of fuel cells. The stability of the PtRuCo, $PtRuCo_x$-450 NP catalysts and PtRu/C was evaluated by CV within the scan widow of -0.2 to 1.0 V in a 0.5 M H_2SO_4 + 1.0 M CH_3OH solution at scan rate of 0.05 V s^{-1}. Fig. 9.11 is the plots of the forward peak current density as a function of the number of cycles. In the case of conventional PtRu/C, the initial activity for the MOR is very high, 1092 A g^{-1}_{Pt}, but decreases rather rapidly with the polarization cycle. After ~1000 cycles, the current density drops to 273 A g^{-1}_{Pt}, only 25% of the initial peak current density, indicating the poor structural stability of the conventional PtRu/C catalysts. The PtRuCo alloy catalysts show significantly better stability as compared with the conventional PtRu/C catalysts, the activity is reduced to 49% of the original activity after 1000 cycles. The $PtRuCo_x$ annealed at 450^{o}C, $PtRuCo_x$-450, shows excellent structural stability. After 1000 cycles, the anodic peak current is 821 A g^{-1}_{Pt}, ~74% of the initial value and substantially higher than 192 A g^{-1}_{Pt} and 273 A g^{-1}_{Pt} obtained on PtRuCo and PtRu/C catalysts, respectively. The significant enhancement of microstructural stability of $PtRuCo_x$-450 electrocatalysts is most likely related to the specific Co rich PtRuCo-core and PtRu skinned shell structures, achieved by the subsequent dealloying and annealing treatment. This is consistent with the observation reported by Wang et. al that long-term cycling does not change the microstructure of PtNi alloy for oxygen reduction after successive dealloying and annealing treatment.[32] Wang et al also demonstrated that annealing Pt_3Co NPs at 400 or 700 ^{o}C resulted in the ordered Pt_3Co intermetallic cores with a 2-3 atomic-layer-thick platinum shell, and this structure show superior stability for oxygen reduction.[50] The interaction or bonding between the Pt NPs and CNTs may also play an important role in the electrocatalytic activity and stability of CNTs supported Pt-based NPs. Zhou et al. investigated the interaction between Pt NPs and CNTs using X-ray absorption near edge structures (XAENES).[63]

They showed that the crystalline Pt NPs interact with CNTs through synergic binding involving charge redistribution between C2p-derived states and Pt5d bands due to the presence of unsaturation in the graphene sheets (delocalized π orbitals). Such bonding scheme would facilitate the uniform dispersion and immobilization of Pt-based NPs on the CNT surface, which would prevent lateral diffusion of Pt NPs under fuel cell operating conditions.

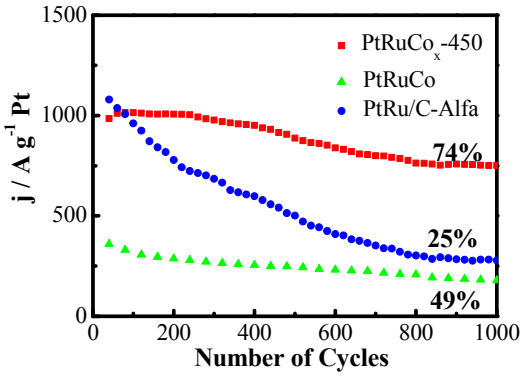

Figure 9.11. Plots of forward peak current density for the MOR on PtRuCo, $PtRuCo_x$-450 and PtRu/C electrocatalysts measured in 0.5 M H_2SO_4 + 1.0 M CH_3OH solution at the scan rate of 0.05 V s^{-1}.

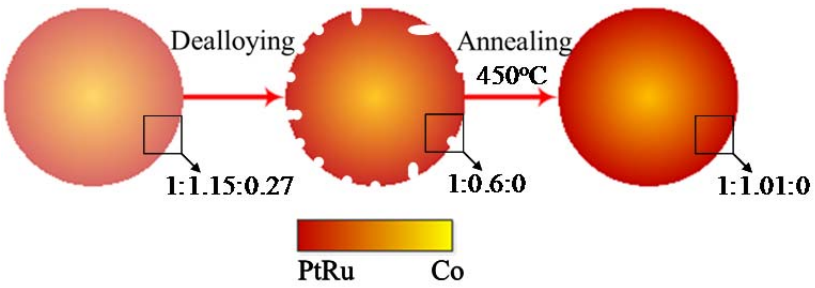

Figure 9.12. Schematic of Co core PtRu shell formation after successive dealloying and annealing of PtRuCo alloy NPs assembled on CNTs. The black box indicate the ratio of Pt:Ru:Co.

The significant difference in the atomic ratio of PtRuCo and $PtRuCo_x$ annealed at different temperatures as analyzed by ICP and XPS, and the HAADF-STEM-EDS mapping of $PtRuCo_x$-450 demenstrated the formation of Co-rich PtRuCo core PtRu-rich shell structure after sequential dealloying and annealing process. The

composition of Pt:Ru:Co = 1:1.15:0.27 from the XPS analysis for the PtRuCo alloy NPs assembled on the CNTs indicate that cobalt precursor, Co^{2+} may have a high affinity for the self-assembly on PEI-functionalized CNTs, probably due to its small ionic size as compared to $PtCl_6^{2-}$ and Ru^{2+}. Dealloying treatment of PtRuCo in HNO_3 acid would leach Co from the surface layer, leaving the $PtRuCo_x$ NPs with a Pt-rich PtRu shell with Pt:Ru ratio of 1:0.56. The deviation of the PtRu ratio from 1:1 may explain the relatively low activity of $PtRuCo_x$ as compared to that after the annealing (Fig. 9.10B). Annealing at 450^{o}C would lead the segregation and rearrangement of PtRu surface layer, demenstrated by the formation of ～1 nm thick PtRu shell with Pt:Ru ratio of 1:1 (see Fig. 9.6 and Table 9.2). Fig. 9.12 shows schematically the formation of Co-rich PtRuCo core and PtRu-rich shell structured $PtRuCo_x$ NPs supported on CNTs using combined dealloying and annealing treatment. The core-shell $PtRuCo_x$ NPs electrocatalysts not only show significantly enhanced electrocatalytic activity, but also improved CO-tolerance and structural durability for MOR.

9.4 Conclusion

In summary, $PtRuCo_x$ alloy NPs were successfully and homogenously dispersed on PEI functionalized CNTs with targeted PtRuCo atomic ratio through in situ self-assembly and reduction of multi-component Pt, Ru and Co precursor assisted by microwave irradiation. Subsequent dealloying and annealing treatment led to the formation of core-shell structured $PtRuCo_x$ NPs catalysts with Co-rich PtRuCo core and PtRu-rich shell. The obtained catalysts show significantly enhanced activity and stability for MOR and the best activity were obtained on $PtRuCo_x$ annealed at 450^{o}C, $PtRuCo_x$-450. The $PtRuCo_x$-450 catalysts exhibit almost 300% increase in the mass activity for MOR as compared to PtRuCo. The $PtRuCo_x$-450 also shows high activity

and excellent durability, as compared with the conventional PtRu/C catalysts. The specific formed Co-rich PtRuCo core and PtRu-rich shell structure could contribute to the substantially enhanced activity and excellent structural stability of the ternary $PtRuCo_x$ for DMFCs.

Acknowledgement

The project was supported by the Australian Research Council *Discovery Project* funding scheme (project number: DP120102325 & DP120104932) and the Major International (Regional) Joint Research Project of NNSFC (51210002), China. The authors acknowledge the facilities, and the scientific and technical assistance of the National Imaging Facility at the Centre for Microscopy, Characterization & Analysis, and the University of Western Australia, a facility funded by the University, State and Commonwealth Governments.

References:

1. X. Zhao, M. Yin, L. Ma, L. Liang, C. Liu, J. Liao, T. Lu and W. Xing, *Energy & Environmental Science*, 2011, 4, 2736-2753.
2. Y. L. Hsin, K. C. Hwang and C.-T. Yeh, *Journal of the American Chemical Society*, 2007, 129, 9999-10010.
3. P. Ferrin, A. U. Nilekar, J. Greeley, M. Mavrikakis and J. Rossmeisl, *Surface Science*, 2008, 602, 3424-3431.
4. H. Huang and X. Wang, *J. Mater. Chem. A*, 2014, 2, 6266-6291.
5. S. Y. Wang, X. Wang and S. P. Jiang, *Langmuir*, 2008, 24, 10505-10512.
6. B. Wu, D. Hu, Y. Kuang, B. Liu, X. Zhang and J. Chen, *Angewandte Chemie*, 2009, 121, 4845-4848.
7. A. B. A. A. Nassr and M. Bron, *Chemcatchem*, 2013, 5, 1472-1480.
8. K. Sundmacher, *Industrial & Engineering Chemistry Research*, 2010, 49, 10159-10182.
9. C. Hu, Y. Cao, L. Yang, Z. Bai, Y. Guo, K. Wang, P. Xu and J. Zhou, *Applied Surface Science*, 2011, 257, 7968-7974.
10. Y. Lu, Y. Jiang, H. Wu and W. Chen, *The Journal of Physical Chemistry C*, 2013, 117, 2926-2938.

11. S. Maksimuk, S. Yang, Z. Peng and H. Yang, *Journal of the American Chemical Society*, 2007, 129, 8684-8685.
12. L. R. Alden, C. Roychowdhury, F. Matsumoto, D. K. Han, V. B. Zeldovich, H. D. Abruña and F. J. DiSalvo, *Langmuir*, 2006, 22, 10465-10471.
13. O. Guillen-Villafuerte, R. Guil-Lopez, E. Nieto, G. Garcia, J. L. Rodriguez, E. Pastor and J. L. G. Fierro, *International Journal of Hydrogen Energy*, 2012, 37, 7171-7179.
14. V. Neburchilov, J. Martin, H. Wang and J. Zhang, *Journal of Power Sources*, 2007, 169, 221-238.
15. M. K. Debe, *Nature*, 2012, 486, 43-51.
16. X. Zhou, Y. Gan, J. Du, D. Tian, R. Zhang, C. Yang and Z. Dai, *Journal of Power Sources*, 2013, 232, 310-322.
17. S. Wang, S. P. Jiang and X. Wang, *Nanotechnology*, 2008, 19.
18. M. K. Carpenter, T. E. Moylan, R. S. Kukreja, M. H. Atwan and M. M. Tessema, *Journal of the American Chemical Society*, 2012, 134, 8535-8542.
19. Y. Kang, M. Li, Y. Cai, M. Cargnello, R. E. Diaz, T. R. Gordon, N. L. Wieder, R. R. Adzic, R. J. Gorte, E. A. Stach and C. B. Murray, *Journal of the American Chemical Society*, 2013, 135, 2741-2747.
20. K. Kuttiyiel, K. Sasaki, Y. Choi, D. Su, P. Liu and R. R. Adzic, *Nano Letters*, 2012, DOI: 10.1021/nl303362s.
21. Y. Kang, X. Ye, J. Chen, Y. Cai, R. E. Diaz, R. R. Adzic, E. A. Stach and C. B. Murray, *Journal of the American Chemical Society*, 2013, 135, 42-45.
22. H. Chen, D. Wang, Y. Yu, K. A. Newton, D. A. Muller, H. Abruna and F. J. DiSalvo, *Journal of the American Chemical Society*, 2012, 134, 18453-18459.
23. H.-P. Cong, X.-C. Ren and S.-H. Yu, *Chemcatchem*, 2012, 4, 1555-1559.
24. F. A. Viva, M. M. Bruno, M. Jobbágy and H. R. Corti, *The Journal of Physical Chemistry C*, 2011, 116, 4097-4104.
25. C. Zhou, H. Wang, F. Peng, J. Liang, H. Yu and J. Yang, *Langmuir*, 2009, 25, 7711-7717.
26. T. Saida, N. Ogiwara, Y. Takasu and W. Sugimoto, *The Journal of Physical Chemistry C*, 2010, 114, 13390-13396.
27. N. Kakati, J. Maiti, S. H. Jee, S. H. Lee and Y. S. Yoon, *Journal of Alloys and Compounds*, 2011, 509, 5617-5622.
28. M. V. Martínez-Huerta, J. L. Rodríguez, N. Tsiouvaras, M. A. Peña, J. L. G. Fierro and E. Pastor, *Chemistry of Materials*, 2008, 20, 4249-4259.
29. K.-W. Park, J.-H. Choi, K.-S. Ahn and Y.-E. Sung, *The Journal of Physical Chemistry B*, 2004, 108, 5989-5994.
30. M. K. Jeon, K. R. Lee and S. I. Woo, *Langmuir*, 2010, 26, 16529-16533.
31. J. X. Wang, H. Inada, L. Wu, Y. Zhu, Y. Choi, P. Liu, W.-P. Zhou and R. R. Adzic, *Journal of the American Chemical Society*, 2009, 131, 17298-17302.

32. C. Wang, M. Chi, D. Li, D. Strmcnik, D. van der Vliet, G. Wang, V. Komanicky, K.-C. Chang, A. P. Paulikas, D. Tripkovic, J. Pearson, K. L. More, N. M. Markovic and V. R. Stamenkovic, *Journal of the American Chemical Society*, 2011, 133, 14396-14403.
33. D. Wang, P. Zhao and Y. Li, *Sci. Rep.*, 2011, 1.
34. K. Maruya, R. Yamauchi, T. Narushima, S. Miura and T. Yonezawa, *Journal of Nanoscience and Nanotechnology*, 2013, 13, 2999-3003.
35. P. Ochal, J. L. G. de la Fuente, M. Tsypkin, F. Seland, S. Sunde, N. Muthuswamy, M. Ronning, D. Chen, S. Garcia, S. Alayoglu and B. Eichhorn, *Journal of Electroanalytical Chemistry*, 2011, 655, 140-146.
36. S. Alayoglu, A. U. Nilekar, M. Mavrikakis and B. Eichhorn, *Nature Materials*, 2008, 7, 333-338.
37. N. Hodnik, M. Bele and S. Hočevar, *Electrochemistry Communications*, 2012, 23, 125-128.
38. S. Alayoglu, P. Zavalij, B. Eichhorn, Q. Wang, A. I. Frenkel and P. Chupas, *Acs Nano*, 2009, 3, 3127-3137.
39. V. R. Stamenkovic, B. Fowler, B. S. Mun, G. Wang, P. N. Ross, C. A. Lucas and N. M. Markovic, *Science*, 2007, 315, 493-497.
40. L.-L. Wang and D. D. Johnson, *Journal of the American Chemical Society*, 2009, 131, 14023-14029.
41. Y.-C. Hsieh, Y. Zhang, D. Su, V. Volkov, R. Si, L. Wu, Y. Zhu, W. An, P. Liu, P. He, S. Ye, R. R. Adzic and J. X. Wang, *Nat Commun*, 2013, 4.
42. S. Alayoglu, A. U. Nilekar, M. Mavrikakis and B. Eichhorn, *Nat Mater*, 2008, 7, 333-338.
43. N. Muthuswamy, J. L. G. de la Fuente, D. T. Tran, J. Walmsley, M. Tsypkin, S. Raaen, S. Sunde, M. Rønning and D. Chen, *International Journal of Hydrogen Energy*, 2013, 38, 16631-16641.
44. M. Ahmadi, F. Behafarid, C. Cui, P. Strasser and B. R. Cuenya, *Acs Nano*, 2013, DOI: 10.1021/nn403793a.
45. D. Wang, Y. Yu, H. L. Xin, R. Hovden, P. Ercius, J. A. Mundy, H. Chen, J. H. Richard, D. A. Muller, F. J. DiSalvo and H. D. Abruña, *Nano Letters*, 2012, 12, 5230-5238.
46. D. Wang, H. L. Xin, R. Hovden, H. Wang, Y. Yu, D. A. Muller, F. J. DiSalvo and H. D. Abruña, *Nat Mater*, 2012, advance online publication.
47. K. W. Park, J. H. Choi, K. S. Ahn and Y. E. Sung, *Journal of Physical Chemistry B*, 2004, 108, 5989-5994.
48. G. Lee, J. H. Shim, H. Kang, K. M. Nam, H. Song and J. T. Park, *Chem. Commun.*, 2009, DOI: 10.1039/b911068b, 5036-5038.
49. M. Oezaslan, M. Heggen and P. Strasser, *Journal of the American Chemical Society*, 2011, 134, 514-524.
50. D. Wang, H. L. Xin, R. Hovden, H. Wang, Y. Yu, D. A. Muller, F. J. DiSalvo and H. D. Abruña, *Nat Mater*, 2013, 12, 81-87.

51. Y. Sun, L. Zhuang, J. Lu, X. Hong and P. Liu, *Journal of the American Chemical Society*, 2007, 129, 15465-+.
52. F. Bensebaa, N. Patrito, Y. Le Page, P. L'Ecuyer and D. Wang, *Journal of Materials Chemistry*, 2004, 14, 3378-3384.
53. K. C. Park, I. Y. Jang, W. Wongwiriyapan, S. Morimoto, Y. J. Kim, Y. C. Jung, T. Toya and M. Endo, *Journal of Materials Chemistry*, 2010, 20, 5345-5354.
54. P. Strasser, S. Koh, T. Anniyev, J. Greeley, K. More, C. Yu, Z. Liu, S. Kaya, D. Nordlund, H. Ogasawara, M. F. Toney and A. Nilsson, *Nat Chem*, 2010, 2, 454-460.
55. S. Koh and P. Strasser, *Journal of the American Chemical Society*, 2007, 129, 12624-12625.
56. M. Tsypkin, J. L. G. de la Fuente, S. García Rodríguez, Y. Yu, P. Ochal, F. Seland, O. Safonova, N. Muthuswamy, M. Rønning, D. Chen and S. Sunde, *Journal of Electroanalytical Chemistry*, 2013, 704, 57-66.
57. R. Ahmadi and M. K. Amini, *Int. J. Hydrog. Energy*, 2011, 36, 7275-7283.
58. E. Antolini, J. R. C. Salgado and E. R. Gonzalez, *Appl. Catal. B-Environ.*, 2006, 63, 137-149.
59. P. J. Kulesza, B. Grzybowska, M. A. Malik, M. Chojak and K. Miecznikowski, *J. Electroanal. Chem.*, 2001, 512, 110-118.
60. P. Ferrin and M. Mavrikakis, *Journal of the American Chemical Society*, 2009, 131, 14381-14389.
61. C. Bock, C. Paquet, M. Couillard, G. A. Botton and B. R. MacDougall, *Journal of the American Chemical Society*, 2004, 126, 8028-8037.
62. Y. Cheng, C. W. Xu, P. K. Shen and S. P. Jiang, *Appl. Catal. B-Environ.*, 2014, 158-159, 140-149.
63. J. G. Zhou, X. T. Zhou, X. H. Sun, R. Y. Li, M. Murphy, Z. F. Ding, X. L. Sun and T. K. Sham, *Chem. Phys. Lett.*, 2007, 437, 229-232.

Chapter 10: Conclusions and Recommendations

10.1 Conclusions

This thesis includes a series of studies on the electrochemical property of CNTs, and developed different types of CNTs hybrids for water splitting and fuel cells. The thesis consists of two main parts (water splitting and fuel cells) and the conclusions can be made as follow:

1) CNTs with 2-7 concentric tubes or walls show significantly better activity for H_2 evolution, O_2 evolution and O_2 reduction reactions, as compared to typical single-walled and multi-walled CNTs. Such activity is related to the effect of inner tubes of CNTs rather than the surface active sites. The much better activity of CNTs with 2-7 walls is most likely due to the separation of functionality of outer wall and inner tubes and the fast electron transfer between the outer wall and inner tube through electron tunneling. For SWNTs, such separation of functionality is not possible, while effective separation or dual functionality of the CNTs diminishes as the number of walls increases due to the reduced driven forces across the walls or layers of MWNTs.

2) The kinetics and mechanisms of OER on CNTs were studied and the CNTs composed of 2-7 concentric tubes and with an OD of 2-5 nm show significantly higher kinetics for OER. The activity of the CNTs for OER is closely related with the concentration of OH^- groups and is limited by the deprotonation of water. The

favorable kinetics for OER on CNTs that composed of between 2-7 concentric tubes further support the proposed tunneling effect.

3) Zn phthalocyanine functionalized CNTs composed of 2-7 concentric tubes show significantly higher photo-current compared with typical SWNTs and MWNTs due to the better electron separation ability resulted from tunneling effect. The findings explore an opportunity to develop high efficient photo catalysts for water oxidation.

4) One-pot synthesis of metal-CNTs hybrids can be a highly efficient, scalable and low-cost one-step synthesis method for developing highly active and stable catalysts for electrochemical water splitting in alkaline solutions. M-CNTs-Arc with $NiCo_{0.16}Fe_{0.34}$ metal core shows very high activity and superior stability for OER, achieving 100 A g^{-1} at overpotential (η) of 0.29 V and 500 A g^{-1} at η = 0.37 V in 1 M KOH solution. This is probably the highest activity reported for OER in alkaline solutions.

5) PtRu NPs supported on PEI, AP and in less extent PDDA functionalized CNTs exhibit significantly higher electrocatalystic activity and stability for the electro-oxidation of methanol as compared with PtRu supported on THF-CNTs and conventional acid-treated CNTs. The superior activity of PtRu supported on functionalized CNTs is most likely due to the strong interaction between the electron rich nitrogen-containing functional groups of the functionalization agents such as PEI, AP and in less extend PDDA and the PtRu NPs assembled on CNTs.

6) The core-shell $PtRuCo_x$ NPs were prepared through a successive dealloying and annealing treatment of PtRuCo alloy particles. The best results were obtained on dealloyed $PtRuCo_x$ NPs annealed at 450 ^oC, which exhibited a ～1 nm thick PtRu shell and Co rich PtRuCo core. The chronoamperometry studies at 0.4 V (*vs*. Ag/AgCl) show that core-shell structured $PtRuCo_x$ catalysts exhibit a high activity (40 A g^{-1}_{pt}) and significant tolerance towards CO poisoning for MOR as compared with PtRuCo alloy (8 A g^{-1}_{Pt}) and conventional PtRu/C (25 A g^{-1}_{Pt}) electrocatalysts. The core-shell structured $PtRuCo_x$ is also structurally stable, maintaining 74% of the activity after 1000 cycle between -0.2 to 1 V (*vs*. Ag/AgCl), significantly higher than 49% for PtRuCo alloy catalysts and 25% for PtRu/C catalysts under identical test conditions. The substantially enhanced electrocatalytic activity and durability of core-shell structured $PtRuCo_x$ indicate great potential to enhance the catalystic properties by fine-tuning of the nanoscale architecture.

10.2 Recommendations

This thesis focuses on developing CNTs based electrocatalysts for water splitting and methanol oxidation. Future works can be devoted into the following area:

1) Exploring the relationship of inherent properties of CNTs with the electrochemical properties of CNTs is needed by employing computational simulation and calculation. And it might be usefull to detect the tunneling effect of the CNTs or sudy single CNTs using recently developed multi-probe platform based on scanning electrochemical cell microscopy.

2) The excellent electrochemical properties of CNTs do explore an area for developing excellent catalysts based on CNTs composed of 2-7 concentric tubes. Catalyst such as Pt, Pd was supported onto CNTs composed of 2-7 concentric tubes

and show enhanced activity for methanol or ethanol oxidation. Chapter 6 demonstrated, CNTs composed of 2-7 concentric tubes can be idea candidates to develop photo catalysts for water splitting or other applications. Further exploration can be invested into developing CNTs hybrids based on CNTs composed of 2-7 concentric tubes.

3) The one pot synthesis of metal-CNTs hybrids brings opportunities to develop cheap, stable, high active catalysts for water splitting at large scale. Further efforts are needed to explore metal-CNTs hybrids through one pot synthesis for energy conversion and storage.

4) Functionalize the CNTs with different agents can not only control the particle size and distribution, but also tune the activity and the stability. Therefore, further study using theoretical calculation can be invested to explore the relationship between the electrocatalytic performances and the polymer structure.

5) Dealloying and thermal annealing were demonstrated to be an effective method to prepare highly active catalysts with superior stability for methanol oxidation. It is worthy a shot to apply this strategy to develop catalysts for ethanol oxidation, hydrogen evolution etc.

Appendix I

Permission of Reproduction from the Copyright Owner

Title: One-Pot Synthesis of Metal –Carbon Nanotubes Network Hybrids as Highly Efficient Catalysts for Oxygen Evolution Reaction of Water Splitting

Author: Yi Cheng, Chang Liu, Hui-Ming Cheng, et al

Publication: Applied Materials

Publisher: American Chemical Society

Date: Jul 1, 2014

PERMISSION/LICENSE IS GRANTED FOR YOUR ORDER AT NO CHARGE

This type of permission/license, instead of the standard Terms & Conditions, is sent to you because no fee is being charged for your order. Please note the following:

- Permission is granted for your request in both print and electronic formats, and translations.
- If figures and/or tables were requested, they may be adapted or used in part.
- Please print this page for your records and send a copy of it to your publisher/graduate school.
- Appropriate credit for the requested material should be given as follows: "Reprinted (adapted) with permission from (COMPLETE REFERENCE CITATION). Copyright (YEAR) American Chemical Society." Insert appropriate information in place of the capitalized words.
- One-time permission is granted only for the use specified in your request. No additional uses are granted (such as derivative works or other editions). For any other uses, please submit a new request.

BACK CLOSE WINDOW

ELSEVIER ORDER DETAILS

May 24, 2015

This is an Agreement between ("You") and Elsevier ("Elsevier"). It consists of your order details, the terms and conditions provided by Elsevier ("Elsevier"), and the payment terms and conditions.

Order Number	501012668
Order Date	May 24, 2015
Licensed content publisher	Elsevier
Licensed content publication	Electrochimica Acta
Licensed content title	Core–Shell Structured PtRuCox Nanoparticles on Carbon Nanotubes as Highly Active and Durable Electrocatalysts for Direct Methanol Fuel Cells
Licensed content author	None
Licensed content date	Available online 27 January 2015
Licensed content volume number	n/a
Licensed content issue number	n/a
Number of pages	1
Start Page	None
End Page	None
Type of Use	reuse in a thesis/dissertation
Intended publisher of new work	other
Portion	full article
Format	electronic
Are you the author of this Elsevier article?	Yes
Will you be translating?	No
Title of your thesis/dissertation	Carbon Nanotubes Based Nanostructured Catalysts for Water Electrolysis and Fuel Cells
Expected completion date	Jun 2015
Estimated size (number of pages)	
Elsevier VAT number	GB 494 6272 12
Permissions price	Not Available
VAT/Local Sales Tax	Not Available
Total	Not Available

ELSEVIER LICENSE
TERMS AND CONDITIONS

May 24, 2015

This is a License Agreement between Yi Cheng ("You") and Elsevier ("Elsevier") provided by Copyright Clearance Center ("CCC"). The license consists of your order details, the terms and conditions provided by Elsevier, and the payment terms and conditions.

All payments must be made in full to CCC. For payment instructions, please see information listed at the bottom of this form.

Supplier	Elsevier Limited The Boulevard,Langford Lane Kidlington,Oxford,OX5 1GB,UK
Registered Company Number	1982084
Customer name	Yi Cheng
Customer address	Fuels and Energy Technology Institute Perth, WA 6102
License number	3635700327479
License date	May 24, 2015
Licensed content publisher	Elsevier
Licensed content publication	Applied Catalysis B: Environmental
Licensed content title	Pristine carbon nanotubes as non-metal electrocatalysts for oxygen evolution reaction of water splitting
Licensed content author	None
Licensed content date	February 2015
Licensed content volume number	163
Licensed content issue number	n/a
Number of pages	9
Start Page	96
End Page	104
Type of Use	reuse in a thesis/dissertation
Intended publisher of new work	other
Portion	full article
Format	electronic
Are you the author of this Elsevier article?	Yes
Will you be translating?	No
Title of your thesis/dissertation	Carbon Nanotubes Based Nanostructured Catalysts for Water Electrolysis and Fuel Cells
Expected completion date	Jun 2015

ELSEVIER LICENSE
TERMS AND CONDITIONS

May 24, 2015

This is a License Agreement between Yi Cheng ("You") and Elsevier ("Elsevier") provided by Copyright Clearance Center ("CCC"). The license consists of your order details, the terms and conditions provided by Elsevier, and the payment terms and conditions.

All payments must be made in full to CCC. For payment instructions, please see information listed at the bottom of this form.

Supplier	Elsevier Limited The Boulevard,Langford Lane Kidlington,Oxford,OX5 1GB,UK
Registered Company Number	1982084
Customer name	Yi Cheng
Customer address	Fuels and Energy Technology Institute Perth, WA 6102
License number	3635700185280
License date	May 24, 2015
Licensed content publisher	Elsevier
Licensed content publication	Applied Catalysis B: Environmental
Licensed content title	Effect of nitrogen-containing functionalization on the electrocatalytic activity of PtRu nanoparticles supported on carbon nanotubes for direct methanol fuel cells
Licensed content author	Yi Cheng,Changwei Xu,Pei Kang Shen,San Ping Jiang
Licensed content date	October 2014
Licensed content volume number	158
Licensed content issue number	n/a
Number of pages	10
Start Page	140
End Page	149
Type of Use	reuse in a thesis/dissertation
Portion	full article
Format	electronic
Are you the author of this Elsevier article?	Yes
Will you be translating?	No
Title of your thesis/dissertation	Carbon Nanotubes Based Nanostructured Catalysts for Water Electrolysis and Fuel Cells
Expected completion date	Jun 2015
Estimated size (number of pages)	220

Copyright Clearance Center RightsLink®

Home | Create Account | Help | Live Chat

ACS Publications Most Trusted. Most Cited. Most Read.

Title: An Investigation of Thin-Film Ni–Fe Oxide Catalysts for the Electrochemical Evolution of Oxygen

Author: Mary W. Louie, Alexis T. Bell

Publication: Journal of the American Chemical Society

Publisher: American Chemical Society

Date: Aug 1, 2013

LOGIN

If you're a copyright.com user, you can login to RightsLink using your copyright.com credentials. Already **a RightsLink user** or want to learn more?

Quick Price Estimate

Permission for this particular request is granted for print and electronic formats, and translations, at no charge. Figures and tables may be modified. Appropriate credit should be given. Please print this page for your records and provide a copy to your publisher. Requests for up to 4 figures require only this record. Five or more figures will generate a printout of additional terms and conditions. Appropriate credit should read: "Reprinted with permission from {COMPLETE REFERENCE CITATION}. Copyright {YEAR} American Chemical Society." Insert appropriate information in place of the capitalized words.

If credit is given to another source for the material you requested, permission must be obtained from that source.

- Number of Table/Figure/Micrographs is a required field. Please make a selection.

I would like to...	reuse in a Thesis/Dissertation
Requestor Type	Non-profit
Portion	Table/Figure/Micrograph
Number of Table/Figure/Micrographs	-1
Format	Electronic
Select your currency	AUD - $
Quick Price	Click Quick Price

QUICK PRICE CONTINUE

This service provides permission for reuse only. If you do not have a copy of the article you are using, you may copy and paste the content and reuse according to the terms of your agreement. Please be advised that obtaining the content you license is a separate transaction not involving Rightslink.

Note: Individual Scheme and Structure reuse is free of charge and does not require a license. If the scheme or structure is identified as a Figure in the article, permission is required.

To request permission for a type of use not listed, please contact the publisher directly.

Title: Water Oxidation Catalysis: Electrocatalytic Response to Metal Stoichiometry in Amorphous Metal Oxide Films Containing Iron, Cobalt, and Nickel

Author: Rodney D. L. Smith, Mathieu S. Prévot, Randal D. Fagan, et al

Publication: Journal of the American Chemical Society

Publisher: American Chemical Society

Date: Aug 1, 2013

PERMISSION/LICENSE IS GRANTED FOR YOUR ORDER AT NO CHARGE

This type of permission/license, instead of the standard Terms & Conditions, is sent to you because no fee is being charged for your order. Please note the following:

- Permission is granted for your request in both print and electronic formats, and translations.
- If figures and/or tables were requested, they may be adapted or used in part.
- Please print this page for your records and send a copy of it to your publisher/graduate school.
- Appropriate credit for the requested material should be given as follows: "Reprinted (adapted) with permission from (COMPLETE REFERENCE CITATION). Copyright (YEAR) American Chemical Society." Insert appropriate information in place of the capitalized words.
- One-time permission is granted only for the use specified in your request. No additional uses are granted (such as derivative works or other editions). For any other uses, please submit a new request.

If credit is given to another source for the material you requested, permission must be obtained from that source.

Title: An oxygen reduction electrocatalyst based on carbon nanotube-graphene complexes

Author: Yanguang Li, Wu Zhou, Hailiang Wang, Liming Xie, Yongye Liang, Fei Wei

Publication: Nature Nanotechnology

Publisher: Nature Publishing Group

Date: May 27, 2012

Author Request

If you are the author of this content (or his/her designated agent) please read the following. If you are not the author of this content, please click the Back button and select an alternative Requestor Type to obtain a quick price or to place an order.

Ownership of copyright in the article remains with the Authors, and provided that, when reproducing the Contribution or extracts from it, the Authors acknowledge first and reference publication in the Journal, the Authors retain the following non-exclusive rights:

a) To reproduce the Contribution in whole or in part in any printed volume (book or thesis) of which they are the author(s).

b) They and any academic institution where they work at the time may reproduce the Contribution for the purpose of course teaching.

c) To reuse figures or tables created by them and contained in the Contribution in other works created by them.

d) To post a copy of the Contribution as accepted for publication after peer review (in Word or Text format) on the Author's own web site, or the Author's institutional repository, or the Author's funding body's archive, six months after publication of the printed or online edition of the Journal, provided that they also link to the Journal article on NPG's web site (eg through the DOI).

NPG encourages the self-archiving of the accepted version of your manuscript in your funding agency's or institution's repository, six months after publication. This policy complements the recently announced policies of the US National Institutes of Health, Wellcome Trust and other research funding bodies around the world. NPG recognises the efforts of funding bodies to increase access to the research they fund, and we strongly encourage authors to participate in such efforts.

Authors wishing to use the published version of their article for promotional use or on a web site must request in the normal way.

If you require further assistance please read NPG's online author reuse guidelines.

For full paper portion: Authors of original research papers published by NPG are encouraged to submit the author's version of the accepted, peer-reviewed manuscript to their relevant funding body's archive, for release six months after publication. In addition, authors are encouraged to archive their version of the manuscript in their institution's repositories (as well as their personal Web sites), also six months after original publication.

v2.0

BACK CLOSE WINDOW

Title: Polyelectrolyte Functionalized Carbon Nanotubes as Efficient Metal-free Electrocatalysts for Oxygen Reduction

Author: Shuangyin Wang, Dingshan Yu, Liming Dai

Publication: Journal of the American Chemical Society

Publisher: American Chemical Society

Date: Apr 1, 2011

PERMISSION/LICENSE IS GRANTED FOR YOUR ORDER AT NO CHARGE

This type of permission/license, instead of the standard Terms & Conditions, is sent to you because no fee is being charged for your order. Please note the following:

- Permission is granted for your request in both print and electronic formats, and translations.
- If figures and/or tables were requested, they may be adapted or used in part.
- Please print this page for your records and send a copy of it to your publisher/graduate school.
- Appropriate credit for the requested material should be given as follows: "Reprinted (adapted) with permission from (COMPLETE REFERENCE CITATION). Copyright (YEAR) American Chemical Society." Insert appropriate information in place of the capitalized words.
- One-time permission is granted only for the use specified in your request. No additional uses are granted (such as derivative works or other editions). For any other uses, please submit a new request.

If credit is given to another source for the material you requested, permission must be obtained from that source.

BACK CLOSE WINDOW

Title: Nanoscale Electrocatalysis: Visualizing Oxygen Reduction at Pristine, Kinked, and Oxidized Sites on Individual Carbon Nanotubes

Author: Joshua C. Byers, Aleix G. Güell, Patrick R. Unwin

Publication: Journal of the American Chemical Society

Publisher: American Chemical Society

Date: Aug 1, 2014

PERMISSION/LICENSE IS GRANTED FOR YOUR ORDER AT NO CHARGE

This type of permission/license, instead of the standard Terms & Conditions, is sent to you because no fee is being charged for your order. Please note the following:

- Permission is granted for your request in both print and electronic formats, and translations.
- If figures and/or tables were requested, they may be adapted or used in part.
- Please print this page for your records and send a copy of it to your publisher/graduate school.
- Appropriate credit for the requested material should be given as follows: "Reprinted (adapted) with permission from (COMPLETE REFERENCE CITATION). Copyright (YEAR) American Chemical Society." Insert appropriate information in place of the capitalized words.
- One-time permission is granted only for the use specified in your request. No additional uses are granted (such as derivative works or other editions). For any other uses, please submit a new request.

If credit is given to another source for the material you requested, permission must be obtained from that source.

BACK CLOSE WINDOW